A Study of Infrared Femtosecond Laser Irradiation on Monolayer Graphene on SiO_2/Si Substrate

Tianqi Dong

Lucy Cavendish College

University of Cambridge

A thesis submitted for the degree of

Doctor of Philosophy

April 2018

DECLARATION:

This dissertation is the result of my own work and includes nothing which is the outcome of work done in collaboration except as declared in the Preface and specified in the text. It is not substantially the same as any that I have submitted, or, is being concurrently submitted for a degree or diploma or other qualification at the University of Cambridge or any other University or similar institution except as declared in the Preface and specified in the text. I further state that no substantial part of my dissertation has already been submitted, or, is being concurrently submitted for any such degree, diploma or other qualification at the University of Cambridge or any other University or similar institution except as declared in the Preface and specified in the text. It does not exceed the prescribed word and figures limit of 65,000 and 150 respectively.

Tianqi Dong

April 2018

Acknowledgement

First, I would like to express my deepest and sincerest gratitude to Professor Bill O'Neill. Thanks for accepting me in his very welcoming and enthusiastic research group, for providing me with this excellent opportunity to see a broader and brighter side of research at the University of Cambridge. I am grateful for all the support and guidance over the past three years. Working in this group is such a beautiful and enjoyable experience. Thanks for training me to become an independent researcher for every meeting with challenging ideas, for detailed reading my reports and always giving constructive feedback. I have learned not only the rigorous research thinking but also the leadership of the team. I am very honored to witness that the team is growing from ten Ph.D. students when I stepped in and now almost thirty when I am about to leave. He is always encouraging and inspiring. Beyond that, I enjoyed every year group activities. Great sport, great food, great fun.

Special thanks to Dr. Martin Sparks, for taking a keen interest in my research with very inspiring suggestions. I am very thankful to hear that when I am talking to him about my career. He mentioned, developing people is the critical point of an excellent educator, more important than knowledge and technique, which reminds me of the ancient Chinese philosopher Confucius.

I would like to thank my research collaborators Dr. Matteo Bruna, Ugo Sassi, Dr. Silvia Milana, Professor Colm Duncan, Professor Andrea. C. Ferrari, Dr. Karolina Milowska, and Professor Mike Payne, for the fruitful discussion. Without these collaborators, this work could not be smoothly carried on. Thanks, my advisor Dr. Michael D Volder, a passionate scientist and always has thoughtful ideas. Thanks, Dr. Ronan Daly for being helpful and encouraging.

Sophie Fuller and Alice Gregory deserve particular thanks for Ph.D. life support, for organising the group events, and conferences. Thanks to all my laboratory colleagues for making this group such a beautiful place to work. Thanks, senior members of this group: Krste Pangovski, Andrew Cockburn, David Hopkinson, Karen Yu, Wenhe Feng, Matthew Bannister for giving me an overview of the journey of becoming a doctor. Especially, thanks to Dr. Andre Cockburn for the SEM/FIB training. Thanks for my "classmates" Laurent Michaux, Jon Parkins, Andy Payne, Jiho Han, Fransisco, Nicky Soane, for letting the study time in Cambridge very joyful, for the birthday tradition and tea time. I feel so lucky to witness the wedding of Jon and Lily Delimata, Francisco and Kasia, David and Rachel. I appreciate the friendship with the colleagues inside and outside our group, Yoanna Shams, Sarah Jessl, Dr. Chandramohan George, Lily Delimata, Sam Brown, Jason Ten, John Bulmer, Daniel Gortat, Katjana Lange, Diego Punin, Franco Ussi, Chris Wright, Nadeem

Gabbani, Ducle Aguilar, Alexandre Dianz and James Ryley. Institute for Manufacturing is an exciting and friendly place to learn and discuss research. I wish to thank all the lovely colleagues and thank the supportive culture embedded in Cambridge.

Thanks to my college, making a home away from home. Thanks to my tutor Dr. Annette Mahon for the kind help. I have met many inspiring friends in the house and the college choir. I have seen so many talented young women active in different areas, this inspires me a lot, and I will treasure this valuable memory and experience for my lifetime.

Thanks to my sponsor NUDT for funding this research. A special thanks to my mentor Prof. Zejin Liu for all the support and enlightenment. A heartfelt thanks to my family members Zhenkai Dong, Zhenglin Liang, Jifeng De and Tianhao Dong for morally and financially supporting me.

All in all, I thank all the people who have supported me go through this journey directly or indirectly.

Abstract

Graphene is a single hexagonal atomic carbon layer. Since its discovery, graphene is emerging as an exciting and promising new material to impact various areas of fundamental research and technology. It has potentially useful electrical properties for device applications such as graphene photodetectors and graphene-based sensors. This thesis focuses on the femtosecond laser processing of graphene from both scientific and industrial points of view.

Started from the manufacturing process, a new manufacturing route for graphene devices based on a femtosecond laser system is explored. In this thesis, the graphene ablation threshold was determined in the range of 100 mJ/cm^2. In this deposited fluence range, selective removal of graphene was achieved using femtosecond laser processing with little damage to the SiO_2 /Si substrate. This finding supports the feasibility of direct patterning of graphene for silicon-substrate field effect transistors (FETs) as the gate dielectric, silicon dioxide is only negligibly removed (2~10 nm) and no damage occurs to the silicon.

Beyond the selective removal of graphene, the effects of exposing femtosecond laser pulses on a monolayer of graphene deposited on a SiO_2/Si substrate is also studied under subthreshold irradiation conditions. It has been demonstrated that a femtosecond laser can induce defects on exposure. The dependence of the D, G, and 2D Raman spectrum lines on various laser pulse energies was evaluated using Raman Spectroscopy. The I (D)/I (G) ratio was seen to increase with increasing laser energy. The increase in the D' (intravalley phonon and defect scattering) peak at 1620 cm^{-1} appeared as defective graphene. These findings provide an opportunity for tuning graphene properties locally by applying femtosecond laser pulses. Applications might include p-n junctions, and the graphene doping process.

To explore the power absorption process in graphene and the SiO_2/Si substrate, a theoretical model was developed based on the transfer-matrix method. The results revealed that the most significant absorption was in the silicon substrate. The light reflection form each layer was considered. The model shows the temperature oscillations are more significant in the silicon layer compared to the silicon dioxide which can provide a theoretical rationale for the swelling effect observed in the experiments. This model can assist in the choice of laser parameters chosen for future laser systems used in the production of graphene devices.

List of Acronyms and Symbols

RT	Room temperature
SEM	Scanning electron microscopy
AFM	Atomic force microscopy
EDS	Energy dispersive spectroscopy
SLG	Single-layer graphene
BLG	Bi-layer graphene
MLG	Multi-layer graphene
LA	Large area
FET	Field-effect transistors
LCD	Liquid crystal display
OLED	Organic light-emitting diode
ITO	Indium tin oxide
GF	Gauge factor
ITO	Indium tin oxide
OFET	Organic field-effect transistors
CVD	Chemical vapour deposition
GNR	Graphene nanoribbons
SWNT	Single-wall carbon nanotubes
GO	Graphene oxide
MEMS	Micro electromechanical systems
NEMS	Nano-electromechanical systems
CMOS	Complementary metal oxide semiconductor
MSC	Micro-super capacitor
EPC	Electron-phonon coupling
STM	Scanning tunneling microscope
TMM	Transfer matrix method

List of Figures

List of Tables

Contents

Chapter 1 Introduction

1.1 Background

Graphene is a form of carbon with atoms arranged in a hexagonal lattice that was isolated decades earlier [1], [2], as shown in Fig 1.1. Recognised as the world thinnest but strongest material, graphene arouses great interest in scientific research [3], [4]. The extremely high carrier mobility [5], mechanical flexibility [6], and optical transparency [7] make graphene an exciting new material with the potential to impact many areas of fundamental research and high-performance devices [8], [9], [10], [11].

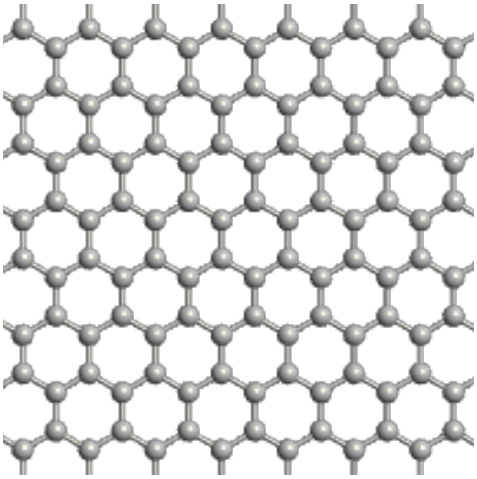

Fig 1. 1 Schematic diagram of graphene.

The current methods applied in patterning graphene are photolithographic techniques. Lithography can precisely fabricate nano/micropatterns. Lithography involves a long sequence of process operations, and in turn increases the risk of polymeric contamination. Furthermore, slow processing and costly procedures may limit the industrial-scale fabrication of graphene devices.

Although femtosecond laser micromachining may not be able to achieve nanoscale resolution [12], its advantages are limited undesirable thermal effects [13], high processing speed, and low cost compared to e-beam lithography. Recent studies have shown the potential for indirect patterning, which offers free-form post-patterning of general graphene. Roberts et al. used a single pulse laser shot (pulse duration 50 fs) to process a clean micro-hole (diameter 20 μm) [14] and Zhang et al. obtained 25 μm wide channels of graphene on a glass substrate by using a 100 fs pulse from a Ti:

sapphire laser with a central wavelength of 800 nm [15]. Sahin et al. achieved a 400 nm wide ablation channel on SiO_2/Si substrates by using a 550 fs laser with a wavelength of 343 nm to prove the capability of the femtosecond laser in nanoscale patterning, with a focus on the generation of periodic graphene stripes without complete removal [16].

Transferring lab-based research into industrial-scale production in the graphene industry is still challenging, especially for the large area production of graphene and graphene device fabrication. This thesis addresses the femtosecond laser's potential integration in graphene devices production, with emphasis on the direct ablation and locally induced defects on graphene.

1.2 Scientific novelty and importance of the investigation

The thesis explores a low-cost, fast and flexible patterning process of graphene that is enabled by a femtosecond laser. Direct removal of graphene on a SiO_2/Si substrate using a laser leads to a lithography-free method for graphene device fabrication. The defect induced by femtosecond laser on graphene surface can also create new functional graphene properties that will potentially increase the range of graphene applications. The absorption study during the femtosecond laser processing on graphene and SiO_2/Si substrate could provide a better insight on the laser interaction mechanism. In general, the success of the scientific research would pave the way for other 2D materials processing and manufacturing techniques.

According to a recent report, the global market for graphene will be over $390 million in 2024 at material level [17] and $25 billion in 2023 in terms of applications [18], [19]. Recently, a significant investment has been made in research which could accelerate the pace into more practical applications of graphene and other new technologies. For instance, the European Union has invested $ 1.3 billion in "The Graphene Flagship" [20]. The UK government has provided £ 235 million to fund graphene-related research [21]. The extremely high heat conductivity (up to 5150 W/ m·K [22]) and superconductivity of single-layer graphene [23] are vital features driving the market as they increase the possibility of integrating graphene-based devices into various applications in the electronics industry. Graphene can be used as an electrode material in solar chips, transistors, integrated chips and solar packaging. Each application will be environmentally friendly, lightweight and practical. For instance, graphene has a large surface to mass ratio and high electrical conductivity, it can be a potential material for electrodes of lithium-ion batteries [24], which could be used in electrically powered vehicles. Additionally, it can be applied in lithium-ion batteries in smartphones, laptops and tablet PCs. It can significantly lower the sizes and weights for such devices.

For the same energy that required to be storage, the higher the surface to mass ratio, the lower the mass required. Thus, graphene can not only lower the sizes but also lower the weight.

1.3 Research aims and objectives

By taking a step forward toward industrial fabrication, the potential of graphene devices could be realised in a cost-effective way. The main aim of this research is to overcome the problems of long sequences of conventional lithography, strict conditions (clean room) and expensive lab process steps for graphene device fabrication by using direct femtosecond laser processing. More specifically, to explore the feasibility using femtosecond laser system in future graphene fabrication technology. In addition, gaining a better understanding of the interaction between femtosecond laser light and monolayer graphene on SiO_2/Si substrates.

To achieve these aims, four fundamental research questions need to be answered:

- Is it possible to use the femtosecond laser pulses to replace lithographic techniques in fabricating graphene channels on SiO_2/Si substrate?
- What is the influence of the femtosecond laser on the SiO_2/Si substrate?
- Can femtosecond laser generate defects on the graphene and what are the properties of the defects introduced into graphene by the fs laser?
- What is the nature of the energy absorption for a graphene, SiO_2/Si substrate during a femtosecond laser pulse?

By understanding the way in which the graphene structure varies with laser processing parameters such as wavelength, frequency, pulse energy, pulse duration, patterning speeds, as well as the underlying physics such as energy absorption, we can take a step forward in designing a controllable femtosecond laser manufacturing process for graphene devices.

1.4 Scope of the thesis

This thesis is structured into seven chapters, a summary of each chapter is given below.

Chapter 2 reviews different fabrication methods for graphene and evaluation techniques, such as Raman spectroscopy. This chapter also summarises the state-of-art patterning techniques on graphene, including electron-beam irradiation, lithography methods, chemical patterning, and laser

processing of single/multi-layer graphene. This provides the background information for this thesis and identifies the research gaps.

Chapter 3 focuses on the material and methods applied in this work. The experimental system applied in this research is detailed, in addition to the study of the femtosecond laser exposure on graphene deposited on SiO_2/Si substrate. Characterisation methods such as optical microscopy, scanning electron microscopy, atomic force microscopy, and Raman spectroscopy are explained.

Chapter 4 investigates the various exposure parameters, such as pulse energies and scan speeds on the monolayer graphene on SiO_2/Si substrate. The focus of this chapter is the ablation effect of the femtosecond laser on the modification of the graphene at the ablated edge, with comparison results conducted in ambient air and nitrogen.

Chapter 5 explores the region of the non-ablated area of graphene on SiO_2/Si substrate after femtosecond laser exposure. The results are analysed with Raman Spectroscopy.

Chapter 6 presents a theoretical study of the energy absorption of the femtosecond laser exposure on a graphene, SiO_2/Si system. It considers the refractive index variation with laser exposure, using matrix transfer method with a Gaussian laser input.

Chapter 7 summarises the main findings of this study with suggestions for future work.

1.5 Publications resulting from this work

Articles:

Tianqi Dong, Martin Sparkes, Colm Durkan, William O'Neill, "Evaluating femtosecond laser ablation of graphene on SiO_2/Si substrate", Journal of Laser Applications, Volume 28, Issue 2.

Tianqi Dong, Karolina Milowska, Martin Sparkes, William O'Neill, Defects induced by femtosecond laser on graphene deposited on SiO_2/Si substrate, in preparation.

Tianqi Dong, Martin Sparkes, William O'Neill, Optical transmission for femtosecond pulsed laser interact with graphene deposited on SiO_2/Si substrate, in preparation.

Conference proceedings &presentations

Tianqi Dong, Martin Sparkes, William O'Neill, A study of defects induced by femtosecond laser on monolayer graphene, Euspen's 16th International Conference&Exhibition, Nottingham, UK, May 2016, proceedings and Poster presentation.

Tianqi Dong, Martin Sparkes, Colm Durkan, William O'Neill, Evaluating femtosecond laser ablation of graphene on SiO2/Si substrate, ICALEO, October, Atlanta, US, 2015, proceedings and Oral presentation.

Tianqi Dong, Femtosecond laser direct micro-cutting graphene for device applications, Ultra-Precision Manufacturing Conference, May, University of Cambridge, 2015, Poster & Oral presentation.

Tianqi Dong, Matteo Bruna, Martin Sparkes, Andrea C. Ferrari, William O'Neill, Femtosecond laser direct micro-cutting of graphene for device applications, presented at Graphene & 2D Materials Conference: From Research to Applications, National Physics Laboratory, London, 12-13 November 2014, poster presentation.

Tianqi Dong, Martin Sparkes, William O'Neill, Fabrication of graphene based on laser-induced shock wave, 1st year Ph.D. conference, the IfM, University of Cambridge, 21st May 2014, Poster & Oral presentation.

Awards:

3rd Place of Poster Prize for euspen's 16th International Conference & Exhibition, Nottingham, UK, May 2016.

1st Place of Best Student Paper Award in 34th the International Congress on Applications of Lasers & Electro-Optics (ICALEO), Atlanta, US, 18th-22nd Oct 2015.

Roger Kelly Award, Best Young Researcher Presentation in 4th International School on Lasers in Materials Science (SLIMS), Venice, Italy, 13th -20th July 2014.

Joint 2nd place of poster prize at the 1st Year Ph.D. Students' Conference at the IfM, 21st May 2014.

Chapter 2 Literature review

2.1 Introduction

This chapter presents the current state of graphene fabrication methods, graphene properties, and its application, as shown in Fig 2.1. Section 2.4 reviews the state-of-the-art of multiple types of graphene patterning techniques, with emphasis on electron beam irradiation, photolithography, plasmas/chemical etching and direct laser cutting. Femtosecond laser pulse interactions with the material, light propagation, absorption mechanisms, plasma formation, as well as the comparison of ultrafast and conventional laser interactions are also reviewed (section 2.5). In sections 2.6, the research gaps and research questions are discussed throughout the literature review.

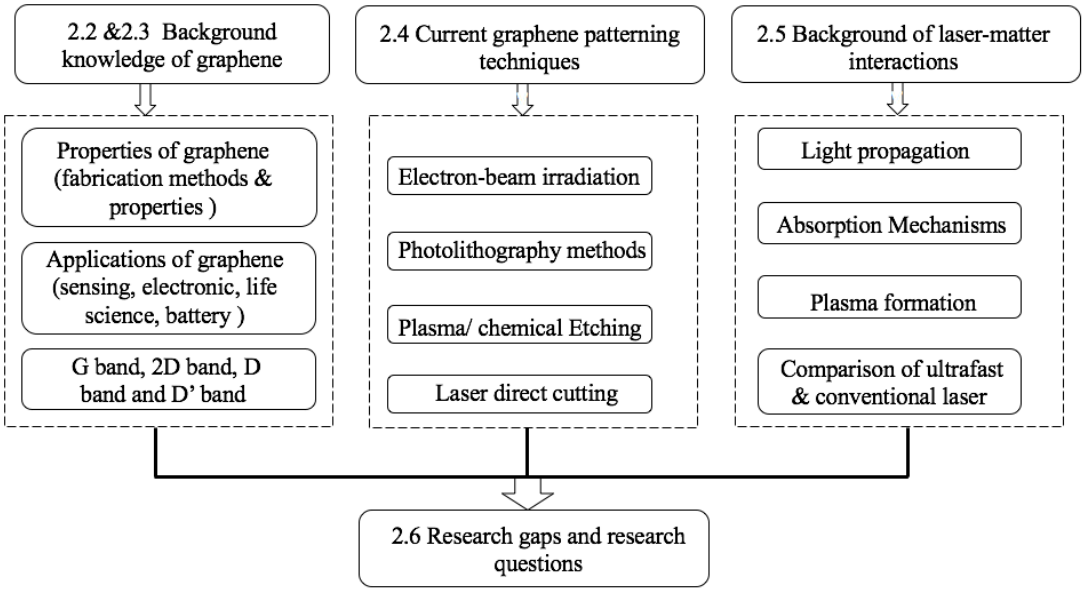

Fig 2. 1 Structure of chapter 2.

2.2 Properties and applications of Graphene

2.2.1 Properties of graphene

Although scientists knew that monolayer graphene existed, it was not until 2004 that this two-dimensional graphene was isolated by Prof. Andre Geim and Prof. Kostya Novoselov [25]. Six years after the ground-breaking isolation of graphene, they were awarded the Nobel Prize in physics in 2010. The first graphene was manufactured using scotch tape. This approach is low cost and easy

but not suitable for large-scale production. The widespread application of graphene required scalable production techniques, several methods have been steadily developed in producing large area and high quantities, necessary for industrial applications. These include mechanical exfoliation [26], chemical vapour deposition [27], [28], [29], liquid-phase exfoliation [30], [31], [32], and synthesis on SiC [33], [34], [35]. Other graphene growth methods such as unzipping carbon nanotubes [36], [37], molecular beam epitaxy [38], [39] and reduction of graphene oxide [40], [41] are also investigated to enrich the possibility of fabrication methods. However, these are unlikely to be used on a large scale since they require higher cost than CVD methods. Table 2.1 summarizes the methods of mass-production of graphene regarding size, cost, and quality. Graphene growth based on CVD method still holds the greatest promise in device applications due to its relatively low cost, high quality, and large area performance.

Table 2. 1 Graphene fabrication methods.

Methods	Properties	Purpose	Ref.
Micromechanical Exfoliation Flakes	Small-scale production, high cost, high quality, uneven films	Research purpose	[42]
CVD (on Ni, Cu) thin films	Moderate scalability, high cost, high quality, temperature (>1000°C)	Touchscreens, solar cells, smart windows, flexible LCDs & OLEDs	[43], [44]
Liquid Phase Exfoliation	High scalability, low yield, moderate quality, low cost, impure	Polymer fillers, Transparent electrodes	[31]
Epitaxial growth on SiC	Low scalability, high cost, high quality, high process, temperature (1500°C), very expensive substrate	Transistors, circuits, interconnect, memory, semiconductors.	[45]
Carbon Nanotube Unzipping	Moderate scalability, high yield, high quality, potentially low cost	FETs, interconnects, NEMs, composites	[37], [46]
Chemical Reduction of Graphite oxide (nanoflakes/powder)	High scalability, low purity, low cost, high defect density	Conductive inks & paints, polymer fillers, battery electrodes, supercapacitors, sensors	[47]

The application potential of graphene is based on its many unique properties, as shown in Table 2.2. Its ability to deform creates great interest in the application of flexible touch screens [48]. The high thermal conductivity suggests that graphene could be applied in applications where thermal management is required [22]. The saturated absorption of light permits it to be used in mode-locking of fiber lasers, acting as a saturable absorber [49]. Its high charge carrier mobility in ambient conditions, allows graphene to be a potential candidate for next generation of high-performance electronics [50].

When the large-scale production of graphene has the same outstanding performance as the best samples fabricated in the research laboratory, graphene will be of even more significant interest for industrial applications.

Table 2. 2 Properties of graphene.

Property	Value	Comparison with other material	Ref.
Tensile strength	~130 Gpa	200 times larger than steel, larger than CNT fibre 8.8 Gpa	[51], [52]
Young's modulus	~1100 Gpa (monolayer graphene)	3 times larger than CNT fibre 357 Gpa	[52]
Thermal conductivity	~4.84×10^{3} to 5.30×10^{3} W $m^{-1}\cdot K^{-1}$	More than 10 times higher than copper, and higher than CNT 3×10^{3} W$\cdot$ $m^{-1}\cdot K^{-1}$	[53], [54]
Charge carrier mobility	2.5×10^{5} $cm^{2}\cdot V^{-1}\cdot s^{-1}$	More than 100 times silicon (1350 $cm^{2}\cdot V^{-1}\cdot s^{-1}$)	[55], [56]
Absorptivity	~2.3% (400 nm ~2.5 μm)	Larger than silicon dioxide (absorption index 10^{-7} @1μm)	[57], [58], [59]

2.2.2 Applications of graphene

Graphene research has made a substantial impact on the range of potential industry applications such as electronics, energy, medicine and desalination. In this section, the well-known applications of graphene in the field of sensing, photodetector, electronic industry are listed, along with new areas in life science and battery industry.

(a) Graphene in field of sensor

Mass production of graphene from either graphene oxide or chemical vapour deposition has been demonstrated for conductive polymer composites that utilize the mechanical and tensile strength of graphene. In the field of sensing, Tian et al. show graphene micro-ribbons (20 μm width, 5mm long) used as a strain sensor with a gauge factor (GF) of up to 9.49 [60]. The graphene strain sensor shows a good linear response to strain and multi-cycle operations. Zhao et al. demonstrated nano-graphene strain sensors with GF over 300 [61], which implies that there is plenty of scope to develop better graphene strain sensors in the future.

(b) Graphene in photodetector

The zero bandgap property of monolayer graphene enables it absorbs photons of all frequencies from ultraviolet to the far infrared [62]. This wide absorption range of graphene makes it possible to work over a much wider wavelength range, compared to current IV and III-V semiconductors based photodetectors. This is because the material's absorption limits the spectral bandwidth. When the bandgap of the photodetector material is larger than the photon energy, the photon becomes transparent to the photodetector. The transparency and physical properties of graphene could make flexible and transparent photodetectors feasible [63]. Also, graphene-based photodetectors are ultrafast (50 GBit/s) [64], which is again due to its high mobility.

(c) Graphene in the electronic industry

Supercapacitors. El-Kady demonstrates a scalable fabrication method of graphene micro-scale supercapacitors over larger areas. The devices are flexible substrate based. With its low leakage current, it can be integrated with energy harvesters to create efficient self-powered micro-supercapacitors [65].

Transparent conductor. Graphene can achieve higher transmission with the same resistance as other materials such as indium tin oxide (ITO), ZnO/Ag/ZnO, single wall carbon nanotubes (SWNTs), etc. [63]. The high electrical conductivity, excellent mechanical strength, low optical absorption, and flexibility of graphene make it a promising alternative solution in replacing the high cost and non-flexible ITO in applications such as liquid crystal display, touch screens, and smart windows, etc.[63].

Logic circuits. The absence of a bandgap forbids the use of monolayer graphene for integrated circuits. For single layer graphene on SiO_2 in large areas there is no bandgap [66], [67], while graphene ribbons have shown bandgap due to lateral confinement [68], [69], [70], [71], [72]. Bilayer graphene can be experimentally made to exhibit a tunable bandgap up to 250 meV with the application of a suitable electrical field and can be potentially engineered up to 0.3 eV [72], [73], [74], [75]. These tunable bandgap properties allow bilayer graphene to hold the potential as a fast switch in logic circuits.

(d) Graphene in life science

It is worth noting that the graphene device was first focused on for its applications in transistors, sensors, etc. Since 2014, applications have become the focus of life sciences [76]. Biomedical applications are still in the early stages of development. In [77], the structure of graphene is applied to enhance the absorption of biomolecules, with the substrate of silicon, gold, and prism. The silicon in the middle layer is used to increase the sensitivity as shown in Fig 2.2. This enlarges the application of the femtosecond laser ablation on graphene on the SiO_2/Si substrate for an extended substrate such as gold etc. For the recent applications in life sciences, a specific area of attention is the merging of artificial tissue components and implants [76], [78], [79]. Graphene substrate has been proposed for the engineering of implants [80], [81], [82], [83]. The graphene is engineered in different thicknesses to allow the controlling of the penetration of various molecules.

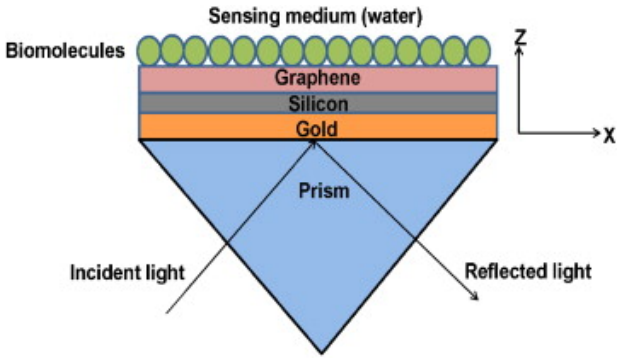

Fig 2. 2 Schematic diagram of prism-based biomolecules sensor using graphene and silicon layers [77].

(e) Graphene in battery filed

As for the battery field, the conventional battery electrodes are significantly improved with the graphene enhancement on the anode surface. There are at least two advantages that graphene can bring into the traditional battery. First, lightweight, thanks to the light and strong graphene structures. Second, is the high capacity energy storage. This is attributed to the large surface area of graphene.

The greater the surface area is, the more ions it can store. Graphene batteries as a concept have been much discussed in recent years [84]. Groups of researchers have focused on graphene supercapacitors, and the graphene battery is aimed at bridging the gap between supercapacitors and lithium ion batteries [85]. In addition, there are reports on the all-electric car with graphene-based batteries [86], [87], and this again is applied with fast charging properties; however, the question is always about mileage range. Lee et al have applied silicon nanoparticles-graphene composites for Li-ion battery anodes with a storage capacity > 2200 mA h g^{-1}. After 200 cycles, the storage capacity decreased by 0.5% per cycle [88]. The positive view towards graphene in batteries is the foundation of its feasibility from both the experimental and conceptual perspective. The challenge is the manufacturing process as well as the real practical product. The laser has shown great potential in fabricating graphene micro-supercapacitors [89], [90], [91].

2.3 Characterisation of graphene

Once the graphene growth methods have been developed, it is essential to discern the characteristics of graphene. On top of a Si wafer with a thickness of 300 nm SiO_2, the monolayer graphene can be observed as a purple-to-violet in colour [66]. For monolayer graphene, scanning electron microscopy (SEM) can be applied to view its surface topography and composition. Atomic force microscopy (AFM) can also find graphene on the substrates. However, the techniques involve electron beam (e-beam) irradiation of the samples may result in damage to the sample [92], and may result in defects giving significant deterioration of the electron and heat conduction properties even at low radiation doses [92]. Therefore, Raman spectroscopy is often applied as a useful method to identify layers of graphene and properties of graphene in a non-invasive way [93], [94].

2.3.1 Principle of Raman spectroscopy

Raman spectroscopy is a spectroscopic technique that relies on Raman scattering of monochromatic light. It obtains vibrational spectra of the material which are determined by molecular and the interatomic bonds. Raman scattering applies the quantum particle interpretation, the laser light strikes a molecular system and is inelasticity scattered. Each molecule having its own vibrational signatures. During the interaction of the incident light and molecules, two scattering effects can occur. One is known as Rayleigh scattering, which has the same frequency of the incident light. The other one is Raman scattering, where the frequency shift of the incident light, being increased or decreased by addition or subtraction of the frequency of the molecular vibration. The resultant higher frequency of the scattered photon is known as anti-stokes, while the lower frequency is known as Stokes shift, shown in Fig 2.3.

Raman scattering is a low-probability process with around 1 in 10^8 photons inelastically scattered. Due to the substantial probability that a molecule stays in the ground vibration state, Stokes Raman scattering is more intense than anti-stokes scattering [95]. Fluorescence can occur at a longer wavelength when electrons are excited to higher electronic energy levels and back to the ground energy level with the emission of a photon [96], [97].

By filtering out the wavelength that closes to the laser line (Rayleigh scattering), the rest of the scattering light (Raman scattering) is collected into a detector. Thus, the information of the vibrational, rotational and other low-frequency modes of the molecules are given.

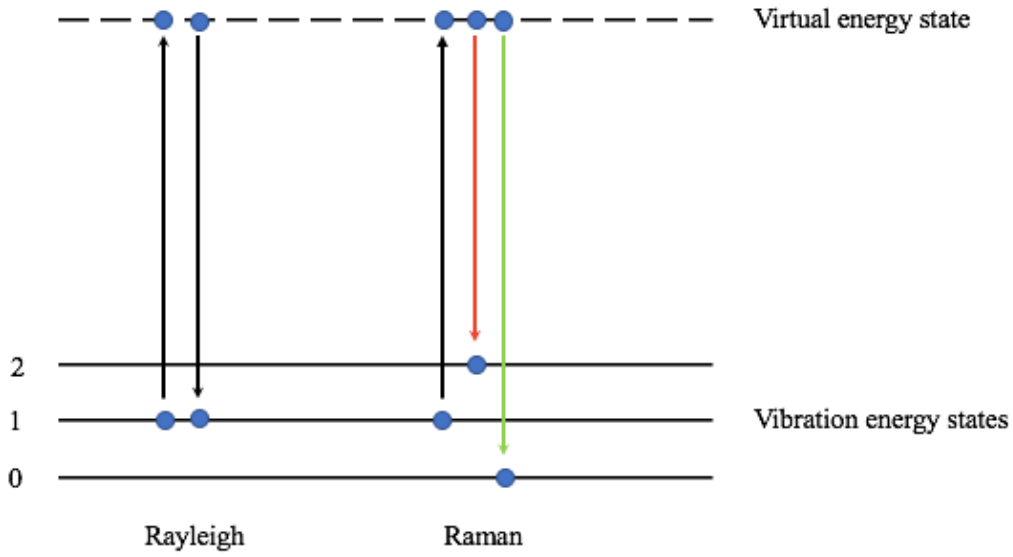

Fig 2. 3 Energy level diagram showing the states involved in Raman spectra. Red row indicates Stokes scattering while the Green arrow indicates anti-stokes scattering.

2.3.2 G band, 2D band, D band and D' band

In graphene, the Stokes photon energy shift caused by laser excitation creates two most definite peaks in the Raman spectrum, namely G band (~1580 cm^{-1}) and 2D band (~2690 cm^{-1}) [98], as shown in Fig 2.4 (a). The 2D band represents two zone-boundary phonons. The bands as shown in Fig 2.4 (b), label as G and 2D, or G', and the D, D', and their combination D+D'.

Before discussing the phonon vibration contribution to the significant Raman bands in graphene, it is necessary to begin with the phonon dispersion. The phonon dispersions of monolayer graphene contain three acoustic (A) and three optical (O) phonons. Among the six-phonon branches, there are four modes in-plane (i) and two-modes out of the plane (o). If the direction of the zone-center mode

is along the C-C bonds, the modes are transverse (T). If the direction is perpendicular to the C-C bond, the modes are longitudinal (L). Both iLO and iTO play a role for the main Raman bands observed in graphene [93], [99], [100], [101].

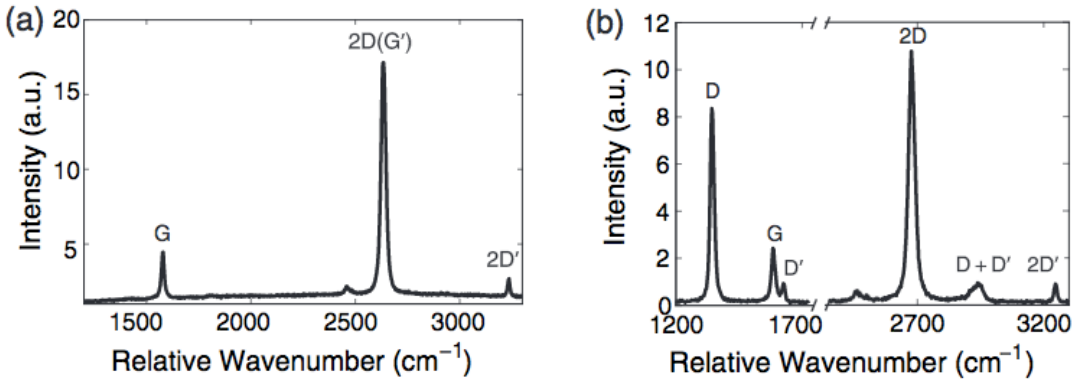

Fig 2. 4 Raman spectra of a graphene (a) A pristine flake (b) A damaged flake [99].

(a) G band and 2D band

The form of G band (~1580cm^{-1}) is attributed to in-plane sp^2 C-C stretching mode, originating from phonons at the first Brillouin zone-center Γ point [102], [103], in Fig 2.4 (a). 2D or G' band appears at around 2700 cm^{-1}, which is originating from the breathing-like in-plane mode of the carbon rings, in Fig 2.5 (b). There are two G band stretching modes of graphene. The mechanism of G band is as shown in Fig 2.5 (a). It starts with an incident photon that excites a virtual electron-hole pair in graphene. Then the electron or the hole is scattered by either an iTO or an iLO zone-center phonon [99], [104].

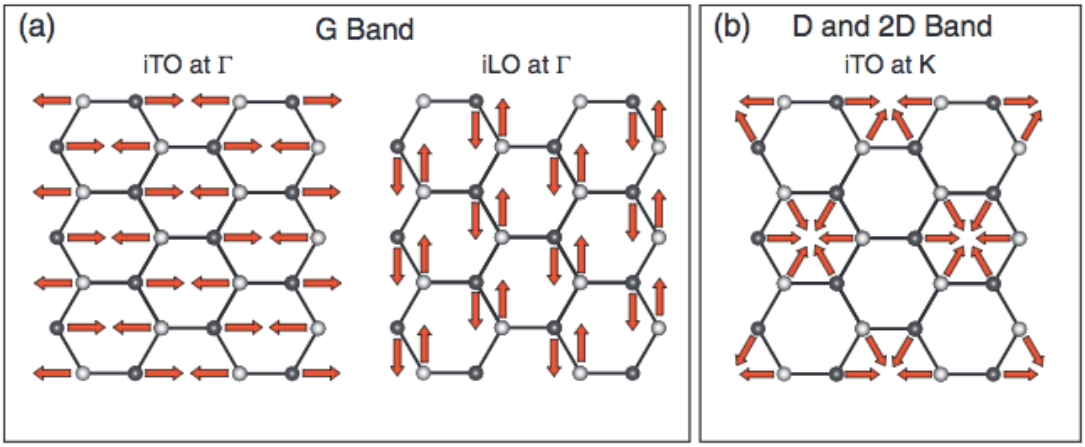

Fig 2. 5 Schematic descriptions of phonon vibrations in graphene that contribute to G band (a), D and 2D band (b) [99].

For the G band generation, when the electron-hole pair is recombined, they emit a photon. For the 2D band generation, there are two different mechanisms, one is double resonance, and the other is triple resonance. For double resonance, the incident light generates an electron-hole pair near the K point. The iTO phonon inelastically scatters an electron/hole to the K' point, and another electron/hole is scattered back by a second iTO phonon. It is called double resonance because this process happens when the incident or scattered photon and the first or second phonon scattering are resonant with the electronic states in graphene. For the triple resonance, the carriers are scattered by iTO photons from the K point to the K' point and emit a photon to recombine. Both resonances meet the energy and momentum conservation law.

(b) D band and D' band

The D band and 2D band share the same description of phonon vibration in Fig 2.5, which is attributed to the breathing-like in-plane mode of the carbon rings. For the D band that occurs near 1350 cm^{-1}, it requires a defect to conserve the momentum, as shown in Fig 2.6 (a). In such case, the electron experiences inelastic scattering through an iTO phonon to the K' point and elastically scattering back from K' point through a defect [105], [106]. The D band shift is half of that in the 2D band due to only one phonon being involved in the D band generation process [93], [107]. The defects can be controlled by using ion bombardment [108], plasma functionalization [109] or electron beam irradiation [110], [111], [112]. Both D band and 2D band happen near both the K and K' point, and they are known as intervalley process [113].

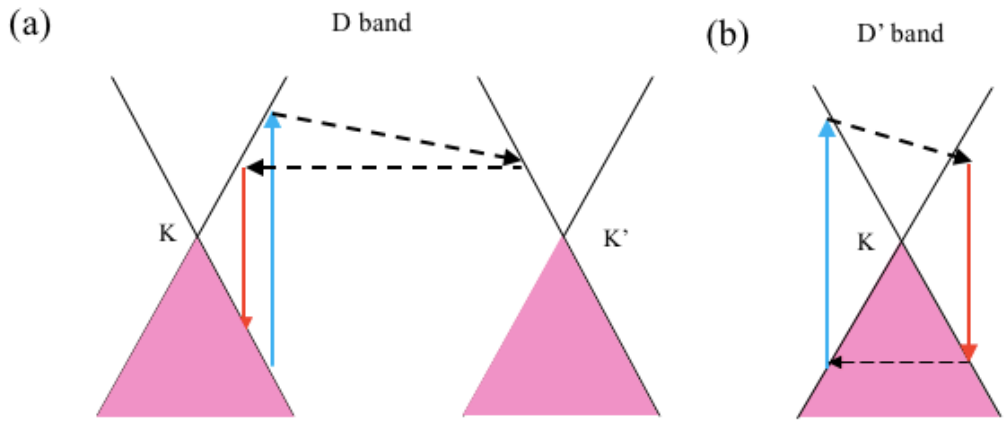

Fig 2. 6 Sketch of intervalley and intravalley Raman scattering bands in graphene. (*a*) D band (*b*) D' band[114].

Unlike the intervalley process which happens in D and 2D band, D' band (at 1620 cm^{-1}) and 2D' band (~3240 cm^{-1}) occurs due to intravalley processes. The mechanism of D' band is similar to the D band, as shown in Fig 2.6 (b). The D peak is associated with an intervalley scattering process in the Brillouin zone (from K point to K' point) [114], [115], [116], [117]. The D' band is connected with an intravalley scattering around the K point or the K' point. Both D' and 2D' band are weaker than the D and 2D band [118], [119]. The 2D' process is the overtone of the D' band, and it is a two-photon process. In general, the defect analysis is based on D band with its ratio compared with that of G band. The D' band gives additional information on the defects in graphene.

2.4 Current Graphene Patterning Techniques

This section aims to review the state of the art technology of graphene patterning techniques, starting from the most commonly used electron beam irradiation to the recently developed femtosecond laser patterning technique. Each of the methods has shown great potential and success in patterning graphene, with advantages and disadvantages, as summarised in Table 2.3.

2.4.1 Electron-beam irradiation

High-energy electron-beam irradiation is often applied for producing graphene nanostructures. Meyer et al. [120] used a focused electron beam in transmission electron microscopy (TEM) to induce deposition of carbon on freestanding graphene membranes and produce nanoscale patterns with the help of periodic grating. Then, Fischbein et al. [121] demonstrated nano sculpting of suspended graphene sheets by the focused electron beam. This technique can produce various structures, such as nanoscale pores, slits, and gaps, shown in Fig 2.7. However, the high energy from the electron beam often generates unexpected defects such as undesired carbon deposition. Reducing electron energy to 80 keV can control such defects, but low-energy beams cannot produce nanoscale patterns efficiently. To solve this problem, Song et al. [122] introduced a method of electron-beam nano sculpting at a temperature above 600℃, which can produce highly mobile carbon atoms to repair the radiation damage. In this way, near-defect-free single-crystalline graphene nanostructures, such as nanoribbons, nanopores, and nanotubes can be produced [123].

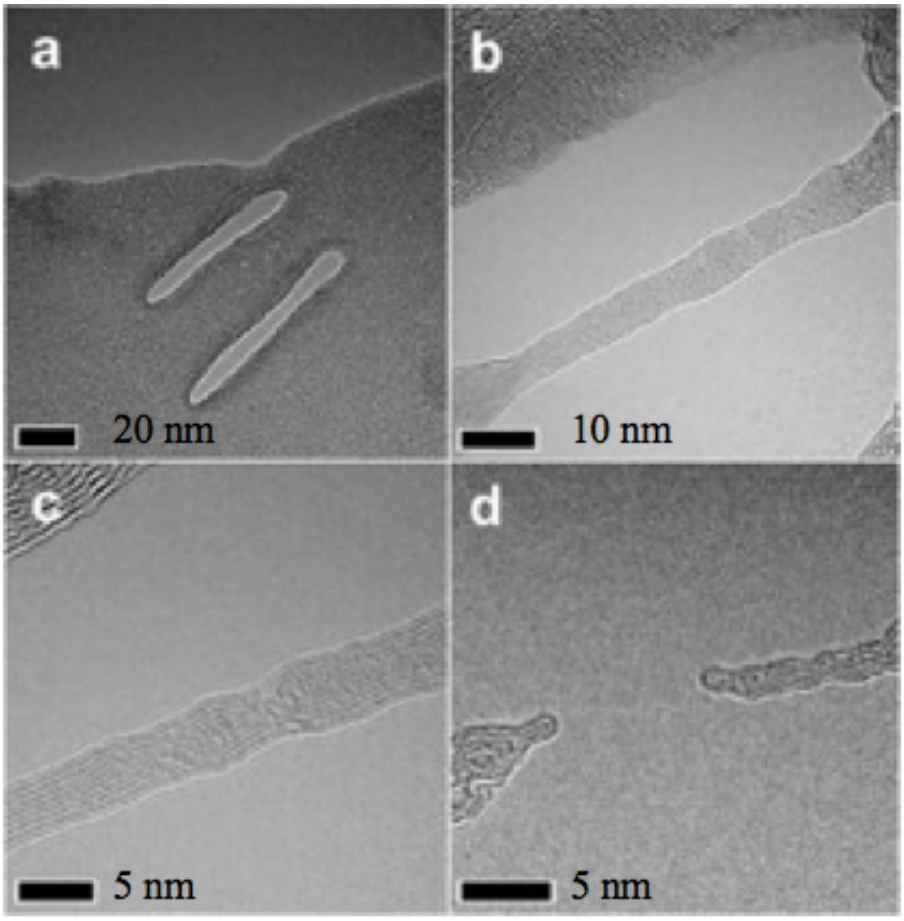

Fig 2. 7 (a) Two ~6 nm lines cut into a graphene sheet. (b) Electron irradiation is continued to create a bridge with ~5 nm wide. (c) A higher resolution of the bridge shows clear atomic order. (d) A small gap opened in the nanobridge by additional electron irradiation [121].

To conclude, generally e-beam irradiation is an ideal technique when combined with in-situ TEM observation. The edge sculpted with a condensed electron beam with C_s (spherical aberration coefficient) corrected can achieve the resolution down to 0.8 nm with a scanning speed of 1 nm/s [124]. This can be applied to explore the possible mechanisms during the evolution of graphene morphology and may be used in graphene nanoribbon fabrication. However, it is difficult to apply e-beam irradiation to fabricate graphene patterns and devices on a large scale at an affordable cost.

2.4.2. Photolithography methods

Photolithography methods have been developed to create graphene nanostructures with pre-designed patterns, for instance, graphene nanoribbons (GNRs), which are strips of graphene with ultra-thin (<50 nm), can be produced down to ~10 nm. The methods employ conventional e-beam lithographical negative resist forming a protective pattern on graphene, which is subsequently exposed to plasma oxygen [125]. The unprotected portion of the graphene is then chemically

removed upon the attack by the reactive plasma and carried into the vapour phase. The pattern on the mask (and the e-beam resist) is then "printed" into the graphene. Scanning tunneling microscope (STM) probe can be used to cleave C-C bonds when operated at a bias voltage (>2 V), much higher than that in topographical measurements (typically ~200 mV) [126]. When the probe advances on graphene in the carving mode, GNRs can be produced as small as 10 nm [127]. The resolution of e-beam lithography depends mainly on the electron beam size and the scattering and propagation of electrons in the resist material. As the de Broglie wavelength of a helium ion is many times smaller than electron beam for the same acceleration voltage, helium ion beam lithography can give an ultimate resolution of 0.5 nm [128], [129], as shown in Fig 2.8.

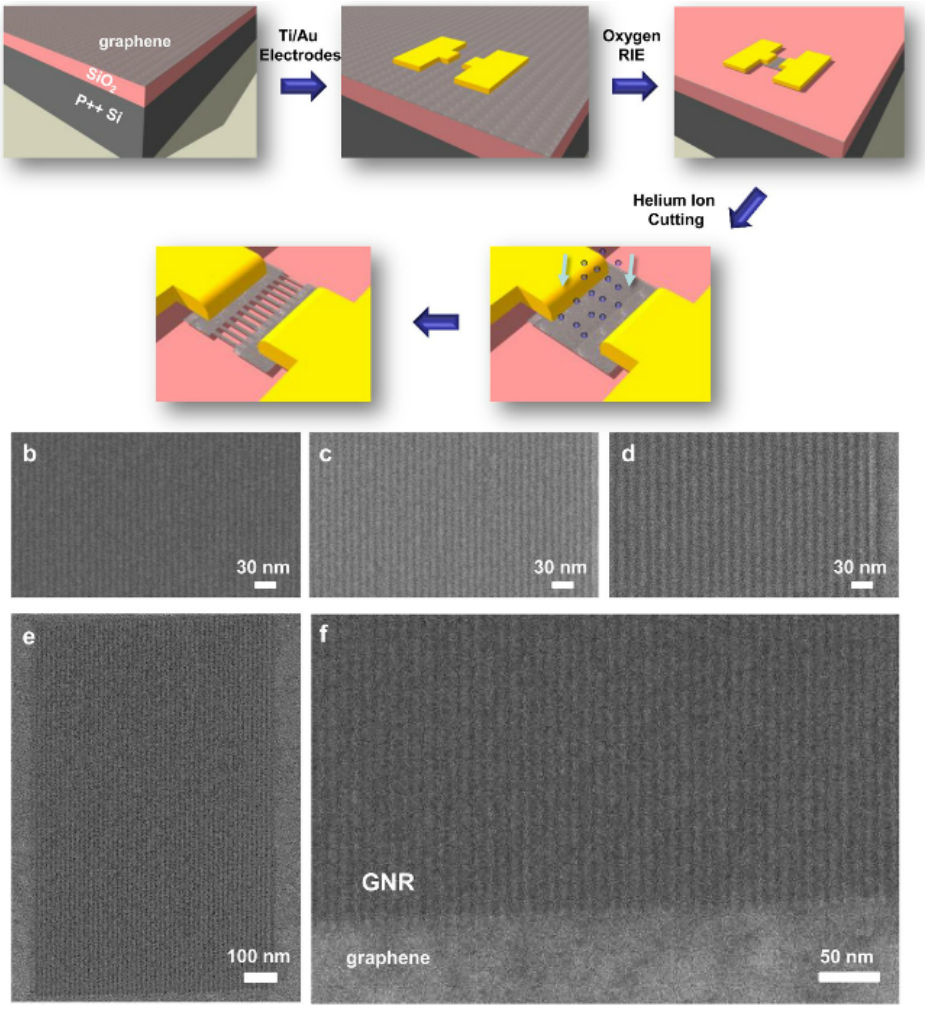

Fig 2. 8 (a) Scheme of GNR arrays fabricated by helium ion beam lithography. (B-D) Helium ion microscope images of (b) 5 nm, (c) 6 nm and (d) 7.5 nm half-pitch arrays. (e) Helium ion microscope image of high aspect ratio GNRs (width × length is 5 nm ×1200 nm). (f) Helium ion microscope image shows the smooth interface between graphene and patterned GNRs. For all images, bright lines represent graphene [129].

Though precise resolution can be achieved, maskless lithography methods using a TEM or scanning helium/neon ion microscope suffer from relatively high costs (mask range from $1,000 to $100,000) [130] and scanning probe methods are usually not well suited for upscaling [131].

2.4.3 Plasma/ chemical etching

Plasma/chemical etching is another conventional technique to pattern graphene. This is generally performed while shielding part of the graphene sheet with a contact mask in the nanometre range [132]. Xie et al. [133] selectively etched graphene nanoribbons and graphene edges with hydrogen plasma. They controlled the hydrogen plasma reaction at 300 °C which prevented hydrogenating the graphene plane. GNRs with less than a 5 nm width was achieved. Dimiev et al. [134] developed a chemical etching route for layer-by-layer removal of graphene. They first sputter-coated zinc on top of multilayer graphene with pre-designed pattern and then removed the zinc and the adjacent single graphene layer in dilute HCl solution [134], as shown in Fig 2.9.

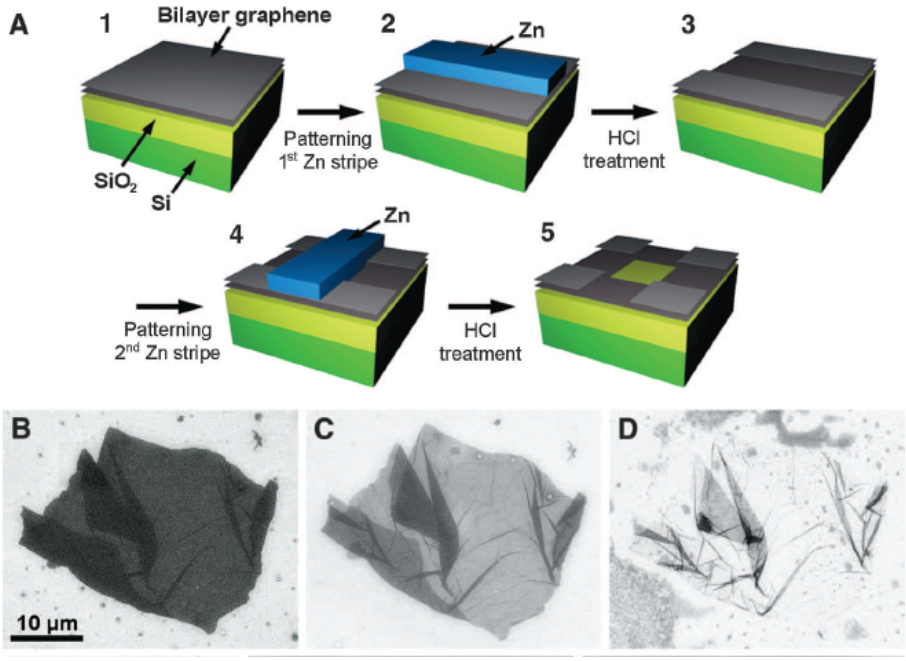

Fig 2. 9 Controlled layer-by-layer removal of graphene. (A) Schematic of the process. SEM image of the same bilayer graphene oxide (GO) flake: (B) original, (C) after the first, and (D) after the second Zn/HCl treatment [134].

The main advantage of solution phase chemical etching/plasma etching is that smoother edges can be fabricated compared to e-beam or scanning probe lithographical methods. However, chemical methods have a lack of architectural control.

2.4.4 Laser direct patterning graphene

Laser directing patterning methods have begun to be investigated due to their potential to offer free-form post-patterning of general graphene devices with high processing speed. Dhar et al. [135] studied the ablation threshold energy density for single and multi-layer graphene and achieved selective ablation/patterning or a thin graphene sheet. In these experiments, micrometre-sized graphene flakes were placed on a 290 nm thick SiO_2 on Si substrates, for observation with optical microscopy. The graphene samples were ablated by a single pulse of a 248 nm, 20 ns laser pulse with increasing laser energy in an Ar atmosphere at room temperature. At very low laser energy densities (0.55 J/cm^2), both single and multi-layer graphene was ablated, and the ablation threshold of graphene decreases rapidly with the increasing numbers of graphene layers originating from the dimensional crossover of thermal conductivity. As the spot size of the excimer laser (~mm) was much larger than the graphene flakes (tens of microns), the whole piece of graphene was affected by laser irradiation. With smaller spot sizes from the ultrafast laser, micro-patterning graphene could be achieved.

Laser shock can also be used in graphene patterning. Li et al. utilised the laser ablation generated shock pressure to create 3D tunable straining in the graphene sheet, as shown in Fig 2.10 [136]. This is an approach for the nanoscale punching of graphene film by using laser-induced shock pressure [137]. Graphene film can be made into a circular mold of around 50 nm in diameter; the critical breaking pressure was measured to be 1.77 GPa. The advantages of this technique are that it is fast, tunable and low-cost. However, this approach is confined to a pre-patterned substrate, and therefore patterning of graphene on non-porous surfaces is inapplicable.

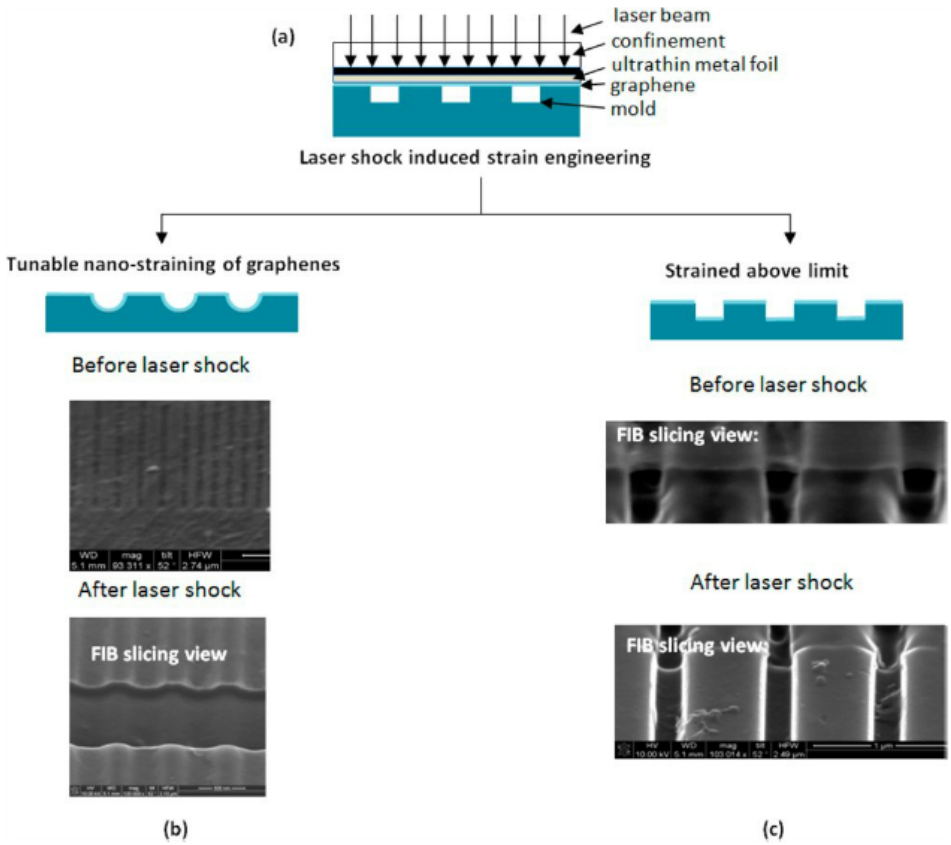

Fig 2. 10 Illustration of the laser shock-induced straining of graphene (a) setup of the laser-induced strain engineering; (b) tunable 3D nano straining of the graphene film when the strain limit is not exceeded. (c) graphene is straining above the strain limit [136].

Another approach to obtaining graphene shapes is to synthesize epitaxial graphene by using the laser-induced deposition with a mask [138]. Lee et al applied a KrF laser (wavelength 248 nm, pulse length 25 ns) to deposit graphene on the Si-rich surface of a SiC [138]. The optical absorption length ($\alpha^{-1} \approx 76$ nm) of SiC is much smaller than the thermal diffusion length in SiC during the laser pulse ($L_T \approx 4.1$ μm), thus the laser can be considered as a surface-heating source on SiC. As a result, the substrate is held at room temperature while the thin SiC surface absorbs the laser light. Furthermore, with a shadow mask in the laser beam path, graphene with different shapes could be synthesized (Fig 2.10). In this method, both synthesis and patterning of graphene can be achieved in one step by simply shaping or masking the laser beam, which makes it surpasses other thermal methods in epitaxial graphene growth on SiC substrate in terms of time-consuming. However, the uniformity and quality of as-produced graphene could deserve a further exploration.

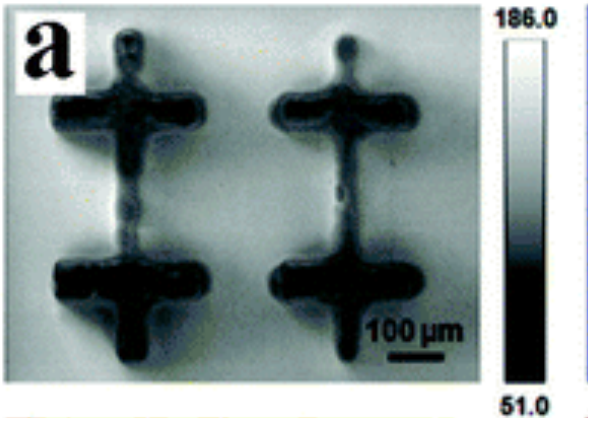

Fig 2. 11 SEM images of a laser-processed SiC with a shadow mask placed in the KrF laser beam path [138].

2.4.5 Femtosecond laser ablation of graphene

The femtosecond laser is more beneficial in patterning graphene for its limited thermal effects compared to the conventional lasers. Currie et al applied Ti: Sapphire laser (wavelength 800 nm, pulse duration 50 fs) to study the laser induced damage of graphene on a sapphire substrate [139]. They found laser-induced damage on graphene. Additionally, the results showed that some modification of graphene lattice could be observed at a laser fluence of 14 mJ/cm^2. Similarly, Roberts et al. studied single pulse laser shot interaction with graphene on a glass substrate, as shown in Fig 2.12. The ablation threshold was found to be around 200 mJ/cm^2 in the range of 50 fs to 1.6 fs [140]. The results also demonstrated a clear micro-hole formed on graphene on the glass substrate. The edges from single shot laser ablation were found to be microscopically clean, which indicates the potential for ultrafast laser micro-patterning of graphene. Besides monolayer graphene ablation, the number of layers of graphene can be precisely controlled by picosecond laser and femtosecond thinning by Lin et al. and Li et al [141], [142].

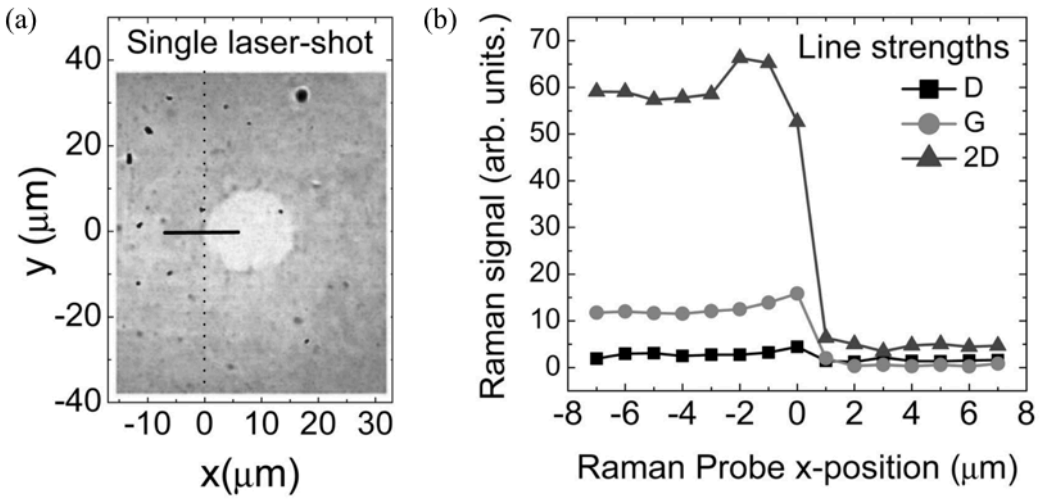

Fig 2. 12 (a) Optical image of the single femtosecond pulse processed spot. (b) Raman probe scan across the edge of damage spot. Raman line strengths are defined as the area under the spectral peak [140].

Zhang et al. further explored the femtosecond laser direct cutting graphene on a glass substrate and obtained a 25 μm wide channels of graphene by using a 100 fs Ti: sapphire laser with a central wavelength of 800 nm, as shown in Fig 2.13 [143]. The ablation threshold of graphene was determined to be 0.16 ~ 0.21 J/cm^2. When the laser fluence was higher than the ablation threshold, graphene was obliterated and ablated rapidly without damaging the glass substrate.

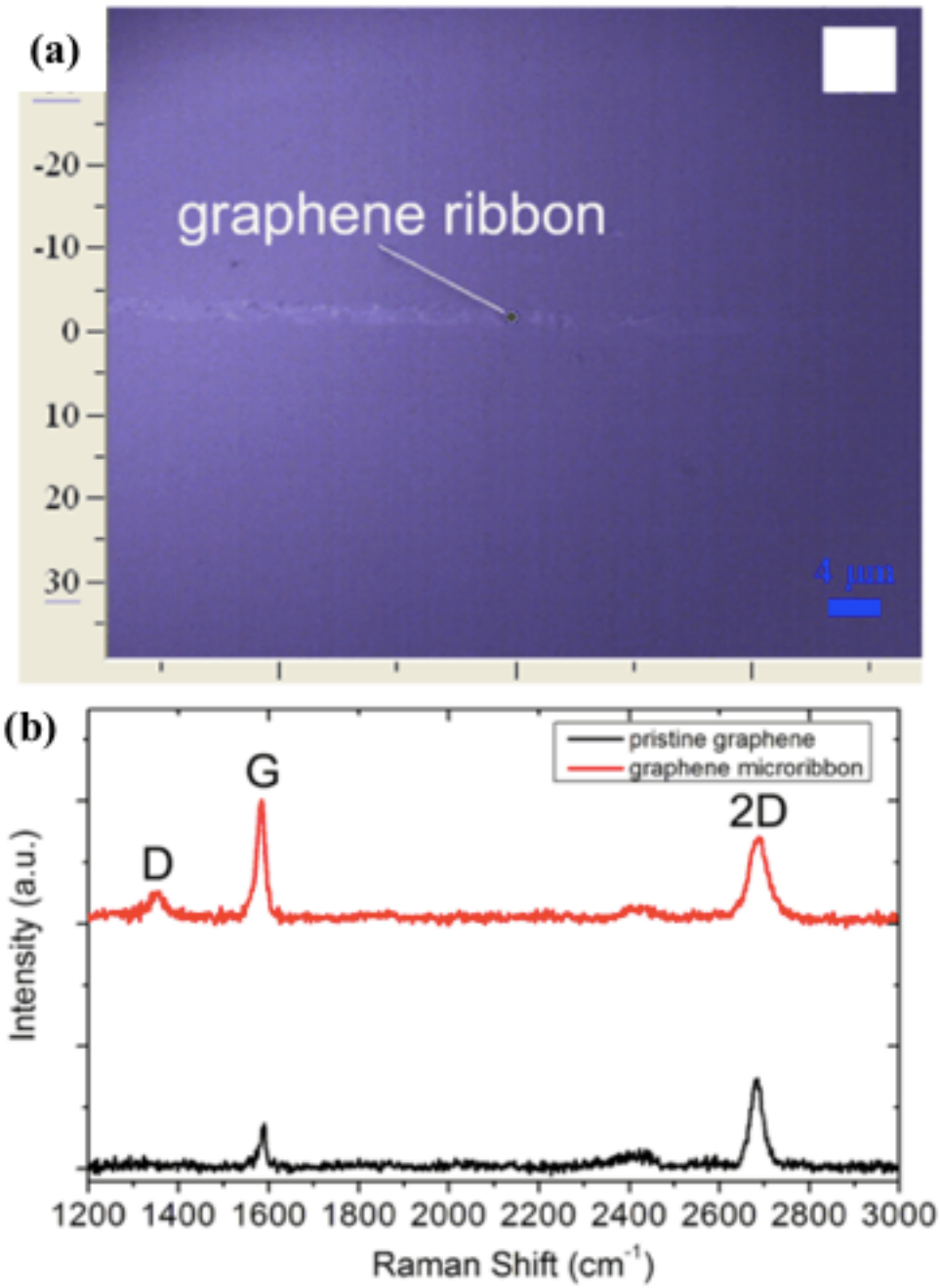

Fig 2. 13 (a) Raman microscope image of one strip of graphene ribbon. (b) Raman spectra of graphene ribbon and pristine graphene [143].

Nanometre-scale patterning of single-layer graphene can be produced on SiO_2/Si substrate through femtosecond laser ablation. Sahin et al. applied a femtosecond laser with pulse duration of 550 fs (wavelength of 343 nm) obtain a 400 nm wide ablation channel on SiO_2/Si substrates but caused damage to the silicon substrate, as shown in Fig 2.14 [144]. It was reported that 400 nm wide ablation channels could be achieved over 100 μm length, by adjusting laser fluence and translation speed. Sufficient gap is left between channels by raster scanning of the sample, which

yields well-ordered periodic structures. By controlling the power and speed, no substrate damage can be achieved. However, the main obstacle for this result is that it has not entirely removed the graphene. In this respect, further study of femtosecond laser ablation on graphene deposited on SiO_2/Si substrates is worth exploring.

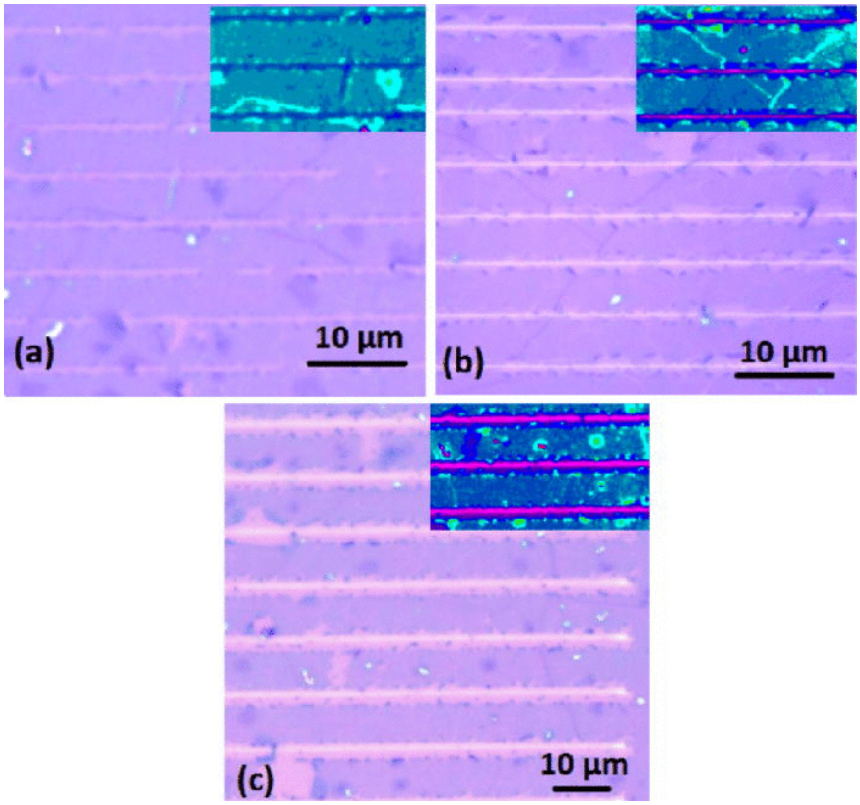

Fig 2. 14 Optical microscope images of produced nanostructures on monolayer graphene. Laser fluence and scan speed values are (a) 120 nJ and 330 µm/s (b) 120 nJ and 100 µm/s (c) 200 nJ and 330 µm/s. Insets are false-colour images, where pink region correspond to damaged Si [144].

It is worth noting that the graphene patterning methods described above have their advantages and disadvantages for the study of precision, controllable, large-scale process as shown in Table 2.3. The femtosecond laser manufacturing of graphene stands out because of its potential to be fast, flexible and an easy procedure for graphene channels. This brings us to the importance of investigating the potential of the femtosecond laser processing of graphene in details and so broadening the applications of the femtosecond laser into the graphene industry.

Table 2. 3 Summary of different techniques for graphene patterning.

Method	Advantages	Disadvantages
1. Electron beam irradiation	Line width can be down to the nanoscale, precise	Unaffordable cost, not for large scale, not a free-form pattern with any shapes
2. Scanning probe lithography		
3. Helium ion beam lithography		
4. Photocatalytic etching	Smooth edge, a low energy required, nanoscale, precise	Increase the risk of contamination, relatively long process
5. Plasma etching		
6. Chemical etching		
7. Excimer laser irradiation	Fast and easy procedure, controllable	High temperature
8. Laser-induced shock patterning		Porous shape limited
9. Femtosecond laser patterning		Precision limited

2.5 Laser-matter interactions

Having known the potential of the femtosecond laser in profiling of graphene, it is necessary to review the related background knowledge in laser-matter interactions.

2.5.1 Light propagation

When light strikes the surface of the material, the discontinuity in the refractive index causes a partial reflection, and the rest of the light is transmitted and through absorbed by the material. For the incident light on a flat surface, according to Fresnel equation [145], the reflection coefficient is

$$R = \left(\frac{\widetilde{n_0} - \widetilde{n_1}}{\widetilde{n_0} + \widetilde{n_1}}\right)^2$$

where $\widetilde{n_1}$ is the refractive index of the material, and $\widetilde{n_0}$ is the refractive index of an incident atmosphere. The complex refractive index $\tilde{n} = n + ik$ where n is the real refractive index and k is extinction coefficient. The real refractive index is defined as:

$$n = \frac{c}{v}$$

Where c is the speed of light in a vacuum and v is the speed of light inside the medium. The transmission coefficient satisfies the energy conservation:

$$T = 1 - R$$

As the light propagates through the material, its intensity will decay due to the absorption of the material. The intensity of decay is a function of depth. The rate is determined material's absorption coefficient α. The absorption coefficient can be expressed in terms of the extinction coefficient k as:

$$\alpha = \frac{4\pi k}{\lambda} \quad 2.1$$

For constant α, the intensity I decay exponentially with depth z according to the Beer-Lambert law [146],

$$I(z) = I_0 e^{-\alpha z} \quad 2.2$$

where I_0 is the intensity at the surface after considering reflection loss. The penetration depth into the material is defined as:

$$\delta = 1/\alpha \quad 2.3$$

which is the depth where the electrical field decays to $1/e$ of the initial value at the surface.

When the medium is thick, the approximation $z \to \infty$ can be made. There are no internal reflections and the propagation of the beam in the medium can be described by absorption and scattering losses:

$$dI = -\int N\sigma I(z)dz \quad 2.4$$

where N represents the number of scattering centers in a $z \to z + dz$ propagation interval and σ is the interaction cross section (absorption, scattering, and luminescence), which is typically dependent on the wavelength.

Material absorption is directly linked to the laser wavelength via the electric field oscillation frequency. Photon energy is transferred to matter via electronic and atomic vibrations. Electronic excitation is dependent on the electronic transition energy ΔE, the band gap inherent in the transition needs to be matched to the photon frequency:

$$\Delta E = \frac{hc}{\lambda} \quad 2.5$$

If direct band gaps are not possible, a photon can still couple into the material via phonon-assisted lattice or molecular coupling.

2.5.2 Absorption mechanisms

Depending on the structure of the material and the photon energy, the absorption mechanisms vary. For semiconductors, if $E_{ph} < E_G$ (E_{ph}: photons energy; E_G: bandgap energy), the light weakly interacts with the semiconductor and passes through as if it were transparent.; if $E_{ph} \geq E_G$, light is strongly absorbed by the material and creates both a majority and a minority carrier [147]. For metals, photon energy is subsequently transferred to the lattice phonons due to intraband absorption or free-carrier absorption when a carrier is excited from a filled state to an unoccupied state in the same band [148]. This absorbed energy can be described by the Drude model, treating the electrons moving in the electric field and with collisions [149], [150]. Notably, interband absorption may also play a role in the laser metal interactions. An increased absorption at certain laser frequencies has been reported in aluminum in [151], [152]. For insulators, if sufficient laser energy is deposited into the surface of a material through linear absorption, material ablation can occur [153], [154].

These treatments have only considered linear optical phenomena. With laser intensities increasing, nonlinear absorption such as multi-photon absorption (Fig 2.14) and avalanche ionization which is based on more inverse bremsstrahlung and impact ionization (Fig 2.15) [155], [156]. The former requires multiple photons to interact simultaneously with an electron, and the sum of their energies must exceed the bandgap energy, electrons are directly excited from the valence to the conduction band [156]. The later involves free carrier absorption by an electron already in the conduction band of the material followed by impact ionization [156]. These processes will increase the absorption coefficient α, which results in the decrease of the threshold fluence.

The process of avalanche ionization requires some seed electrons in the conduction band. It can be described as follows: an electron in the conduction band sequentially absorbs several laser photons. When it absorbs more than the bandgap energy, its energy exceeds the minimum conduction band, then it ionizes another electron by collision, leaving two electrons in the conduction band. As long as the laser field is present during the process, the electron density in the conduction band will grow exponentially [157], [158]. The two temperature model is the typical method used to analyse the energy relaxation between electrons and lattice in conductors and semiconductors [159], [160].

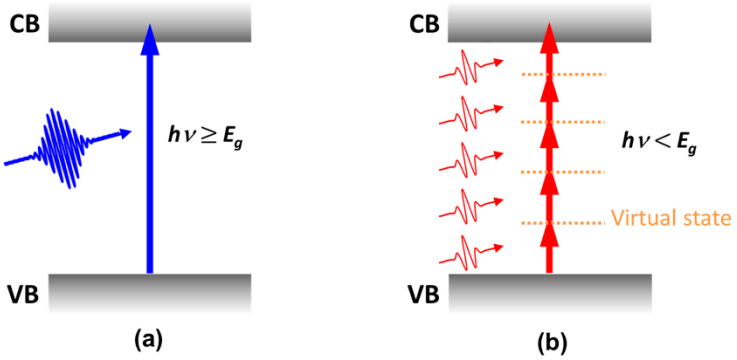

Fig 2. 15 Single-photon absorption (a) and multi-photon absorption (b).

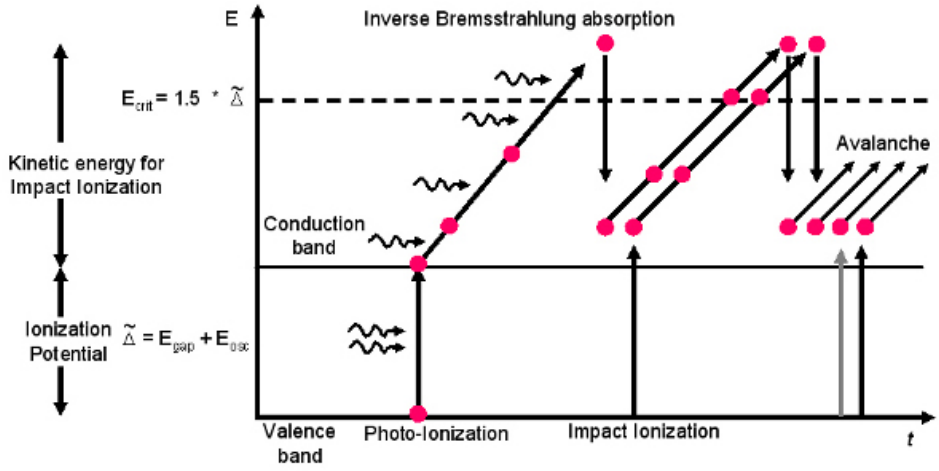

Fig 2. 16 Avalanche absorption process [161].

2.5.3 Comparison of ultrafast and conventional lasers

Conventional laser processing is often conducted with either a continuous wave (CW) or nanosecond (10^{-9}) pulsed lasers [162]. Fig 2.16 shows the effect of laser processing on material by CW, nanosecond (ns), and pico/femtosecond(ps/fs) laser pulses from left to right. For long pulses, the material removal can be achieved by utilising melt expulsion driven by the vapour pressure and the recoil pressure induced by evaporation caused by absorption the laser [163]. For ultrashort pulses, since the energy deposition occurs on a timescale that is shorter compared to atomic relaxation processes, the material removal can be attributed to thermal or non-thermal effects [164]. This mechanism in ultrashort laser pulses results in many advantages in material processing as follows:

(a) an ultrafast laser generates a minimal amount of debris in the form of fine dust that is not bounded to the surface [165], [166].

(b) at high fluence, the ablation rate could be reduced due to the attenuation of the incoming laser irradiation caused by laser-induced plasma [167].

(c) reduction or apparent absence of heat-affected zones occur and result in the fine and sharp features being produced on the surface of materials [168], [169].

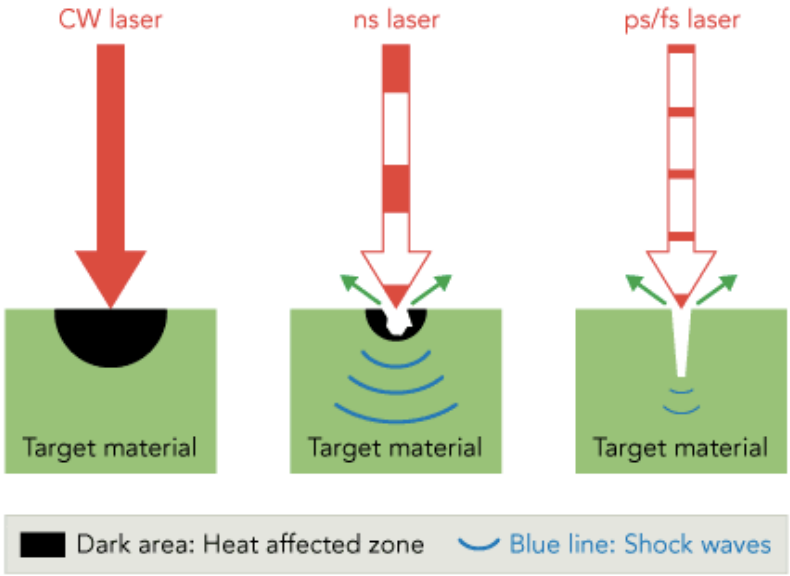

Fig 2. 17 Comparative effects of different types of lasers interact with the target material [170].

In ultrafast laser system, pulse duration, energy, wavelength and repetition rate are essential parameters. As the peak power equals to the pulse energy divided by the pulse duration, high peak power is expected as the pulse duration is ultrashort. In laser-processing, the minimum achievable structure size is determined by the diffraction limit of the optical system ($\frac{\lambda}{2NA}$, NA is the numerical aperture, equal to $nsin\theta$). Notably, sub-wavelength cutting could be achieved by choosing the peak laser fluence slightly above the threshold value. The diffraction limit of laser processing can be exceeded with the control of peak laser fluence slightly above the threshold, as shown in Fig 2.17.

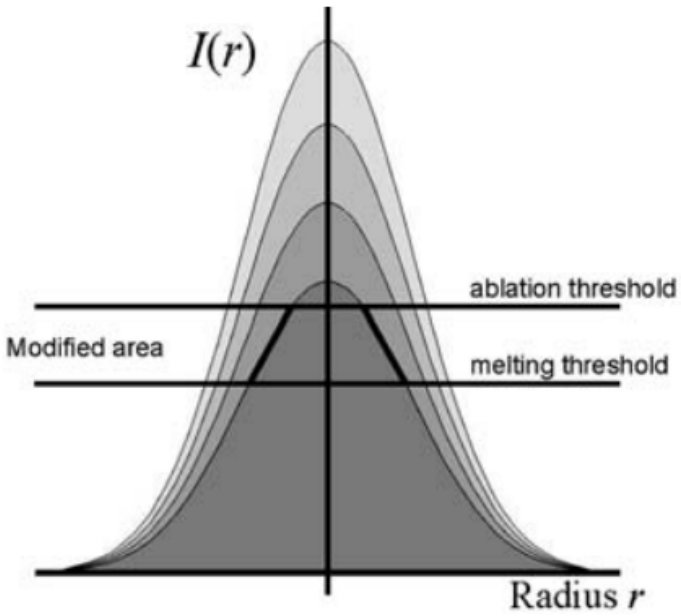

Fig 2. 18 A schematic illustration of overcoming the diffraction limit by taking advantage of the well-defined ablation threshold [171].

The ablation threshold is defined as the minimum energy per unit surface (fluence) required to induce detectable changes in materials. It has been documented that ablation threshold is dependent on pulse duration in metals [172] and dielectric materials [173]. In the process of laser ablation of metals, studies [174], [162] assume that close to the ablation threshold F_{th}, the ablation mechanism is mainly thermal mode, which means the ablation is determined by the heating of the electron gas. The ablation threshold can be calculated through the following equation [175]:

$$F_{th} = \frac{2E_p}{\pi\omega_0^2}\exp\left(-\frac{d^2}{2\omega_0^2}\right) \qquad 2.6$$

where E_p is the pulse energy, ω_0 is the beam spot radius and d is the ablation diameter. In this case, only the central part of the beam can modify the material and, it becomes possible to produce sub-wavelength structures. Ablation occurs when $F \geq F_{th}$, which for a Gaussian beam profile, corresponding to $F = F_0\exp\left(-{d^2}/{d_0^2}\right) \geq F_{th}$, where d_0 is the beam diameter, F is the laser fluence or energy density and F_0 is the maximum laser fluence. Therefore, for the ablated structure size, one expects the following dependence on the peak laser fluency, $d = d_0[Ln(F_0/F_{th}]^{1/2}$.

Despite laser ablation threshold, there is laser-induced damage threshold. It is an intensity of fluence that is just high enough to facilitate noticeable damage. It depends not only on material properties

but also the number of pulses irradiated locally. The incubation effect describes the dependence of laser-induced damage threshold on the number of pulses: within a range of the number of pulses, the threshold drops dramatically after the first laser shots; with more laser shots, the threshold reaches a constant level eventually. The relationship between the laser-induced damage threshold of a single pulse and multiple pulses is expressed as [176]:

$$F_{th}(N) = F_{th}(\infty) + [F_{th}(1) - F_{th}(\infty)]e^{-k(N-1)} \quad 2.7$$

in which k is an empirical parameter: the larger it is, the fewer pulses it takes to reach the saturation when $F_{th}(\infty) = F_{th}(N)$.

2.6 Research gaps

The road mapping of graphene industry is shown in Fig 2.18. From the start of this project, the aim of the graphene flagship is to shift the existing graphene laboratory work into industrialized graphene application. Femtosecond laser processing of graphene belongs to the production & processing sector, aiming to embed femtosecond laser manufacturing into graphene production to broaden production methods as well as decrease the manufacturing cost.

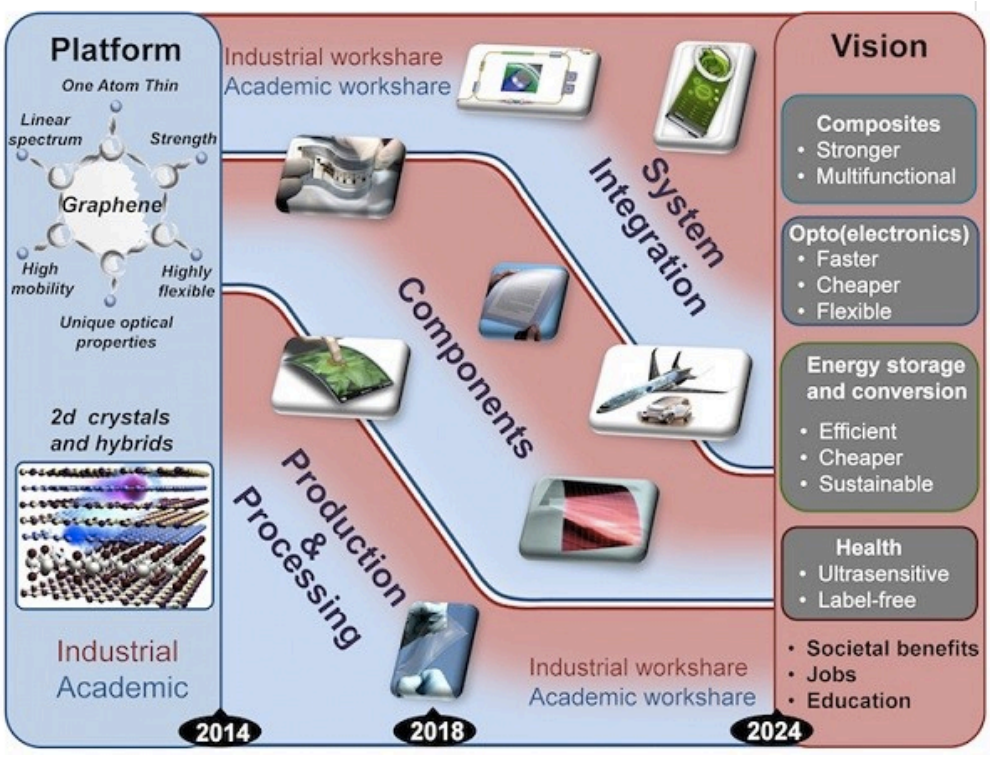

Fig 2. 19 Road mapping of graphene industry [177].

As discussed in section 2.4, a number of graphene patterning techniques have been reviewed and the advantages of the femtosecond laser in its application for manufacturing graphene device have been identified. Although the laser graphene ablation study on the various substrates have been studied, there is still a lack of attention on the substrate absorption behaviour. Because the graphene device is commonly deposited on the SiO_2/Si substrate, this research focuses on the ablation process after femtosecond laser processing to achieve selective removal of graphene. The condition of the SiO_2/Si substrate will influence the operation of the graphene device. For instance, silicon dioxide plays an important role in Complementary Metal Oxide Semiconductor (CMOS), as an insulating layer between the gate and channels. If the laser energy is intense, it will penetrate through SiO_2 and in turn cause impurities in the substrate. Therefore, this may cause a malfunction of the fabricated device.

- Hence, whether the femtosecond laser can achieve a controllable selective removal of graphene on SiO_2/Si substrate is underexplored. Moreover, the influence on the SiO_2/Si substrate after the femtosecond laser ablation of graphene is lack of study.

The femtosecond laser can be applied in the device fabrication. Moreover, because of the precise control of pulse energy and deposited fluence, its application may be extended to the area of controlling the properties of graphene such as to introduce defects on the surface of monolayer graphene deposited on SiO_2/Si substrate.

- Therefore, the second research gap is lack of study on the femtosecond laser interaction with graphene under subthreshold conditions.

Researchers have explored the femtosecond laser ablated graphene on different types of substrates. However, there is still lack of studies on the absorption mechanism of SiO_2/Si substrate during the process of a Gaussian shape temporal intensity profile laser pulse. A multi-layer absorption model can provide a better theoretical insight to the absorption mechanism.

- Thereby, the third research gap is lack of theoretical understanding of the absorption mechanism of SiO_2/Si substrate during the process of a Gaussian shape laser pulse.

2.7 Summary

This chapter reviewed the properties and applications of graphene, and its characterisation methods, especially Raman spectroscopy. The state of the art of graphene patterning techniques are reviewed.

After identifying the advantage of using femtosecond laser processing of graphene, the mechanism of femtosecond laser interactions with materials, including plasma effect, absorption, and incubation effects are described. Three research gaps are defined. First, there is a lack of study on selective removal of graphene on SiO_2/Si substrate by using femtosecond laser. Second, to the best of author's knowledge, the femtosecond laser interaction with graphene under subthreshold conditions is still underexplored. Third, a theoretical understanding of the absorption energy distribution of SiO_2/Si substrate during the process of Gaussian temporal intensity pulse should be provided. By fulfilling these research gaps, this research explores the controllability and feasibility of using femtosecond laser in the future graphene technology.

Chapter 3 Research methodology

3.1 Introduction

This research explores the feasibility of using femtosecond laser to process graphene, with a more specific aim towards the understanding of three important aspects, namely substrate reaction under ablation of graphene layer, graphene surface defects under sub-ablation and the absorption of the substrate. The theoretical modelling is presented separately in Chapter 6. It aims to provide a theoretical understanding of the absorption of SiO_2/Si substrate during exposure of Gaussian shape laser pulse. Chapter 3 focuses on detailing the experimental methods applied in this thesis, and to plot a clear picture about the design, configuration and development of the experiments in furthering the understanding of the experiments delivered in chapter 4 and 5. Section 3.2 describes the material and experimental design in this study. Section 3.3 lists the configuration of the applied laser system and its procedure. Section 3.4 demonstrates the evaluation methods applied in this research.

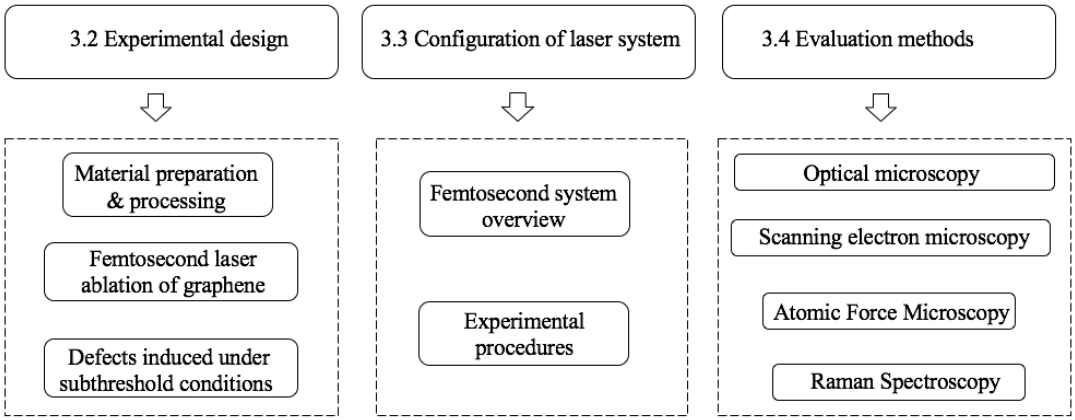

Fig 3. 1 Schematic diagram of chapter 3.

3.2 Experimental design

3.2.1 Principle of experimental design

As described in Chapter 2, the most commonly used method associated with graphene device fabrication is photolithography. This technique involves patterning graphene channels and followed up with metal deposition. For patterning graphene, it includes a total of five sub-steps (in Fig. 3.2): spin coating resist, resist soft baking, laser writing of a reversed pattern, developing and etching. Similar operations are applied to deposit metal on the graphene. This long process costs two weeks'

time in the laboratory and the multi-step preparation increases the risk of contamination. The proposed lithography-free methods to obtain a desired graphene pattern can be achieved by selective use of femtosecond laser processing parameters. The success of the fine cutting pattern technique could shorten the as-described device fabrication process and guarantee the finest cutting quality without inducing undesired damage. Beyond exploring the feasibility of the direct patterning of graphene by using a femtosecond laser, the production of using laser pulses under sub-threshold irradiation is also studied.

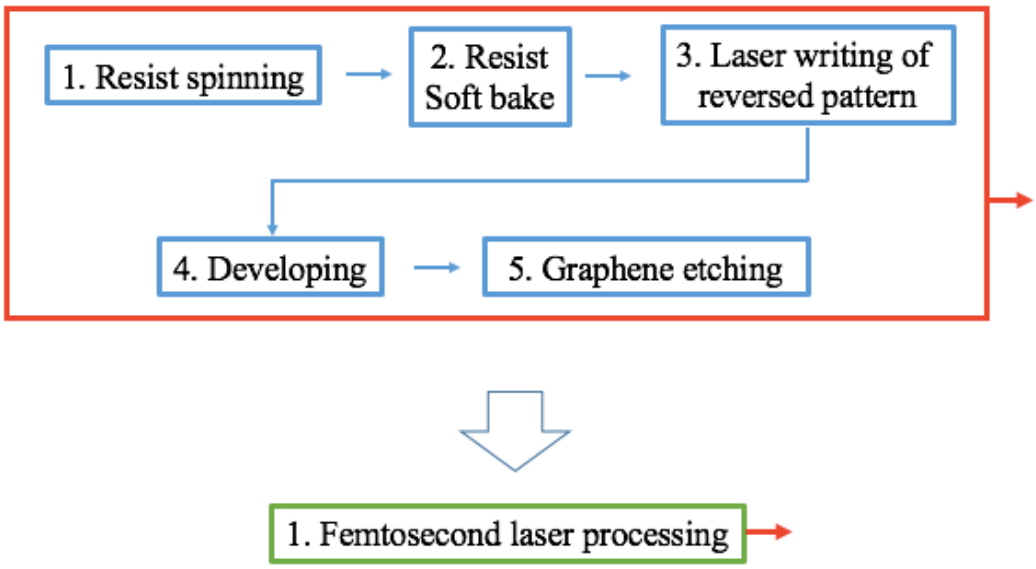

Fig 3. 2 Procedure of graphene device preparation for graphene. Traditional lithograph (red box) and femtosecond laser processing (green box).

3.2.2 Material preparation

(a) Growth of CVD graphene

As discussed in Chapter 2,section 2.2, among the growth methods of graphene, CVD graphene can produce high mobility and can be grown on a large area. It has been shown that many metals such as Cu, Ni, Pd, Pt, along with their alloys can be applied as effective catalysts for graphene growth under different conditions. Cu has been found to support the growth of a single layer of graphene ascribed to a very low carbon solubility (<0.001 atomic %) from hydrocarbon. Fig 3.3 illustrates a schematic of an experimental set up for CVD growth monolayer graphene by Cu or Ni catalyst. It contains a high-temperature tube furnace and a quartz vacuum chamber. The growth condition is controlled by several mass flow controllers (MFC) and a pressure control system.

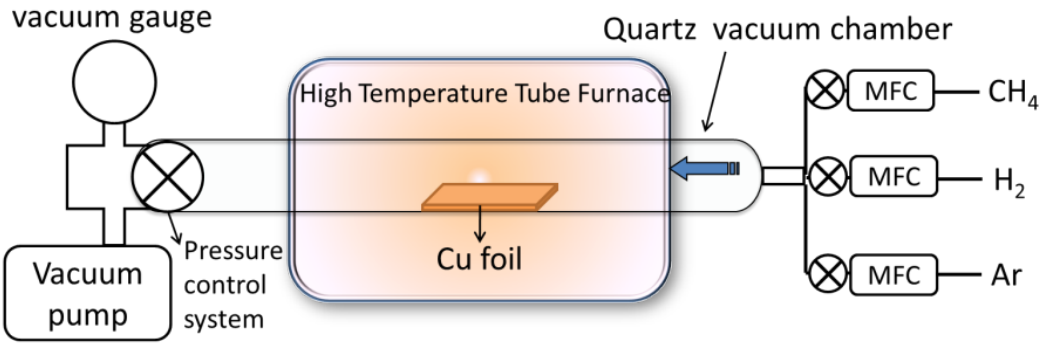

Fig 3. 3 Schematic diagram of CVD growth of graphene set up [178].

The scenario of CVD growth of graphene can be described as follows. First, a feedstock of carbon is decomposed on the catalyst surface and the released carbon atoms react on the catalyst surface at high temperature (e.g., 1000℃). Second, the diffusive carbon atoms join each other on the catalyst surface and force carbon clusters of various sizes. The continuous graphene growth starts when a carbon cluster is greater than the size of the 2D nucleus of graphene. Third, the matured graphene clusters continue to absorb decomposed carbon atoms around them. A graphene island appears with a specific shape. Finally, these graphene islands meet each other during the phase growth until the whole surface is covered with graphene. During this process, grain boundaries occur between single crystalline islands.

After growth, the quality and uniformity of monolayer graphene are monitored by Raman spectroscopy (Renishaw InVia^{TM} focal Raman spectroscopy) equipped with a 100X objective (numerical aperture NA=0.85).

(b) Transfer process

The graphene was grown on copper with a thickness of one layer, and then transferred onto a SiO_2/Si substrate. The transfer process of graphene from copper onto other substrates commonly uses chemical etching, as shown in Fig 3.4. The process begins by spin-coating a thin polymeric layer to provide a supportive framework for the transfer. In this research, a ~ 500 nm thick layer of polymethyl methacrylate (PMMA) is spin coated on top of the single layer graphene/ Cu sample. The underneath Cu substrate is then etched away by ammonium persulfate (APS) in DI water. After the Cu is completely dissolved, the floating membrane (PMMA) is moved into DI water for cleaning APS residuals and then transferred onto SiO_2/Si substrate. The polymeric film is dissolved in acetone after drying.

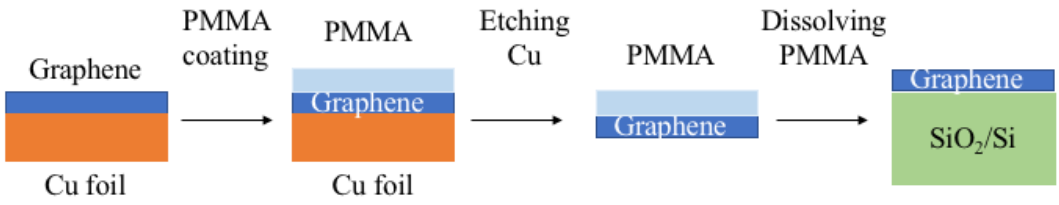

Fig 3. 4 CVD graphene transfers to SiO_2/Si substrate.

(c) Cleanness steps

The cleaning process is in three steps. First, immerse the graphene sample in Acetone for 5 min to dilute the contamination on graphene. Second, directly put graphene sample into IPA (isopropanol) for 2 min and then dip into DI water immediately because the delay in transferring graphene into DI water could damage the graphene surface. The last step is to dry the graphene sample with Nitrogen gun and then located the sample in a transparent box, as shown in Fig 3.5.

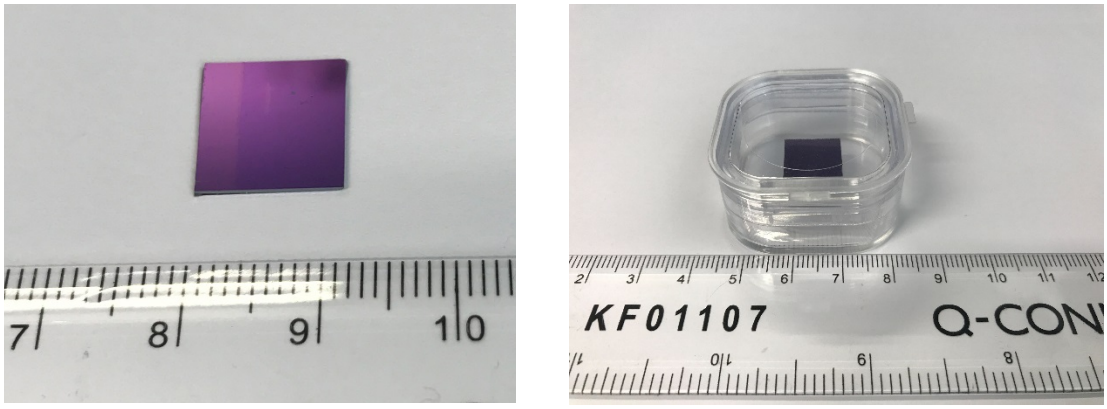

Fig 3. 5 Optical images of graphene sample. Left: Graphene deposited on SiO_2/Si substrate. Right: Graphene in the container.

3.2.3 Femtosecond laser system processing of graphene

The proposed plan is to use a femtosecond laser to pattern graphene on the SiO_2/Si substrate directly aiming to shorten the process of the graphene patterning steps. In general, SiO_2 has been used as an insulator to avoid the flow of charge directly from gate to the conducting layer in MOSFET. Thus, an appropriate graphene removal process requires limited damage to this substrate.

The research method and logic flow are shown in Fig 3.6. Monolayer graphene deposited on the SiO_2/Si substrate is chosen for this research. The remarkably wide absorption range of graphene for monolayer graphene is appealing property for transparent and flexible optoelectronic devices.

Starting from the monolayer graphene on the SiO_2/Si substrate, a series of femtosecond laser pulses are fired on the surface of graphene. Three possible outcomes can be observed: the substrate is damaged; graphene is ablated; no significant effect.

The next step in the evaluation of graphene is analysing and confirming the existence of graphene via Raman measurement. For a partial removal of graphene, the G and 2D peaks will exist. For a complete removal of graphene, these two peaks will disappear. For a detailed substrate condition exploration, AFM can be applied to topography measurement and surface potential on the ablated area. SEM is employed for the edge examination and cut width measurement. By knowing the cut width of the sample, the ablation threshold can be calculated from the following equation [175]:

$$F_{th} = \frac{2E_p}{\pi\omega_0^2} \exp\left(-\frac{d^2}{2\omega_0^2}\right)$$

where E_p is the pulse energy, ω_0 is the beam spot radius after the focusing lens and d is the ablation diameter. The ablation diameter is estimated with the kerf width.

Notably, the electronic ions from SEM measurement could introduce a small amount of doping and weak damage. Tewelderbrhan et. al reported that disorder D peak increased with low energies (5-20 keV) [110] and attributed it to the e-beam irradiation, however, Choi et. al demonstrated the e-beam-induced D mode originated only from the irradiated amorphous carbon other than the e-beam itself at 1 kV [179]. Given that there is a debatable mechanism on the increased D peak, to ensure the accuracy of Raman measurement on the laser ablation on graphene, SEM measurement is carried out after the Raman spectroscopy, with the same parameters and same condition.

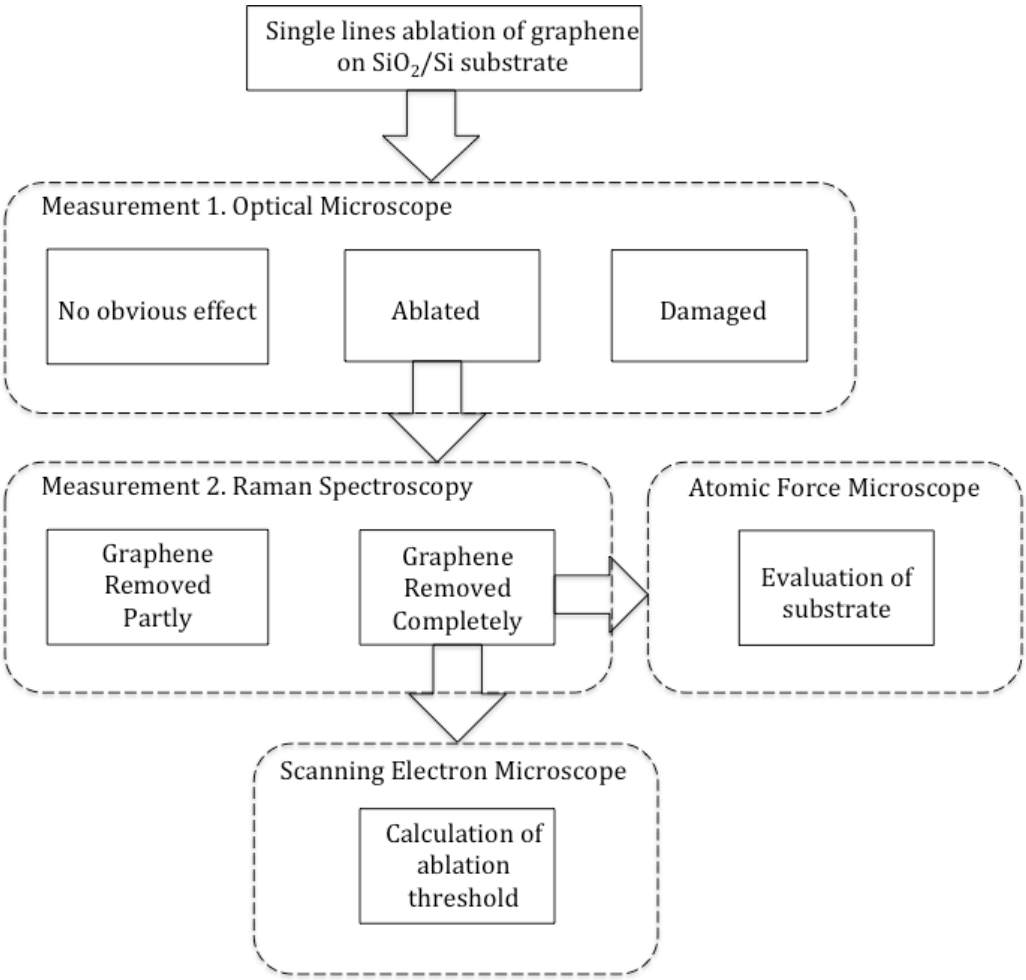

Fig 3. 6 Experiment procedure of analyzing single lines exposure after irradiation of a femtosecond laser.

3.2.4 Femtosecond laser-induced defects on graphene

This research aims to analyse the effect of the femtosecond laser pulses interaction with a single layer of graphene under sub-threshold condition. The idea is to study whether the femtosecond laser could generate controllable defects on graphene. This could provide a promising technique to combine ultrafast laser treatment with a selective doping process to achieve graphene doping, and enhance the range of application for graphene devices.

The experiments focus on the defects induced on graphene, which was examined by Raman spectroscopy. The experimental results were predicted to be useful for the quantitative interpretation of the interaction of monolayer graphene with the femtosecond laser pulses. Three main topics were considered in the investigation.

1. Whether or not sub-threshold photon energy changes the properties of graphene;

2. Whether there exists a defect induced threshold for the femtosecond laser;

3. Whether the defects of graphene correspond with the pulse energy or are independent of the pulse energy.

The experimental flow is similar to the femtosecond laser ablation of graphene. Starting from the low intensity of laser exposure on the CVD growth of monolayer graphene sample transferred on SiO_2/Si substrate, the sample is examined by Raman spectroscopy. Unlike the substrate evaluation in the femtosecond laser ablation, this research is focused on the defects evaluation, which relies on the Raman spectroscopy measurement. The collected data are analysed by I(D)/I(G) and other Raman lines, providing information on the property of defects generation caused by the interaction between the femtosecond laser and graphene on the SiO_2/Si substrate.

3.3 Femtosecond laser system

The principle of femtosecond lasers is based on the chirped pulsed application. Gratings are applied to stretch a laser pulse and followed by amplification steps without disturbance the optical elements aligned. After that, the laser pulse is recompressed by using a conjugated system to achieve a femtosecond pulse duration output.

3.3.1 Description of the femtosecond laser system

Fig 3.7 shows the schematic diagram of the femtosecond laser system (Amplitude Systèmes Satsuma) and Fig 3.8 shows the femtosecond processing system. For the processing stage, the mechanical shutter is used to turn the laser on/off. When the laser light comes out, the beam diameter can be measured with a beam profiler (Spiricon LBA-FW-SCOR20). The 1/4 wave plate is used to control the polarisation of light. The diffractive attenuator (Del Mar DVA-800) is used to finely tune the laser power, allowing only the order of zero diffraction to pass and divert higher orders. The objective lens (Comar Optics 12-OI-09) is used for machining graphene on the SiO_2/Si substrate. The laser was circularly polarised and focused by a NA=0.35 objective lens (Comar Optics, 12 OI 09) with a focal length of 12.7 mm. The spot diameter is 4.16 μm.

For the real-time observing stage, a dichroic mirror (Thorlabs DMLP1180L) is applied before the objective lens with a reflectivity of 98.3% at 1030 nm. Sufficient visible light passes through the dichroic mirror into an in-line CMOS confocal camera (Thorlabs DCC 1645 C), enabling real-time adjustment of the beam focus and processing path of the beam. The transmission is measured as

89.7%. The CNC stage move in x, y, z directions. The Aerotech A3200 software is a machine controller based on G-code, and the whole stage has a position accuracy of ±100 nm on all axes.

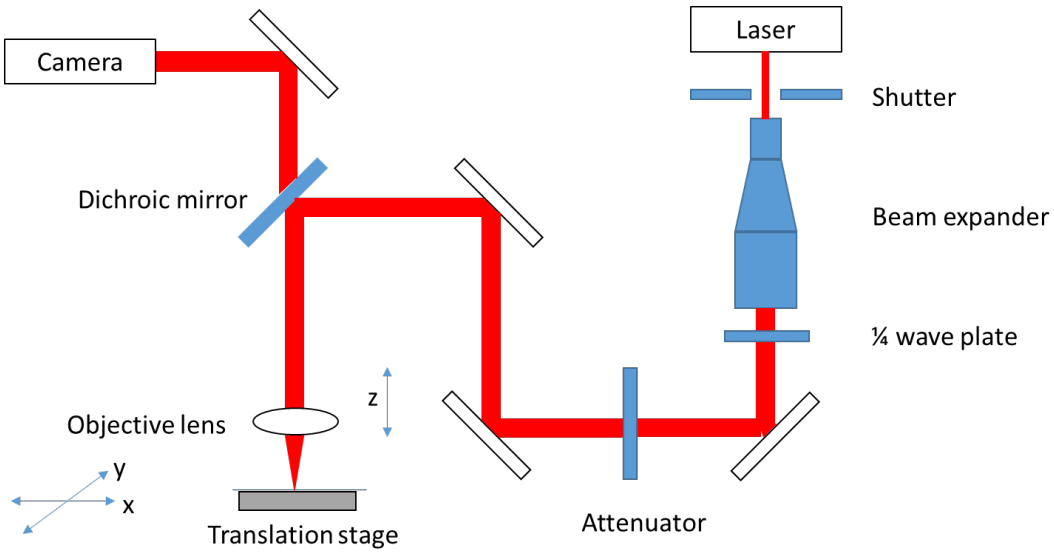

Fig 3. 7 Schematic of the experimental setup of the femtosecond laser machining system.

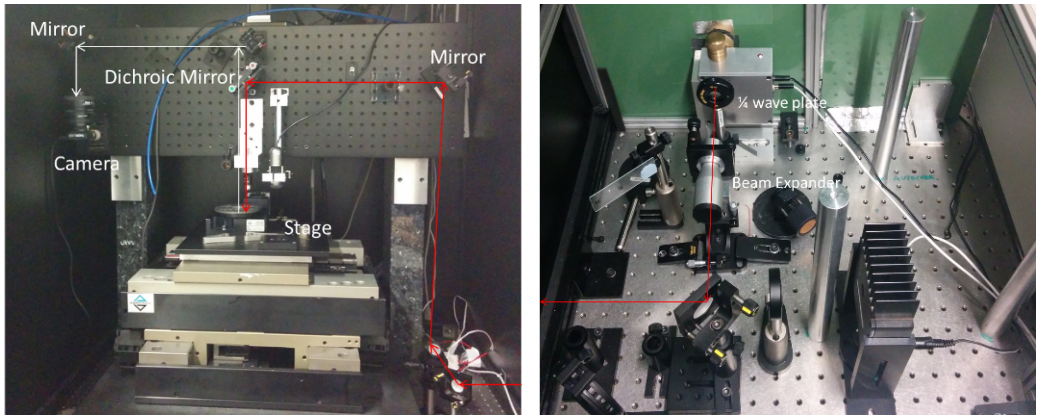

Fig 3. 8 Amplitude Systèmes Satsuma laser processing platform.

Table 3. 1 Femtosecond laser specification.

Laser model	**Amplitude Systèmes Satsuma**
Wavelength	1030 nm
Pulse duration	280 fs
Repetition rate	0.001-2000 kHz
Maximum Power	5.9 W
Beam radius	2.2 mm
M^2	1.1

The laser parameters are calculated and described as below:

Wavelength (μm): the wavelength of a fibre laser is determined by the lasing material.

Repetition rate (kHz): number of laser pulses per second.

Pulse energy (nJ): $\text{pulse energy} = \frac{\text{Average power}}{\text{Laser repetition rate}}$.

Pulse width (fs): full width half maximum for Gaussian shape.

Peak power: pulse energy/ pulse width.

Fluence (J/cm^2): the energy of the laser beam/the exposed area. the uniform fluence over the beam area is assumed, even if the beam is a Gaussian shape.

Spot size (μm): exposed area of the Gaussian laser beam. A constantly exposed spot size is assumed for fluence calculations.

Laser beam peak intensity: $I_p = \frac{\text{Peak fluence}}{\text{Pulse duration}}$.

3.3.2 Femtosecond laser procedure

All the optical elements are positioned to ensure the beam is delivered to the centre of the objective optic.

The power is measured with a laser power meter (Thorlabs PM100D, power range 100 pW to 200W, Available wavelength 185 nm – 25 μm) by selecting the wavelength of 1030 nm. The average pulse energy is calculated from the repetition rate and the average laser power.

A "UC480 Viewer" (Thornlabs) that captures the in-situ laser light from the confocal camera. It aids control of the Aerotech 3200 CNC stage and focus finding. The adjustment of Z axis is made to observe the smallest spot. Typically, the edge of graphene sample (~500 μm thickness) is pasted on a glass microscope slide (1.1mm thickness) with copper foil tape to avoid the slipping during the processing.

3.4 Evaluation methods

The quality of graphene is examined both before processing and after processing. On top of a Si wafer with a thickness of 300 nm SiO_2, the monolayer graphene can be observed as a purple-to-violet in colour. For monolayer graphene, scanning electron microscopy (SEM) can be applied to view its surface topography and composition. The detailed processed path can be used for the

ablation threshold calculation. Atomic force microscopy (AFM) gives topography information of graphene on the substrates and the status of the substrate after ablation. Raman spectroscopy is used to observe the positions of the bands for a particular region of graphene sample. Energy dispersive spectroscopy (EDS) can determine the chemical composition of the sample through the analysis of characteristic X-Ray emissions of the sample which is being excited using an electron beam.

3.4.1 Optical microscopy

The optical microscope is a reliable method to observe graphene on different types of substrate. Although graphene is not entirely transparent, the atomic thickness makes it invisible to the naked eye. A bright contrast allows graphene to be seen with a careful selection of the substrate. The visible difference in graphene and substrate is based on Fresnel theory. The thickness of silicon dioxide needs to be very precise and the difference as little as 15 nm can make single-layer graphene invisible. For example, when placing graphene on SiO_2/Si substrate with a carefully chosen thickness of silicon dioxide, graphene can be assessed under an optical microscope. A SiO_2/Si substrate with 300 nm SiO_2 layer is light purple, which appears a deeper purple when graphene is present. Blake et al studied the visibility of graphene depend on the thickness and the layers of graphene, and the light wavelength as shown in Fig 3.9 [180]. A comparison of graphene sample on top of a Si wafer with a standard thickness of 300 nm is shown in Fig 3.9 (a) and (c) shows another sample on a 200 nm SiO_2 thickness on Si. In Fig 3.9 (b) demonstrates that the main contrast of layers in green light for 300 nm. The graphene The blue filter can make graphene visible on 200 nm SiO_2. To conveniently observe graphene in white light under a microscope, in this research, monolayer graphene is deposited on SiO_2/Si substrate with a 300 nm SiO_2.

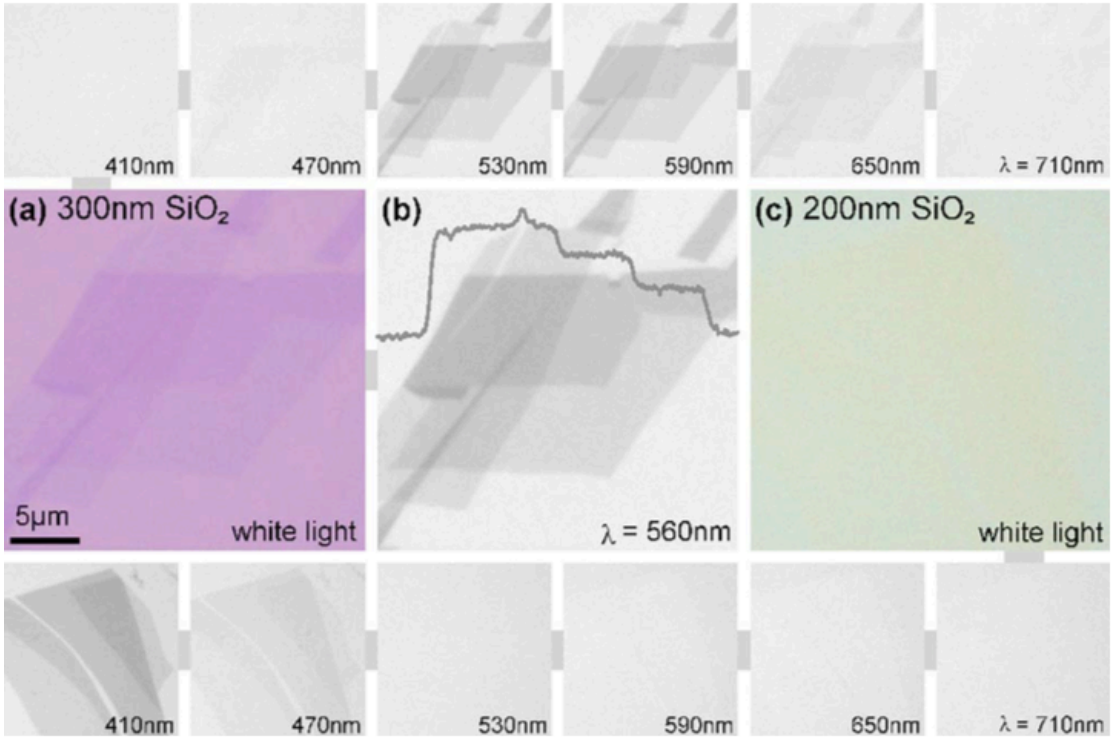

Fig 3. 9 Optical images of different layers of graphene on SiO_2/Si substrate. (a) graphene on 300 nm SiO_2 under white light (b) green light (c) another graphene sample on 200 nm SiO_2. Top and bottom present the same flacks in (a) and (c) respective but illuminated through different bandpass filter [180].

3.4.2 Scanning electron microscopy (SEM)

SEM offers a high-quality resolution for precise structural features on sample surfaces. In this research, a ZEISS 1640 Crossbeam SEM was used to obtain images for high-resolution examination of graphene kerfs.

Fig 3.9 shows the schematic structure of scanning electron microscopy. The electrons are emitted in a vacuum from an electron gun and then focused on the surface of the sample through condenser lenses. The images are produced by collecting the backscattered electrons or secondary electrons from the graphene surface. The secondary electron gives morphological and topographic data while the backscattered electron presents the compositional information on the surface. The 2D graphic can be built up by scanning the area of interest.

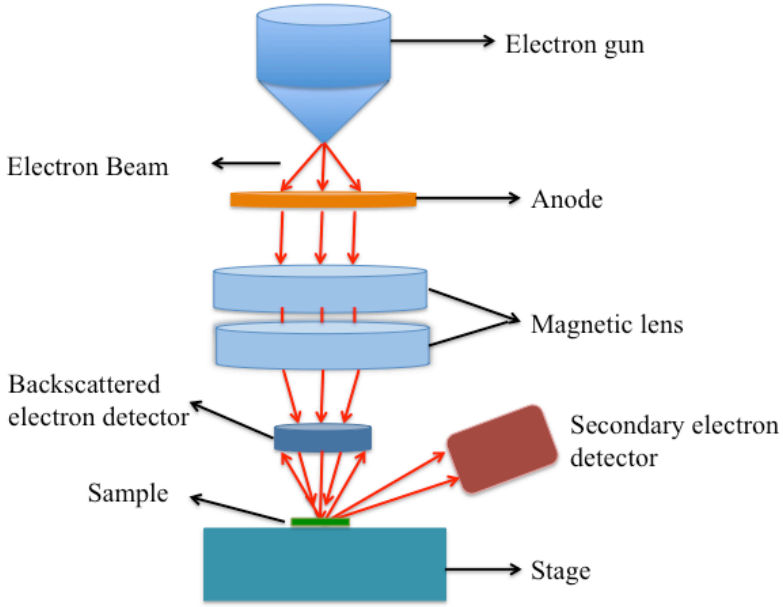

Fig 3. 10 Schematic graph of Scanning electron microscopy.

3.4.3 Atomic force microscopy (AFM)

Atomic force microscopy (AFM) belongs to the family of scanning probe microscopy (SPM). It requires a physical probe for the measurement. Given that AFM is not an optical technique, the resolution is not limited by diffraction. Instead, it is determined by the size of the tip that is applied. The typical resolution is on the order of 10 nm or sub-nm resolutions. Fig 3.10 shows the schematic structure of atomic force microscopy. A cantilever with a small sharp tip scans the surface of the sample. Forces between the tip and surface of the sample lead to a deflection of the cantilever. The force-distance curve under AFM is shown in Fig 3.11. The deflection is then measured with a laser and a detector. The forces that can be measured in AFM include chemical bonding, mechanical contact force, electrostatic force, etc. Depending on the application, the AFM can be operated in contact and non-contacting mode and tapping mode.

In contact mode, the tip is close or touching to the surface. The tip can be affected by the repulsive force with the atoms, and subsequently with their electron clouds, as the distance is as close as 0.1nm to 100 nm. The force can be estimated with Hooke's law because the displacement is the only controllable parameter from the detected deflection of the cantilever. In this mode, low stiffness cantilevers are required to reduce the risk of collision. The cantilevers have to be much softer than the bonds between sample atoms to ensure the cantilever deforms more than the sample [181]. The resultant image represents the topographic map of the scanned area.

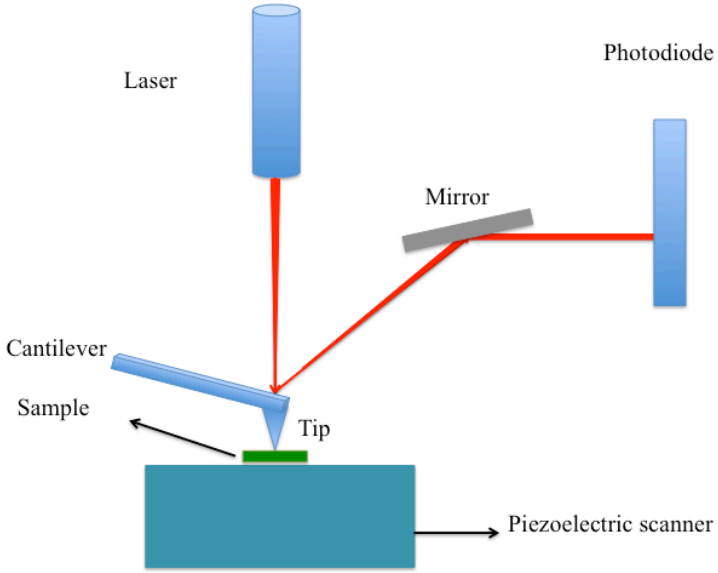

Fig 3. 11 Schematic of AFM measurement.

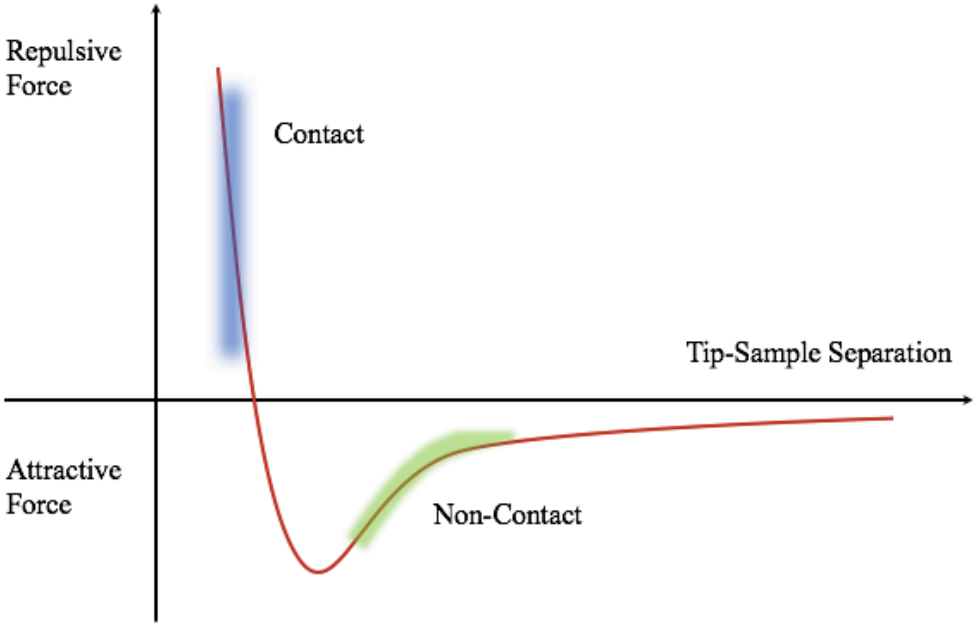

Fig 3. 12 Schematic of AFM force curve verse tip sample distance. In repulsive regime (Blue) the tip is in hard contact with the surface. In attractive regime (green), the tip is pulled towards the surface. No deflection occurs when the tip is far from the sample.

In non-contact mode, the tip is above the surface by approximately 50 - 150 Angstrom. It is applied in the situation where any contact might influence the surface substrate in a subtle way. The overall force is attractive and much weaker than in the contact mode. Therefore, the tip must oscillate and changes in the resonance frequency, amplitude, and/or phase are used, to measure the difference in height. However, in the fluid containment layer, the oscillations of the cantilever may be trapped in the coating providing a lower topological resolution than in contact mode.

Tapping mode is an improvement for AFM in measuring soft samples. It overcomes the problems associated with adhesion, electrostatic forces, friction and other difficulties. Tapping modes alternately place the tip in contact with the surface of the sample and by lifting the tip off the surface. By oscillating the cantilever at, or close to, its resonant frequency, the tapping mode image can be implemented in ambient air. A feedback loop is applied in tapping mode between the cantilever and the detector to keep the oscillation amplitude constant. When the oscillating cantilever starts to contact the surface intermittently, the energy loss causes the reduction of the cantilever oscillation, which is used to identify the surface features.

When using AFM to measure graphene on a SiO_2/Si substrate, the sample needs to go through the cleaning process first to ensure little or no contamination on the surface. In this research, Kelvin Probe Force Microscopy (KPFM), as a non-contact variant of AFM has been applied in measuring the potential between the tip and surface, as well as the topography. KPFM can give information on the electronic state and the composition of the measured structure on the surface of the solid. It can observe the work function of the surface at the atomic scale. The work function relates to the reconstruction of the surface, doping, etc. The difference between the work function is named as the contact potential difference, V_{CPD}.

For a contact potential measurement, a lock-in amplifier is applied to detect the cantilever oscillation frequency at ω. The voltage applied between the sample and tip consist of a DC bias V_{DC} and AC voltage $V_{AC}\sin(\omega t)$ at ω. V_{DC} will be modulated to ensure the electrostatic forces between the sample and the tip is zero during the scan. As a consequence, the response at ω becomes zero, which minimise the ω term to the contact potential.

There are two primary KPFM detection techniques: amplitude modulation KPFM (AM-KPFM) and frequency modulation KPFM (FM-KPFM). AM-KPFM applies an AC bias between the sample and the tip. This AC bias frequency is selected to be the resonant frequency of the AFM cantilever. The KPFM feedback uses the oscillation amplitude as an input to adjust a DC bias until the oscillation amplitude is zero, when $V_{CD} = V_{CPD}$. AM-KPFM is based on electronic force while FM-KPFM rests on an electronic force gradient. When the electric force gradient is adjusted, by an AC bias, the resonant frequency of the cantilever will be adjusted.

3.4.4 Raman spectroscopy

Raman spectroscopy is a powerful tool to verify the presence of graphene and the properties of graphene [114], which is a technique based on inelastic scattering.

Raman spectroscopy is performed with a laser-based microscope. Photons of light are focused on the sample through the microscope objective at a defined magnification. The Raman microscope contains an optical microscope, an excitation laser, a monochromator, optical filters, a spectrometer and an optical detector, as shown in Fig 3.12. The reflected light from the substrates is composited of elastic and inelastic scattering light when an incident light fires on the surface sample. Elastic scattering which has the same frequency of incident light that is Rayleigh scattering (green lines in Fig 3.12). The inelastic scattering is given anti-stokes Raman scattering (higher frequency in blue lines in Fig 3.12) and stokes Raman scattering (lower frequency in red lines in Fig 3.12). In fact, both Rayleigh scattering and Raman scattering provide useful information on graphene. Rayleigh scattering offers the opportunity to observe the graphene on a typical 300 nm SiO_2 on Si substrate under an optical microscope. Raman scattering has proven to be an incredibly powerful tool to characterise graphene in terms of the layers, defect densities, etc. that occur when the photon loses part of its energy during the interaction process, though it has a much lower probability than Rayleigh scattering.

Raman spectroscopy applied in this research is Renishaw InVia micro-spectrometer with a 514 nm wavelength from an Ar^+ laser excitation. The objective is 100× with a numerical aperture of 0.9. The Raman laser spot size was 0.7 μm. The laser power was tuned to be lower than 1mW to prevent damaging the graphene [113].

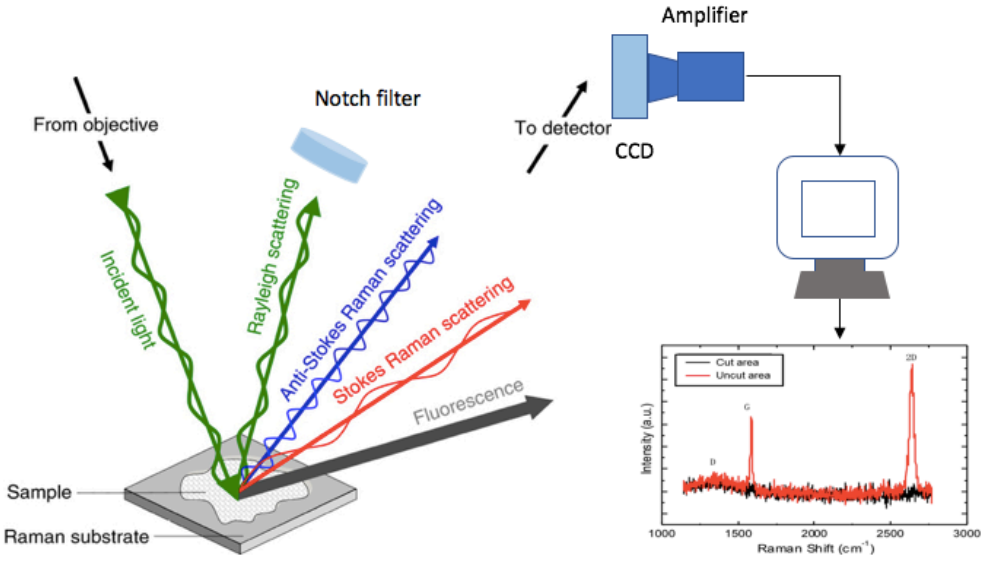

Fig 3. 13 The schematics of the Raman system.

Typically, little preparation is required for samples undergoing Raman analysis. The sample is manually controlled to achieve focus when placed on the stage. After the selection of the area of interest, the acquired spectrum at a single point is generated in seconds through a charged-couple device (CCD) detector.

As a non-invasive, non-destructive method, Raman microscopy provides a fast characterisation technique that can perform a real-time scan. Raman spectroscopy achieves this by measuring the relative intensities of each peak, which are directly proportional to the relative concentrations of the compounds.

The diffraction limit is defined by the laser wavelength and microscopy objective that is used. In theory, it is the diffraction that limits the spatial resolution. The equation is given as below

$$d = \frac{\lambda_0}{2nsin\theta}$$

Where λ_0 is the laser wavelength and θ is the incident angle, and $NA = nsin\theta$ known as the numerical aperture of the microscope objective that is used.

The vast majority of research plots Raman spectra, as a function of the energy difference between an incident and the scattered photon energy, which is also known as "Raman Shift". Historically, the spectral was plotted in wavenumbers, and the value is related to energy, giving

$$\Delta\omega(cm^{-1}) = \left(\frac{1}{\lambda_0(nm)} - \frac{1}{\lambda_1(nm)}\right) \times \frac{(10^7 nm)}{(cm)}$$

3.4.5 Energy dispersive spectroscopy (EDS)

Energy dispersive spectroscopy (EDS) can detect the chemical composition of the sample. The principle of the localised chemical analysis is to make use of the X-ray spectrum emitted by the sample when the sample is bombarded with a focused electron beam. For graphene sample, as graphene itself is conducting, this measurement is taken after SEM measurement.

The EDS in conjunction with SEM allows elemental identification and provides a very powerful tool for evaluating the laser ablation process, residues, etc. The EDS software applied in this study is "AZtec" version 2.2, Oxford instruments NanoAnalysis.

3.5 Summary

This chapter introduced the principal experimental research methodology. It started with an outline of the research methodology. After that, the equipment and methods employed in this study are described, including graphene growth and transfer, satsuma ultrafast laser systems, and post analysis tools (Optical microscope, SEM, AFM and Raman spectroscopy). The SEM provides high-resolution image on the processed surface and the edges. The knowledge of different modes in AFM measurement can help analyse the substrate surface morphology of the substrate after ablation. Raman measurement examines the graphene with its vibration modes appearing on the observed lines. Data are collected by appropriate microscopes, and the obtained micrographs were the object for analysing processes. More specifically speaking, the laser process system, as the critical platform for manufacturing graphene has been explained in order to understand the laser exposure process in Chapter 4 and Chapter 5.

Chapter 4 Femtosecond laser ablation of graphene on SiO_2/Si substrate

4.1 Introduction

This chapter attempts to answer the first research question on exploring the feasibility of fabricating graphene devices on SiO_2/Si substrate. The chapter tests two approaches: single line processing of graphene on a SiO_2/Si substrate and area removal of graphene on SiO_2/Si substrate, as shown in Fig 4.1. The analysis is carried out based on the single line experiments to understand the laser processing effects on both graphene and the underlying substrate. More specifically, the objectives of this chapter are as follows:

1. Identify the processing requirements for removing graphene on the SiO_2/Si substrate.
2. Analyse the edge quality of graphene after laser ablation.
3. Evaluate the SiO_2 substrate response to the incident laser energy.
4. Establish the process of developing area graphene channels by using femtosecond laser.

Previous studies on femtosecond laser interaction with graphene explored the interaction of a single pulse on graphene on a glass substrate. Another approach to patterning graphene on a SiO_2/Si substrate was able to not wholly remove graphene due to the close damage threshold between the silicon substrate (~100 mJ/cm^2) and graphene (150 mJ/cm^2) [144]. Therefore, the challenge exists to control the laser process parameter to achieve the selective ablation of graphene on SiO_2/Si substrate without damaging the Si substrate, or even the thin SiO_2 layer (~300 nm). In this cahpter, the apporach is investigated for the single line tracks and more applicable channel structure of graphene to reveal the impact of the experimental parameters.

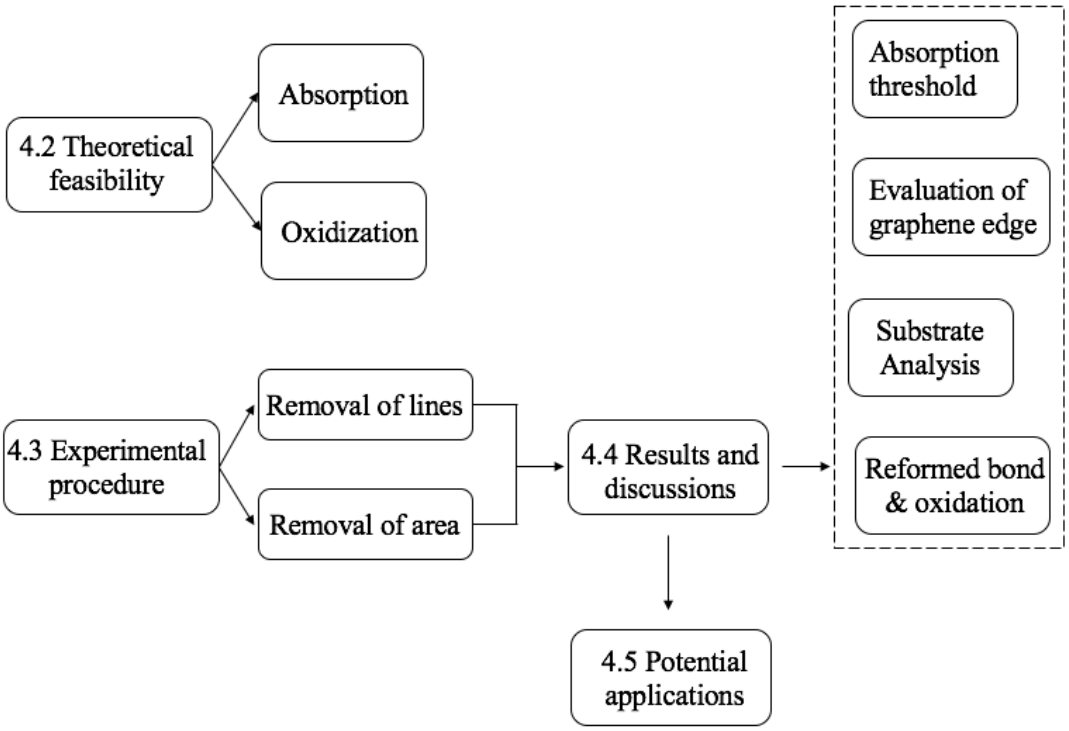

Fig 4. 1 Structure of chapter 4.

4.2 Theoretical feasibility

This section identifies the essential factors that need to be evaluated for laser processing of graphene. The purpose is to develop a laser manufacturing approach to process graphene on SiO_2/Si substrate without damaging the Si substrate. Due to the absorption of graphene, 2.3 % of light (300 nm < λ< 1100 nm) [182] with the SiO_2 layer absorbed less than 6% in the same range compared to silicon [59]. It means most of the light will be absorbed in the silicon. As silicon has a low ablation threshold, it is easy to suffer damage through exposure of the laser light.

4.2.1 Absorption

It is known that the laser parameters strongly influence material processing through linear absorption, and ablation may occur. By good choice of laser wavelength and pulse energy, selective ablation can be achieved in theory. As shown in Table 4.1, laser light penetrates Si with an absorption depth of around 300 μm at a wavelength of 1030 nm [183]. The damage threshold of Si is reported to be around 340 mJ/cm^2[144]. This is higher than that of Si at 343 nm (~100 mJ/cm^2) as indicated in the literature [144]. Thus, this range of thresholds offers the potential to enable complete removal of graphene without causing damage to the Silicon substrate.

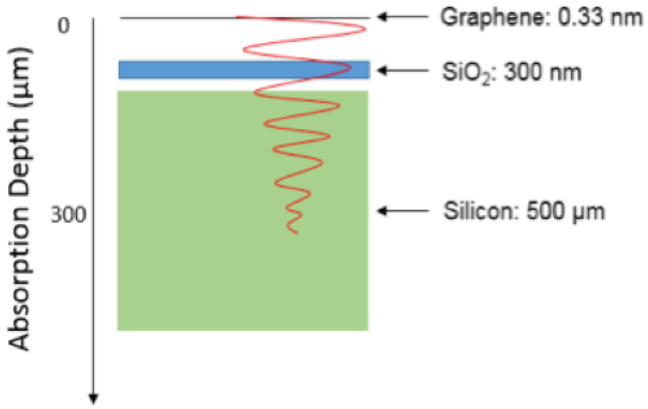

Fig 4. 2 Schematic of light penetration depth of graphene on SiO_2/Si substrate at 1030 nm.

Table 4. 1 Light absorption of graphene on SiO_2/Si substrate at 1030 nm.

Material	Thickness	Absorptivity	Ref.
Graphene	0.33nm (Monolayer)	2.3%	[182]
SiO_2	300nm (Thickness)	~1%	[184]
Si	500 μm	61%	[185]

4.2.2 Oxidization

Oxidization is regarded as one of possible contribution occurrence of the D peak during the laser processing of graphene [15] (800 nm, 100 fs, 1 KHz),[144](343 nm, 550 fs, 1 KHz) [186] (780 nm, 164 fs, 1KHz). The high peak intensity from the femtosecond laser can break down the carbon-carbon bond in graphene, which may further cause oxidization. Meanwhile, considering the lower bond energy of Si-C compared to the energy required to form SiO_2, one hypothesis is that the laser could break the carbon bond as well as break the SiO_2 form new bonds between silicon and carbon on the surface of the substrate. If the hypothesis is proved to be true, then the generated SiC will cause contamination on the graphene channels. The chemical reaction for the formation of SiC (over 2500 °C) is written as [187]:

$$SiO_2(s) + 3C(s) = SiC(s) + CO(g)$$

Table 4. 2 Average bond energies.

Bond	Average bond energy (kJ/mol)	Ref.
Carbon bond in graphene	480~580	[123]
Si-O bond in SiO_2	408	[188]
Si-C	360	[189]

4.3 Experimental Procedure

The nomenclature for describing the effects on graphene on SiO_2/Si Substrate after laser processing is listed as below:

1. Damaged: Laser-induced damage to SiO_2/Si Substrate appears visible under an optical microscope at 20× magnification.
2. Ablated: Monolayer graphene removed by laser from SiO_2/Si Substrate by examining with Raman spectroscopy.
3. No apparent effect: Smooth graphene under an optical microscope with no visible removal/change under SEM.
4. Cleanness on the edge: No other bonds formed during the laser process.

4.3.1 Removal of graphene-single line tracks

A single line track means the laser path that interacts with graphene in one directional scan. Multiple experiments are conducted from higher over ablated graphene down to slight ablated graphene. The set of experiments define the ablation windows. Assuming there is no incubation effect, the width of the patterning line would be always equal to the diameter of single-shot site, the estimation of pulse number was proposed in [89], which is expressed as $N = \frac{\Phi}{v/f_{rep}}$, where Φ is the laser beam diameter, ν represents processing speed and f_{rep} is pulse repetition rate, shown in Fig 4.3.

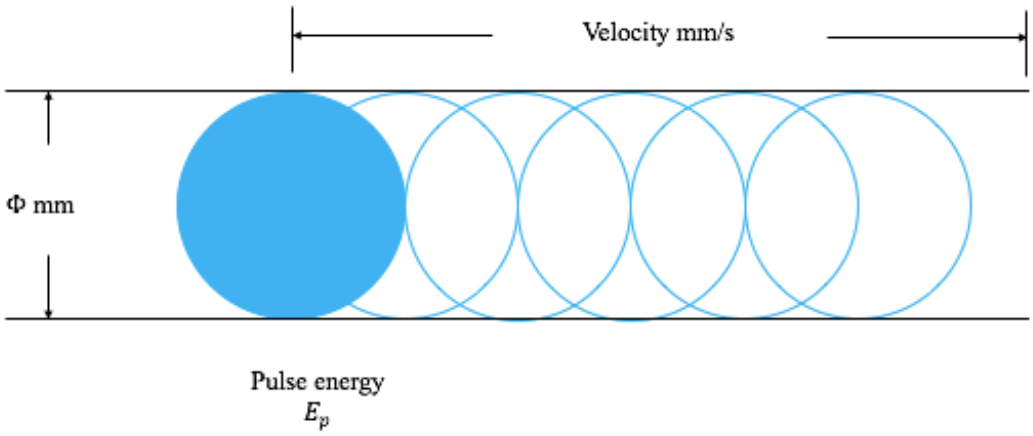

Fig 4. 3 The pulse number is estimated from the pulse overlap of a train of spot that moved at a constant speed ν, where Φ is the beam diameter.

The ablation area can be expressed as: $Area = \phi \cdot v \cdot t$ (mm^2), where t stands for the processing time.

The average pulse energy is calculated from the equation $E_p = P_{av}/f_{rep}$, where P_{av} is the average power that measured from the power meter.

The energy per unit area is also known as the deposited fluence (in J/cm^2) is calculated from the pulse energy, repetition rate and translation speed [190],

$$F = \frac{E_p f_{rep}}{\phi v}$$

Initially, a range of laser pulse energies are used for the experiment. The edge qualities were examined with SEM and Raman spectroscopy for different setting of speed and pulse energy. Experiments with the same setting of speeds and pulse energies were repeated in both air and nitrogen condition to investigate the potential oxidization.

4.3.2 Removal of graphene-area

After defining the ablation threshold thought the line tracks and evaluation of the ablation line area. The outer contour of any pattern should be removed to obtain the proposed lithography-free method in patterning graphene channels. The results were set with the same laser processing parameter but different scanning gaps between each path. The average gaps with 1 μm, 1.5 μm, and 2 μm of femtosecond laser process steps have been studied and the results are shown in the following section.

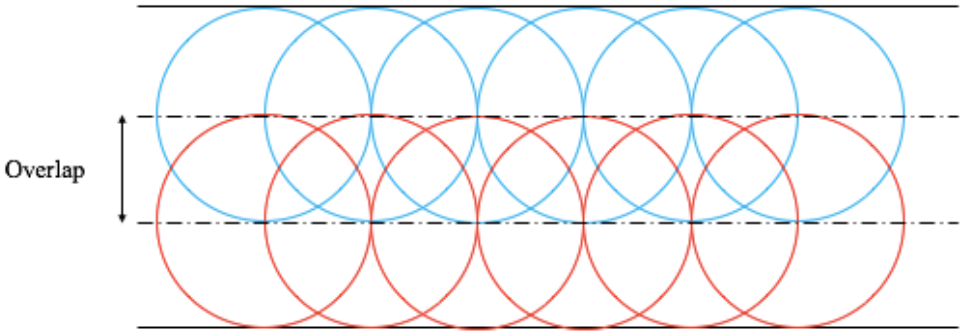

Fig 4. 4 A schematic of laser removing graphene area.

4.4 Results and discussion

4.4.1 Removal of graphene-lines

(a) Single lines removal of graphene

Graphene line removal was studied in ten groups of different laser pulse energies and scanning speeds at the set repetition rate of 5 kHz. The pulse numbers are calculated in Table 4. 3. Scanning speeds were ranged from 0.05 to 3 mm/s with three different levels of pulse energies (5.90 nJ, 12.1 nJ, 23.4 nJ, 45.3 nJ).

Table 4. 3 Calculated pulse numbers vs transition speeds.

Speed (mm/s)	0.05	0.1	0.25	0.5	0.75
Pulse numbers	416	208	83	41.6	27.7
Speed (mm/s)	1	1.5	2	2.5	3
Pulse numbers	20.8	13.86	10.4	8.32	7

Fig 4.5 shows the optical images of the lines processing of graphene on SiO_2/Si substrate. The black lines imply the graphene is damaged with pulse energy of 45.3 nJ, which have been examined by SEM. The black lines on the damage region were the remains ejected from the SiO_2/Si substrate. The lines with bright colour were where the graphene is removal with no significant damage to the substrate. Similar results occurred with 12.1 nJ. The lines with pulse energy of 12.1 nJ are clearly lighter than those with pulse energy of 23.4 nJ. However, the lines processed with pulse energy of 5.90 nJ have shown no observable evidence of cutting and ablation, based on the results from the optical microscope. From the optical images, we can see that different processing energies can cause different effects on the substrate. The laser peak fluence for a Gaussian beam can be calculated as

$F_{peak} = \frac{E_p}{\frac{\pi w^2}{2}}$, where E_p is the pulse energy, w is the focus radius. Thus, the calculated peak fluence is 0.177 J/cm^2 for 12.1 nJ, and 0.343 J/cm^2 for 23.4 nJ.

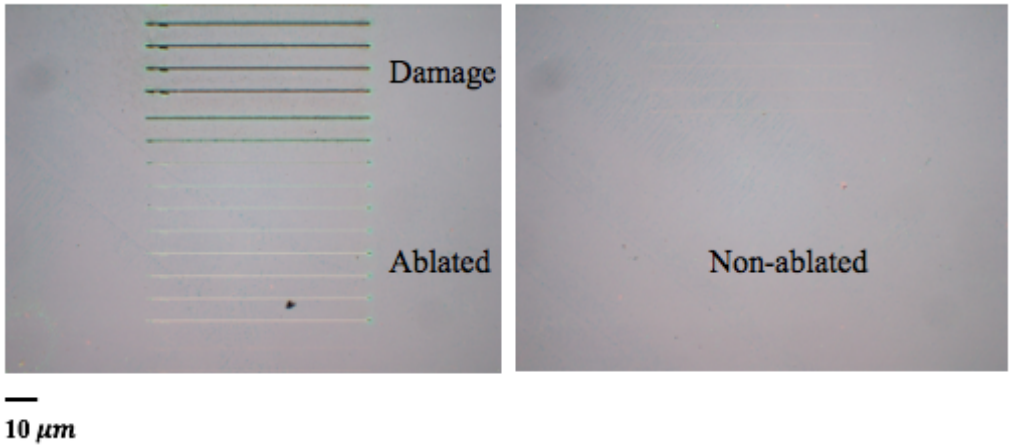

Fig 4. 5 Optical images of the processing lines after a femtosecond laser ablation. Based on the different status of the substrate, those lines are separated into damage (black lines), ablated (lines), non-ablated area (no observed lines) of graphene.

Table 4. 4 Deposted fluence caculation for pulse energy of 23.4 nJ@ 5kHz.

Speed (mm/s)	0.05	0.1	0.25	0.5	0.75
Deposited fluence (J/cm^2)	56.19	28	11.23	5.61	3.74
Speed (mm/s)	1	1.5	2	2.5	3
Deposited fluence (J/cm^2)	2.80	1.81	1.41	1.12	0.936

(b) SEM of graphene line removal

In this section, scanning electron microscopy (SEM) are employed to further investigate the processed lines, as shown in Fig 4.6. If the scanning speed is slow (at a speed of 0.05 mm/s), the high deposited fluence of 56.19 J/cm^2 results in the damage of the SiO_2/Si substrate as shown in the last picture of Fig 4.6. The ejected remains from the substrate charged during SEM measurement. The edge of the curve is rough and in the middle of the lines has shown white areas.

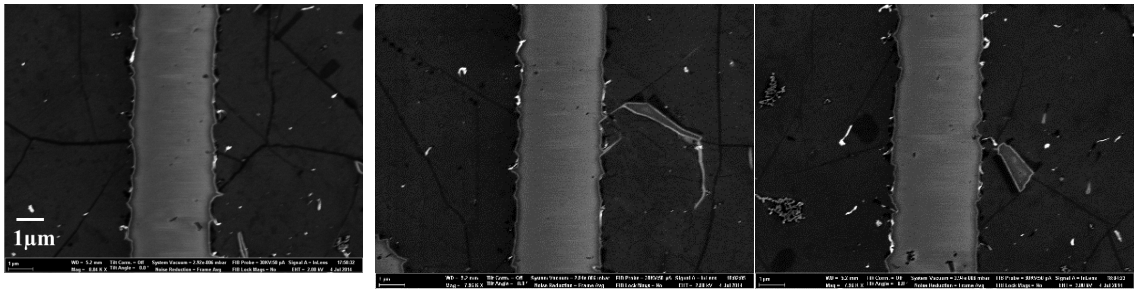

0.936 J/cm^2 1.12 J/cm^2 1.41 J/cm^2

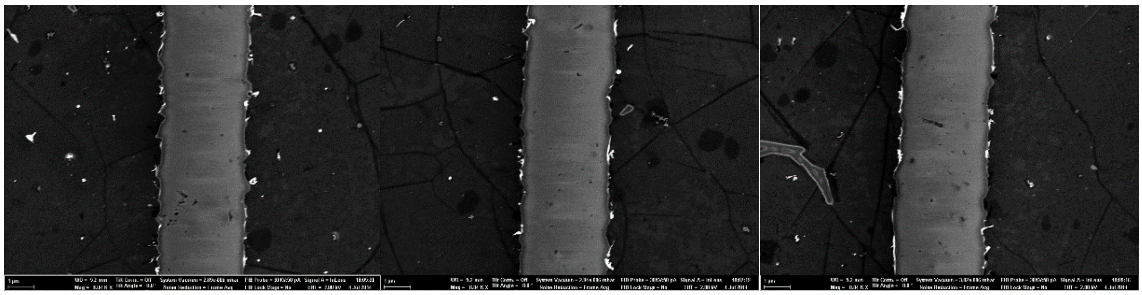

1.81 J/cm^2 2.80 J/cm^2 3.74 J/cm^2

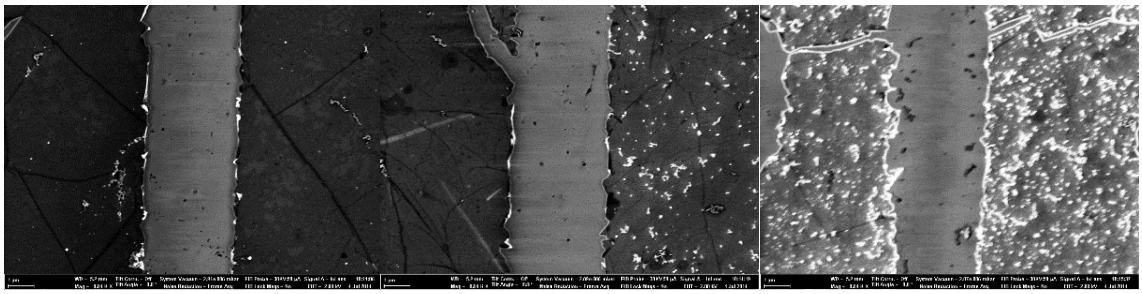

5.61 J/cm^2 11.23 J/cm^2 28 J/cm^2

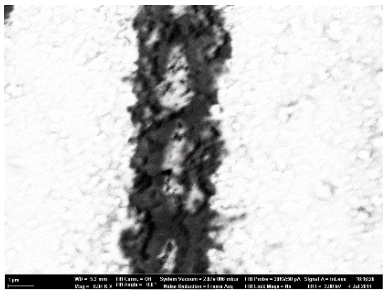

56.19 J/cm^2

Fig 4. 6 SEM image of the cut kerf of various deposited fluence, with the same scale as shown in the first picture with deposited fluence (0.936 J/cm^2).

4.4.2 Ablation threshold

(a) Kerf width

Kerf width is defined as the width of graphene that removed by a laser beam cutting process. Fig 4.7 demonstrates the variation of kerf width with various scanning speeds. The kerf width decreases with the transition speed. If we assume each pulse are independent of each other and there is no incubation effect, then the kerf width should be all the same to all speeds, as long as the laser pulse energy is the same. However, we have observed the kerf change with the speed for the same pulse energy. For the same pulse energy, the laser operates at a lower speed, energy of laser pulses may accumulate. As a result, the superposition of the tails areas of multiple Gaussian shape laser beams may pass beyond the ablation threshold and cause a further increase in the width of ablation channel. If the operating speed is higher, the graphene is subject to a lower number of laser pulses per area. When the scanning speed is passed beyond a given threshold, the superposition of multiple pulse energy in a local area is less significant. Thus, the width of the channel is decreased to a stable value. In practice, a low standard deviation of the kerf width is preferable, because it indicates a more controllable process. From Fig 4.7, it shows the standard deviations are low and stable with a scanning speed between 0.5 mm/s and 3 mm/s. It is more applicable and controllable. Therefore, it is more desirable to be used in the future laser manufacturing process. The waviness on the edge of the kerf is attributed to slight variations of both the stage movements and laser giving the pulse-to-pulse difference in diameter. The variation of the kerf width with the deposited fluence is given in Fig 4.8. The kerf width increases with the deposited fluence, reaching the largest kerf with of 3.67 ± 0.31 μm.

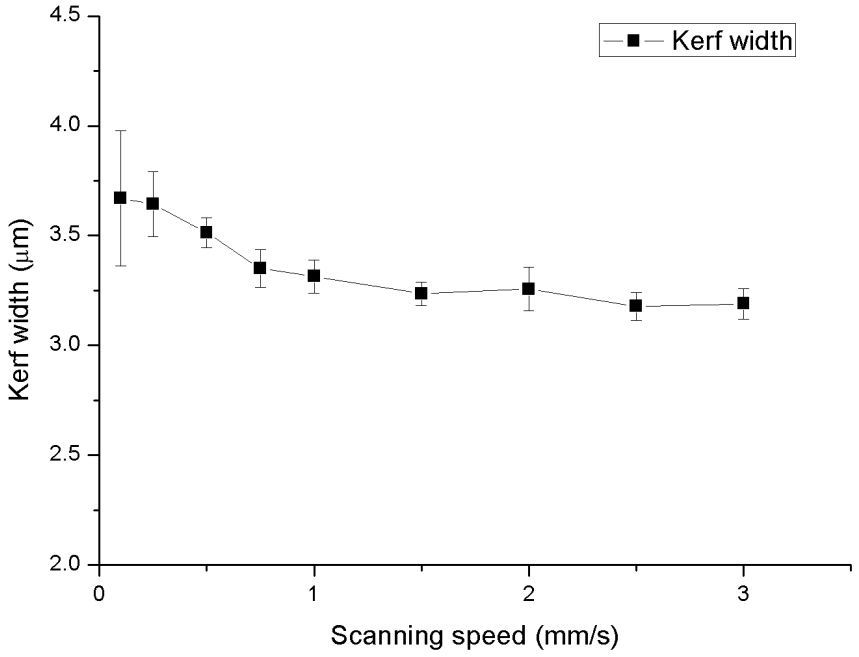

Fig 4. 7 Variation of kerf width with various scanning speeds.

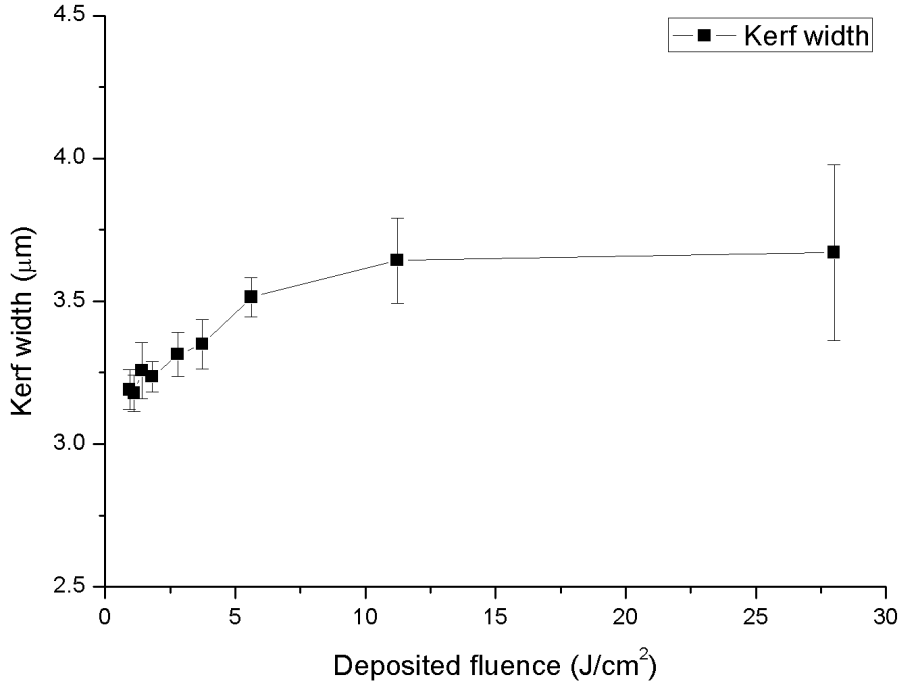

Fig 4. 8 Variation of kerf width with deposited fluence.

(b) Ablation threshold

If the pulse is independent of each other and there is no incubation effect, the kerf width should be identical to different speeds. However, our experiments provide the otherwise, the kerf width is changing with the speed. Therefore we can see the various kerf width contains the information of the incubation effect. Therefore we have substituted the information of the various the kerf width into the equation to estimate the ablation threshold equation 4.1, [88]:

$$F_{th} = \frac{2E_p}{\pi\omega_0^2} \exp\left(-\frac{d^2}{2\omega_0^2}\right) \tag{4.1}$$

where $E_p$stands for the pulse energy, $\omega_0$is the beam spot radius after the focusing lens and d is the ablation diameter. Fig 4.9 has shown the calculated femtosecond laser ablation based on the experimental results.

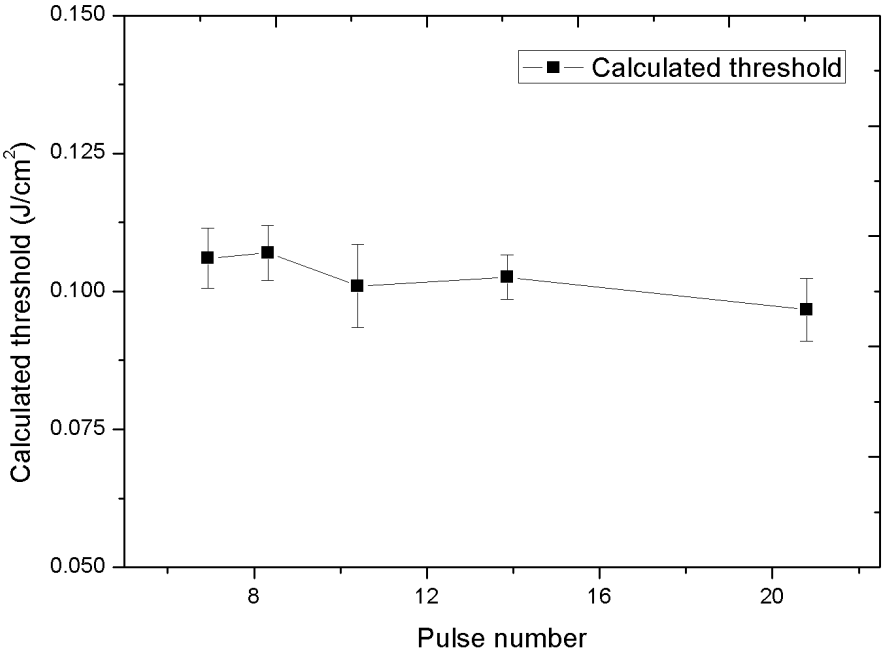

Fig 4. 9 Calculated damage threshold below the deposited fluence of 3 J/cm^2.

The results of the calculations can be triangulated by an alternative approach as shown in the dot lines. The incubation effect can be expressed as equation 4.2 [89],

$$F_{th}(N) = F_{th}(1)N^{s-1} \quad (4.2)$$

Where $F_{th}(1)$ and $F_{th}(N)$ are the single-shot and N- shot damage thresholds, respectively. S is known as incubation coefficient, which quantifies the degree of incubation behaviour. Incubation effect is defined as the recombination of laser pulses irradiation locally. Within a range of the number of pulses, the laser-induced damage threshold decreased remarkably. The experimental results of ablation thresholds in Fig 4.7 can also be well presented by using equation 4.2 (fit dot lines). The best fit single-shot damage threshold is 0.139 J/cm^2 , and incubation coefficient is calculated as 0.87. The estimated single-shot ablation thresholds are within the range reported by with the literature, as listed in Table 4.6. Moreover, the incubation coefficients for both cases are similar. They all together provide a statistical proof of a low ablation threshold (90 mJ/cm^2) found by experiments are caused by the incubation effect. The advantage of the discovered lower ablation threshold shows the way to remove graphene without apparent ablation of the substrate.

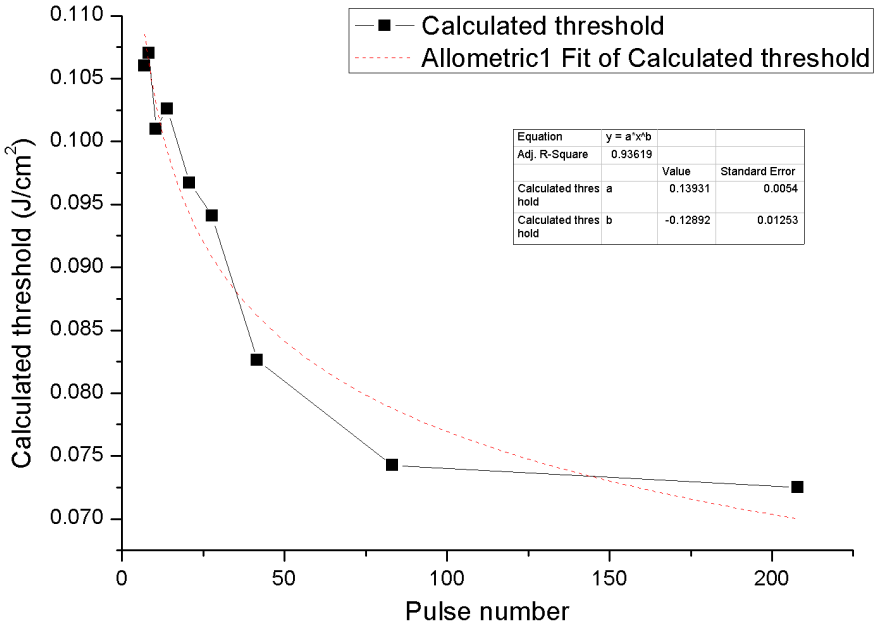

Fig 4. 10 Experimental (black solid curve) and the fitting results (red dash line) of damage thresholds of graphene under different pulse numbers. The fitted dot lines are $F(N) = 139N^{-0.13}$, where N stands for the pulse numbers.

Table 4. 5 At repetition rate 1 kHz, reported damage threshold fluence of graphene.

Wavelength	Pulse Duration	Threshold (mJ/cm^2)	Ref.
790 nm	50 fs~1.6 ps	~200	[140]
800 nm	100 fs	160~210	[143]
343 nm	550 fs	~150	[144]

The optical image with 0.48 J/ cm^2 illustrated in Fig 4.11. Raman spectroscopy of the cutting area is plotted in Fig 4.12. On the unprocessed area, the intense G and 2D peaks occurred at around 1580 cm^{-1} and 2700 cm^{-1} respectively. Within the cut line area, the G and 2D peaks have disappeared. It implies that the laser has completely removed the monolayer graphene in the processed region. The measurements and analysis have shown that the graphene has been completely removed when the deposited fluence is 0.48 J/cm^2.

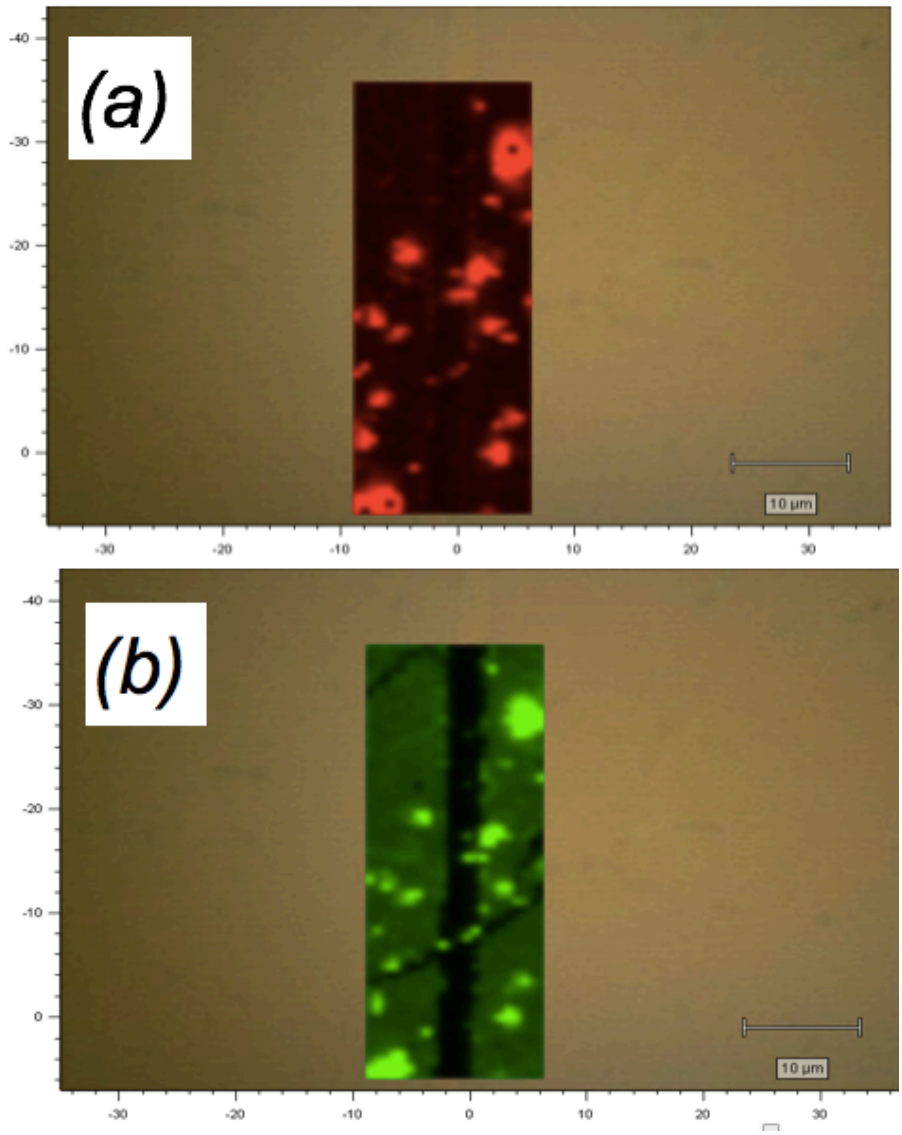

Fig 4. 11 Optical images of the cut base and uncut area on the graphene deposited on SiO_2/Si substrate, 0.48 J/cm^2.

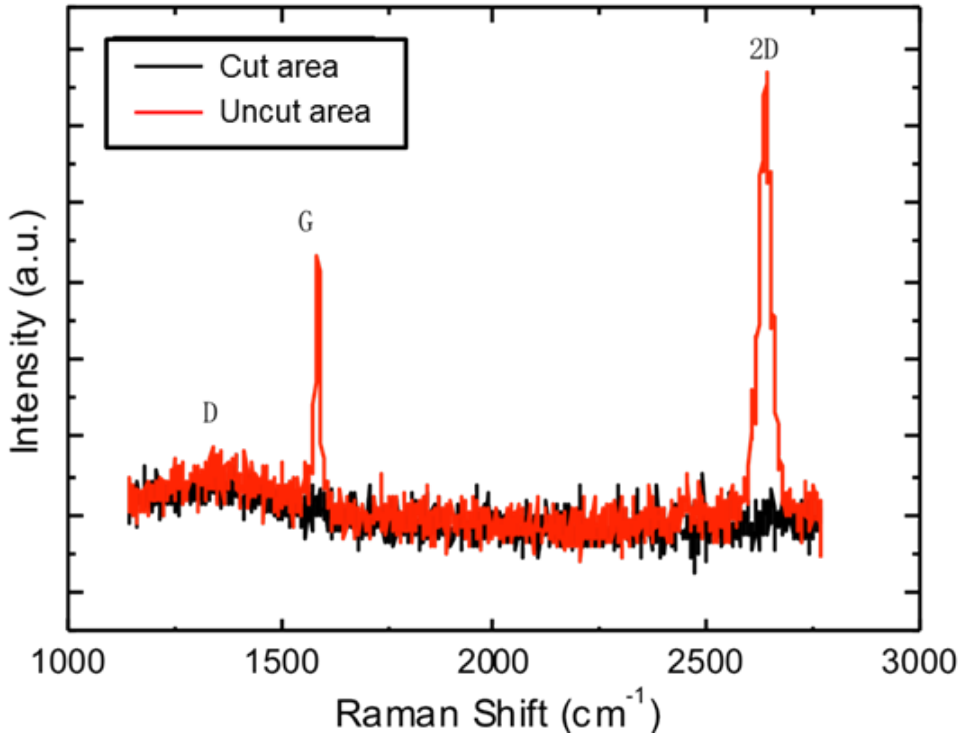

Fig 4. 12 Raman spectra of the cut base and uncut area on the graphene deposited on SiO_2/Si substrate, deposited fluence 0.48 J/cm^2.

4.4.3 Evaluation of ablated graphene edge

(a) Edge quality

The edge quality is also used to evaluate the performance and select the optimal parameters for laser processing. The cutting quality can be observed through SEM images. Fig 4.13 gives detailed information on the edge quality of a uniform cutting a channel with a width of 3.24 ± 0.04 μm. The brighter area on the cutting edge might be caused by oxidization, or graphene curved. This will be further examined in section 4.4.4.

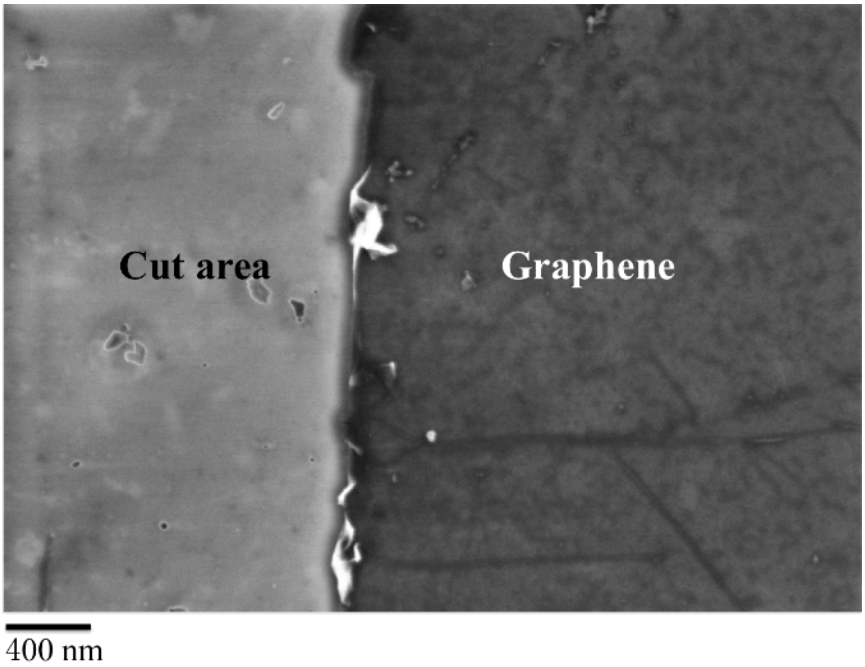

Fig 4. 13 SEM image of a femtosecond laser ablation process. The process parameters are with pulse energy of 1.81 J/cm^2. The edge of the ablation is focused to be evaluated.

(b) Defect at edge

The precision of cutting and the limited damage zone effect of femtosecond can be examined by a particular focused on the edge. To characterize the subtle edge modification, the edge of the ablated sample was scanned with the Raman microscope. In Fig 4.14 (a), the red dotted lines denote the boundaries of a line processed with 2.85 J/cm^2. When $y = -19$ μm, $x = 0$ μm indicates the edge. $x = 2$ μm, $x = 4$ μm, and $x = 6$ μm represent the distance from the edge. The Raman spectra on Fig 4.13 (b) illustrates the four positions along $y = -19$ μm. The low intense disorder-induced D peak, at around 1350 cm^{-1} at $x = 2$ μm, $x = 4$ μm, and $x = 6$ μm are overlapped and have a distinguishable different compared to the D peak at $x = 0$μm. On the edge ($x = 0$ μm), the defect-activated D and D' peak were observed. This showed no discernible laser-induced collateral damage near the cutting edge, which could be regarded as one of the benefits of using an ultrafast laser.

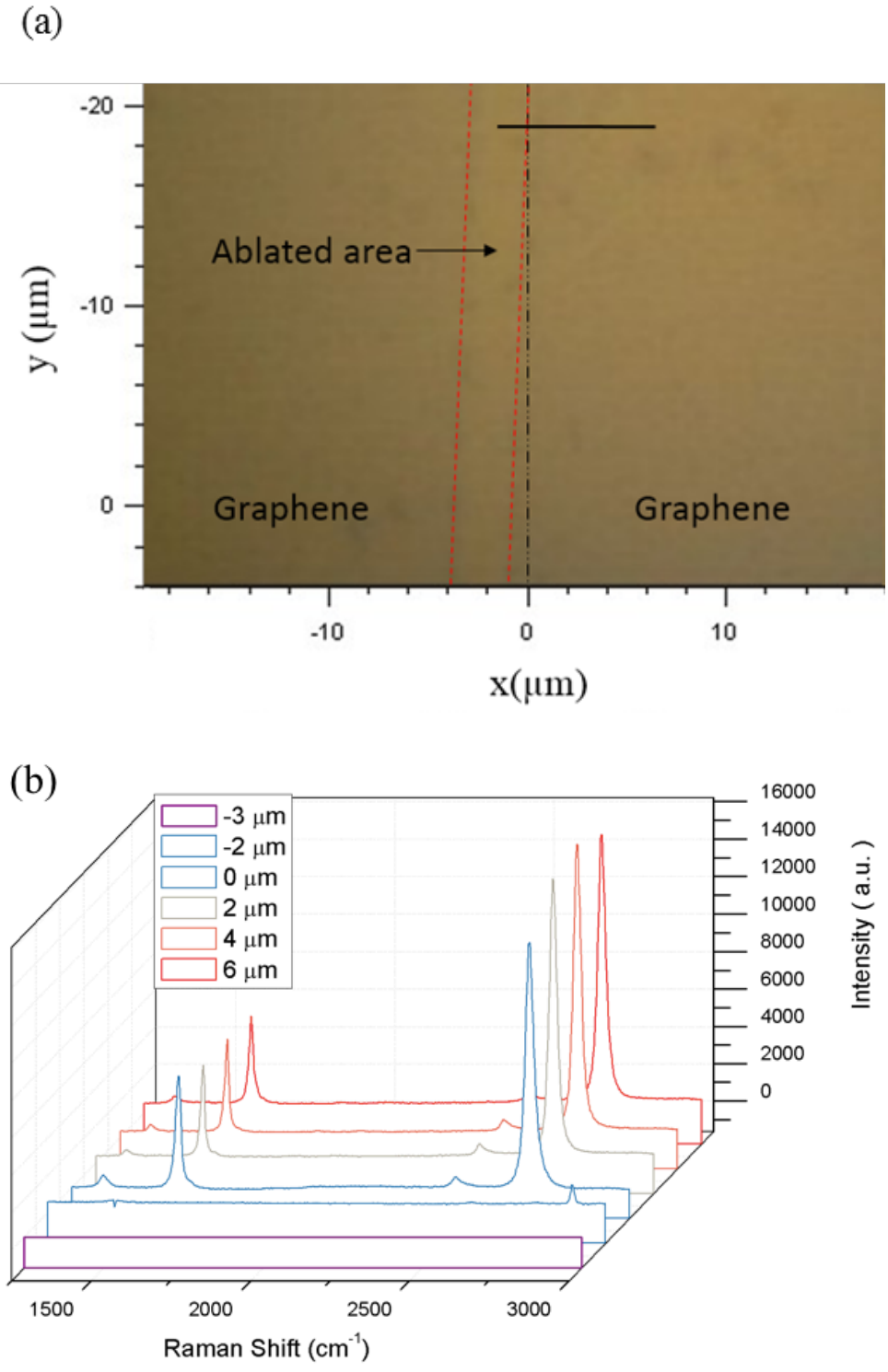

Fig 4. 14 Optical image of the femtosecond pulse ablated area with the focus on the edge of the graphene (a) and Raman spectra at x=-3, -2, 0,2,4,6 µm, indicates D, G and 2D peak (b) at different locations.

The calculated ratios of $I(D)/I(G)$ at $x = 0$ µm, $x = 2$ µm, $x = 4$ µm, and $x = 6$ µm are 0.11, 0.069, 0.07 and 0.079, respectively (Fig 4.15). This illustrates that during the femtosecond laser

ablation process, there is little influence on the area beyond 2 μm. This demonstrates the prospect using a femtosecond laser to create a graphene area that is clear and undamaged.

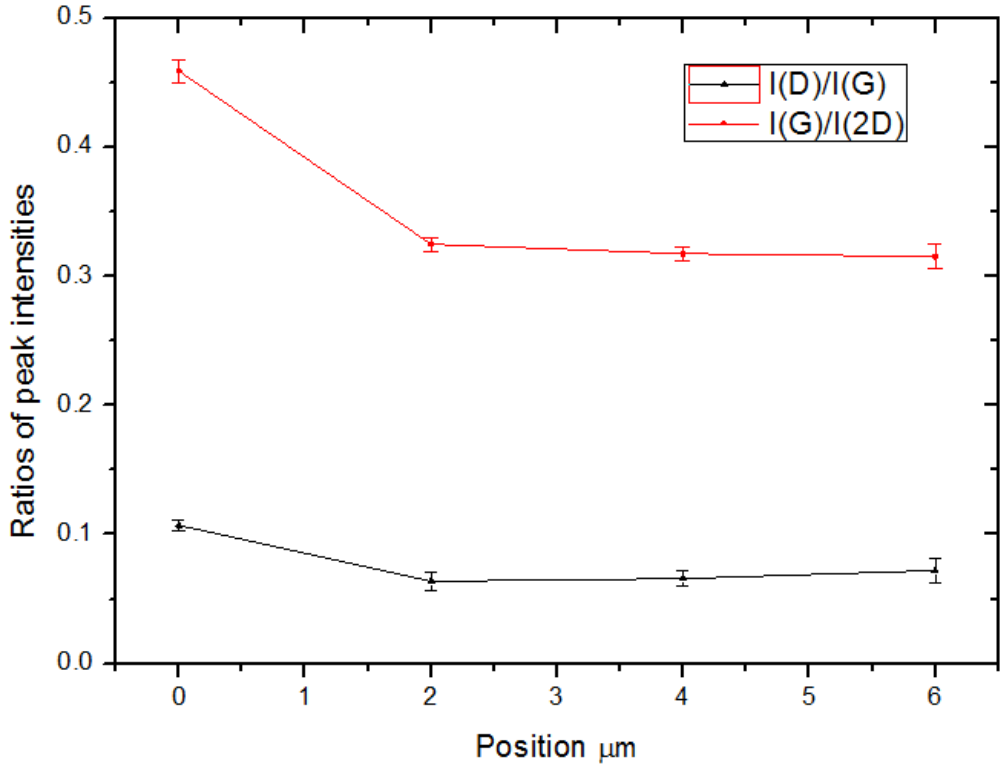

Fig 4. 15 Ratios of peak intensities at the edge area of graphene at x=0, 2, 4, 6 μm, where x=0 stands for the edge.

The future analysis on the laser affected region at $x = 1$ μm, another sample with a fluence of 5.61 J/cm^2 was measured with Raman at the edge $x = 0$ μm, $x = 1$ μm, the graphene ablated region as well as the non-ablated region as a reference. Even though the sample was processed with higher laser fluence than that shown in Fig 4.14 and 4.15, the sample at $x = 1$ μm still shown a decrease of I(D)/I(G) and I(G)/I(2D). This again indicated that at x=0, where stands for the edge, the D peak increase. Hence, there is no evidence of the D peak that increased in the region that is 1 μm from the ablation line. This could enlarge the potential of the femtosecond laser ablation process for graphene micrometre-scale devices.

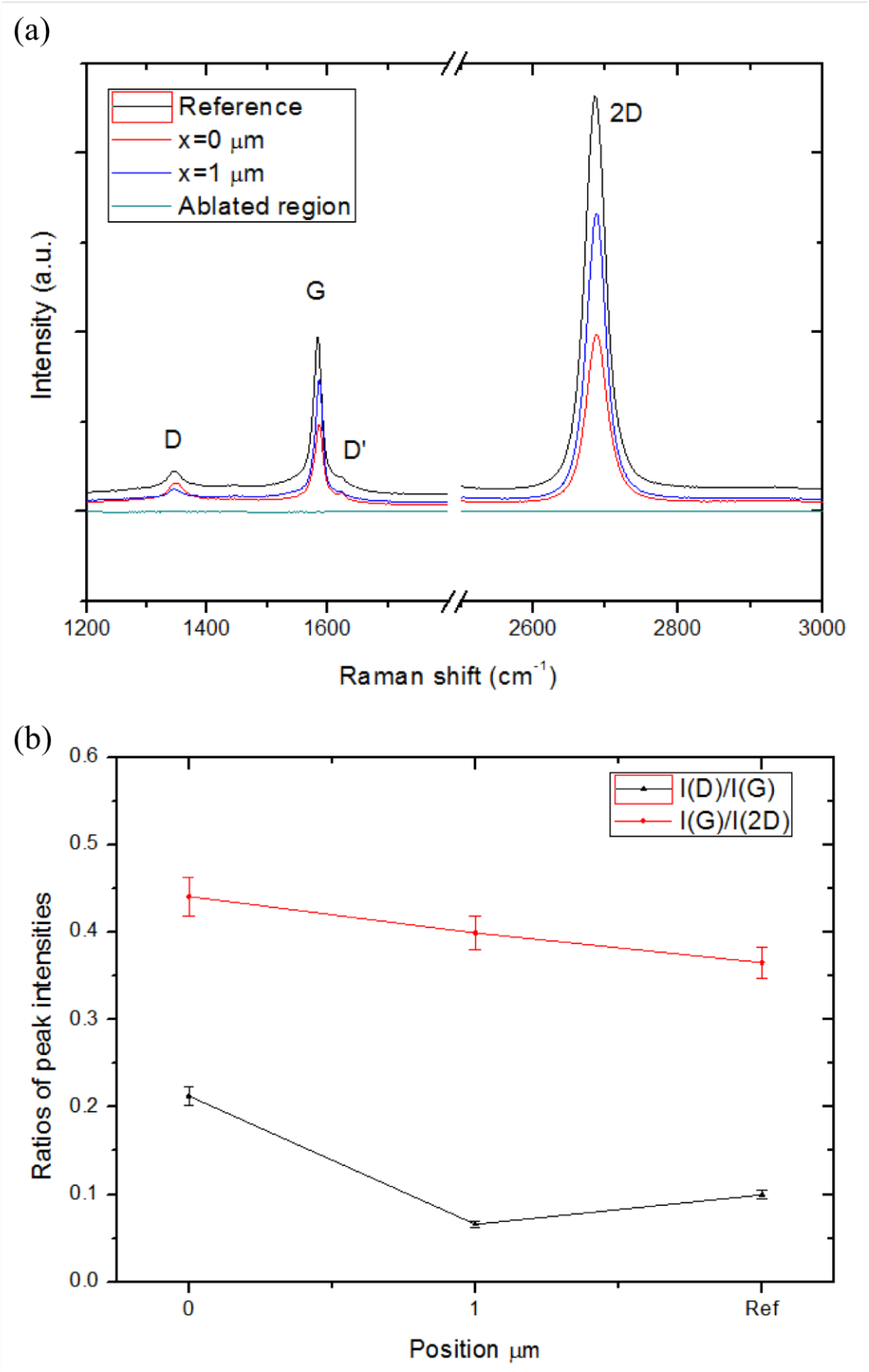

Fig 4. 16 Raman spectra (a) and ratios of peak intensities (b) at x=0, 1 μm, and reference.

The edge shows a higher D peak compared to the further areas. The higher D peak remains to be fully understood since this might be caused by the ultrafast laser pulse. However, the edges break the translation symmetry of graphene; they can be treated as defects [191], [192]. It is known that the D peak could be caused by the edge itself. In the literature, a possible contribution to this D peak was argued to be oxidation [15], [182], [186]. However, the explanation requires further validation. Thus, the later section of Kelvin Prove Force Microscopy will examine the material of edge in detail with the measurement of the potential difference between the cut region and the non-ablated graphene region.

4.4.4 Substrate Evaluation

The lower ablation threshold for graphene achieved in this process can avoid damage to the Si substrate. Furthermore, the smaller ablation threshold can also preserve the SiO_2 film, so that it could be used in a graphene field effect transistor (FET) device. As for optimising further fabrication steps of using the femtosecond laser to pattern graphene for devices, a thorough examination of potential damage is necessary.

(a) Topography of kerf under air condition

To explore the quality and dimension of the post-ablation graphene sample, tapping mode of atomic force microscopy (AFM) was applied. As illustrated in Fig 4.17, the dashed circle indicates an example that the graphene rolls up at the edge, which is also observed using SEM as shown in Fig 4.13. A representative line-section across the ablated region (along with the light blue line in Fig 4.17 (a)) is shown in Fig 4.17 (b). The edge step height is around 6 nm. Compared with the thickness of SiO_2 of 300 nm, there is limited evidence of any removal of SiO_2 and no noticeable damage to the silicon substrate. The kerf width is measured to be 3.37 μm. The peak fluence is calculated to be 261 mJ/cm^2.

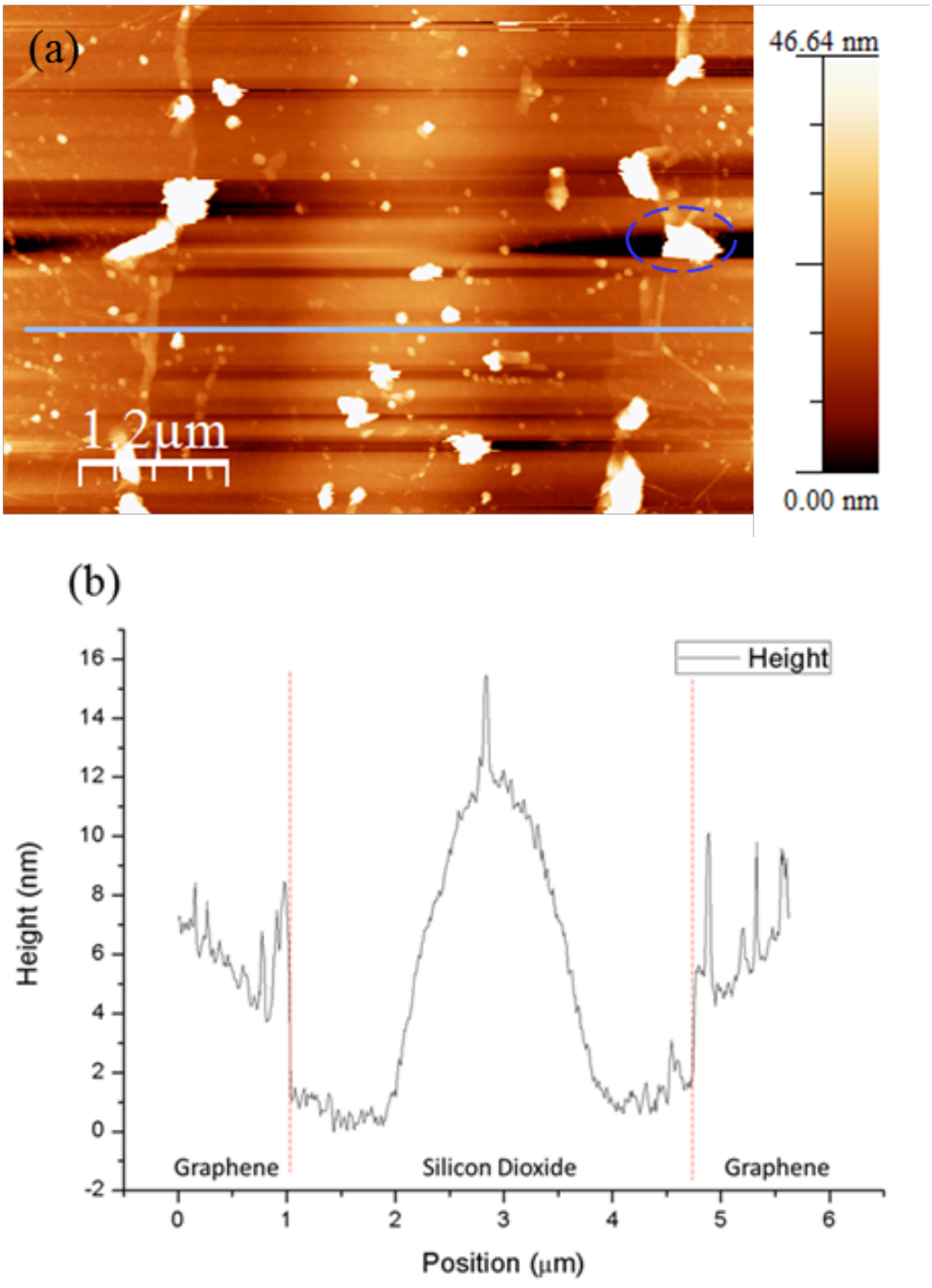

Fig 4. 17 (a) AFM topography image of a cut kerf with deposited fluence 0.71 J/cm^2 (b) gives the cross-section map along the path shown by the horizontal line in (a).

In the cross-section map as shown in Fig 4.17 (b), a Gaussian-shaped swelling on the surface of the substrate appears in the central region. Considering the silicon ablation threshold which is around 430 mJ/ cm^2 at the wavelength of 1030 nm, the processing peak fluence (261 mJ/cm^2) is below the

Si ablation threshold. This may indicate the swelling is sub-ablation phenomena. The femtosecond laser process is a “cold” procedure, which means the thermal effect is limited in the surrounding area. Therefore, the thermal expansion is mainly caused by the energy absorbed in the impacted region.

As discussed in section 4.2.1, Si has a higher energy absorptivity compared to SiO_2 and graphene at such wavelength. Hence, the absorbed energy of Si in the impacted region could be one of the major contributors to the swelling effect. Also, the peak fluence during the process is slightly above the SiO_2 melting threshold, which may cause the shape change of the SiO_2 layer.

(b) Topography of kerf under the N_2 condition

For the ablation of graphene under the N_2 environment, similar Gaussian shape swelling effect was observed as shown in Fig 4.18, the ablation depth of SiO_2 is around 3 nm.

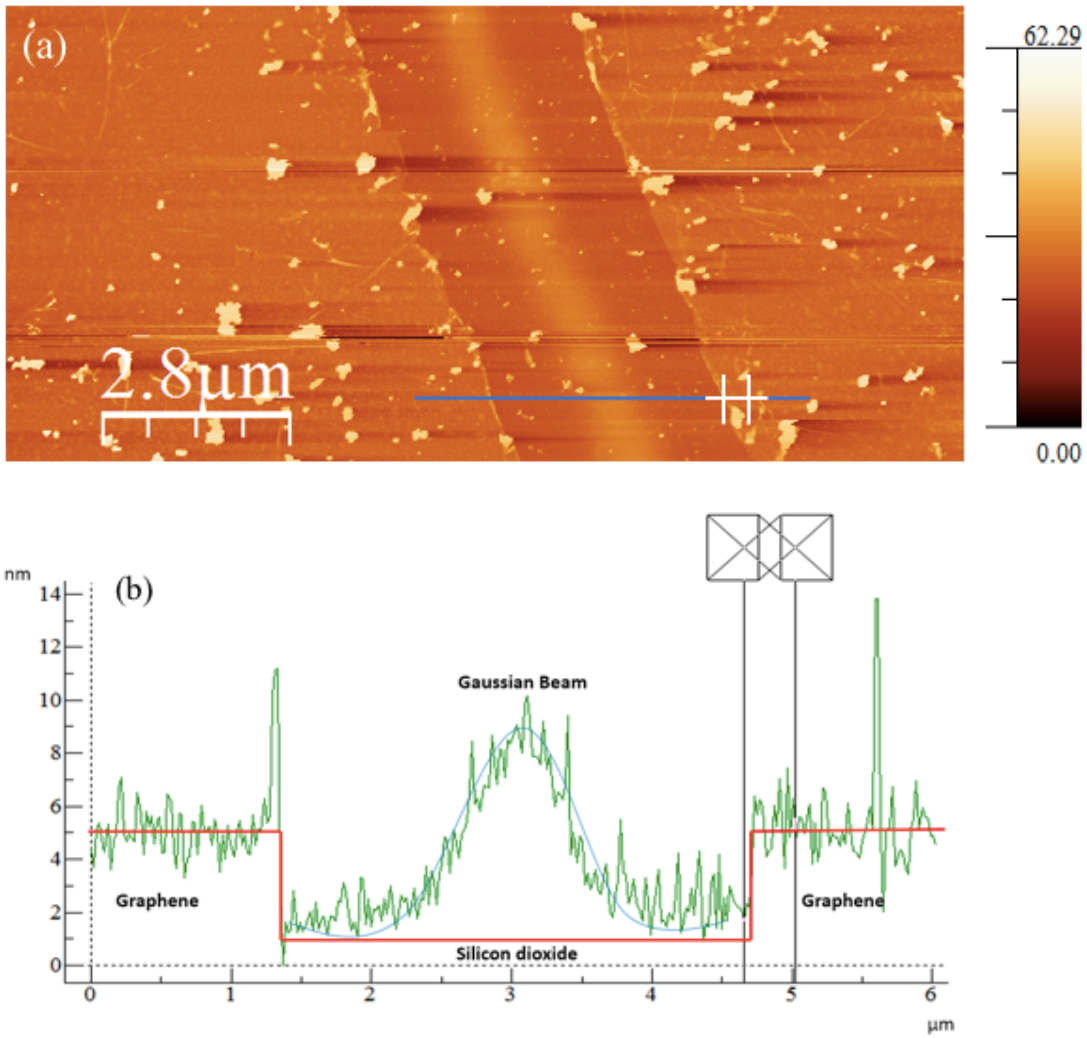

Fig 4. 18 (a)AFM topography image of a cut kerf with a deposited fluence of 2.85 J/cm^2, under N_2 condition. (b) Cross section map along the path shown by the horizontal line in (a).

4.4.5 Analysis of reformed bonds

The previous analysis work demonstrates that both graphene near the cutting edge and the Si substrate were not affected during the ablation process. A slight change happened to the edge and SiO_2, where a small increased D peak appears at the edge, and a Gaussian shape swelling occurs at the SiO_2 surface. Up to now, the hypothesis is that the laser could break the carbon bond as well as break the SiO_2 to form new bonds between silicon and carbon on the surface of the substrate, as well as the modification of the cutting edge, which needs further analysis.

(a) KPFM of the edge under air condition

To further explore the substrate condition in the cut region, AFM was applied in Kelvin probe force mode, and the amplitude modulation measurement method was selected. The experiments were

carried out under ambient conditions and with Nitrogen as a reference experiment. This is to evaluate whether the oxygen in the ambient air influences the process of ultrafast pulse interaction with graphene deposited on SiO_2/Si substrate. The quantitative mapping of the surface potential is provided with Kelvin probe force microscopy (KPFM), which probes contact potential difference (CPD) between the sample and the conducting probe. Fig 4.18(a) shows the CPD image of the same cut kerf as shown in Fig 4.16 (a), indicating a clear and uniform potential difference ΔV_{CPD} between graphene and SiO_2, which was measured to be $\Delta V_{CPD} \approx 30\ mV$.

The edges were distinguishable and showed a definite step in potential between the substrate and the rest of the graphene. This suggests no modification of other bonds, which supports that D peak generated at the edge of graphene was not due to the oxidation due to laser etching as explained in [15], [182], [186]. In Fig 4.19 (a), the folded flake of graphene at the edge experienced a higher surface potential of around 40 mV. This is consistent with findings of others, mentioning that the surface potential increases with the number of layers of graphene [193], [194]. In the SiO_2 region, the KPFM contrast is relatively uniform with a ~15 mV variation. Since ΔV_{CPD} between graphene and SiC is around 100 mV, the much lower contrast of 15 mV implies no formation of SiC as a result of a chemical reaction between the Si and graphene [194]. These results indicate that during the femtosecond ablation process, there is no evidence of modification of SiO_2.

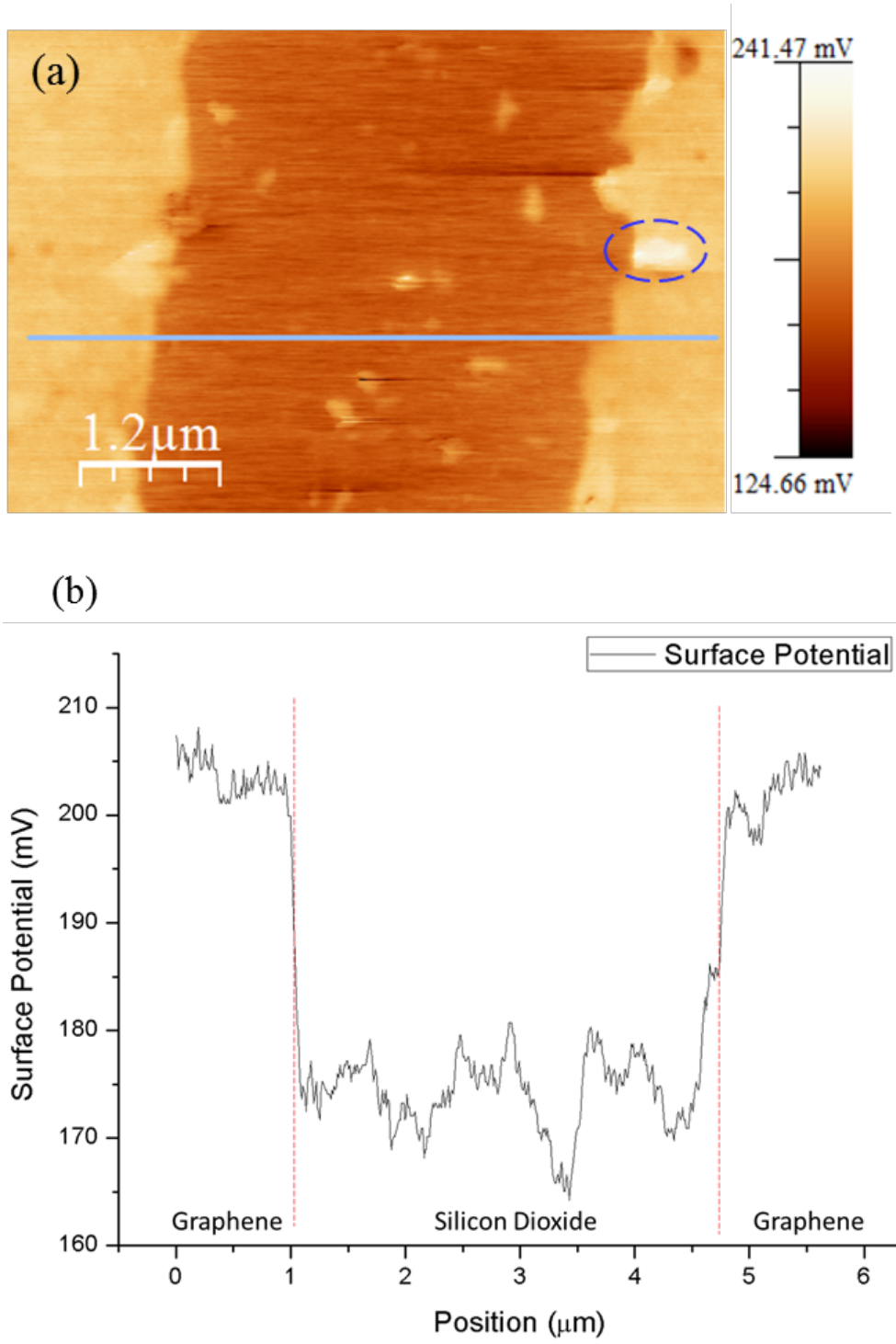

Fig 4. 19 (a) Kelvin probe force microscopy (KPFM) surface potential map of the cut kerf shown in Fig 4.16 (a) region. The dashed circle indicated that at the edge the graphene flake has folded over itself to create bilayer graphene, which has a higher CPD than the monolayer graphene (b) Cross section and surface potential maps along the path shown by the blue horizontal line in (a).

(b) KPFM of the edge under the N_2 condition

The cut edge of graphene has been examined with the same laser parameters. The edge processed with the same laser parameters with nitrogen and has also been observed under KPFM. The images in Fig 4.20 show that the edge is a clean cut.

Fig 4.20 gives an overall surface potential mapping on the kerf and edge. Fig 4.21 demonstrates a closer look at the edge area. This region is chosen particularly for the rough surface on the left side compared to the clean right side. As atomic force is a precision measurement and the tip could collect the redeposit this might cause specific measurement errors on the left side. Stepping down the height can be seen from the cross-section region. After around 2 μm, a similar clear step between the SiO_2 surface and graphene has appeared. This image demonstrates that the quality of roughness of graphene on the SiO_2/Si substrate does not influence the sharpness of the clear edge difference from the substrate, but the grain boundary can affect the edge shape after ablation.

Until now, both the edge surface potential information and the comparison of those cut under nitrogen suggested that there was no oxidization at the edge of the ablation on graphene.

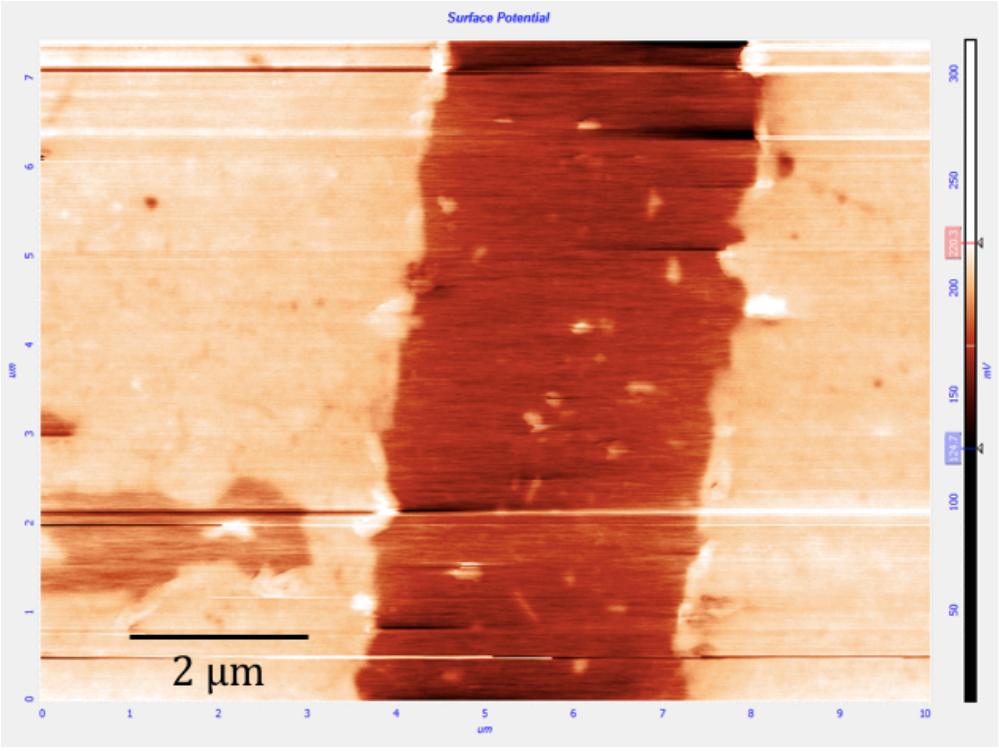

Fig 4. 20 The surface potential of graphene ablation kerf under deposited fluence 2.85 J/cm^2 under Nitrogen condition.

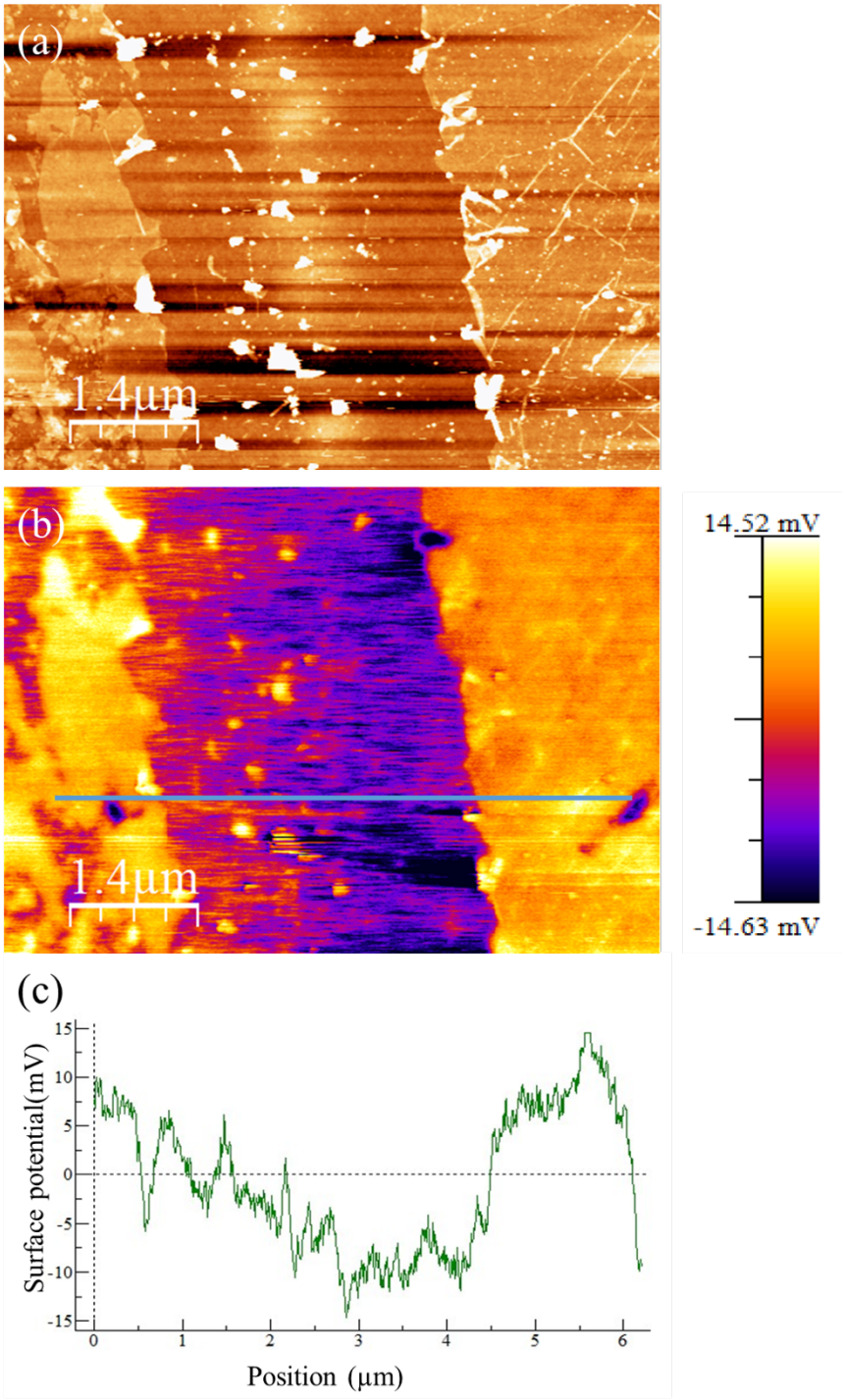

Fig 4. 21 (a) Kelvin probe force microscopy (KPFM) surface potential map of ablated kerf under Nitrogen condition with a deposited fluence of 2.85 J/cm^2. (b) Surface potential maps. (c) Cross section and surface potential maps along the path shown by the blue horizontal line in (b).

4.4.6 Area removal of graphene

Based on the success of removal of graphene on single lines, the area removal is attained in ambient condition by multiple lines removed with different gaps between two lines, with pulse energies of 28.35 nJ. The single line deposited energy can be calculated as shown in Table 4.6.

Table 4. 6 Key parameters settings and experimental results.

Sample order	**Sample A**	**Sample B**	**Sample C**	**Sample D**	**Sample E**
Scanning speed	0.5 mm/s	0.5 mm/s	0.5 mm/s	1.5 mm/s	1.5 mm/s
Space/gap	2μm	1μm	1.5 μm	1 μm	1 μm
Deposited fluence	4.6 J/cm^2	5.5 J/cm^2	5 J/cm^2	1.8 J/cm^2	1.8 J/cm^2
Graphene channel	I(D)/I(G): 0.167	I(D)/ I(G): 0.251	I(D)/I(G): 0.121	I(D)/I(G): 0.129	I(D)/I(G): 0.134
Outside graphene	Not removal	Removal	Removal	Not removal	Not removal

In Fig 4.22, the results showed that a good graphene channel and a good substrate surface are attainable with 1 μm gaps. With 2 μm gaps, graphene has only been partially removed. While 0.5 μm has resulted in an over-ablation, the shape of graphene channel has been damaged. In theory, these set of parameters should all removal the graphene. However, the Sample D and Sample E have not succeeded in removal graphene, this may be attributed to the over ablation of sample B, the higher intensity may move the sample slightly. A repeated deposited fluence of 1.82 J/cm^2 was conducted on the graphene sample, the parameter setting is as shown in Table 4.7. To guarantee the width of processed graphene channel has at least 10 μm, the width of the channel is set to be 14.35 μm to provide a bigger than 2 μm's residue on both sides of the channel. Four clear rectangle-shaped graphene channels are shown in Fig 4.23~Fig 4.28. The effect of the damage on the substrate due to swelling causes the uneven after graphene removal. Raman spectroscopy has examined the quality of graphene channel and the outside area. In Raman mapping (Fig 4.28), graphene channels show a distinguishable G peak, while the outside ablated area shows a dramatic drop in G peak.

Table 4. 7 Parameter setting for additional experiment to validate the result.

Pulse energy	19.62 nJ
Scanning speed	0.5 mm/s
Space/gap	1 μm
Deposited fluence	3.79 J/cm^2

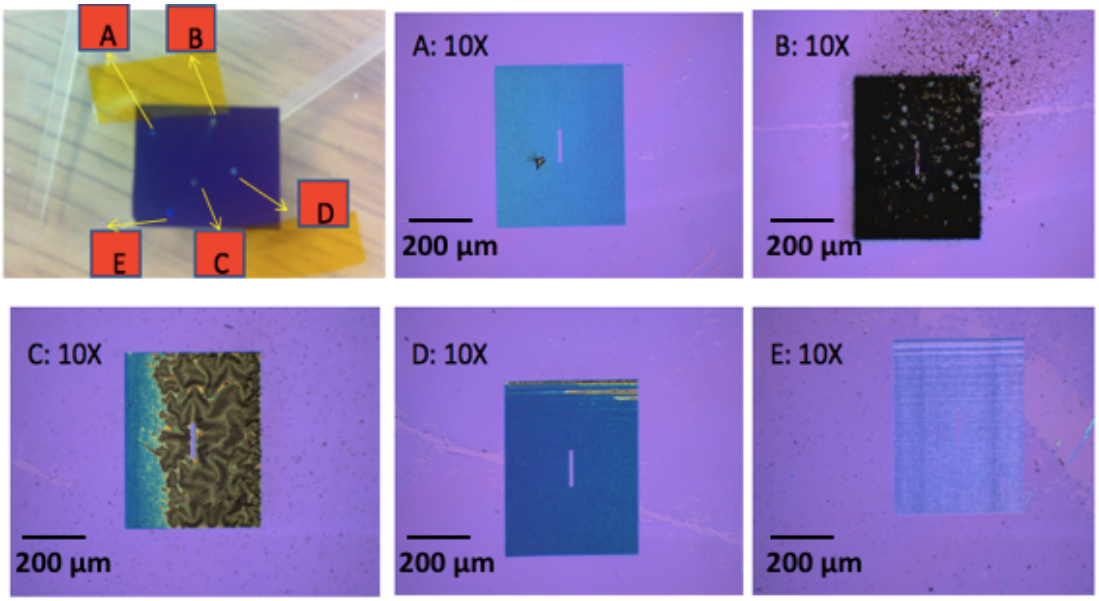

Fig 4. 22 Square processing with pulse energy of 28.35 nJ. A: 2 μm space/gap, speed: 0.5 mm/s B: 1 μm space/gap, speed: 0.5 mm/s C: 1.5 μm space/gap, speed: 0.5 mm/s D: 1 μm space/gap, speed: 1.5 mm/s E: 1 μm space/gap, speed: 1.5 mm/s.

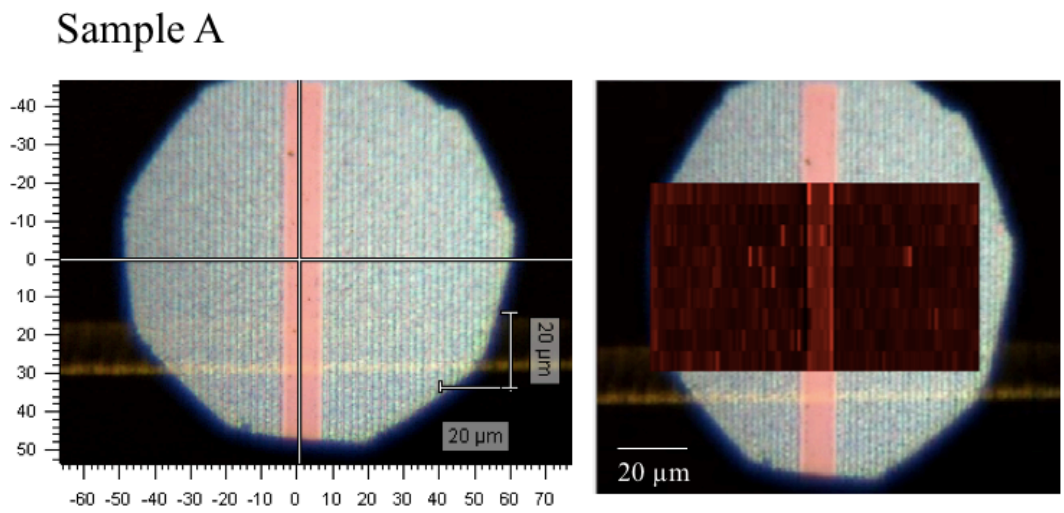

Fig 4. 23 Raman results of sample A, the graphene channel is undamaged, however in the outside region, the graphene is not completely removed.

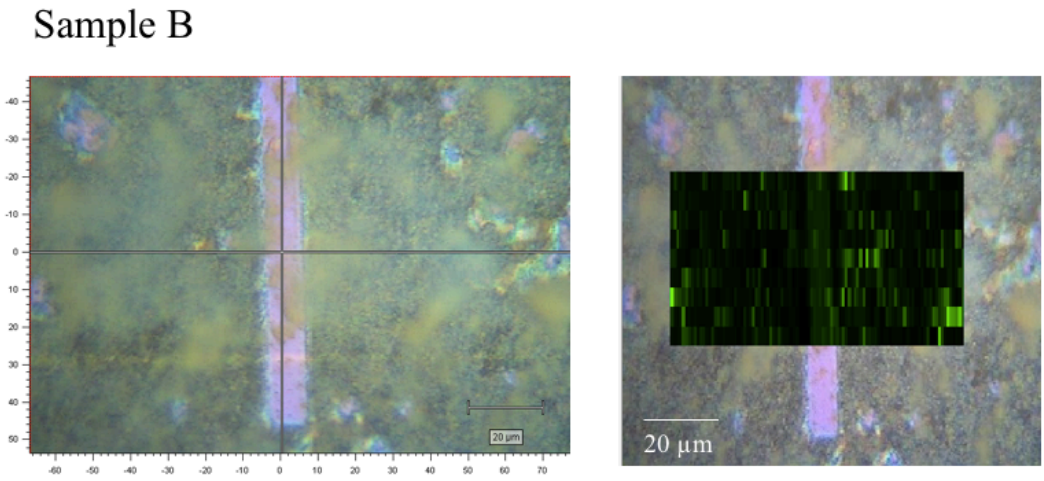

Fig 4. 24 Raman results of sample B, the graphene channel is damaged, the outside region indicates no graphene.

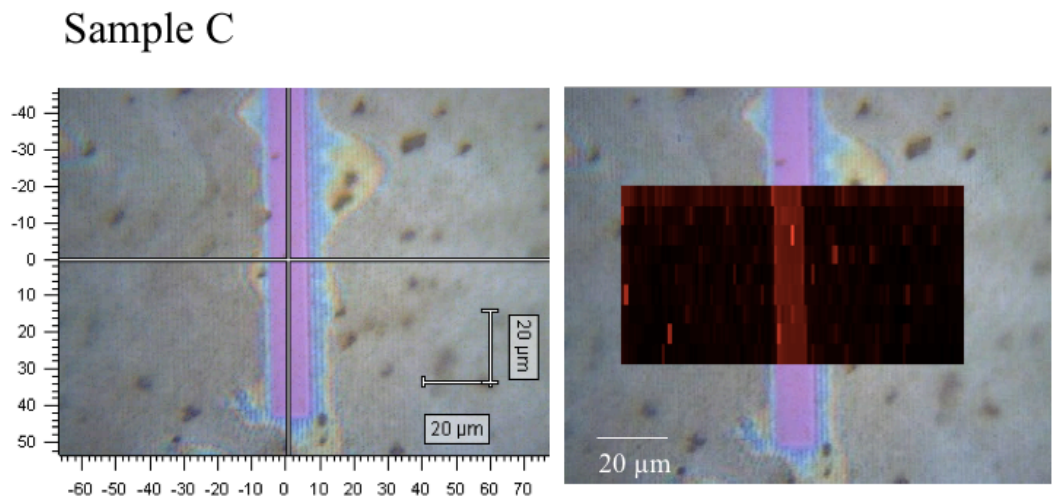

Fig 4. 25 Raman results of sample C, the graphene channel is undamaged. The outside region has no graphene but it is not uniform.

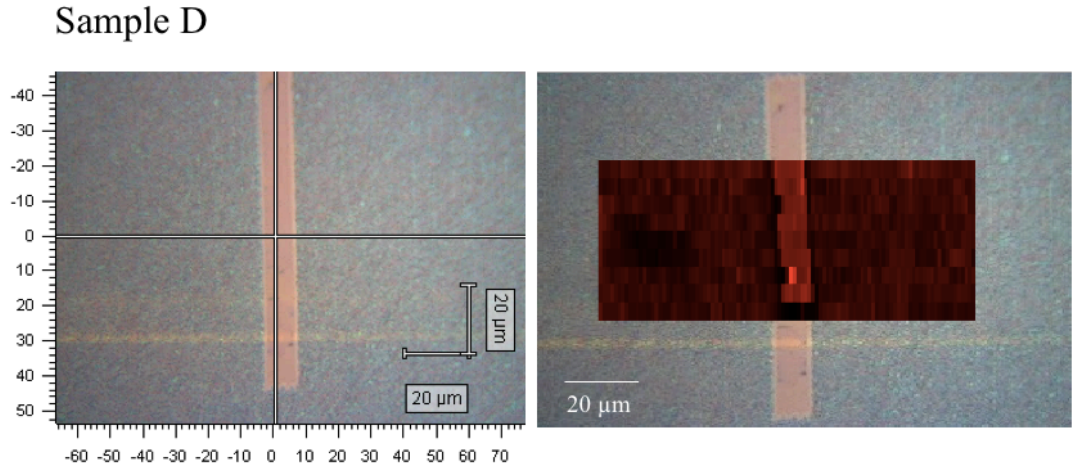

Fig 4. 26 Raman results of sample D, the graphene channel is undamaged. However, in the outside region, the graphene is not completely removed.

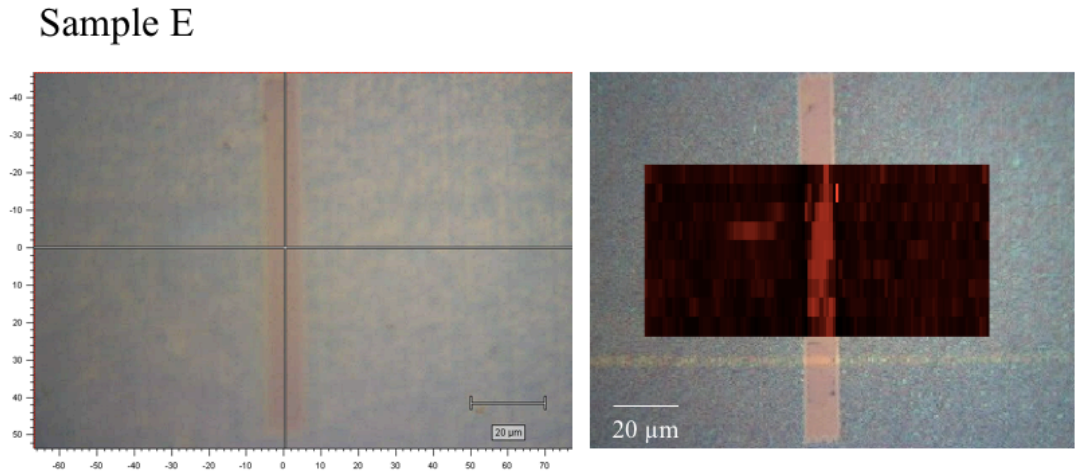

Fig 4. 27 Raman results of sample E, the graphene channel is undamaged. Graphene is not removed in the outside region.

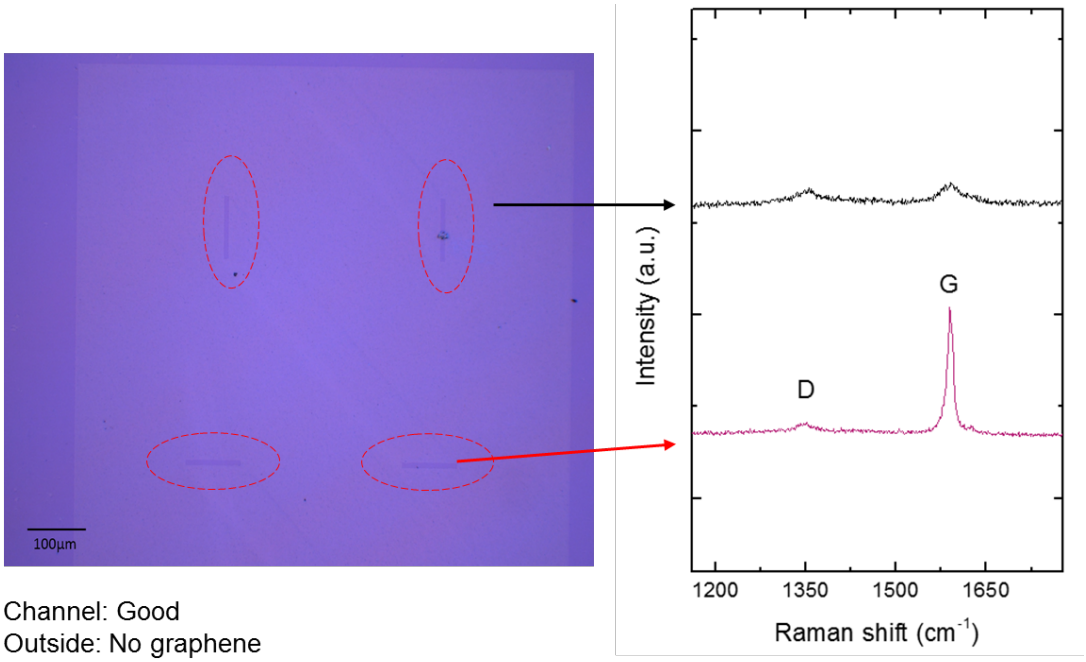

Fig 4. 28 Left: The processed graphene channel (10 µm×100 µm), outside region 200 µm. Right: Raman map of the measured graphene ablated area (Black line) and the isolated graphene (Red line). Sample processed 3.79 J/cm^2.

4.4.7 Analysis of the kerf and debris

(a) EDS on the kerf

Fig 4.29 showed the EDS image of over ablated region with the fluence of 56.19 J/cm^2, the kerf has a low signal of O element, but has a high signal of Si. This indicated that the SiO_2 is removed under the over ablated region. Fig 4.30 showed the EDS image of the selectively removed region with the fluence of 0.71 J/cm^2, the kerf has shown smooth O element and Si element. This indicated the SiO_2 layer was still on the top surface of Si and the silicon was not ablated. By comparing these results, it confirmed that at low fluence, with precise control of the femtosecond laser, selective removal of graphene without ablating Si substrate can be achieved.

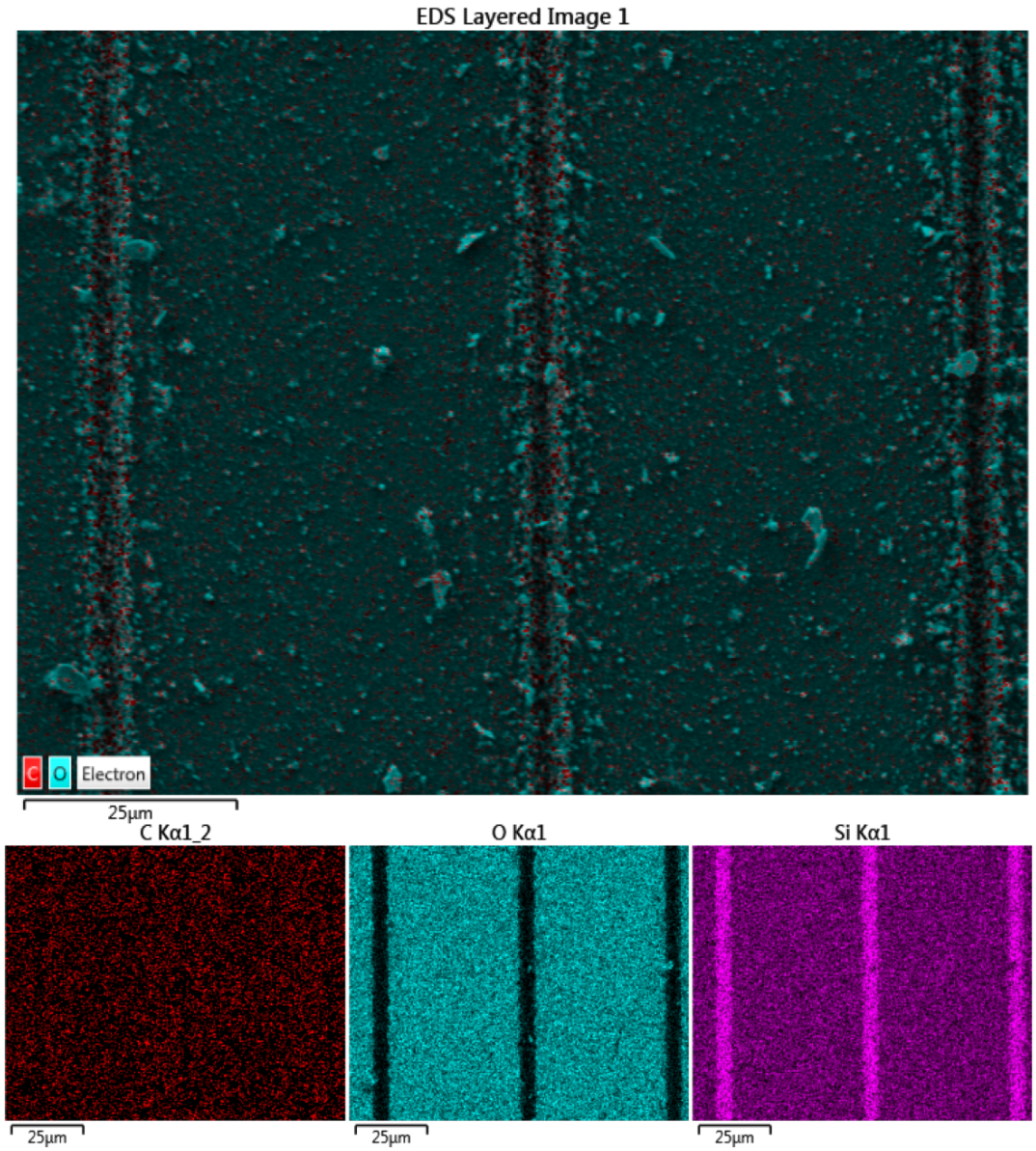

Fig 4. 29 EDS image of over ablated region (56.19 J/cm^2). Red stands for C, blue stands for O, and pink stands for Si.

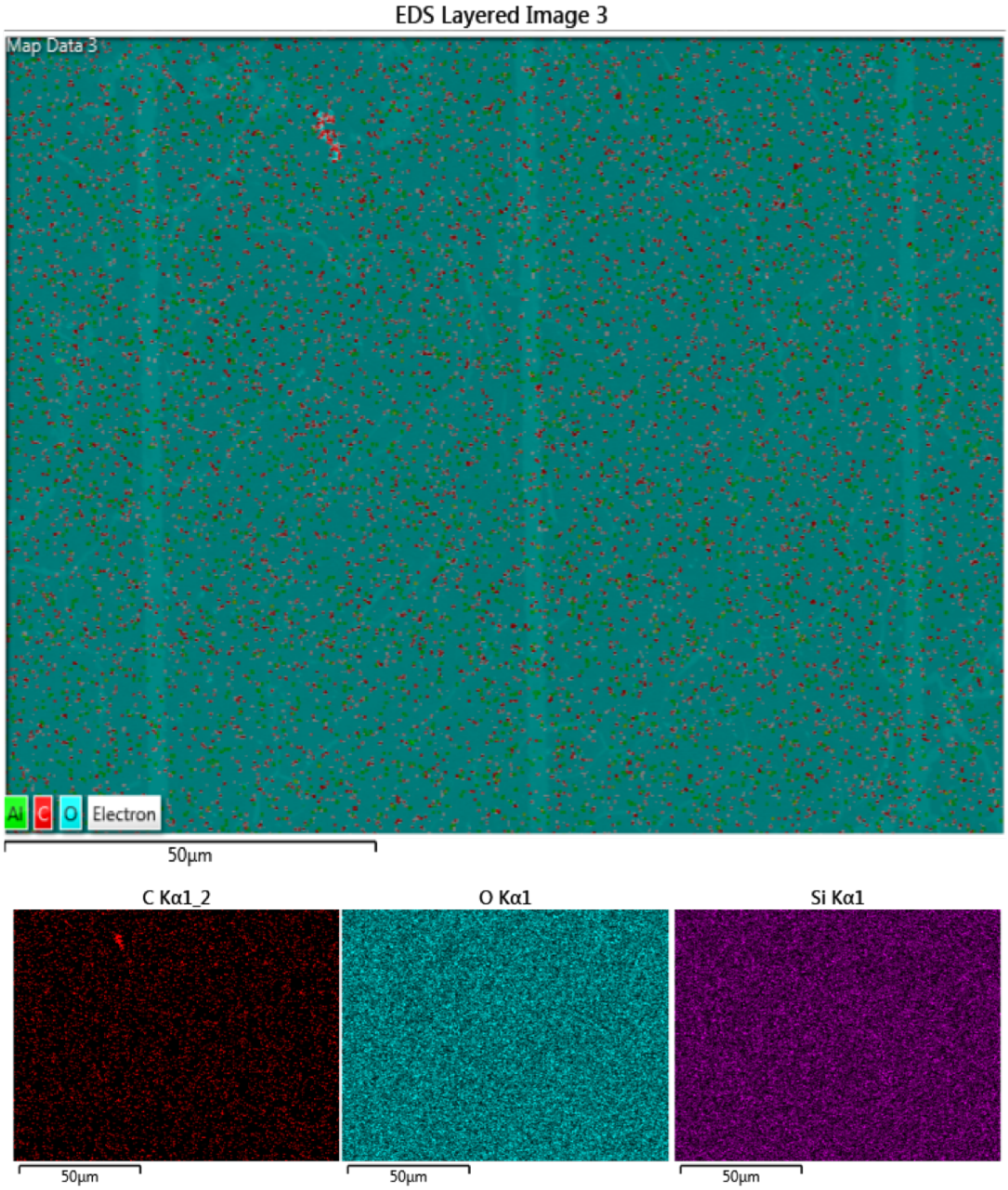

Fig 4. 30 EDS image of selectively removed region (0.71 J/cm^2). Red stands for C, blue stands for O, and pink stands for Si.

(b) EDS on the debris

Fig 4.16 (a) have shown some debris flakes on the sample. Whether the debris is from graphene or the ablated SiO_2 is still unexplored. It is necessary to analyse the chemical bonds by EDS. Fig 4.31 and Fig 4.32 demonstrated the debris measurement under over ablated line (56.19 J/cm^2) and selectively removed line (0.71 J/cm^2) respectively. In Fig 4.31, the spectrum 2 measured the debris on the edge while spectrum 3 measured the surface of graphene in the non-ablated region.

Comparing these two spectrums, both of them have significant signals of Si and O element. As the sample applied in this research is monolayer graphene, the C element signal appeared not that strong. Since the SiO_2 is ablated in the kerf (Fig4.29), through the element measurement, the debris around the ablated line is likely to be SiO_2 flakes.

In the low fluence ablation (0.71 J/cm^2), the debris at the edge was measured in spectrum 5 Fig 4.32. Compare with the surface of graphene in the non-ablated region (spectrum 6 in Fig 4.32), the debris has a similar signal intensity of Si, O elements, and other impurities. In the ablated region (spectrum 4), other impurity elements (Ca, Fe, Cu) disappeared, giving a clear Si, O, C element signal. Not surprisingly, the Si signal appeared stronger in the ablated area (spectrum 4 in Fig 4.32) compared with spectrum 5 &6, because the graphene was removed in the ablated region and the SiO_2 was still examined in the kerf (Fig 4.30).

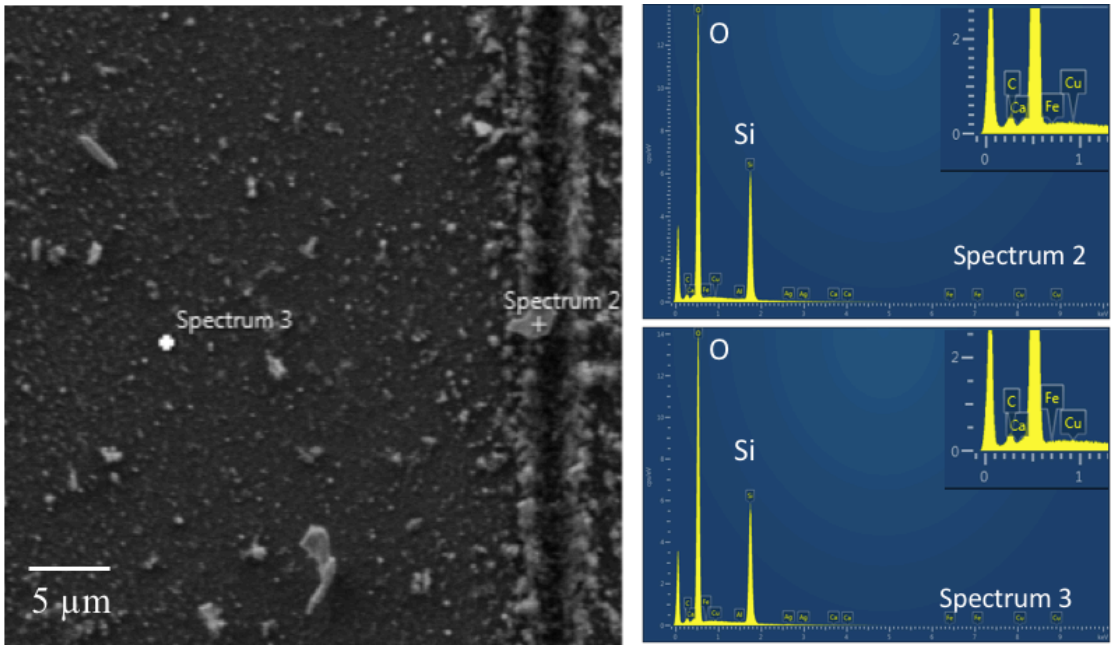

Fig 4. 31 EDS image of the debris after laser ablation with the fluence of 56.19 J/cm^2. The element C signal is zoomed in, as shown in the top right at Spectrum 2&3. Spectrum 2 measured the debris at the edge of ablation line, while spectrum 3 measure the graphene surface.

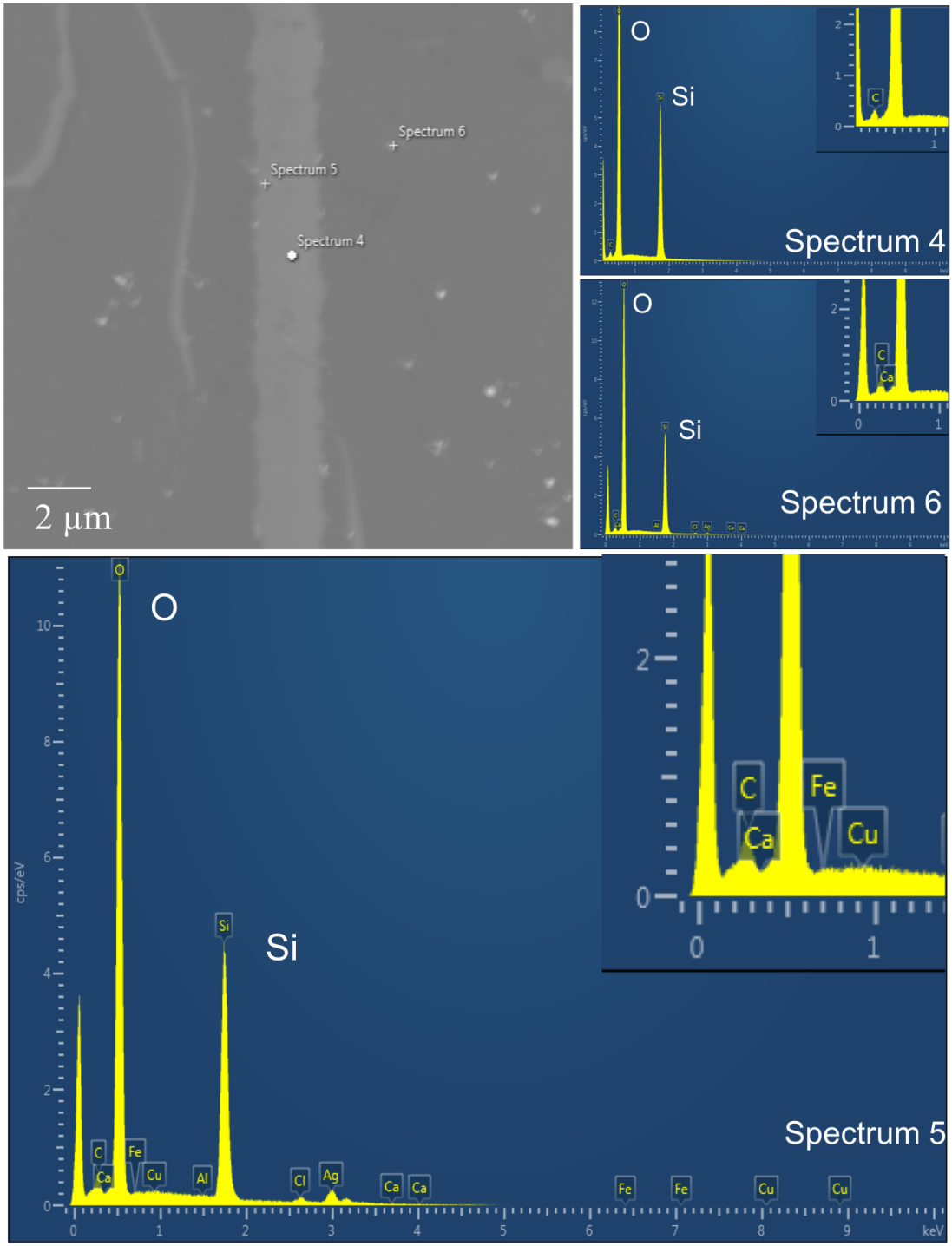

Fig 4. 32 EDS image of the debris after laser ablation with the fluence of 0.71 J/cm^2. The element C signal is zoomed in, as shown in the top right at Spectrum 4,5,6. Spectrum 4 measures the ablated region. Spectrum 5 measures the debris at the edge of the ablation line. Spectrum 6 measures the surface of graphene in the non-ablated region.

4.5 Potential applications

In [195], remarks have been made that graphene devices that can be developed from graphene deposited on a SiO_2/Si substrate, and femtosecond laser is an important way to realise the micro-scale production. For a broader application in the femtosecond laser ablation on monolayer graphene deposited on SiO_2/Si substrate, a distinction in expectations should be made among different types of devices. For instance, graphene sensors, which ascribe to the absorption and desorption in graphene, can consider if it is possible for a single gas module to be detected. Other silicon-based graphene devices, such as transistor[196], photodetector [197], [198], biosensor [77], and solar cell [199], [200], MEMS/ NEMS (micro-and nano-electromechanical system) [201], could be possibly achieved with the femtosecond laser in a similar way. For graphene FETS, regarding the challenging question on the zero bandgaps, this could be achieved with nanoribbon, since the edge quality analysed in this thesis has shown some potential in fabricating the graphene nanoribbons application. For example, with a square shape laser pulse to reduce the energy imbalanced, accompanied with the nanometre variations at the edge, and the precision of the machining stage, the clean ablation of graphene deposited on SiO_2/Si substrate has a great opportunity in graphene FETs.

4.6 Summary

This chapter explored the possibility of lithography-free patterning of graphene by using femtosecond laser; a 280 fs fiber laser has been evaluated for patterning of monolayer graphene on a SiO_2/Si substrate. The results have demonstrated that the femtosecond laser is a useful technique for direct laser profiling of single-layer graphene on the SiO_2/Si substrate. The conclusive remarks of the cutting process and evaluation methods are listed as below.

1. Among the selected pulse energies of the cutting process, the optimum channel was produced with a speed of 1.81 J/cm^2 (pulse number ~13.8). The width was measured to be 3.24 μm under SEM.
2. The area process of graphene has been achieved. The Raman analysis demonstrated the rest of graphene is remain undamaged after the removal.
3. An abaltion threshold that is lower than the values reported in the extant literature of ablation threshold was achieved. The incubation effect caused by the accummulation of multiple laser pulsese could use as one of the explanantion for the lower ablation threshold.
4. The lower ablation thresholds of graphene on SiO_2/ Si enables a complete removal of graphene. The AFM results indicate that selective removal of graphene was obtained and caused negligible substrate damage. These benefit from the lower ablation threshold of graphene relative to both

SiO_2 and Si.

5. The observed swelling effect could be attributed to the interaction of the laser and Si substrate. The high absorption of the substrate has caused Gaussian shaped swelling effects.
6. The observation on the graphene edge has confirmed the limited influence of the femtosecond laser ablation. The Raman spectroscopy has found increased D peak in the proximity of the machined channel. The AFM measurement of Kelvin probe force microscopy on potential energy has proved that the D peak in the cutting edge was attributed to graphene edges, rather than oxidation as a result of laser processing. The D peak shown at the edge is because the edge breaks the translation symmetry of graphene.

To conclude, this chapter has proved the possibility of femtosecond lasers to process graphene patterns. The one region time costs 4 hrs. If the substrates are plastic, this process can be used as roll-to-roll for scalable industrial parameters of manufacturing. It only needs to choose suitable parameter settings for industrial applications.

Chapter 5 Femtosecond laser-induced defects in graphene

5.1 Introduction

This chapter answers the third research question and explores femtosecond laser interaction with graphene under the ablation threshold to induce defects. Previous research has demonstrated that defects can be induced by α beam irradiation [202], and electron-beam irradiation [203]. Induced defects in graphene can deliver changes to the properties of graphene, such as creating a bandgap by using chemical treatments such as fluorinated graphene [204]. Moreover, defects can allow the dopant control of graphene (either n-type or p-type) [205], [206]. The main objective of this chapter is to test following hypotheses:

1. A femtosecond laser can induce defects in graphene,

2. The defect on graphene can be tuned by changing the intensity of the femtosecond laser.

Area processing is discussed in this chapter with various pulse energies, as shown in Fig 5.1. The hypotheses were tested and examined by Raman spectroscopy and the resulting defects are analysed.

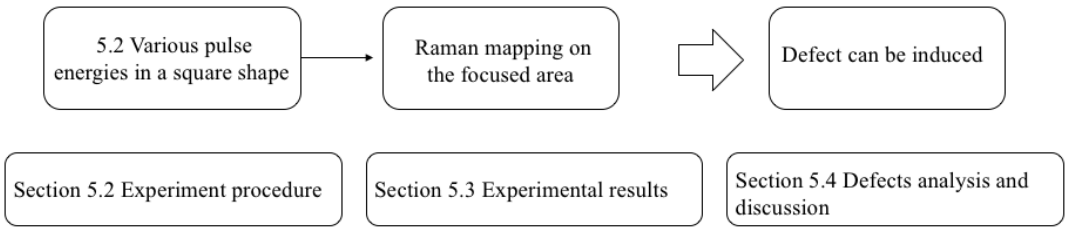

Fig 5. 1 Schematic diagram of chapter 5.

5.2 Experiment procedure

Monolayer graphene was grown at the Cambridge Graphene Centre on 25 μm copper foil by chemical vapour deposition methods and then transferred onto a 300 nm SiO_2/Si substrate with an area of 4 cm^2. The care was taken so that the impurity of the monolayer graphene is transferred onto the substrate is minimised. Laser processing was undertaken, see Fig 5.2, using an Amplitude

Systèmes Satsuma, 280 fs, 1030 nm (verified using APE PulseCheck USB) at room temperature at ambient condition.

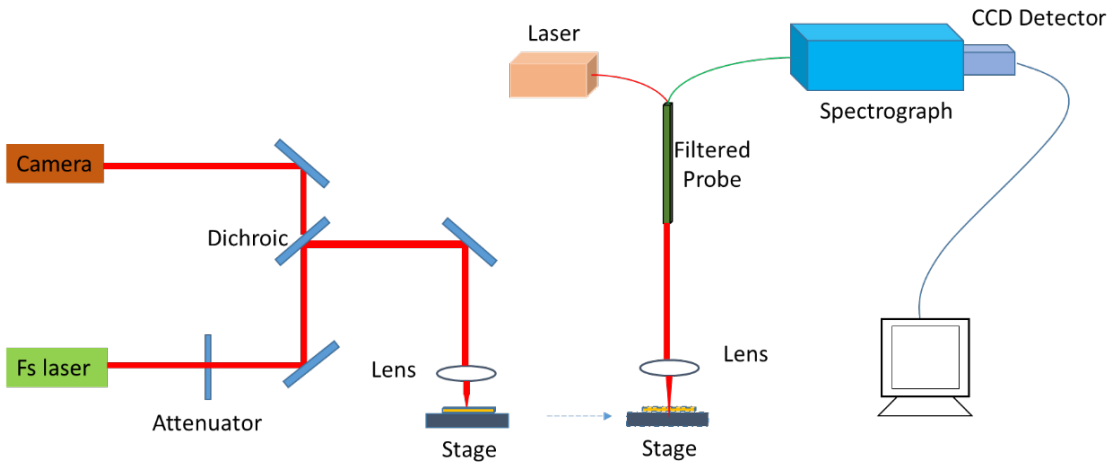

Fig 5. 2 Experimental setup of fs laser inducing defects on graphene. Left: processing set up. Right: Raman measurement set up.

The laser was circularly polarised and focused by a NA=0.35 objective lens (Comar Optics, 12 OI 09) with a focal length of 12.7 mm. The spot diameter is 4.16 μm. This is calculated by $r = \frac{M^2 \lambda f}{\pi w}$, where M^2 factor represents the beam quality, f stands for the focal length of the lens, w is the incident beam radius. The processed area was controlled by the motion of a high-precision translation stage (±100 nm). Graphene was processed by exposure under a range of pulse energies, and the power was fine-tuned with a diffractive attenuator (Del Mar DVA-800). The Aerotech A3200 software not only controls the stage of finding the focus but also guides the laser process path. The programming automatically accompanies the platform.

To study the detail of defects generation with the pulse energy, the energy was selected as 2 nJ, 1 nJ, 0.4 nJ, 0.2 nJ and 0.1 nJ, with a process speed fixed at 0.1mm/s. The laser peak fluence for a Gaussian beam can be calculated as $F_{peak} = \frac{E_p}{\frac{\pi w^2}{2}}$, where E_p is the pulse energy, w is the focus radius. Thus, these sets of pulse energies were calculated with the peak fluence of 31.75 mJ/cm^2, 14.7 mJ/cm^2 , 5.8 mJ/cm^2 , 2.9 mJ/cm^2, and 1.4 mJ/cm^2 (as tabulated in Table 5.1 and Table 5.2).

Table 5. 1 Measurement power and calculated pulse energy.

Measured Power (500 kHz, mW)	**1.2**	**0.55**	**0.22**	**0.11**	**0.055**
Pulse energy (nJ)	2.16	0.99	0.396	0.198	0.099

Table 5. 2 Calculated processing fluence with the pulse energy.

Pulse energy (nJ)	**≈2**	**≈1**	**≈0.4**	**≈0.2**	**≈0.1**
Peak fluence (mJ/cm^2)	31.75	14.5	5.8	2.9	1.4

Fig 5.3 demonstrates the laser scanning path to form a 5 µm ×6 µm processed rectangular. The laser pulse scanning at a fixed speed, moving to +x for 1 µm, together with the beam diameter of around 4 µm. In total +x direction is 5 µm. Then, then moved 2 µm towards –y direction, and scanning back with the same speed. The reason for 2 µm pulse overlap is to ensure the area is evenly deposited, as demonstrated in Fig 5.4. Marks are made with higher exposure to assist the sample finding under Raman measurement.

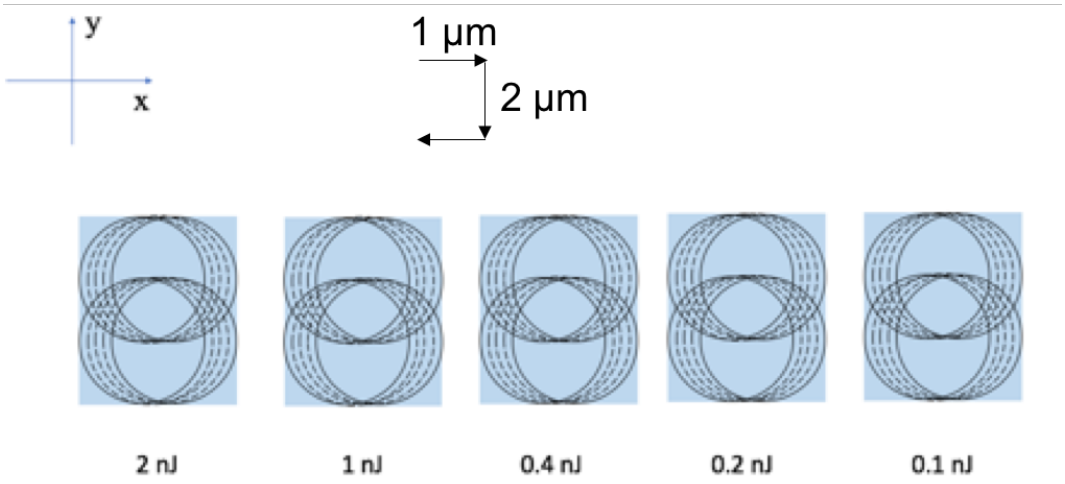

Fig 5. 3 Scanning patterns for sub-threshold laser irritation of graphene.

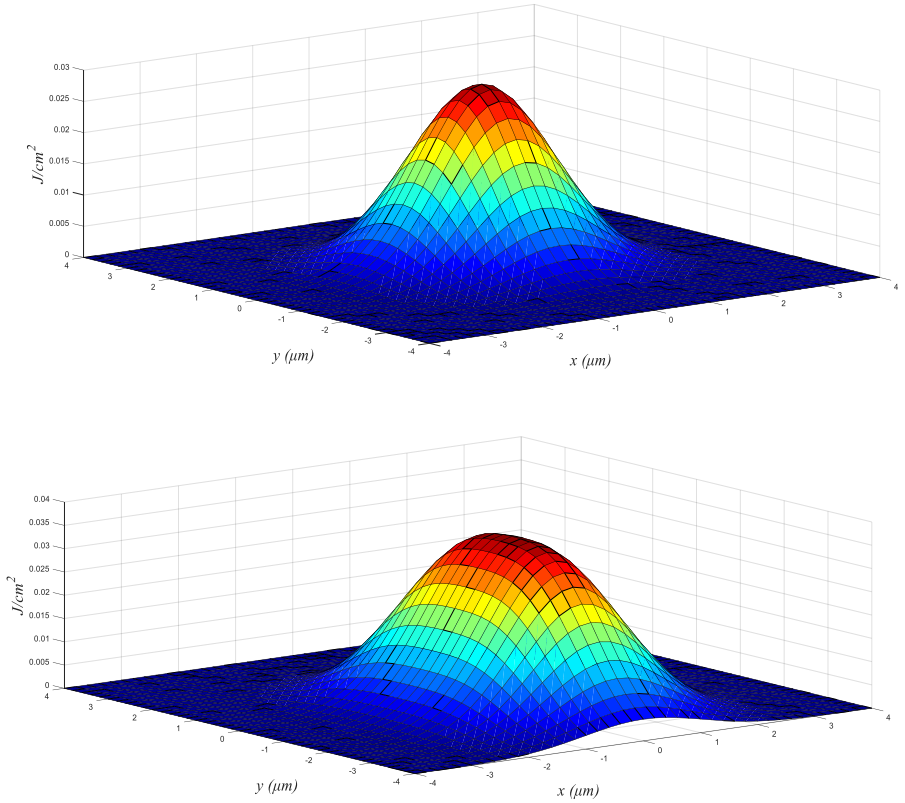

Fig 5. 4 Schematic diagram of a single Gaussian shape beam with pulse energy of 2 nJ and two Gaussian beams with 2 µm overlap.

For the Raman measurement, a 514 nm laser excitation with a 100x objective was used to analyse the exposed area. With the same settings of scanning speed and the pulsed overlap, the pulse energy is the only variable to affect the defect generation process on the surface of graphene.

5.3 Experimental results

5.3.1 Raman spectra-focused area

Fig.5.5 shows the results of Raman Spectroscopy on the irradiation area on the graphene, as illustrated in section 5.2. We are interested in creating defects on graphene, thus only D and G peaks were measured. Intense D and D' peaks are shown on the irradiated surface, which demonstrates that a femtosecond laser could induce a defect on the surface of the monolayer graphene sample.

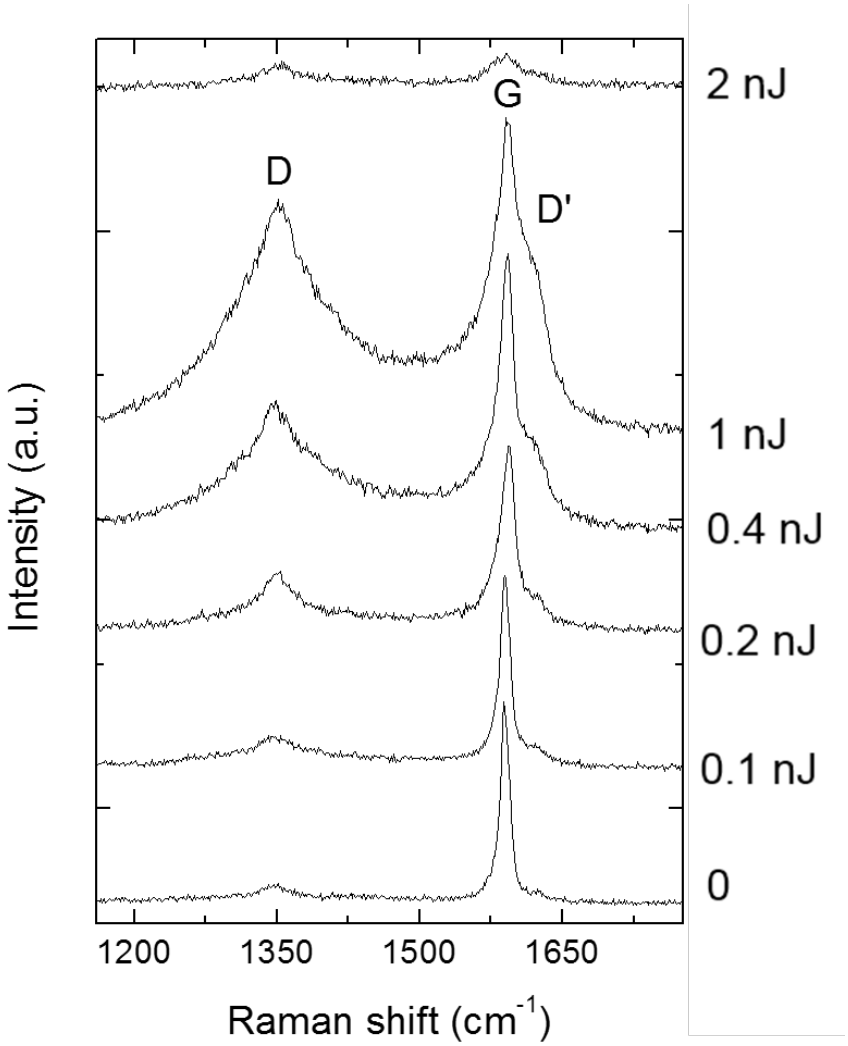

Fig 5. 5 Experimental Raman data of irradiated area by a femtosecond laser with different pulse energies at the same scanning speed of 0.1 mm/s.

The graphene on the substrate has been ablated with a pulse energy of 2 nJ, which is confirmed by the absence of a G peak. This result agrees well with the ablation threshold when removing graphene from the substrate as discussed in Chapter 4. When we compared the intensity of the D peaks with different laser energies, the growth trend on the D and D' has peaked with increased pulse energies. The shifting of the D peaks towards lower numbers was also observed in the Raman spectra. The Raman signal intensity is given by equation 5.2 [207],

$$I = CNI_0\sigma\Omega\ell F(T) \qquad 5.2$$

where I is the Raman signal intensity, C is a constant, N is the number density, I_0 is the laser intensity, σ is the Raman cross-section, Ω is the scattering solid angle, and l is the length of the observed segment of the laser beam; F(T) stands for a temperature dependent factor determined by

the spectral width and the resolution of the detection system and the investigated molecule. An increasing D peak indicated a larger scattering solid angle.

In Raman spectroscopy, the shifting of peaks towards a lower or higher wavenumber is related to the bond length of molecules. The longer bond length causes it to shift to a lower wavenumber and vice versa. Thus, the shift in the D peaks, with the irradiated energy suggests that the bond length in graphene becomes longer after the irradiation. With the detailed examination of the Raman spectra illustrated in Fig 5.9, an increase in the D' trend can be clearly observed from the mapping. The D' peak has not been as extensively studied as the G peak or D peak, this is for two reasons. First, the D' peak has relatively little intensity compared to the D peak. Secondly, the D' peak appears as a small peak on the tail of G peak. In experiments, for average defect concentration, the D' peak can be clearly distinguished from the G peak, with a relatively large intensity that is up to 1/3 of the intensity of the G peak [113].

To explore the femtosecond laser effects of the graphene surface on top of the SiO_2/Si substrate, further analysis of these Raman maps was investigated. These investigations were delivered in four parts: I(D)/I(G) ratio, A(D)/A(G) ratio, I(D')/I(D) ratio, FWHM (G) and FWHM (D). The parameters of the D peaks and the G peaks (intensity ratio of the area, and width) are typically used to characterise the material. The I(D)/I(G) ratio (peak height) is ascribed to the increase in the number and the size of sp^2 clusters.

In the exposed area of graphene samples, the pulsed laser defect is induced in a stochastic manner. The proof can be seen from the previous experiment, as there is no clear separation between the defect area and non-defect area. The intensity of the defect is gradually increased with the pulse energies, instead of having a defect threshold. This indicates the defect, induced by a femtosecond laser, is non-deterministic. However, the probability of the defect is related to the laser pulse energy.

In principle, the carbon atomic vibration originating from photon excitation can be represented by a harmonic oscillator with a specific oscillation frequency (ω_q), which is similar to a mass-spring oscillation process. Consequently, the Raman peak is the response of the system that resonates ω_q with a damped energy $\Gamma_q/2$ excited by an external force of frequency ω. Therefore, the intensity of the Raman peaks can be expressed as equation 5.3 [191]:

$$I(\omega) = \frac{2I_0}{\pi\Gamma_q}\frac{1}{\left(\omega-\omega_q\right)^2+\Gamma_q^2/4} \qquad 5.3$$

In Raman, the resonation frequency is usually much larger than the damped energy ($\omega_q \gg \Gamma_q$), thus, equation 5.3 can be simplified as a Lorentzian peak with FWHM=Γ_q. Usually, the spectra data was fitted with a Lorenz peak function. An example of software fitting is given by the data collected for the irradiation area with a laser pulse energy of 1 nJ as shown in Fig 5.6.

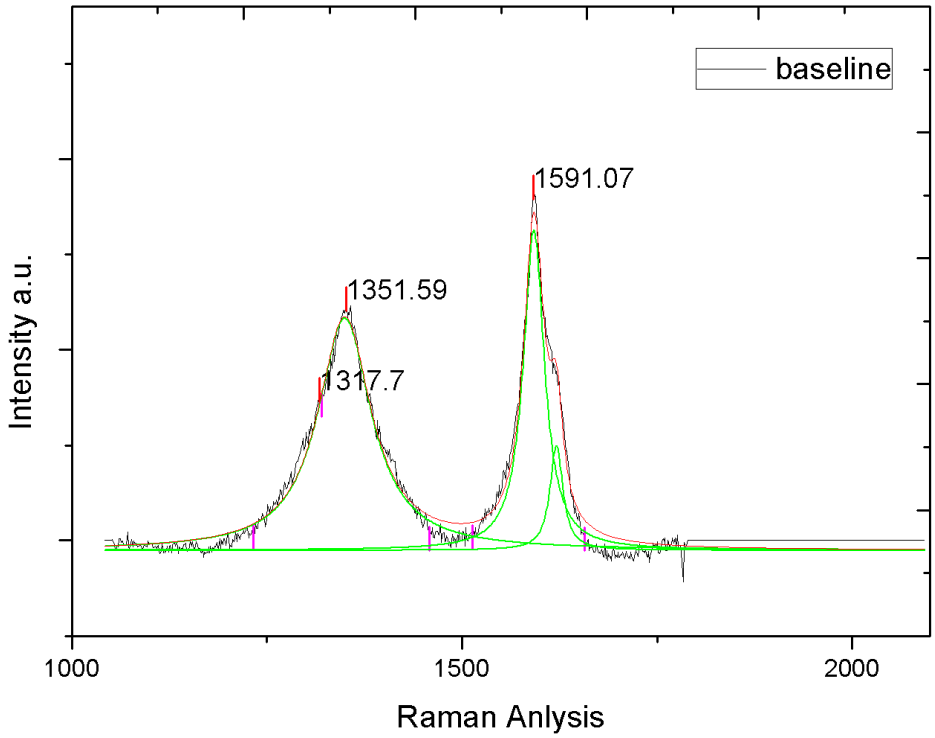

Fig 5. 6 An example of Lorenz fit function of a Raman spectrum with the pulse energy of 1 nJ.

5.4 Defects analysis and discussion

5.4.1 Intensity ratio of D peak and G peak

As described previously in section 5.3, the intensity ratios of the D and G peaks (peak height) were plotted as the function of laser fluence. Here, the defects are defined as a laser-induced defect, compared with the reference measurement on the Raman spectra of the graphene area without femtosecond laser irradiation.

Before laser ablation, the I (D)/I(G) ratio has shown a linear growth in relation to laser energy when the pulse energy is smaller than 1 nJ, as shown in Fig 5.7.

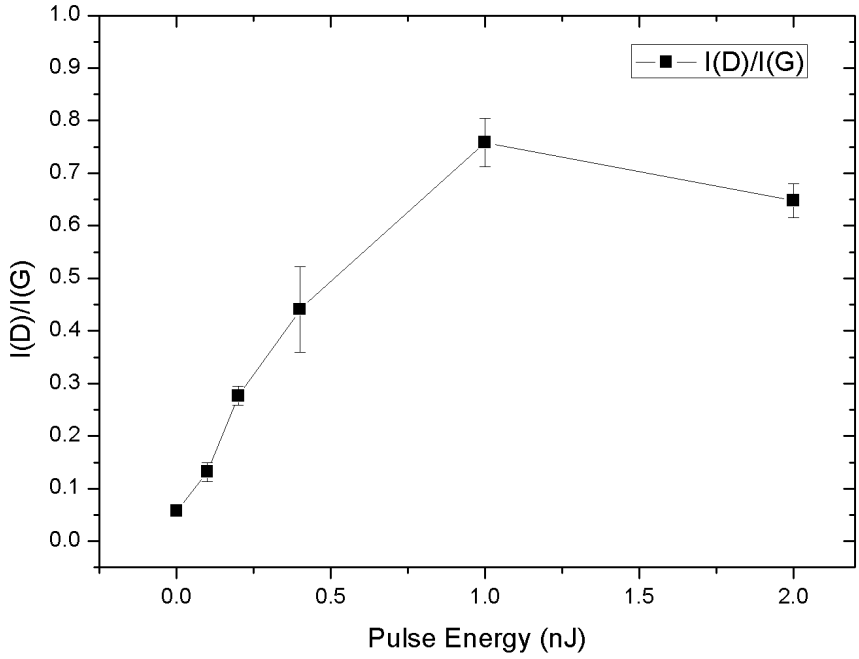

Fig 5. 7 Variation of I(D)/I(G) with different pulse energies at fixed processing speed 0.1mm/s.

The crystal grain size and the amount of disorder were estimated based on the D band intensity. This theory was developed by Cancado et al [192]. They refined the model by analysing the dependence of L_D (the average distance between point defects) with the laser energy (E_L^4):

$$\frac{I_D}{I_G} \approx \frac{4.3 \times 10^3}{E_L^4 L_D^2} \qquad 5.4$$

The average distance between the point defects can be plotted as shown in Fig 5.8.

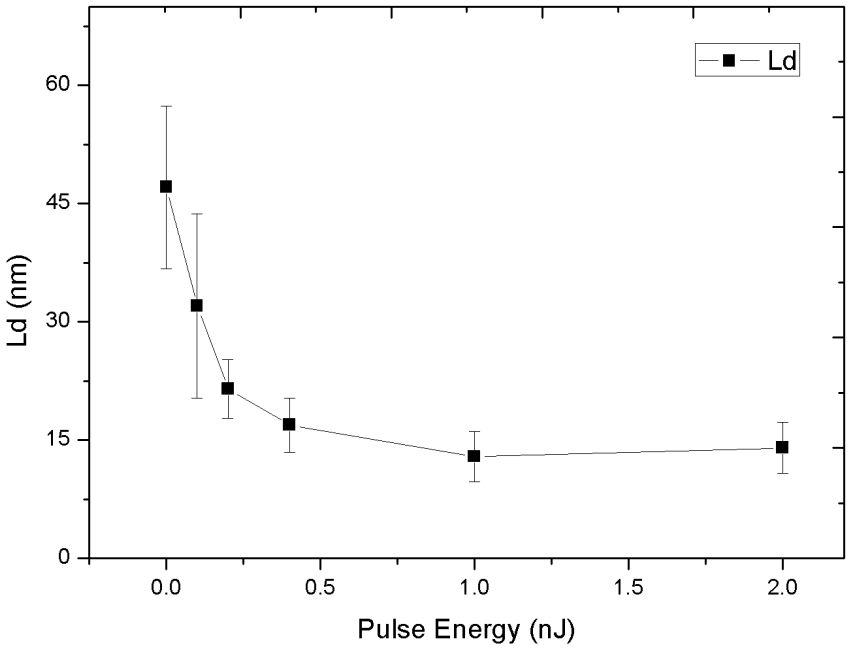

Fig 5. 8 Variation of inter-defect distance with pulse energies.

5.4.2 Area ratio of D peak and G peak

In this section, the area ratio of D peak and G peak are explored as a function of the pulse energies deposited on the graphene sample. Before further discussion, it is important to note A(G) is defined as the area of the G peak, with a similar notation of A(D) for the D peak area. Studying the A(D) and A(G) ratio with Raman spectroscopy has proven to be a versatile tool when studying the property of graphene [114]. As for the study of the I(D)/I(G) ratio, it is efficient and accurate for determining the quality of graphene. When researchers realised the benefits of the defects in graphene, scientists have started to explore the Raman spectroscopy's unique application in the study of disorder graphene.

Fig 5.9 has shown the variation of the A(D)/A(G) with the pulse energy deposited on the graphene. The A (D)/A (G) curve shows a different trend compared with I(D)/I(G) ratio. The area ratio of D peak over G peak shows a steep to 0.4 nJ. After that, the rate of increase slows down until it reaches the maximum at 1 nJ and then fall off. Typically, groups refer I(D)/I(G) as the ratio of the peak heights, because the difference between the height ratio and area ratio is not so crucial for their similar peak width in disordered graphite. However, in this study on the femtosecond laser-induced

disordered monolayer graphene, the D peak area was broadened, making they have a different increasing rate.

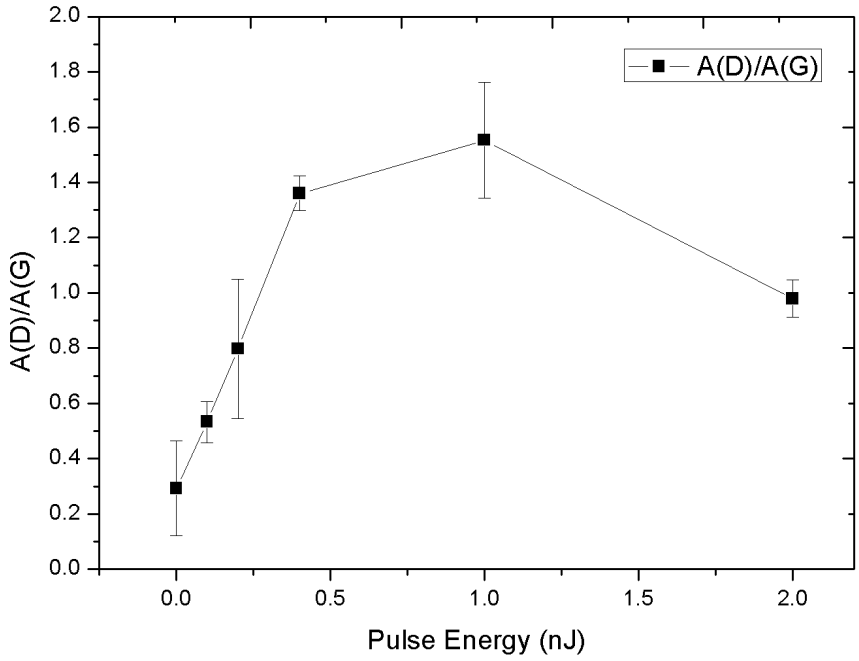

Fig 5. 9 The ratio of A (D)/A (G) as a function of laser pulse energy under the ablation threshold.

In the peak area ratio of A (D)/A (G), the Raman spectra can be interpreted in three phases, that depends on graphene disorder and graphene existence. The first phase relates to a pulse energy smaller than 0.4 nJ. In this phase, the pulse energy is the factor that increases the defects. The second stage occurs between a pulse energy of 0.4 nJ and 1 nJ. In the second phase, the pulse energy has increased the defect slowly for the region caused by the intense energy, which is shown in the height of the D peak. As for the third stage, this is where the graphene has gradually disappeared and is removed from the substrate, appearing as a gradual decrease in both height and area.

5.4.3 Type of defects

(a) Vacancy, sp^3 and boundary-like defects

For the femtosecond laser-induced defect on the surface of graphene, it can be classified as the vacancy-like defect, sp^3 defect and boundary-like defects (Fig 5.10). In vacancy defects, one or more carbon atoms are removed from the original hexagonal lattice. In sp^3 defects, referred to as a topological defect in [208], atoms are not removed but there is a rotation of the bonding angles

between the carbon atoms. In boundaries like defects, a few atoms are removed to generate a boundary in the graphene. Besides these types of defects, there are also impurity defects where the carbon atom is swapped for another atom. This form of defect is not the primary focus of study in this research.

In our case, a relatively large defect is made in the graphene sample that is generated from a femtosecond laser. The intensity of the D' peak is relatively large. It is now meaningful to compare the results of this study with those given in the literature.

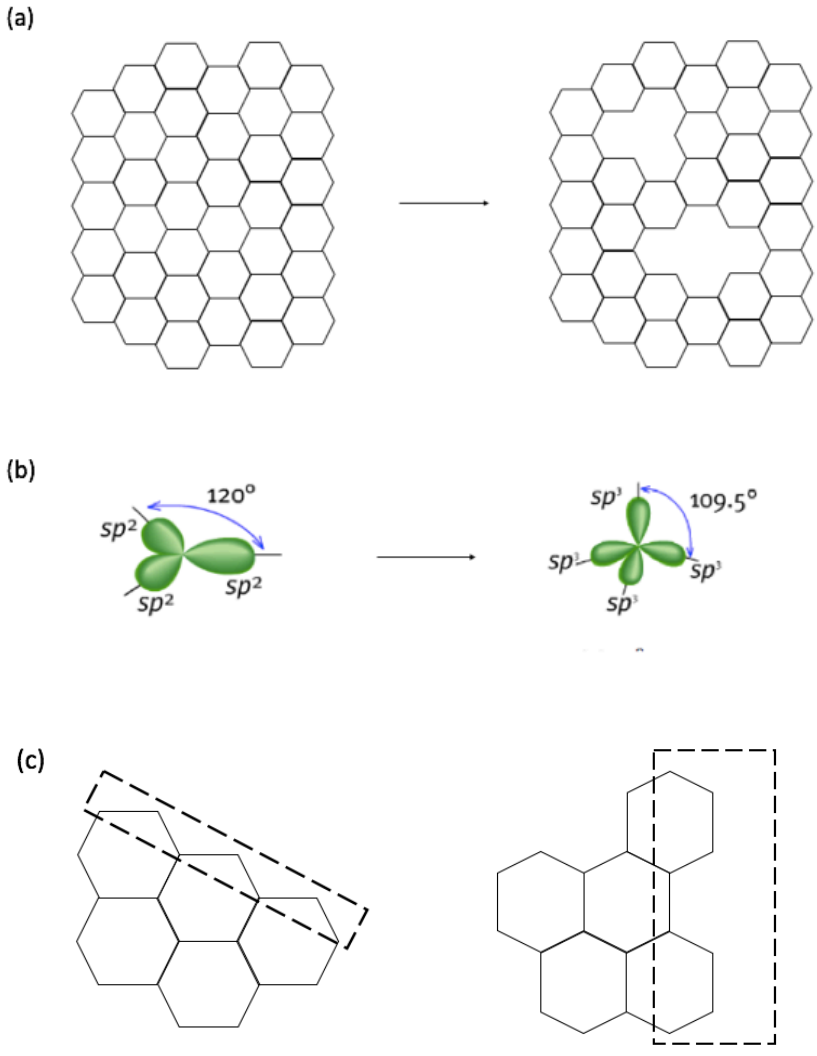

Fig 5. 10 Types of defects caused by ionisation (a) Vacancy-like defect;(b) sp^3defect; (c) boundary-like defect.

(b) I(D)/I(D') ratio

The D and D' intensities are directly proportional to the defect concentration, which gives rise to the different behaviours of the Raman peak intensities. The plotted I(D)/I(D') is given in Fig. 5.11. The calculation is the same as the I(D)/I(G), considering the peak heights by the Lorenz fit. In the graph, a clear increasing trend was also observed in I (D)/I (D') as a function of femtosecond laser pulse energies under the ablation threshold.

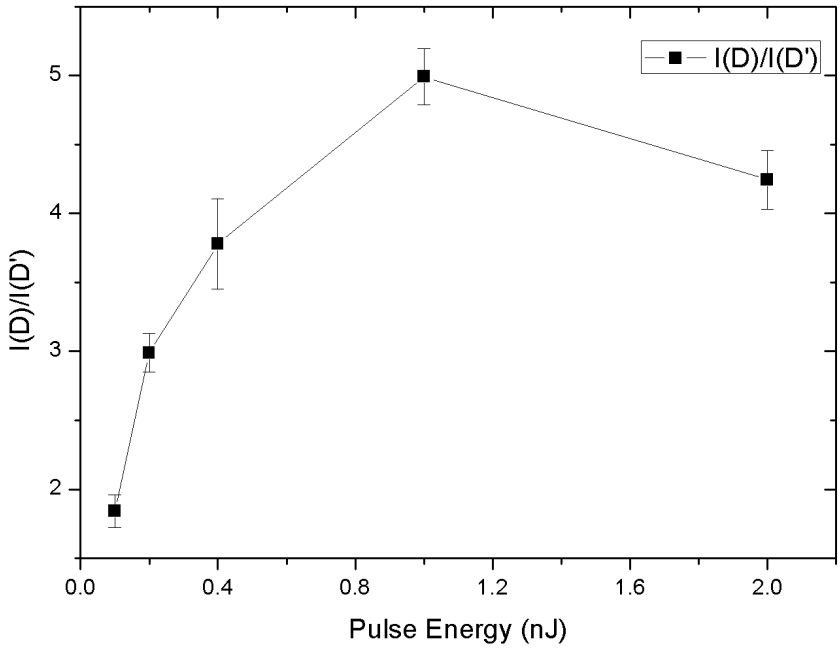

Fig 5. 11 Variation of I(D)/I(D') with different pulse energies at fixed processing speed 0.1mm/s.

Defects have been studied by previous workers under the intensity ratio between the D and D' peaks. A.Eckmann et al. have defined the vacancy-like (hopping) defect having a ratio of ~ 7 and boundary-like defect 3.5 [113]. In these results, the defects created with the pulse energy of 0.4 nJ and 2 nJ and 1 nJ had ratios of 3.68, 3..56 and 4.99 respectively. For pulse energy of 0.4 nJ and 2 nJ is more likely to be boundary-like. The ratio pulse energy of 1 nJ tends to be related to a combination of boundary-like defects and vacancy-like defects. The defects created with a pulse energy of 0.1 nJ and 0.2 nJ, I(D)/I(D') ratio was 1.84 and 2.98, these ratios more close to boundary-like defect than the vacancy-like defect.

5.4.4 FWHM (G) and FWHM (D)

(a) FWHM of G peak

The full width at half maximum height (FWHM) is an important parameter to characterize the Gaussian distribution. In the specific case of the G path, the damping energy FWHM (G) that gives origin to the G band depends on the strength of the electron-phonon coupling (EPC) at the Γ point (the first Brillouin zone in graphene). The EPC is the result of the degeneracy of the phonon dispersion at the Γ point [209], [210]. In Fig 5.12, FWHM of G lines increased gradually with the increase of pulse energy under the ablation threshold.

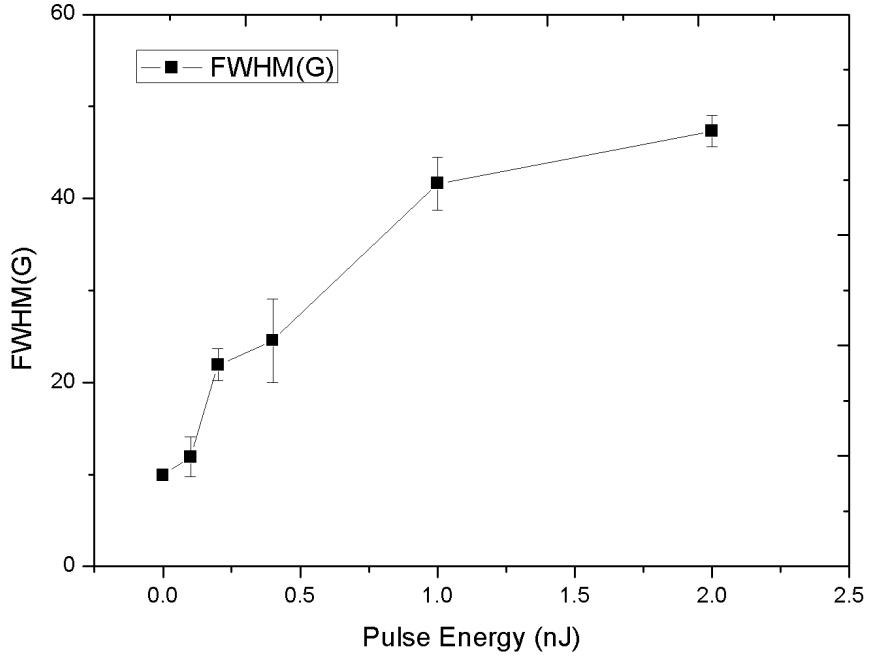

Fig 5. 12 FWHM (G) varies with the pulse energies.

As the FWHM is always increased with temperature, and if the increased pulse energy generates more heat, then it is expected to observe an increase in the FWHM of G peak and D peak. The increased trend of the FWHM graph of G peaks not only indicated that the temperature rose with the pulse energy, but also indicates the increased electron-phonon coupling in graphene. The FWHM (G) has contributed from two components: one due to the EPC (Γ_{EPC}) and another due to the interaction with other phonons. However, the major factor is expected to be due to the EPC, since the interaction with other phonons is weak compared with the electron-phonon coupling. For that

reason and for theoretical analysis, it is easier to assume that FWHM (G) $\approx \Gamma_{EPC}$ for mathematical convenience. Hence, FWHM(G) is can be calculated as shown in equation 5.5 [211]:

$$FWHM(G) = \frac{2\,Slope^{LO}(\Gamma)\omega_{\Gamma}}{v_F} \qquad 5.5$$

where $Slope^{LO}(\Gamma)\omega_{\Gamma}$ stands for the LO phonon at the Γ point.

(b) FWHM of D band

Having found the FWHM of the G band, it is necessary to analyse the FWHM of D band, as the width of D band contains the information of the expanded D band.

The growth of the FWHM of D-line and G-line with an increase of the pulse energy was observed, as well as the area ratio of D and G peaks. However, unlike a clear upwards trend as seen in FWHM (G), the FWHM (D) has experienced a dramatic jump from the 0.2 nJ and 0.4nJ and another jump from 0 nJ to 0.1nJ, as shown in Fig.5.13. After a pulse energy of 0.4 nJ, the FWHM (D) remained stable and dropped down a little after the ablation point. FWHM (D) increases much more than FWHM (G) for decreasing L_D (the average distance between point defects). The results of the FWHM (D) show no clear dependence of the pulse energy. Also, unlike the clear increase in the trend of the FWHM (G) with the defects in the graphene, the FWHM (D) does respond to the same trend. It does not expend its width.

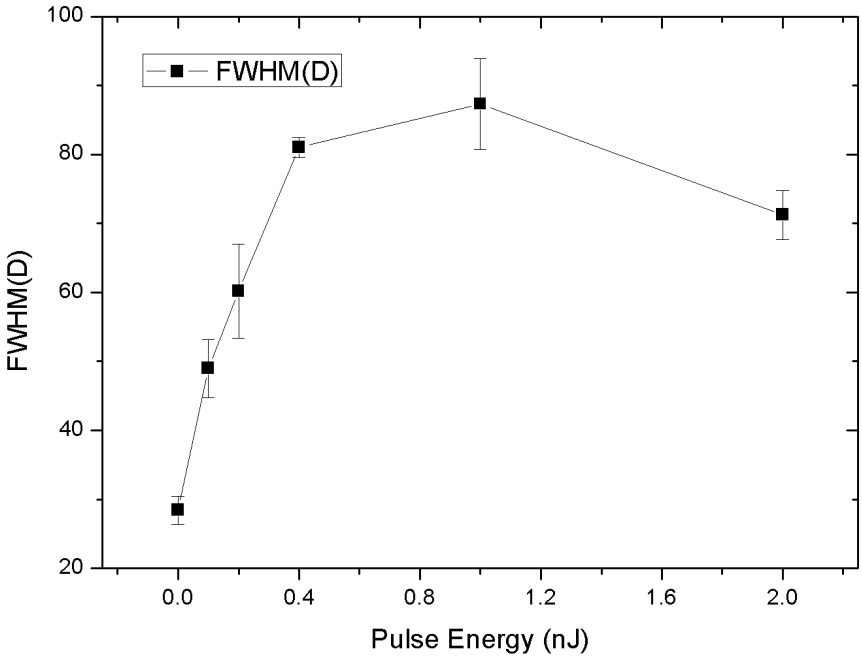

Fig 5. 13 FWHM (D) varies with the pulse energies.

5.4.5 Intensity ratio of G peak and 2D peak

The intensity ratio of G peak and 2D peak at the laser irradiation area is plotted in Fig 5.14. The I(G)/I(2D) ratio increased gradually from non-irradiation area to 0.4 nJ and then jumped up to 1.81 with the pulse energy of 1 nJ. At 2 nJ the graphene is ablated, with a low ratio of G and 2D peak. This supportive information again confirmed the defection generation by a femtosecond laser is pulse energy depended. When the energy closes to the ablation threshold, the D peak increases and the 2D peak experience a drop. Together, this contributes to the increase in the I(G)/I(2D) ratio.

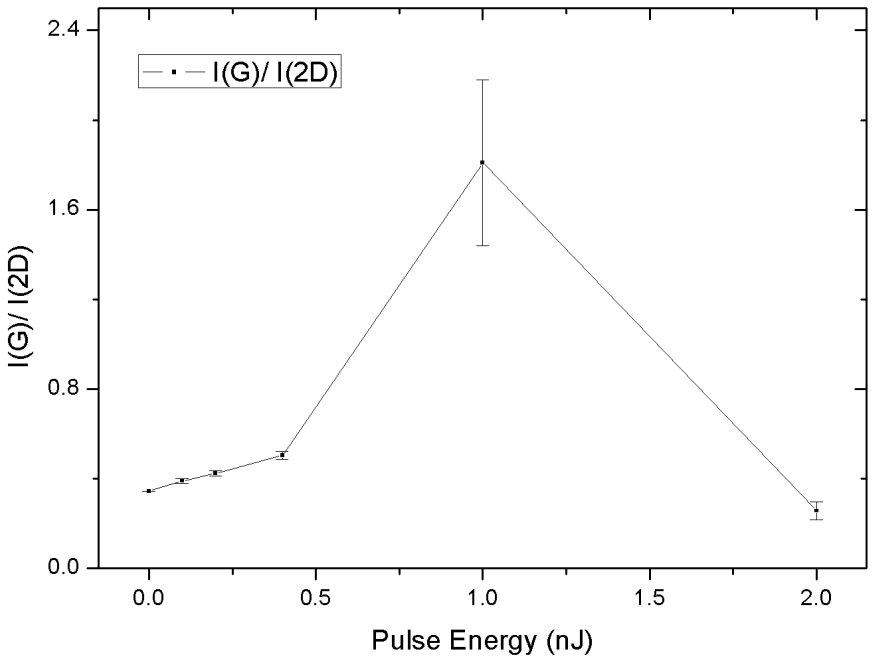

Fig 5. 14 Variation of I(G)/I(2D) with different pulse energies at fixed processing speed 0.1mm/s.

5.4.6 Shape of the defect

From above discussion, at a pulse energy of 1 nJ, peak fluence of 14.5 mJ/cm^2, the graphene is defective. As the I(D)/I(D') ratio at 1nJ indicates there is a combination of vacancy defect and boundary-like defect. Considering the Gaussian distribution of laser beam, the centre of the beam has the largest energy. In such case, femtosecond laser might remove several atoms in the centre region of the laser beam. In this section, the properties of graphene in different vacancy shapes are calculated through Density Function Theory. The electron band structure on the shapes of vacancy defect with a regular ring shape and irregular shape is plotted as shown in Fig 5.15. The irregular shape of vacancy has a less stable system compared to the regular one. The bandgap is opened in the irregular shape vacancy defect as shown in Fig 5.15.

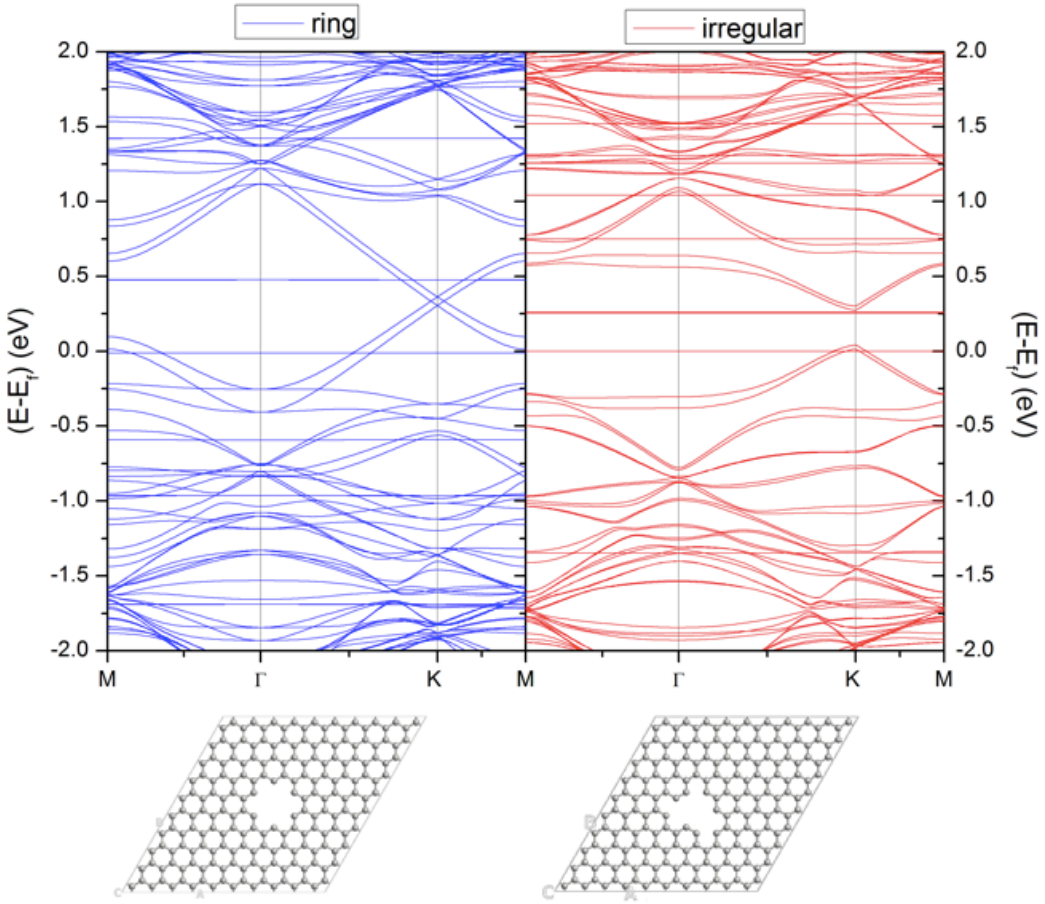

Fig 5. 15 Electron band structure of graphene with regular ring vacancy (left) and irregular vacancy(right). Both ring vacancy and irregular vacancy removed 12 C atoms.

5.5 Potential industrial applications

Explicitly considering the effects of defects, both in their nature and the quality, can have a substantial impact on the chemical and physical properties of graphene [113], [192], [212]. Control of the location of defects by ultrafast lasers provides a new processing route for graphene-based materials with novel properties [113], [192]. For instance, the electrical conductivity of graphene can be influenced by defects in the scattering of electron waves. In addition, dopant atoms can change the local electronic structure or inject a charge into the electron systems of sp^2 bonded carbon materials. Around the defects, weaker bonds can affect the thermal conductivity of the material and reduce the mechanical strength [98].

Graphene can be treated as a zero-bandgap semiconductor. By shifting the Fermi level in graphene through an external electric field, the electrical transport characteristics of graphene can be tuned

between p-and n-type. Graphene-based p-n junctions have attracted strong interest [213], [214], [215].

5.6 Summary

In this chapter, a new area of femtosecond laser-induced defects on monolayer graphene, deposited on the SiO_2/Si substrate is studied. The hypothesis is that the femtosecond laser could induce controlled defects under sub-ablation threshold processing conditions. The Raman spectra of the irradiated area after femtosecond laser exposure gave much insight into the process. Here are the main findings in this chapter.

1. Defects can be created in both single point exposure and area processing by using a femtosecond laser, with a pulse energy in the range from 0.1n J to 2 nJ. For the irradiated area, intense D and D' peaks are present with a scanning speed of 0.1mm/s, demonstrating that the femtosecond laser can introduce defects on monolayer graphene. Defects increased gradually with the increase of laser pulse energy.
2. The peak intensity ratio of D peak and G peak shows an increased trend with a dramatically sharp increase up to a pulse energy of 1 nJ and then has steadily risen until the G peak disappears when the pulse energy is 2 nJ. The maximum concentration of defects was found to occur with 1 nJ pulse energy. The average distance between the point defect is calculated to be 12 nm to 46 nm depends on the pulse energies.
3. Along with the increase of D peak, a growth of D' peak at 1620 cm^{-1} appeared with the increase of pulse energy. The D and D' intensities are also directly proportional to the defects concentration. In this deposition range, as demonstrated, the ratio of I(D)/I(D') has not shown evidence of sp^3 defect generation. For pulse energy of 0.1, 0.2 and 0.4 nJ, the defect is more likely to be boundary-like defects. For pulse energy of 1 nJ, the ratio of I(D)/I(D') suggests a combination of vacancy-like defects and boundary-like defects.
4. The Full-width half maximum of G band and D band increased. The maximum of FWHM (G) is around 50 cm^{-1}, which is smaller than that of D band. This indicates the expansion of D band increases with the increase of pulse energy.
5. The analysis of the peak area of G band and D band ratio gives significant information on the Raman spectra analysis of the defective graphene. It suggests the growth of the defect is developed into two stages. One is increased linearly and dramatically with the pulse energy smaller than 0.4 nJ, and the next stage is a slow growth until the maximum.

To conclude, this chapter has demonstrated the possibility of applying femtosecond lasers to introduce defects into monolayer graphene in a controllable way. This approach holds promise to extend its material properties through selective doping and thereby increase the application potential of the material. Having investigated the experimental results on femtosecond laser ablation of graphene and generate of defects on graphene, the next chapter will focus on the absorption process during these process, aiming to provide a more fundamental insight on the femtosecond laser irradiation on graphene deposited on SiO_2/Si substrate.

Chapter 6 Absorption model study in graphene-SiO_2-Si system

6.1 Introduction

Absorption of light is a concept that is studied in many branches of science, including chemistry [216], [217], physics [218], [219], biology [220], [221], etc. In femtosecond laser interaction with materials, absorption of laser light is the process by which energy is transferred to the material. The input laser energy is transformed into thermal energy. The interactions between the laser and the material can lead to phase change and structured modification [222], [223], [224]. Chapter 4 has presented the phenomena of ablation of graphene and the swelling effect of the underlying SiO_2/Si substrate. This chapter will investigate the laser energy absorption of SiO_2/Si substrate in order to shed light on the swelling effect, in order to provide a better understanding of the laser processing of graphene/SiO_2/Si systems.

The main purpose of the chapter aims to understand the energy absorbed by the silicon dioxide and silicon substrate during a femtosecond Gaussian shape laser processing of graphene and in turn provide a rationale for swelling phenomena as shown in Fig 6.1.

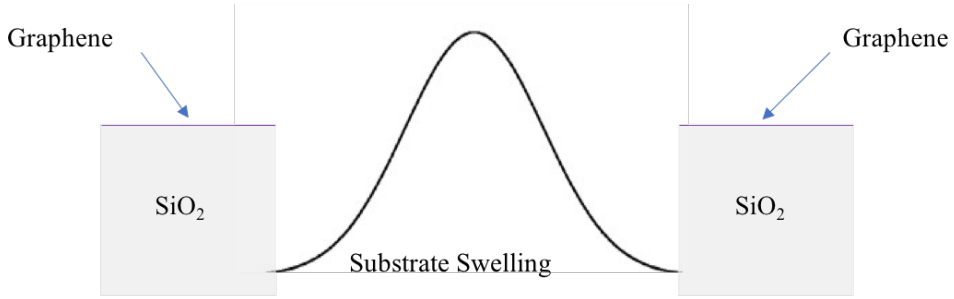

Fig 6. 1 Schematic illustration of the substrate swelling phenomena happens during the femtosecond laser ablation (experimental data in chapter 4).

In this chapter, an absorption model for the graphene, SiO_2, Si substrate system is developed, which will consider the reflection on different materials. From the best knowledge of the author, such model has not been done in the literature. Because the silicon substrate is capped by a thin layer of silicon dioxide and the reflective index of silicon changes with the temperature, it adds additional complication on the modelling.

The simulated energy absorption model can provide at least two significant advances in understanding the femtosecond laser processing of graphene on SiO_2/Si substrate. First, the absorption model itself imparts a picture of the energy distribution in graphene and the substrate. Second, it provides supportive facts in the understanding of the substrate involvement during the femtosecond process, especially swelling effects observed in chapter 4.

6.2 Model construction

Fig 6.2 demonstrates the schematics of the basic physic picture of the light propagation in graphene, SiO_2, Si substrate. The reflection bouncing in the SiO_2 middle layer with thickness enables the enhancement of violet-purple light constructive interference in the white light source. At the laser light of a wavelength of 1030 nm, the SiO_2 is almost transparent, and Silicon has a penetration length of 300 μm. This knowledge assisted the success in achieving selective ablation of graphene with non-damage/ablated substrate. In this chapter, to explore the time dependence temperature profile and the energy absorption during the femtosecond scale, it requires further discussion on the modelling at femtosecond scale. This model considers a single pulse as the input energy, with a Gaussian shape, providing the interaction information of laser light with the Graphene, SiO_2 and Si substrate in femtosecond scale.

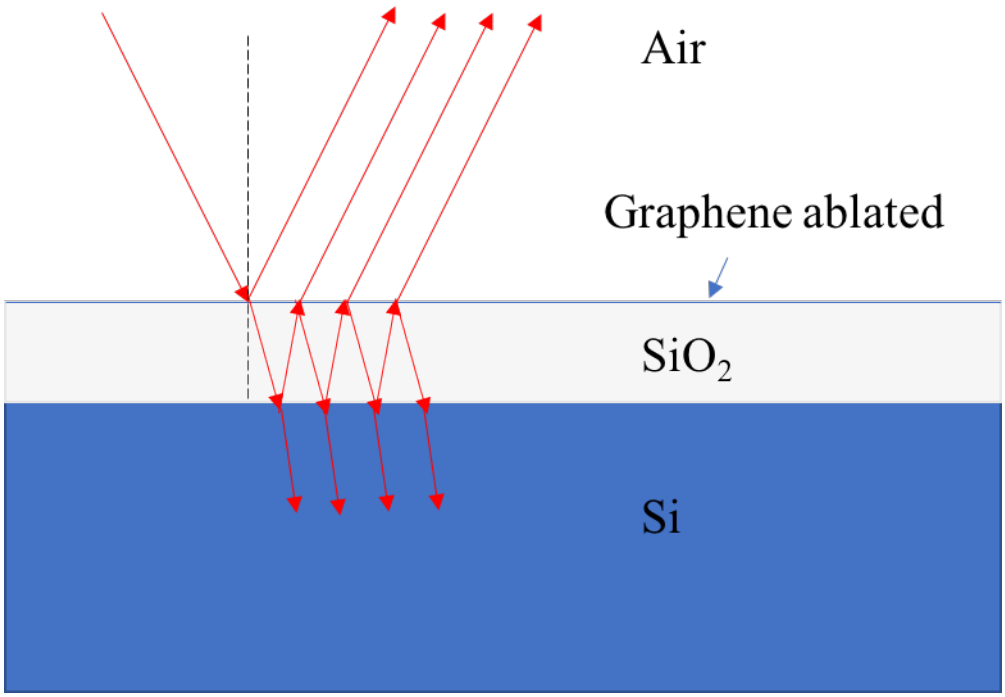

Fig 6. 2 Schematics of laser graphene-SiO_2-Si substrate interaction.

6.2.1 Model consideration

In this complex system, we have three different property of materials and three interfaces. The first interface boundary is graphene and air. The second interface boundary is graphene and SiO_2. The third interface is SiO_2 and Silicon. For the three types of material, zero bandgap graphene, insulator SiO_2, and semiconductor Silicon respond to light differently.

(a) Graphene interact with light

Upon laser irradiation, the electron of graphene absorbs the light and becomes excited. Hot electron gas is produced. In near infrared region (the laser light wavelength is 1030 nm), graphene absorbance is primarily attributed to interband transition. This response is nearly frequency independent with 2.3% absorption of the light, determined by the fine structure constant ($\alpha\pi$, where $\alpha = e^2/4\pi\varepsilon_0\hbar$) [57]. SiO_2 is an insulator, the bandgap is sufficiently large hence no carriers are excited across the bandgap, which means no free carrier absorption and SiO_2 is optically transparent. The graphene absorption in femtosecond scale has been demonstrated by two temperature model. First, electrons of graphene absorb the photon energy. Second, the phonon absorbed the energy. A single carbon bond energy is given around 5~6 eV (interplanar sp^2 bond) under ambient condition [123]. This suggests that in total breaking one such bond requiring four to five photons from 1030 nm laser wavelength, as $E(eV) = 1.2$ for 1030 nm. The laser pulse interacts with graphene, with the fast

vibrational electrons that may cause the weakness of the bonds between carbon atoms, until the graphene is removed. This could be one of the explanations on the graphene ablation.

(b) Heat process

Given that graphene only absorbs light one atomic layer thick with a nearly constant absorption of 2.3%, the strong absorption of Si substrate at 1030 and the reflections in the surface of SiO_2 is the main concern in understanding the substrate. For ultrafast laser material processing, the laser pulse durations much shorter than the time it takes for the electron and lattice to reach thermal equilibrium, this is the reason to apply two temperature model of graphene. For SiO_2 with a sufficiently large bandgap, it is unlikely to have a free carrier with ultrafast pulse irradiation. Thus, it is fair to assume that the electron and lattice thermal equilibrium is insignificant. For the thermal transport study, there are Fourier theory and non-Fourier theory. The former considers the heat transport as a diffusive process. The energy flow is driven by a temperature gradient. The later one considers heat flow as ballistic, driven by point to point transport of energy quanta. The applied theory in thermal transport relies on the relation between the heat area dimension and the mean free path of phonons in the underlying heat sink [225]. In this study, the heat area dimension is the laser diameter, D, which is 4.16 μm, larger than the nm free path of the phonon. Hence, Fourier law can be applied in the SiO_2/Si substrate thermal study.

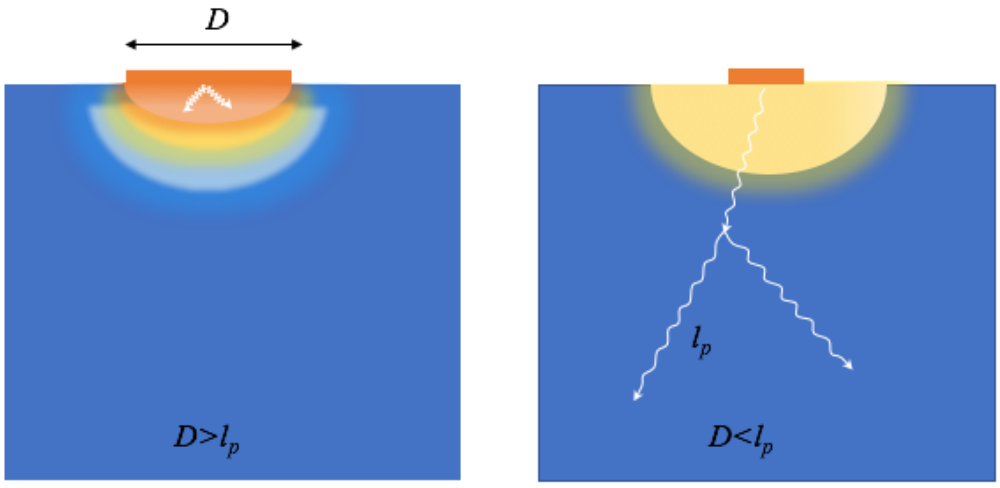

Fig 6. 3 Schematic illustration of diffusive ($D>l_p$) and ballistic ($D< l_p$) thermal transport across the interface, where D is the length scale and l_p is the mean free path of phonon [225].

6.2.2 Model sketch

Enlightened by models to investigate the temperature profile and energy absorption profile in metal, semiconductor, and semiconductor [226], [227], in this section, a theoretical model is developed to investigate the temperature and energy absorption profile in the graphene-SiO_2-Si substrate system. The advantage of the femtosecond laser is limited heat affected zone in the surrounding graphene. Hence, without loss of generality, the model can be effectively treated as one dimensional (along with the laser propagation direction) model. The refractive changes together with the wave interference in the middle layer SiO_2 will modify the absorption energy in graphene and the temperature field in the graphene-SiO_2-Si system. Thus, the absorption model will treat the SiO_2-Si system as a thin layer film structure using the transfer matrix method. The new model also considers an empirical value of graphene absorbed 2.3% of the laser energy [185]. The results of the temperature profile in the SiO_2-Si system by a femtosecond laser are presented.

The logical structure of the model shown in Fig 6.4. It starts from the total energy in the system which is enthalpy. Based on the Fourier law and the energy conservation, the heat transfer equation is given. To solve the equation, implicit finite difference algorithm is applied with layer separation and initial boundary conditions. Through Maxwell equations and using the same layer separation and initial boundary conditions, we consider the reflection and transmission in each layer. The temperature profile, the energy absorption can be calculated by iteration.

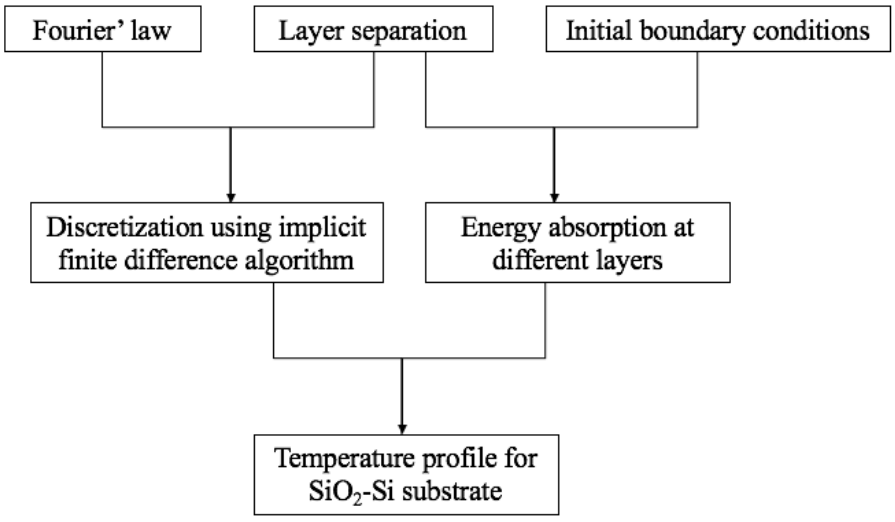

Fig 6. 4 The logic structure of thermal transport and energy absorption model.

6.2.3 Model description

The sketch of the basic structure with stratified multilayers separation for SiO_2/Si substrate is shown in Fig 6.5. A silicon dioxide layer of thickness d_o is capped on the silicon substrate of thickness d_s. The laser beam is illuminated on the surface of silicon dioxide by a pulsed laser beam with a diameter of 4.16 μm. The laser light penetration during the femtosecond scale in the order of tens micrometres. In this model, the top surface of silicon dioxide film is denoted as $x = 0$. For each of the silicon dioxide and silicon, the reflectivity index varies with the temperature and energy absorption is calculated.

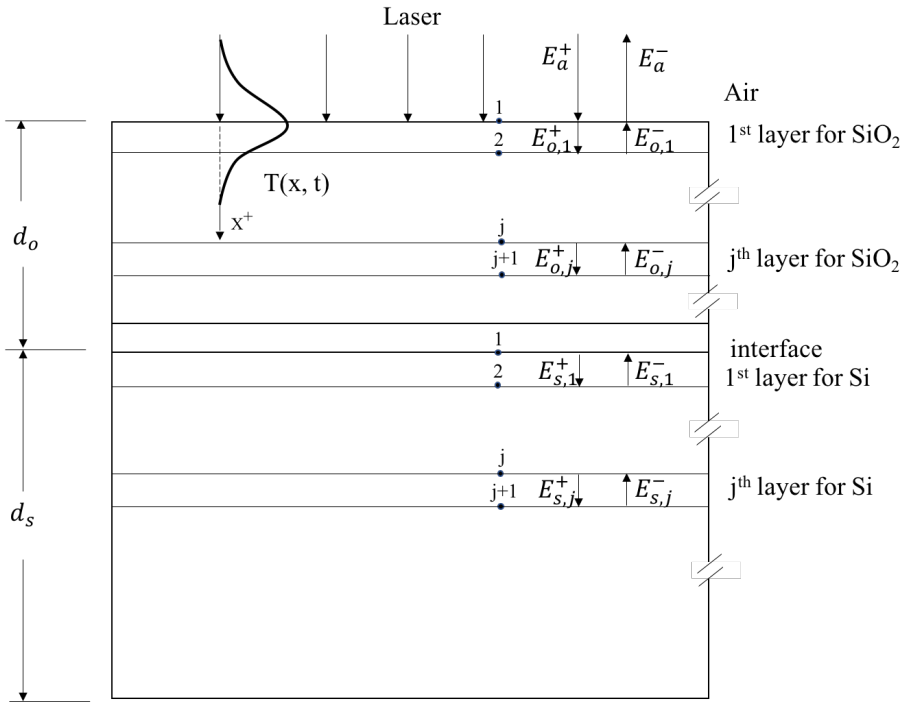

Fig 6. 5 Schematic graph of the heat propagation in the silicon dioxide-silicon in a multilayer, stratified structure.

6.2.4 Model assumption

The model is formulated under following assumptions:

1. The model assumes the graphene is ablated. As a result, the swelling effect is only cause by SiO_2-Si substrate.
2. Because silicon dioxide is an insulator, it has no carrier density and carrier thermal conductivity. Hence, it is hard to model the dynamic between lattice temperature and carrier temperature. Therefore, the model is developed based on one temperature only.
3. The heat transfers at the centre of the laser beam can be deemed as one dimensional.

4. The convection and radiation losses from the surface of the silicon dioxide are negligible.
5. The structure is isothermal before interacting with the laser.
6. The magnetic field and electric field have a periodic temporal structure that is dependent on $e^{i\omega t}$.

6.2.5 Nomenclature in this model

Q	Input energy	r	Fresnel reflection coefficient
$\mathcal{H}$	Enthalpy in the system	R	Reflectivity
ΔT	Temperature difference	n	Real part of reflective index
c	Speed of light	$\boldsymbol{n}$	Complex reflective index
C_p	Specific heat	N	Number of layers in the silicon dioxide film
d	Layer thickness	P	Temporal profile of the incident laser light intensity
d_o	Silicon dioxide thickness	Q_{ab}	Absorbed energy by the thin silicon dioxide, Silicon substrate per unit volume, per unit time
d_s	Silicon thickness	t	Time
$\mathbf{E}$	Electric field vector	t_p	Length of laser pulse
$\mathbf{H}$	Magnetic field vector	T	Temperature
F	Laser fluence	T_∞	Ambient temperature, T=300K
$\boldsymbol{S}$	Poynting vector	x	Coordinate in the normal to the sample surface direction
S	Magnitude of the pointing vector, normalized with the incident energy flux	ε	Complex electric permittivity
i	Imaginary unit	λ	Laser light wavelength in vacuum
κ	Thermal conductivity	μ	Magnetic permeability
k_{ext}	Extinction coefficient of silicon	ρ	Density
$k_{ext,s}$	Extinction coefficient of silicon at 300K	τ	Transmissivity
$\mathcal{M}$	Transmission matric	ω	Light frequency

subscripts		superscripts	
a	air	+	Forwards wave propagation along the direction of incident laser light
o	Silicon dioxide	-	Reflected wave propagation
s	Silicon	*	Complex conjugate

6.3 Modelling the heat transfer in graphene-silicon dioxide-silicon film

Absorbed optical energy by the laser beam is manifested as heat. In this context, it means the energy deposited within the thin film structure by laser irradiation changes the localized temperature. The change in enthalpy $\mathcal{H}$ equals to the change in the internal energy of the system, for a unit volume this can be expressed as [228]:

$$\frac{d\mathcal{H}}{dt} = \rho c_p \Delta T$$

Where ρ is density, c_p is the specific heat capacity and ΔT is the temperature difference. According to the Fourier's law, heat propagation can be expressed by the equation below [229] :

$$\frac{dQ}{dt} = -\kappa \nabla T$$

where κ is the thermal conductivity Q is the input energy and ∇T indicates the temperature gradient (the temperature change over the depth of the substrate). For energy flows in a small volume, it will either change the enthalpy or flow out the low amount. In this study, we also need to consider the extra source of energy Q_{ab} caused by the absorbed optical radiation during propagation. Therefore, the equation is described as,

$$Q_{ab} - \nabla \frac{dQ}{dt} = \frac{d\mathcal{H}}{dt}$$

$$Q_{ab} + \nabla(\kappa \nabla T) = \rho c_p \Delta T \qquad 6.1$$

It is common to assume the heat transfer at the centre of a laser beam is one-dimensional. Here, the direction of heat propagation is considered as along x^+ path, which is perpendicular to the graphene surface, pointing from the ambient air to the graphene, silicon dioxide, silicon substrate, as shown in Fig. 6.2.

Hence, the one-dimensional expression of equation 6.1 is shown as

$$Q_{ab}(x,t) + \frac{\partial}{\partial x}\left(\kappa(T)\frac{\partial T(x,t)}{\partial x}\right) = (\rho C_p)(T)\frac{\partial T(x,t)}{\partial t} \tag{6.2}$$

For silicon dioxide film, the thermal conductivity κ_1 is a constant $1.4\,\mathrm{Wm^{-1}K^{-1}}$. In addition, specify heat capacity does not change with temperature. Thus, it can be described as: $(\rho C_p)(T) = \rho_1 C_{p:1} = 2.64 \times 10^6 \mathrm{Jm^{-3}K^{-1}}$, where ρ_1 stands for the density of the silicon dioxide, and $C_{p:1}$represents the special heat capacity of the silicon dioxide. Thus, equation 6.2 becomes:

$$Q_{ab}(x,t) + \kappa_1\frac{\partial^2 T(x,t)}{\partial x^2} = \rho_1 C_{p:1}\frac{\partial T(x,t)}{\partial t} \tag{6.3}$$

For silicon film, the thermal conductivity is a function of temperature $\kappa_2(T) = 2.99 \times 10^4/(T - 99)$ ($\mathrm{Wm^{-1}K^{-1}}$). Moreover, the specify heat capacity of silicon is also a function of temperature$(\rho C_p)(T) = \left(1.474 + 0.17066 \times \frac{T}{300}\right) \times 10^6 \mathrm{Jm^{-3}K^{-1}}$. Hence, equation 6.2 becomes:

$$\begin{aligned}\frac{\partial}{\partial x}\left(\kappa_2(T)\frac{\partial T(x,t)}{\partial x}\right) &= \frac{\partial \kappa_2(T(x,t))}{\partial x}\frac{\partial T(x,t)}{\partial x} + \kappa_2(T)\frac{\partial^2 T(x,t)}{\partial x^2} \\ &= \left[\frac{\partial \kappa_2(T)}{\partial T} + \kappa_2(T)\right]\frac{\partial^2 T(x,t)}{\partial x^2} \\ &= (\rho C_p)(T)\frac{\partial T(x,t)}{\partial t} - Q_{ab}(x,t)\end{aligned} \tag{6.4}$$

6.4 Finite difference algorithm

Finite difference algorithm is an algorithm developed to approximate differentiation equations. In this case, the algorithm is used to approximate the temperature diffusion along x. In general, the finite difference algorithm contains four steps: layer separation, expression temperature diffusion equation in finite difference form, identify the boundary conditions, and calculate the temperature profile with circular reference iteration.

6.4.1 Layer separation

In the experiment, the graphene-SiO_2-Si structure is composed of a graphene film with 0.33 nm thickness, a SiO_2 film with 300 nm and Silicon film with 500 μm. For the SiO_2 film, a unified layer separation (5 nm) is applied. With the unified layer separation, the SiO_2 film can be represented by 60 layers. From Silicon film, the same layer separation is employed. for silicon film, this study focuses on a study the first 400 layers, with the thickness of each layer is 5 nm (in total 2 μm). It is worthwhile to notice that the distance of layer separation is chosen as a balance of the complexity of the finite difference algorithm and the accuracy of the approximation.

6.4.2 Finite difference form of temperature diffusion equation

To represent the temperature diffusion with finite difference form, we need to expand the temperature function at $x + \Delta x$ and $x - \Delta x$ with Tayler series:

$$T(x + \Delta x, t) = T(x, t) + \Delta x \frac{\partial T(x,t)}{\partial x} + \frac{\Delta x^2}{2} \frac{\partial^2 T(x,t)}{\partial x^2} + \frac{\Delta x^3}{6} \frac{\partial^3 T(x,t)}{\partial x^3} + \mathcal{O}(\Delta x^4)$$

$$T(x - \Delta x, t) = T(x, t) - \Delta x \frac{\partial T(x)}{\partial x} + \frac{\Delta x^2}{2} \frac{\partial^2 T(x,t)}{\partial x^2} - \frac{\Delta x^3}{6} \frac{\partial^3 T(x,t)}{\partial x^3} + \mathcal{O}(\Delta x^4)$$

$$\mathrm{T}(x + \Delta x, t) + T(x - \Delta x, t) = 2T(x, t) + \Delta x^2 \frac{\partial^2 T(x,t)}{\partial x^2} + 2\mathcal{O}(\Delta x^4)$$

Hence

$$\frac{\partial^2 T(x,t)}{\partial x^2} \approx \frac{T(x + \Delta x, t) + T(x - \Delta x, t) - 2T(x, t)}{\Delta x^2} \tag{6.5}$$

6.4.2 Identify the boundaries conditions

The model assumes the energy loss from the surface of the graphene-SiO_2-Si layer through convection and radiation is negligible by comparing with the high laser intensity. Hence,

$$\left.\frac{\partial T(x,t)}{\partial x}\right|_{x=0} = 0 \tag{6.6}$$

Also, the temperature cannot completely penetrate the SiO_2-Si layer in the femtosecond timescale. Therefore, it is reasonable to assume the bottom of the Si substrate is at ambient temperature：

$$\mathrm{T}(\mathrm{x} = 300 + 2000\ \mathrm{nm}, \mathrm{t}) = \mathrm{T}_\infty$$

Finally, it assumes the temperature of the SiO_2-Si film at time $\mathrm{t} = 0$ is identical to the ambient temperature：

$$T(x, 0) = T_\infty \tag{6.7}$$

6.4.3 Calculate the temperature profile with circular reference iteration

To simplify the notation, this study uses T_i^n represents the temperature at $T(i\Delta x, n\Delta t)$ and Q_i^n describe the energy absorbed at $Q_{ab}(i\Delta x,\ n\Delta t)$. For the silicon dioxide film, by substituting equation 6.5 into 6.3, we have

$$Q_i^n + \kappa_1 \frac{T_{i+1}^n + T_{i-1}^n - 2T_i^n}{\Delta x^2} = \rho_1 C_{p:1} \frac{T_i^{n+1} - T_i^n}{\Delta t}$$

To avoid the unnecessary oscillation, the implicit finite different algorithm is applied to evaluate the spatial derivatives at the time step $\mathrm{n} + 1$. Therefore, the following equation can be derived,

$$Q_i^n + \kappa_1 \frac{T_{i+1}^{n+1} + T_{i-1}^{n+1} - 2T_i^{n+1}}{\Delta x^2} = \rho_1 C_{p:1} \frac{T_i^{n+1} - T_i^n}{\Delta t} \tag{6.8}$$

Equation (6.8) can be transferred to

$$T_i^{n+1} - T_i^n = \frac{\kappa_1 \Delta t}{\rho_1 C_{p:1} \Delta x^2} \left(T_{i+1}^{n+1} + T_{i-1}^{n+1} - 2T_i^{n+1}\right) + \frac{\Delta t}{\rho_1 C_{p:1}} Q_i^n$$

By using s_1 denotes $\frac{\kappa_1 \Delta t}{\rho_1 C_{p:1} \Delta x^2}$ and b_1 for $\frac{\Delta t}{\rho_1 C_{p:1}}$, we can simplify the relation between T^{n} and $\mathrm{T}^{\mathrm{n+1}}$ into

$$T_i^n = -s_1 T_{i+1}^{n+1} + (1 + 2s_1) T_i^{n+1} - s_1 T_{i-1}^{n+1} - b_1 Q_i^n, i \in \mathbb{N}^+, i < 60$$

For the silicon film, by substituting equation (6.5) into (6.4), we have

$$\left(\rho \mathrm{C_p}\right)(\mathrm{T}) \frac{\mathrm{T_i^{n+1}} - \mathrm{T_i^n}}{\Delta \mathrm{t}} = \left[\frac{\partial \kappa_2(\mathrm{T})}{\partial \mathrm{T}} + \kappa_2(\mathrm{T})\right] \frac{\mathrm{T_{i+1}^{n+1}} + \mathrm{T_{i-1}^{n+1}} - 2\mathrm{T_i^{n+1}}}{\Delta \mathrm{x}^2} + \mathrm{Q_i^n} \tag{6.9}$$

Equation 6.9 can be transferred to

$$T_i^{n+1} - T_i^n = \frac{\left[\frac{\partial \kappa_2(T)}{\partial T} + \kappa_2(T)\right]\Delta t}{(\rho C_p)(T)\Delta x^2}\left(T_{i+1}^{n+1} + T_{i-1}^{n+1} - 2T_i^{n+1}\right) + \frac{\Delta t}{(\rho C_p)(T)} Q_i^n$$

By using s_2 denotes $\frac{\left[\frac{\partial \kappa_2(T)}{\partial T} + \kappa_2(T)\right]\Delta t}{(\rho C_p)(T)\Delta x^2}$ and b_2 for $\frac{\Delta t}{(\rho C_p)(T)}$, we can simplify the relation between T^n and T^{n+1} into

$$T_i^n = -s_2 T_{i+1}^{n+1} + (1 + 2s_2)T_i^{n+1} - s_2 T_{i-1}^{n+1} - b_2 Q_i^n, i \in \mathbb{N}^+, i \geq 60$$

To programme the relation into Matlab, we need to express it in a matrix format.

$$T^n = AT^{n+1} - BQ^n$$

$$A^{-1}(T^n + BQ^n) = T^{n+1} \qquad 6.10$$

where T^n is the vector of temperature for all layers at time $n\Delta t$ and Q^n is the vector of energy absorbed for all layers at time $n\Delta t$. Where

$$A = \begin{bmatrix} 1+s_1 & -s_1 & 0 & 0 & 0 & 0 & 0 & 0 & 0 \\ -s_1 & 1+2s_1 & -s_1 & 0 & 0 & 0 & 0 & 0 & 0 \\ 0 & \ddots & \ddots & \ddots & 0 & 0 & 0 & 0 & 0 \\ 0 & 0 & -s_1 & 1+2s_1 & -s_2 & 0 & 0 & 0 & 0 \\ 0 & 0 & 0 & -s_1 & 1+2s_2 & -s_2 & 0 & 0 & 0 \\ 0 & 0 & 0 & 0 & -s_2 & 1+2s_2 & -s_2 & 0 & 0 \\ 0 & 0 & 0 & 0 & 0 & \ddots & \ddots & \ddots & 0 \\ 0 & 0 & 0 & 0 & 0 & 0 & -s_2 & 1+2s_2 & -s_2 \\ 0 & 0 & 0 & 0 & 0 & 0 & 0 & -s_2 & 1+s_2 \end{bmatrix}$$

$$B = \begin{bmatrix} \frac{\Delta t}{\rho_1 C_{p:1}} \\ \vdots \\ \frac{\Delta t}{\rho_1 C_{p:1}} \\ \frac{\Delta t}{(\rho C_p)(T)} \\ \vdots \\ \frac{\Delta t}{(\rho C_p)(T)} \end{bmatrix}$$

Where B is $[1\times 460]$ vector of Q_i^n where the first 60 values represent Q_i^n in silicon dioxide layers with the value of $\frac{\Delta t}{\rho_1 C_{p:1}}$ and later 400 values represent Q_i^n in the silicon layer with the value of $\frac{\Delta t}{(\rho C_p)(T)}$.

6.5 Modeling of pulsed laser irradiation of graphene-SiO_2-Si layers

Section 6.3 focuses on modelling the energy absorption in the substrate namely the energy absorption in silicon dioxide film and silicon. The modelling applies Maxwell equations.

For pulsed laser interaction with the material, the material response plays a significant role during the process. As for this study, the graphene, SiO_2, silicon substrate as pre-manufacturing materials, it is essential to investigate the underneath physics in the multi-layers' system. The interaction of pulsed laser irradiation may lead to phase change and structural modifications in the material [230]. In addition, the thermal gradients across the interaction area cause the changes in the material complex refractive index. These changes, together with the wave interference, influence the energy absorption [231]. Transfer matrix method (TMM) is applied based on thin film optics theory to present the absorption effect in a rigorous manner [231].

In thin film optics theory, assuming that the electric field and the magnetic field are periodic in time with a time dependence factor $e^{i\omega t}$, where ω is the light frequency, Maxwell's equations for the complex electric and magnetic field vectors are described as [232]:

$$\nabla \times \mathbf{H} = \mathrm{i}\omega\varepsilon\mathbf{E}$$

$$\nabla \times \mathbf{E} = -\mathrm{i}\omega\mu\mathbf{H}$$

Along the direction of propagation, the energy flux is given by the time-averaged magnitude of the Poynting vector [232]:

$$\boldsymbol{S} = \frac{1}{2} Re(\boldsymbol{E} \times \boldsymbol{H}^*)$$

In the model, the laser energy flux propagates along with x-direction can be measured as the time averaged magnitude of the Poynting vector S_{av}. Based on the Poynting theorem, we have

$$S_{av} = \frac{1}{2} Re(E \times H^*)$$

where E and H are the expression of the electrical field and magnetic field. To derive the E and H, the transition matrix of the stratified films need to be constructed. According to the description in the previous layer separation section, the silicon structure with silicon dioxide capping is divided into 460 layers. Such multi-layer structure is well applied in modelling of the semiconductor film [233], [234]. Because the film is composed of different materials and each of them has various refractive indexes and thermal properties, the transition matrixes of silicon dioxide film and silicon film should be constructed individually.

6.5.1 Energy absorption of Silicon dioxide film

In the silicon dioxide film, the transition matrix of the j^{th} layer $\mathcal{M}_{o,j}$ expresses as:

$$\mathcal{M}_{o,j} = \begin{bmatrix} \cos\left(\frac{2\pi}{\lambda} n_o \Delta x\right) & \frac{i}{n_o} \sin\left(\frac{2\pi}{\lambda} n_o \Delta x\right) \\ \frac{i}{n_o} \sin\left(\frac{2\pi}{\lambda} n_o \Delta x\right) & \cos\left(\frac{2\pi}{\lambda} n_o \Delta x\right) \end{bmatrix}$$

where d_o is 5 nm and $n_o = 1.5132$ as extinction coefficient is 0 for silicon dioxide layers. Because the refractive index of silicon dioxide invaries with temperature, the overall transition matrix of the silicon dioxide film $\mathcal{M}_o$ can be expressed as

$$\mathcal{M}_o = \prod_{j=1}^{60} \mathcal{M}_{o,j}$$

By using $\mathcal{M}_o$, the reflection Fresnel coefficient of the silicon dioxide film

$$r_{F,o} = \frac{(\mathcal{M}_o(1,1) + \mathcal{M}_o(1,2)n_s)n_a - (\mathcal{M}_o(2,1) + \mathcal{M}_o(2,2)n_s)}{(\mathcal{M}_o(1,1) + \mathcal{M}_o(1,2)n_s)n_a + (\mathcal{M}_o(2,1) + \mathcal{M}_o(2,2)n_s)} = \sqrt{R_o}$$

n_s is the complex refractive index at the top surface of the silicon film and n_a is the refractive index of air. The reflectivity of the structure R_o represents the square of the ratio between the magnitude of the electrical field that propagated backward (along $-x$) out of the silicon dioxide layer and the electrical field the propagate forward (along x) into the silicon dioxide layer. Because the plane wave is an incident on the film, the electric field amplitude on the top layer of silicon dioxide E_o^+ can be represented by the S_{av} as

$$E_o^+ = \sqrt{\frac{2\mu c S_{av}}{n_a}}$$

where the μ is the magnetic permeability and c is the speed of light. Based on the reflectivity of the silicon dioxide layer

$$\frac{|E_o^-|^2}{|E_o^+|^2} = R_o = |r_{F,o}|^2$$

$$E_o^- = \sqrt{\frac{2\mu c S_{av}}{n_a}}|r_{F,o}|$$

With the transition matrix $\mathcal{M}_o$, the electrical field propagated forward along the x direction into the silicon layer E_s^+ can be calculated by using the transmission Fresnel coefficient $t_{F,o}$.

$$t_{F,o} = \frac{2n_a}{(\mathcal{M}_o(1,1) + \mathcal{M}_o(1,2)n_s)n_a + (\mathcal{M}_o(2,1) + \mathcal{M}_o(2,2)n_s)}$$

$$|t_{F,o}|^2 = \frac{|E_s^+|^2}{|E_o^+|^2}$$

Hence

$$|E_s^+|^2 = \frac{2\mu c S_{av}|t_{F,g}|^2}{n_a}$$

Thus, E_s^+ can be expressed as

$$|E_s^+|^2 = \frac{2\mu c S_{av}|t_{F,g}|^2}{n_a}$$

After calculating E_o^-, the electrical field and magnetic field in the first layer of silicon dioxide film can be calculated as

$$E_{o,1}(x) = E_o^+ e^{-i\frac{2\pi n_o x}{\lambda}} + E_o^- e^{i\frac{2\pi n_o x}{\lambda}}$$

$$H_{o,1}(x) = \frac{n_o}{\mu c}(E_o^+ e^{-i\frac{2\pi n_o x}{\lambda}} - E_o^- e^{i\frac{2\pi n_o x}{\lambda}})$$

$$\forall\ 0 < x \leq 5\ \text{nm}$$

The electrical field and magnetic field in the second to sixty layers of silicon dioxide film can be evaluated recursively.

$$E_{o,j}(x) = E_{o,j}^+ e^{-i\frac{2\pi n_o(x-\Delta x(j-1))}{\lambda}} + E_{o,j}^- e^{i\frac{2\pi n_o(x-\Delta x(j-1))}{\lambda}}$$

$$H_{o,j}(x) = \frac{n_o}{\mu c}(E_{o,j}^+ e^{-i\frac{2\pi n_o(x-\Delta x(j-1)}{\lambda}} - E_{o,j}^- e^{i\frac{2\pi n_o(x-\Delta x(j-1))}{\lambda}})$$

$$\forall\ 5 < x \leq 300\ \text{nm}, 2 \leq j \leq 60, j \in \mathbb{N}$$

where

$$E_{o,j}^+ = \frac{1}{2}\{E_{o,j-1}^+ 2e^{-i\frac{2\pi n_{o,j-1}(\Delta x(j-1))}{\lambda}}\}$$

$$E_{o,j}^- = \frac{1}{2}\{E_{o,j-1}^- 2e^{i\frac{2\pi n_{o,j-1}(\Delta x(j-1))}{\lambda}}\}$$

After determining the $E_{o,j}(x)$ and $H_{o,j}(x)$, the energy absorption in the j^{th} silicon dioxide layer can be expressed as

$$Q_{o,j}(x,t) = \frac{P(t)}{n_a|E_o^+|^2}\frac{dRe\left(E_{o,j}(x) \times H_{o,j}(x)^*\right)}{dx}, \forall\ 0 < x \leq 300\ nm, 1 \leq j \leq 60, j \in \mathbb{N}$$

where $P(t)$ is the temporal profile of the laser intensity with Gaussian shape after the absorption by the monolayer graphene, can be expressed by the equation below [235]:

$$P(t) = (1 - 2.3\%)\frac{2F\sqrt{ln2}}{\sqrt{\pi}t_p}(1 - R_{g:o})e^{-4(ln2)\frac{t}{t_p}^2}$$

We can calculate $Q_{o,j}^n$ as equation 6.11

$$Q_{o,j}^{n} = \frac{P(n\Delta t)}{n_a|E_o^+|^2}\frac{dRe\left(E_{o,j}(j\Delta x) \times H_{o,j}(j\Delta x)^*\right)}{dx} \quad 6.11$$

6.5.2 Energy absorption in silicon film

The energy absorption in the silicon film is more complicated than the silicon dioxide film because of the reflective index of silicon changes with temperature. n_s signifies the complex refractive index of the silicon layer, which is a linear function of temperature and can be further expressed by [236],

$$\boldsymbol{n_s} = n_R + a_s(T - 300) - ik_{ext,s}e^{\frac{T-293}{430}}$$

where n_R is the real part of the refractive index of silicon at 300K, a_s is the linear temperature coefficient of refractive index, and $k_{ext,s}$ is the extinction coefficient at silicon at 300K.

The j^{th} layer transition matrix in silicon is denoted as $\mathcal{M}_{s:j}$.

$$\mathcal{M}_{s:j} = \begin{bmatrix} \cos\left(\frac{2\pi}{\lambda}\mathbf{n_s}\Delta x\right) & \frac{i}{n_s}\sin\left(\frac{2\pi}{\lambda}\mathbf{n_s}\Delta x\right) \\ \frac{i}{\mathbf{n_s}}\sin\left(\frac{2\pi}{\lambda}\mathbf{n_s}\Delta x\right) & \cos\left(\frac{2\pi}{\lambda}\mathbf{n_s}\Delta x\right) \end{bmatrix}$$

The overall transition matrix of the 400 silicon layers can be expressed as

$$\mathcal{M}_s = \prod_{j=1}^{400}\mathcal{M}_{s,j}$$

The reflection Fresnel coefficient of the silicon film is:

$$r_{F,s} = \frac{\left(\mathcal{M}_s(1,1) + \mathcal{M}_o(1,2)\right) - \left(\mathcal{M}_o(2,1) + \mathcal{M}_o(2,2)\right)}{\left(\mathcal{M}_o(1,1) + \mathcal{M}_o(1,2)\right) + \left(\mathcal{M}_o(2,1) + \mathcal{M}_o(2,2)\right)} = \sqrt{R_s}$$

By using the reflectivity of silicon film R_s, we can calculate the E_a^- which indicates the amplitude of the electric field propagated backward from silicon film into silicon dioxide film.

$$\frac{|E_s^-|^2}{|E_s^+|^2} = R_s = \left|r_{F,s}\right|^2$$

Once E_a^- is determined, with the similar approach in silicon dioxide layer, we can calculate the energy absorption in the silicon layer. In the first silicon layer, the electrical field and magnetic field in the first layer of silicon film can be calculated as

$$E_{s,1}(x) = E_s^+ e^{-i\frac{2\pi n_{s,1}(x-300)}{\lambda}} + E_s^- e^{i\frac{2\pi n_o(x-300)}{\lambda}}$$

$$H_{s,1}(x) = \frac{n_o}{\mu c}\left(E_s^+ e^{-i\frac{2\pi n_{s,1}(x-300)}{\lambda}} - E_s^- e^{i\frac{2\pi n_{s,1}(x-300)}{\lambda}}\right)$$

$$\forall\ 300 < x \leq 305\ \text{nm}$$

where $n_{s,1}$ is the complex refractive index of the first silicon layer. The electrical field and magnetic field in the second to four hundred layers of silicon dioxide film can be evaluated recursively.

$$E_{s,j}(x) = E_{s,j}^+ e^{-i\frac{2\pi n_{s,j}(x-\Delta x(j-1)-300)}{\lambda}} + E_{s,j}^- e^{i\frac{2\pi n_{s,j}(x-\Delta x(j-1)-300)}{\lambda}}$$

$$H_{s,j}(x) = \frac{n_o}{\mu c}\left(E_{s,j}^+ e^{-i\frac{2\pi n_{s,j}(x-\Delta x(j-1)-300)}{\lambda}} - E_{s,j}^- e^{i\frac{2\pi n_{s,j}(x-\Delta x(j-1)-300)}{\lambda}}\right)$$

$$\forall\ 305 < x \leq 2300\ \text{nm}, 2 \leq j \leq 400, j \in \mathbb{N}$$

where

$$E_{s,j}^+ = \frac{1}{2}\left\{E_{s,j-1}^+\left[1 + \frac{n_{s,j-1}}{n_{s,j}}\right]e^{-i\frac{2\pi n_{s,j-1}(\Delta x(j-1)+300)}{\lambda}} + E_{s,j-1}^-\left[1 - \frac{n_{s,j-1}}{n_{s,j}}\right]e^{i\frac{2\pi n_{s,j-1}(\Delta x(j-1)+300)}{\lambda}}\right\}$$

$$E_{s,j}^- = \frac{1}{2}\left\{E_{s,j-1}^+\left[1 - \frac{n_{s,j-1}}{n_{s,j}}\right]e^{-i\frac{2\pi n_{s,j-1}(\Delta x(j-1)+300)}{\lambda}} - E_{s,j-1}^-\left[1 + \frac{n_{s,j-1}}{n_{s,j}}\right]e^{i\frac{2\pi n_{s,j-1}(\Delta x(j-1)+300)}{\lambda}}\right\}$$

After determining the $E_{s,j}(x)$ and $H_{s,j}(x)$, the energy absorption in the j^{th} silicon layer can be expressed as

$$Q_{s,j}(x,t) = \frac{P(t)}{n_a|E_a^+|^2}\frac{dRe\left(E_{s,j}(x) \times H_{s,j}(x)^*\right)}{dx}, \forall\ 300 < x \leq 2300\ \text{nm}, 1 \leq j \leq 400, j \in \mathbb{N}$$

We can calculate the $Q_{s,j}^n$ as

$$Q_{s,j}^{n} = \frac{P(n\Delta t)}{n_a |E_o^+|^2} \frac{dRe\left(E_{s,j}(j\Delta x + 300) \times H_{s,j}(j\Delta x + 300)^*\right)}{dx} \quad 6.12$$

By combining equation 6.11 and 6.12, we can calculate the Q^n in equation 6.10. Hence, we can calculate the T^{n+1} recursively.

6.6 Result analysis through the simulation

6.6.1 Numerical example

To validate the model in section 6.4 and 6.5, a numerical case is demonstrated by considering a laser intensity of 5.19×10^{10} W/cm^2 and t_p is the pulse duration 280 femtoseconds. In the model, the reflectivity of silicon dioxide film $R_o = 0.0417$ does not change over time, because the n_o does not change with temperature. However, the refractive index of silicon film n_s varies with time. Hence, the reflectivity of silicon film R_s also varies temporally.

Fig 6.6 shows the time average magnitude of Poynting vector for the silicon substrate capping with silicon dioxide. It indicates a high variation in the SiO_2 layer. The Poynting vector in the silicon layer decays with the increase of the distance but with limited variation considering the timescale (during the pulse width 280 fs). The signal between $0 < x \leq 300$ nm indicates the time-averaged Poynting vector in the silicon dioxide film. It shows that the time-averaged Poynting vector in silicon dioxide film is time homogeneous, such that the Poynting vector at different times is completely overlapped in the region $0 < x \leq 300$ nm. In the silicon film ($300 < x \leq 2300$ nm), the magnitude of the time-average Poynting vectors decays both spatially and temporally. In the experiment, we apply a Gaussian shape laser pulse. The distributed energy absorption will heat up or cool down the local temperature over time. Hence, it may cause the oscillation in local temperature. The energy absorption and temperature profile are demonstrated in Fig 6.7 and Fig 6.8 respectively with similar variation depend on the depth. In Fig 6.8, the temperature change on the underneath silicon substrate varies much more compared to the variation in silicon dioxide, this result suggests that silicon substrate is more likely to be the main reason that may cause the swelling, due to it being subject to relatively large thermal dynamics compare with silicon dioxide. The Si absorbs the energy, and the significant temperature differential causes the thermal expansion. Thermal expansion influence the silicon dioxide which swells in volume. In addition, the peak fluence is slightly above the melting threshold of SiO_2, such that the reformation of SiO_2 appears to be irreversible. It is worth to notice that the expansion of the Si is one of the explanations for the

swelling phenomena. The author does not exclude that there are other factors that also contribute to the swelling phenomena.

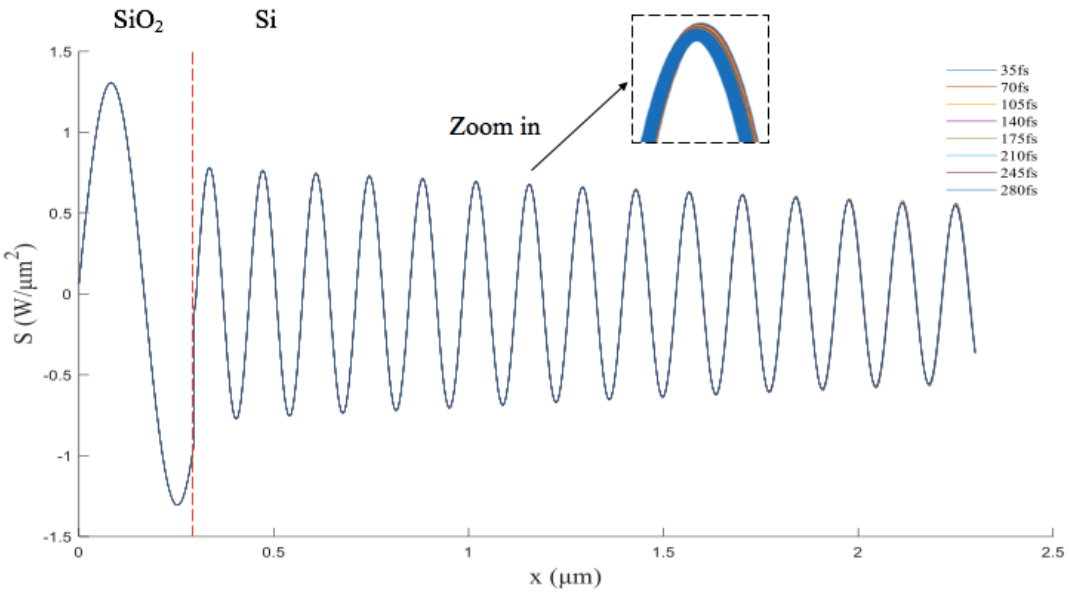

Fig 6. 6 Time-average magnitude of Poynting vector for the SiO_2/Si substrate.

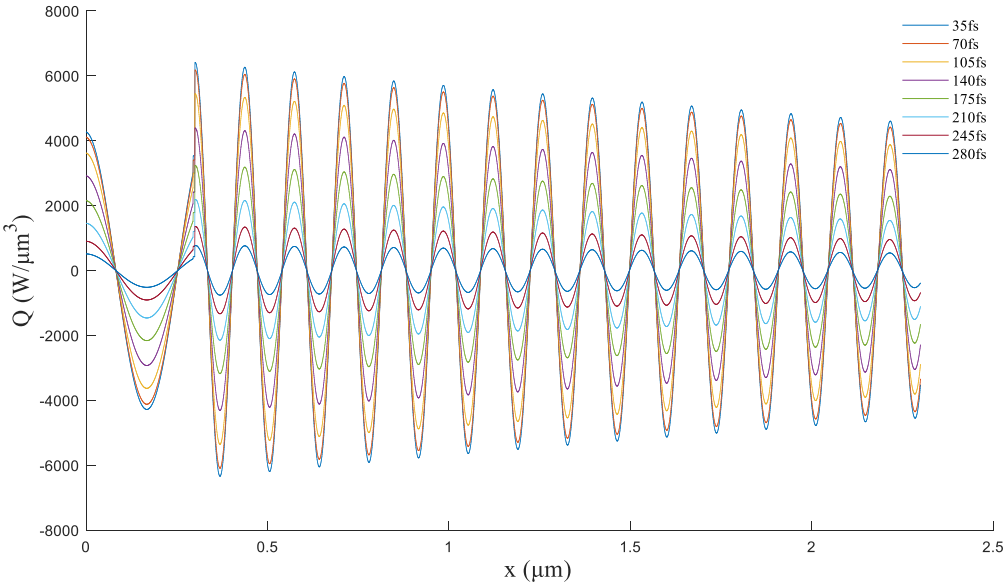

Fig 6. 7 Energy absorption for the SiO_2/Si substrate.

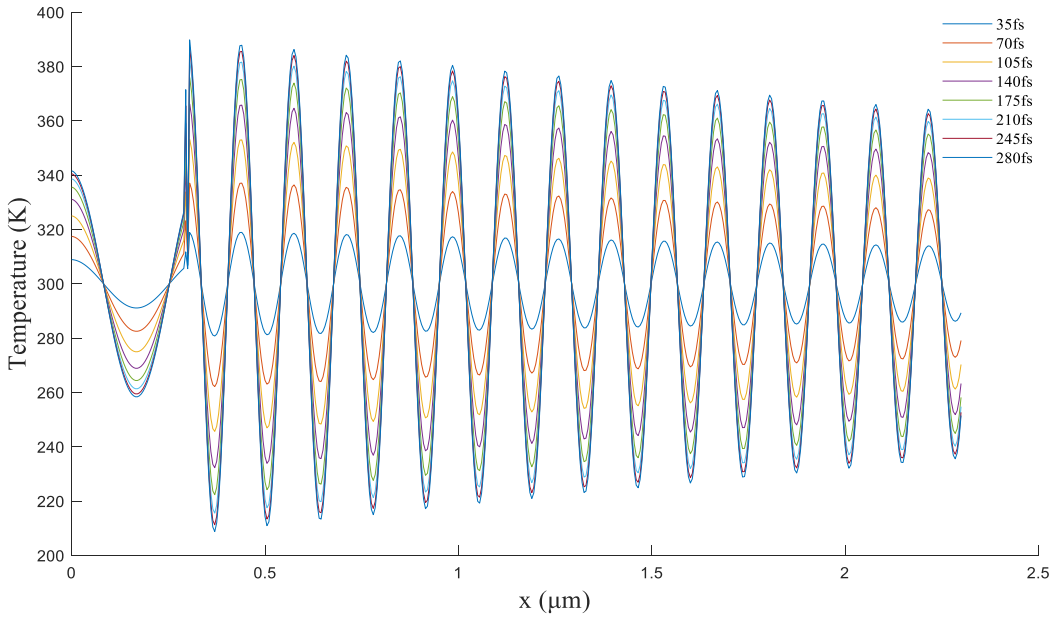

Fig 6. 8 Temperature profile for the SiO_2(0~300 nm)/Si substrate.

6.6.2 Experimental analysis

The cross-section with a sample with a laser intensity of 5.19×10^{10} W/cm^2 processing an ablated line of graphene at the speed of 1.5 mm/s were measured as shown in Fig 6.9. The cross-section was cut through focused ion beam with 30 kV and 500 pA, with deposition of platinum. The SEM image was the cross-section of the SiO_2/Si substrate after ablation with tilt correction. There is a clear boundary between Pt and SiO_2/Si substrate (Fig 6.9). The cross-section of SiO_2/Si substrate is smooth. Further analysis of the elements was mapped with EDS. As shown in Fig 6.10, the signal of Si and C elements are evenly distributed. The O element experiences a drop when mapping on the Si.

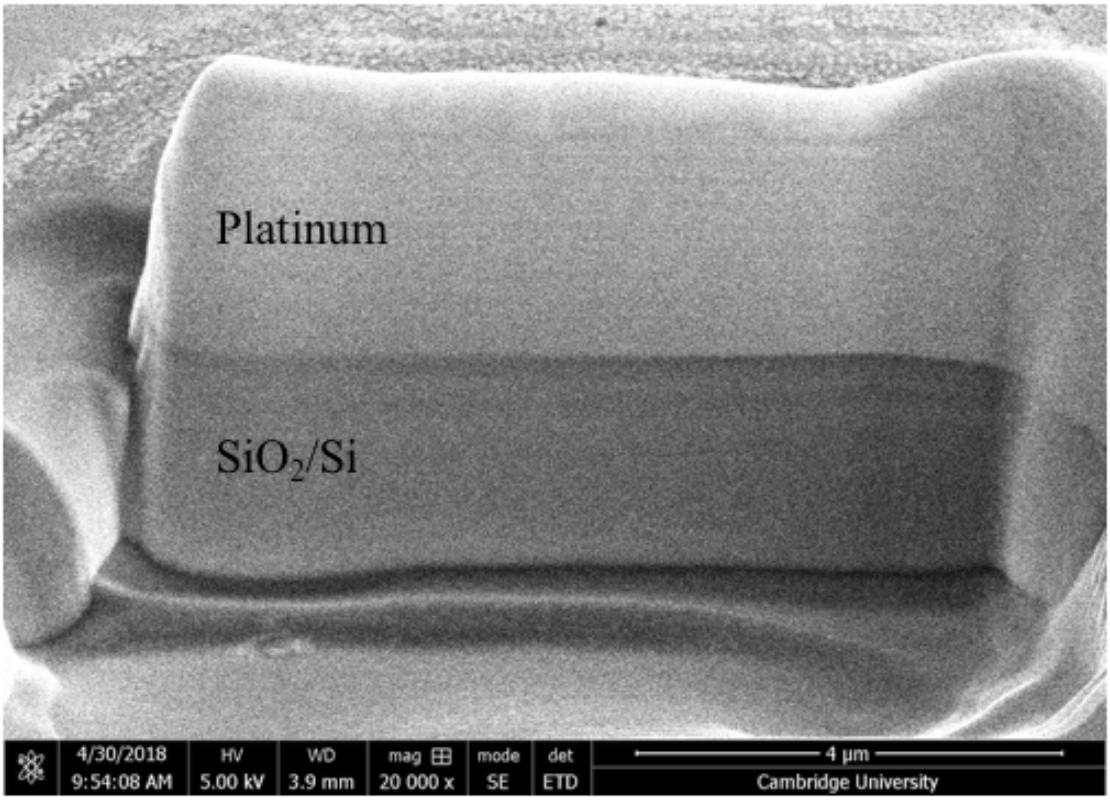

Fig 6. 9 Cross-section of the ablated region on the SiO_2/ Si substrate.

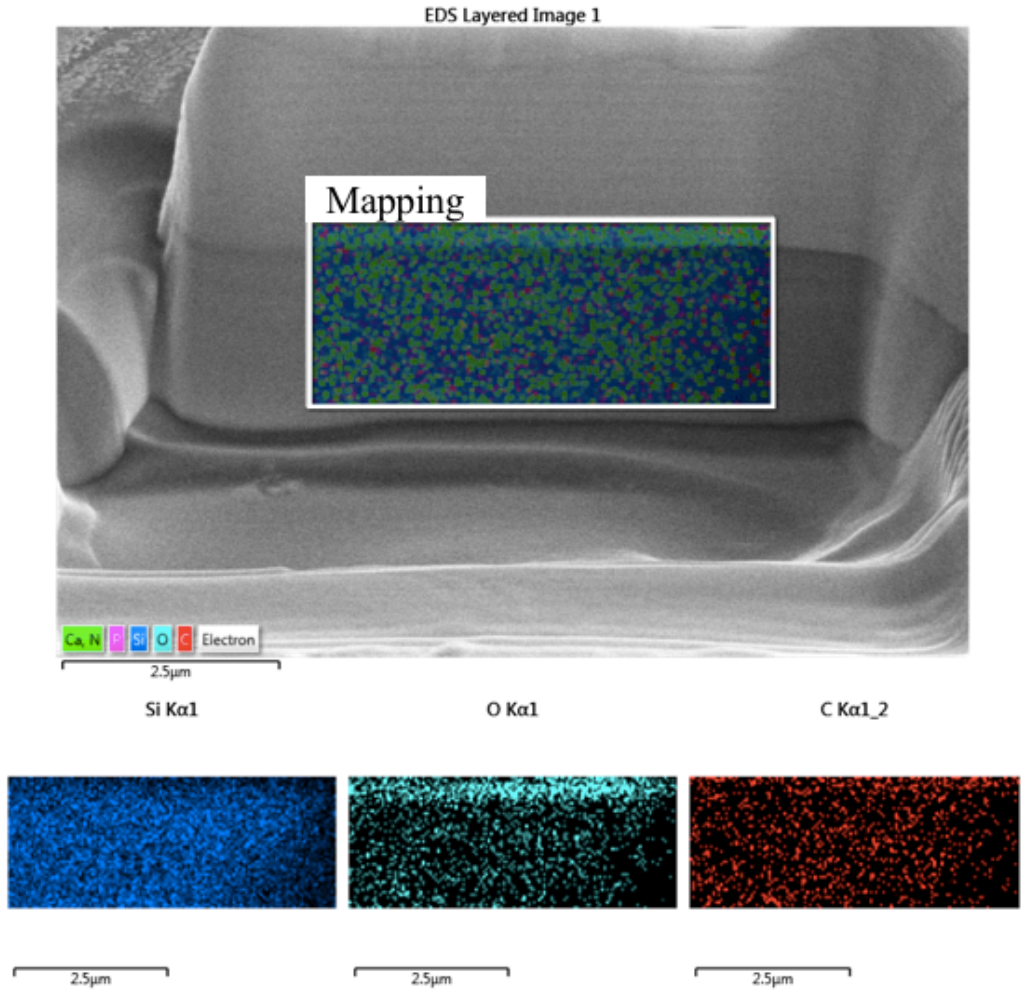

Fig 6. 10 EDS mapping of the cross-section of the ablated region on the SiO_2/ Si substrate.

6.7 Summary

In this chapter, a numerical absorption model for the graphene, silicon dioxide, silicon film structure is developed. The model combines the implicated finite difference algorithm and energy absorption for thin layer films and generates meaningful insights for the energy absorption and temperature oscillation in the silicon dioxide-silicon substrate.

1. In femtosecond laser irradiation, the Poynting vector for the silicon dioxide and silicon substrate varies with the irradiated time, compared to the energy absorption and temperature.
2. In the silicon dioxide layer, the temperature oscillation increased with time but has no significant changes over distance. In the silicon layer, the temperature oscillation grew with time and decreased with the distance. This implies the silicon substrate could be the main cause of the swelling effect.

Chapter 7 Conclusions and future work

7.1 Introduction

The aim of this Ph.D. is to explore the effect of the ultrafast laser on the monolayer graphene deposited on SiO_2/Si substrate and identify its potential in manufacturing. To achieve it, both experimental and theoretical methods are implemented to investigate the graphene ablation, induced defects and substrate interactions with ultrafast laser light.

This chapter provides a summary of the research and highlights the findings from chapter 4, 5 and 6. Section 7.2 summarises the logic of the study presented. Section 7.3 revisits the research questions in Chapter 1 and concludes the answers. The main contributions and novelties of this study are listed in Section 7.4. Limitations of the femtosecond laser manufacturing in the graphene industry and recommendations for future study are listed in Section 7.5.

7.2 Summarising the research

This research explores the potential of the femtosecond laser in a graphene device application from three aspects. First, the optimal process window of selective removal of graphene without damaging the SiO_2/Si substrate are identified. The results show the femtosecond laser provides high-quality ablation and no discernible laser-induced damage in the graphene close to the ablated edge. Second, the experiment shows the induced defects are controllable through laser pulse energies. Growths of defects with the increasing pulse energy were found. This provides insights into the control of functional properties of graphene. Third, a theoretical model is developed to study the absorption of SiO_2/Si substrate. The numerical results support the observations from previous experiments and plot a detailed temperature profile of the SiO_2/Si substrate.

The literature review (Chapter 2) articulates the background knowledge related to this research. It highlights the achievements of the graphene devices, the state-of-art fabrication methods including lasers, as well as the significance of Raman spectroscopy in the graphene measurement. Through the literature review, three research gaps are identified in the area of using a femtosecond laser to process the graphene deposited on SiO_2/Si substrate. In chapter 3, the experimental method is mainly presented. This includes the experimental procedure and evaluation methods. Chapter 4 shows both the graphene effects and substrate evaluation by using a femtosecond laser. The properties of graphene are measured by Raman spectroscopy. The edge quality is characterised by SEM, while

the substrate is evaluated with AFM. Both are under ambient condition and under nitrogen condition it has been tested, to prove the non-oxidation in the near ablation region. A further study on the performance of femtosecond laser under the sub-threshold condition on a graphene deposited on SiO_2/Si substrate sample was demonstrated in Chapter 5. Additionally, the impact of pulse energy has been justified for the different ratio of graphene D peak and G peak before the material ablation. The results demonstrated an excellent dependence with the femtosecond laser pulse energies. To gain a deeper understanding of the absorption distribution from the femtosecond laser into the graphene deposited on SiO_2/Si substrate, an absorption model based on thin film optics was developed and analysed. The experiments and models in the thesis explore and analyse the process of using femtosecond laser processing graphene on SiO_2/Si substrate. It is an important step towards femtosecond laser manufacturing graphene devices.

7.3 Revisit research questions

In this section, the four research questions put forward in chapter 1 are revisited. The investigation and the answers found from the research are emphasised.

Research Question 1: Is it possible to use the femtosecond laser pulses to replace lithographic techniques in fabricating graphene channels on SiO_2/Si substrate?

In Chapter 4, the advantage of using femtosecond laser with the wavelength of 1030 nm, and pulse duration of 280 fs are listed as follows:

- The experiments showed that the femtosecond laser can generate selective removal of graphene without noticeable damage the substrate (section 4.4.1).
- Lower ablation threshold (~100 mJ/cm^2) can be achieved with the femtosecond laser (section 4.4.2).
- Direct laser profiling of monolayer graphene with a clean edge is examined with Raman spectroscopy (section 4.4.3).

Because of the three advantages of the femtosecond laser, it shows the potential capability of replacing the first step of lithography and produce uncontaminated graphene devices.

Research Question 2: What is influence of the femtosecond laser on the SiO_2/Si substrate underneath?

The substrate after graphene ablation has been tested by experiments. The influence of the femtosecond laser on the SiO_2/Si substrate can be generalised into following aspects:

- Limited (2 ~12 nm) swelling effect appears at the substrate due to the high absorption (section 4.4.4)
- The surface potential of the ablated area on the substrate is smooth, with a clear contrast with the graphene, as illustrated in Fig 4.19 and Fig 4.20.

Therefore, the results show apart from swelling effect, there is no significant undesirable influence on the substrate.

Research Question 3: Can femtosecond laser generate defects on the graphene and what is the property of the defects introduced into graphene by the fs laser?

Chapter 5 studied and analysed the induced defects by femtosecond lasers via Raman spectroscopy. The experimental results demonstrated the femtosecond laser cannot only induce the defects on the surface of graphene, but also can control the defects through the laser pulse energy under sub-threshold irradiation. The defects have shown a discernible dependence on the pulse energy with the same scanning speed, or femtosecond laser deposition fluency. The following properties of the defects have also been explored in this chapter, such as I(D)/I(G), A(D)/A(G), I(D)/I(D'), FWHM (G), FWHM (D) and I(G)/I(2D). This investigation expands the general femtosecond laser's involvement in surface modification of graphene.

This part of the research conducted in this thesis helps the understanding of how the femtosecond laser interacts with graphene in the broader way from both a scientific interest and an application-driven point of view.

Research Question 4: What is the nature of energy absorption for a graphene, SiO_2/Si substrate during femtosecond laser pulse?

A theoretical model is formulated in Chapter 6 to address the research question 4. The numerical results of energy absorption and temperature profile of the substrate have been plotted on Fig 6.7 and Fig 6.8. The results have shown the temperature is more significantly oscillated in silicon layer compared to the silicon dioxide film. This provides a theoretical rationale for the swelling effect which is observed in the experiments.

7.4 Novelties and Contributions

7.4.1 Novelties of the research

The novelties of this study are summarised as follows:

1. A lower threshold for laser ablation of graphene has been achieved, compared to the value reported in the literature. This enables a complete removal of graphene, with limited influence on the substrate. Thus, femtosecond laser manufacturing in principle can replace the first step of patterning by lithography for graphene device fabrication.
2. The defects generated under the sub-threshold condition by the femtosecond laser is first studied and demonstrated. The Raman mapping and analysis of defects, on the one hand, provided a detailed information for understanding the defects.
3. An absorption model has been developed to provide insights into the process of a Gaussian shaped laser pulse interacts with the SiO_2/Si substrate. To the best of the author's knowledge, this particular type of scenario has never been studied.

7.4.2 Contributions of the research

This research contributes to the following five aspects:

1. It has proved the selective removing of graphene from the SiO_2/Si substrate by the femtosecond laser. It is a valuable evidence to demonstrate the potential of the femtosecond laser in graphene patterning for device application.
2. It has proved that the D peak in the cutting edge was attributed to the graphene edges, rather than oxidation caused by laser processing under an ambient condition and a nitrogen condition. It demonstrates the operation environment of femtosecond laser manufacturing is relatively easier to attain, because the graphene devices won't be contaminated by oxidations in the ambient condition.
3. The research discovered femtosecond laser can induce the defects as well as control the defects. This demonstrates the controllability of using a femtosecond laser to achieve the surface modification of graphene.
4. An absorption model has been developed to provide a good insight on the absorption of the SiO_2/Si substrate. The numerical results can be used to explain the experimental observations.
5. The experimental and theoretical results all together create a positive step towards a practical femtosecond laser manufacturing for graphene devices.

7.5 Possible limitations

This thesis has highlighted the exotic properties of graphene and its potential applications in the next generation of high-performance electronics. To obtain graphene-based devices, the current leading methods of patterning graphene are selectively presented, including electron-beam irradiation, lithography methods, and chemical etching. Though these methods it can pattern graphene devices down to a nanoscale, as they are an expensive and time-consuming procedure, and could impede the upscaling of the development of the graphene market towards the industry. Ultrafast laser processing has the potential as a flexible and affordable manufacturing technique to pattern graphene and modifying graphene due to its limited thermal effect and high processing speed.

Femtosecond laser micromachining is a rapid process which unitises the ultrashort laser pulse properties to unprecedentedly control the desired microstructure of the materials without damaging the surroundings. However, as the highest resolution of femtosecond laser cutting is about 50 nm, it will be challenging to take it down to the nanoscale as with lithography methods.

7.6 Future work- femtosecond laser manufacturing system

This section proposes the femtosecond laser manufacturing system for industrial processing strategies towards graphene-based materials. The current challenges and crucial issues in designing and improving future investigation of the femtosecond laser integrated system graphene integrated devices are also discussed in this section. It will demonstrate the laser manufacturing, which is used in assisting graphene device applications for industrial scales production in a much broader way. This includes the work from this study in the femtosecond laser processing and other femtosecond laser techniques towards the graphene-based devices. Fig 7.1 has shown a strategy for femtosecond laser processing in graphene devices. Recent developments in femtosecond laser-related fabrication of a graphene device, and the state-of-the-art applications are listed. As mentioned before, the embedding of a femtosecond laser system could shorten the device fabrication process, and avoid contamination through the multiple patterning processes. In recent years, the femtosecond laser writing on graphene [237] and thinning of graphene [142] has been proved. This study's exploration of femtosecond laser ablation graphene, and the induced defects on the graphene surface on a SiO_2/Si substrate enlarges the role of the femtosecond laser in graphene device production. Besides this, the absorption model on the analysis of the graphene-SiO_2-Si system will enable the results to be analysed with a deeper understanding. The model can also be interpreted with femtosecond laser interaction (writing, ablation, thinning, surface modifications, etc.) with other substrates. These

processes can potentially unleash the graphene device potential in large-scale manufacturing under ambient conditions.

In Fig 7.1, the green boxes stand for the experimental discoveries in this thesis. From left to right, the potential femtosecond laser procedure includes femtosecond laser direct writing on graphene. Unlike the CVD growth of graphene, this process is facing the challenge of controlling the layers and quality of graphene. The femtosecond induced defect information may be considered during the controlling procedure. The next femtosecond laser application is the precise thinning of graphene layers one by one. For this astonishing femtosecond laser process can generate into at least two areas. First, this method can produce bilayer graphene in an efficient way, in which the bandgap can break down the barrier in graphene transistor applications. Second, such a method can also fabricate monolayer graphene to open up opportunities in manufacturing, at least, and reduce the waste of an unsuccessful growth of graphene in a particular layer in an environmental energy-saving way.

Last but not the least, this study addresses the manufacturing process of monolayer graphene on SiO_2/Si substrate on the right side of Fig 7.1. This is also the emphasised studied area in this research. This project mainly focused on the integrated femtosecond laser system in an energy-related field that can provide efficient, cost-effective, energy-saving ways towards producing a graphene device. In this project, it started from monolayer graphene deposited on a SiO_2/Si substrate. Currently, this type of graphene product can be easily pursed from the graphene producer. Though it is still in the stage of improvement in both quality and price reducing, monolayer graphene is the most convenient product as well as being most direct into graphene device application. In this research, the femtosecond laser has proved to be effective in removal, flexible patterning, and surface modification. This opens a successful femtosecond laser manufacturing rout towards graphene devices in a single step and a lithography-free manner.

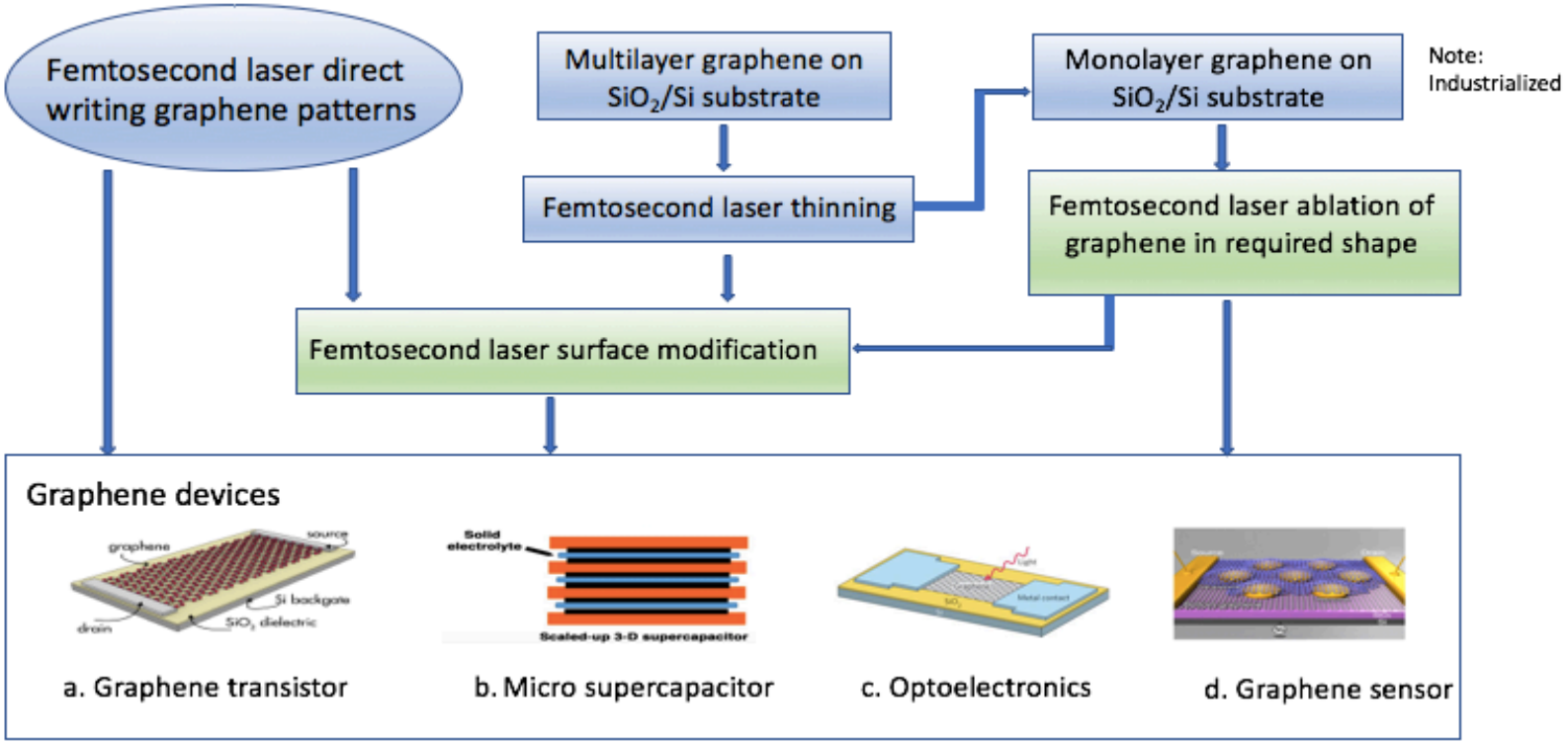

Fig 7. 1 The schematic illustration of femtosecond laser processing in graphene-based devices. a. graphene transistor [238]; b. micro supercapacitor [239]; c. Optoelectronics [63]; d. Graphene sensor [240]. The green boxes indicate the findings in this thesis.

References

[1] M. S. Dresselhaus and P. T. Araujo, 'Perspectives on the 2010 Nobel Prize in Physics for Graphene', *ACS Nano*, vol. 4, no. 11, pp. 6297–6302, Nov. 2010.

[2] K. S. Novoselov *et al.*, 'Electric Field Effect in Atomically Thin Carbon Films', *Science*, vol. 306, no. 5696, pp. 666–669, Oct. 2004.

[3] M.-Q. Yang, N. Zhang, and Y.-J. Xu, 'Synthesis of fullerene–, carbon nanotube–, and graphene–TiO2 nanocomposite photocatalysts for selective oxidation: a comparative study', *ACS Appl. Mater. Interfaces*, vol. 5, no. 3, pp. 1156–1164, 2013.

[4] A. Tiwari, *Graphene materials: fundamentals and emerging applications*. John Wiley & Sons, 2015.

[5] K. I. Bolotin *et al.*, 'Ultrahigh electron mobility in suspended graphene', *Solid State Commun.*, vol. 146, no. 9–10, pp. 351–355, Jun. 2008.

[6] G. Anagnostopoulos *et al.*, 'Mechanical Stability of Flexible Graphene-Based Displays', *ACS Appl. Mater. Interfaces*, vol. 8, no. 34, pp. 22605–22614, Aug. 2016.

[7] L. A. Falkovsky, 'Optical properties of graphene', *J. Phys. Conf. Ser.*, vol. 129, p. 012004, Oct. 2008.

[8] Y. Zhang, Y.-W. Tan, H. L. Stormer, and P. Kim, 'Experimental observation of quantum Hall effect and Berry's phase in graphene', *ArXiv Prepr. Cond-Mat0509355*, 2005.

[9] F. Xia, T. Mueller, Y. Lin, and P. Avouris, 'Ultrafast graphene photodetector', in *Lasers and Electro-Optics (CLEO) and Quantum Electronics and Laser Science Conference (QELS), 2010 Conference on*, 2010, pp. 1–2.

[10] A. Tzalenchuk *et al.*, 'Quantum Resistance Standard Based on Epitaxial Graphene', *ArXiv Prepr. ArXiv09091220*, 2009.

[11] B. Cho *et al.*, 'Graphene-based gas sensor: metal decoration effect and application to a flexible device', *J. Mater. Chem. C*, vol. 2, no. 27, pp. 5280–5285, 2014.

[12] A. A. Tseng, K. Chen, C. D. Chen, and K. J. Ma, 'Electron beam lithography in nanoscale fabrication: recent development', *IEEE Trans. Electron. Packag. Manuf.*, vol. 26, no. 2, pp. 141–149, 2003.

[13] K. Sugioka and Y. Cheng, 'Ultrafast lasers—reliable tools for advanced materials processing', *Light Sci. Appl.*, vol. 3, no. 4, p. e149, 2014.

[14] A. Roberts, D. Cormode, C. Reynolds, T. Newhouse-Illige, B. J. LeRoy, and A. S. Sandhu, 'Response of graphene to femtosecond high-intensity laser irradiation', *Appl. Phys. Lett.*, vol. 99, no. 5, p. 051912, 2011.

[15] W. Zhang *et al.*, 'Ti: sapphire femtosecond laser direct micro-cutting and profiling of graphene', *Appl. Phys. A*, vol. 109, no. 2, pp. 291–297, 2012.

[16] R. Sahin, E. Simsek, and S. Akturk, 'Nanoscale patterning of graphene through femtosecond laser ablation', *Appl. Phys. Lett.*, vol. 104, no. 5, p. 053118, 2014.

[17] M. Kemp, 'Unlocking the potential of graphenes for the development of multi-scale composites–Functionalization via plasma', *Reinf. Plast.*, vol. 60, no. 5, pp. 332–334, 2016.

[18] S. Zhu, F. Luo, B. Zhu, and G.-X. Wang, 'Toxicological effects of graphene oxide on Saccharomyces cerevisiae', *Toxicol. Res.*, 2017.

[19] M. Srivastava, J. Singh, T. Kuila, R. K. Layek, N. H. Kim, and J. H. Lee, 'Recent advances in graphene and its metal-oxide hybrid nanostructures for lithium-ion batteries', *Nanoscale*, vol. 7, no. 11, pp. 4820–4868, 2015.

[20] A. Saini, 'EU Graphene Flagship project aims for technological breakthroughs', *Mrs Bull.*, vol. 39, no. 5, p. 393, 2014.

[21] P. Sallomi and P. Lee, *Technology, Media, & Telecommunications Predictions 2016*. Deloitte, 2016.

[22] S. Ghosh *et al.*, 'Extremely high thermal conductivity of graphene: Prospects for thermal management applications in nanoelectronic circuits', *Appl. Phys. Lett.*, vol. 92, no. 15, p. 151911, 2008.

[23] A. D. Bernardo *et al.*, '*p*-wave triggered superconductivity in single-layer graphene on an electron-doped oxide superconductor', *Nat. Commun.*, vol. 8, p. ncomms14024, Jan. 2017.

[24] J. Hassoun *et al.*, 'An advanced lithium-ion battery based on a graphene anode and a lithium iron phosphate cathode', *Nano Lett.*, vol. 14, no. 8, pp. 4901–4906, 2014.

[25] K. S. Novoselov, 'Nobel lecture: Graphene: Materials in the flatland', *Rev. Mod. Phys.*, vol. 83, no. 3, p. 837, 2011.

[26] M. Yi and Z. Shen, 'A review on mechanical exfoliation for the scalable production of graphene', *J. Mater. Chem. A*, vol. 3, no. 22, pp. 11700–11715, 2015.

[27] W. Liu, H. Li, C. Xu, Y. Khatami, and K. Banerjee, 'Synthesis of high-quality monolayer and bilayer graphene on copper using chemical vapor deposition', *Carbon*, vol. 49, no. 13, pp. 4122–4130, 2011.

[28] C. Miao, C. Zheng, O. Liang, and Y.-H. Xie, 'Chemical vapor deposition of graphene', in *Physics and applications of graphene-experiments*, InTech, 2011.

[29] C. Mattevi, H. Kim, and M. Chhowalla, 'A review of chemical vapour deposition of graphene on copper', *J. Mater. Chem.*, vol. 21, no. 10, pp. 3324–3334, 2011.

[30] J. N. Coleman, 'Liquid-phase exfoliation of nanotubes and graphene', *Adv. Funct. Mater.*, vol. 19, no. 23, pp. 3680–3695, 2009.

[31] Y. Hernandez *et al.*, 'High-yield production of graphene by liquid-phase exfoliation of graphite', *Nat. Nanotechnol.*, vol. 3, no. 9, pp. 563–568, 2008.

[32] M. Lotya *et al.*, 'Liquid phase production of graphene by exfoliation of graphite in surfactant/water solutions', *J. Am. Chem. Soc.*, vol. 131, no. 10, pp. 3611–3620, 2009.

[33] V. Y. Aristov *et al.*, 'Graphene synthesis on cubic SiC/Si wafers. Perspectives for mass production of graphene-based electronic devices', *Nano Lett.*, vol. 10, no. 3, pp. 992–995, 2010.

[34] Z. G. Cambaz, G. Yushin, S. Osswald, V. Mochalin, and Y. Gogotsi, 'Noncatalytic synthesis of carbon nanotubes, graphene and graphite on SiC', *Carbon*, vol. 46, no. 6, pp. 841–849, 2008.

[35] Z.-Y. Juang *et al.*, 'Synthesis of graphene on silicon carbide substrates at low temperature', *Carbon*, vol. 47, no. 8, pp. 2026–2031, 2009.

[36] A. Hirsch, 'Unzipping carbon nanotubes: a peeling method for the formation of graphene nanoribbons', *Angew. Chem. Int. Ed.*, vol. 48, no. 36, pp. 6594–6596, 2009.

[37] L. Jiao, L. Zhang, X. Wang, G. Diankov, and H. Dai, 'Narrow graphene nanoribbons from carbon nanotubes', *Nature*, vol. 458, no. 7240, pp. 877–880, 2009.

[38] J. Park *et al.*, 'Epitaxial graphene growth by carbon molecular beam epitaxy (CMBE)', *Adv. Mater.*, vol. 22, no. 37, pp. 4140–4145, 2010.

[39] E. Moreau, F. J. Ferrer, D. Vignaud, S. Godey, and X. Wallart, 'Graphene growth by molecular beam epitaxy using a solid carbon source', *Phys. Status Solidi A*, vol. 207, no. 2, pp. 300–303, 2010.

[40] L. T. Le, M. H. Ervin, H. Qiu, B. E. Fuchs, and W. Y. Lee, 'Graphene supercapacitor electrodes fabricated by inkjet printing and thermal reduction of graphene oxide', *Electrochem. Commun.*, vol. 13, no. 4, pp. 355–358, 2011.

[41] S. Pei, J. Zhao, J. Du, W. Ren, and H.-M. Cheng, 'Direct reduction of graphene oxide films into highly conductive and flexible graphene films by hydrohalic acids', *Carbon*, vol. 48, no. 15, pp. 4466–4474, 2010.

[42] Y. Zhu *et al.*, 'Graphene and graphene oxide: synthesis, properties, and applications', *Adv. Mater.*, vol. 22, no. 35, pp. 3906–3924, 2010.

[43] A. N. Obraztsov, 'Chemical vapour deposition: making graphene on a large scale', *Nat. Nanotechnol.*, vol. 4, no. 4, pp. 212–213, 2009.

[44] M. Losurdo, M. M. Giangregorio, P. Capezzuto, and G. Bruno, 'Graphene CVD growth on copper and nickel: role of hydrogen in kinetics and structure', *Phys. Chem. Chem. Phys.*, vol. 13, no. 46, pp. 20836–20843, 2011.

[45] H. Matsunami and T. Kimoto, 'Step-controlled epitaxial growth of SiC: High quality homoepitaxy', *Mater. Sci. Eng. R Rep.*, vol. 20, no. 3, pp. 125–166, 1997.

[46] D. V. Kosynkin *et al.*, 'Longitudinal unzipping of carbon nanotubes to form graphene nanoribbons', *Nature*, vol. 458, no. 7240, pp. 872–876, 2009.

[47] S. Stankovich *et al.*, 'Synthesis of graphene-based nanosheets via chemical reduction of exfoliated graphite oxide', *carbon*, vol. 45, no. 7, pp. 1558–1565, 2007.

[48] D. J. Lipomi, J. A. Lee, M. Vosgueritchian, B. C.-K. Tee, J. A. Bolander, and Z. Bao, 'Electronic Properties of Transparent Conductive Films of PEDOT:PSS on Stretchable Substrates', *Chem. Mater.*, vol. 24, no. 2, pp. 373–382, Jan. 2012.

[49] Z. SUN *et al.*, 'Ultrafast fiber laser mode-locked by graphene based saturable absorber', in *Conference on Lasers and Electro-Optics*, 2010, p. CTuR1.

[50] D. Li and R. B. Kaner, 'Graphene-based materials', *Nat Nanotechnol*, vol. 3, p. 101, 2008.

[51] M. Pumera, A. Ambrosi, A. Bonanni, E. L. K. Chng, and H. L. Poh, 'Graphene for electrochemical sensing and biosensing', *TrAC Trends Anal. Chem.*, vol. 29, no. 9, pp. 954–965, Oct. 2010.

[52] M. Miao and J. H. Xin, *Engineering of High-Performance Textiles*. Woodhead Publishing, 2017.

[53] R. W. Powell, C. Y. Ho, and P. E. Liley, 'Thermal conductivity of selected materials', NATIONAL STANDARD REFERENCE DATA SYSTEM, 1966.

[54] M. Sharon and M. Sharon, *Graphene: An Introduction to the Fundamentals and Industrial Applications*. John Wiley & Sons, 2015.

[55] D. Mandal, R. Kar, S. Das, and B. K. Panigrahi, *Intelligent Computing and Applications: Proceedings of the International Conference on ICA, 22-24 December 2014*. Springer, 2015.

[56] G. W. Ludwig and R. L. Watters, 'Drift and Conductivity Mobility in Silicon', *Phys. Rev.*, vol. 101, no. 6, pp. 1699–1701, Mar. 1956.

[57] R. R. Nair *et al.*, 'Fine Structure Constant Defines Visual Transparency of Graphene', *Science*, vol. 320, no. 5881, pp. 1308–1308, Jun. 2008.

[58] K. F. Mak, M. Y. Sfeir, Y. Wu, C. H. Lui, J. A. Misewich, and T. F. Heinz, 'Measurement of the Optical Conductivity of Graphene', *Phys. Rev. Lett.*, vol. 101, no. 19, p. 196405, Nov. 2008.

[59] R. Kitamura, L. Pilon, and M. Jonasz, 'Optical constants of silica glass from extreme ultraviolet to far infrared at near room temperature', *Appl. Opt.*, vol. 46, no. 33, pp. 8118–8133, 2007.

[60] H. Tian *et al.*, 'Scalable fabrication of high-performance and flexible graphene strain sensors', *Nanoscale*, vol. 6, no. 2, pp. 699–705, 2014.

[61] J. Zhao *et al.*, 'Ultra-sensitive strain sensors based on piezoresistive nanographene films', *Appl. Phys. Lett.*, vol. 101, no. 6, p. 063112, 2012.

[62] K. F. Mak, L. Ju, F. Wang, and T. F. Heinz, 'Optical spectroscopy of graphene: from the far infrared to the ultraviolet', *Solid State Commun.*, vol. 152, no. 15, pp. 1341–1349, 2012.

[63] F. Bonaccorso, Z. Sun, T. Hasan, and A. C. Ferrari, 'Graphene photonics and optoelectronics', *Nat. Photonics*, vol. 4, no. 9, pp. 611–622, Sep. 2010.

[64] D. Schall *et al.*, '50 GBit/s photodetectors based on wafer-scale graphene for integrated silicon photonic communication systems', *Acs Photonics*, vol. 1, no. 9, pp. 781–784, 2014.

[65] M. F. El-Kady and R. B. Kaner, 'Scalable fabrication of high-power graphene micro-supercapacitors for flexible and on-chip energy storage', *Nat. Commun.*, vol. 4, p. 1475, Feb. 2013.

[66] K. S. Novoselov *et al.*, 'Electric field effect in atomically thin carbon films', *science*, vol. 306, no. 5696, pp. 666–669, 2004.

[67] A. H. Castro Neto, N. M. R. Peres, K. S. Novoselov, and A. K. Geim, 'The electronic properties of graphene', *Rev. Mod. Phys.*, vol. 81, no. 1, pp. 109–162, Jan. 2009.

[68] Y.-W. Son, M. L. Cohen, and S. G. Louie, 'Energy Gaps in Graphene Nanoribbons', *Phys. Rev. Lett.*, vol. 97, no. 21, p. 216803, Nov. 2006.

[69] X. Li, X. Wang, L. Zhang, S. Lee, and H. Dai, 'Chemically Derived, Ultrasmooth Graphene Nanoribbon Semiconductors', *Science*, vol. 319, no. 5867, pp. 1229–1232, Feb. 2008.

[70] Z. Chen, Y.-M. Lin, M. J. Rooks, and P. Avouris, 'Graphene nano-ribbon electronics', *Phys. E Low-Dimens. Syst. Nanostructures*, vol. 40, no. 2, pp. 228–232, 2007.

[71] L. Yang, C.-H. Park, Y.-W. Son, M. L. Cohen, and S. G. Louie, 'Quasiparticle Energies and Band Gaps in Graphene Nanoribbons', *Phys. Rev. Lett.*, vol. 99, no. 18, p. 186801, Nov. 2007.

[72] M. Evaldsson, I. V. Zozoulenko, H. Xu, and T. Heinzel, 'Edge-disorder-induced Anderson localization and conduction gap in graphene nanoribbons', *Phys. Rev. B*, vol. 78, no. 16, p. 161407, 2008.

[73] P. Gava, M. Lazzeri, A. M. Saitta, and F. Mauri, 'Ab initio study of gap opening and screening effects in gated bilayer graphene', *Phys. Rev. B*, vol. 79, no. 16, p. 165431, 2009.

[74] T. Ohta, A. Bostwick, T. Seyller, K. Horn, and E. Rotenberg, 'Controlling the electronic structure of bilayer graphene', *Science*, vol. 313, no. 5789, pp. 951–954, 2006.

[75] Y. Zhang *et al.*, 'Direct observation of a widely tunable bandgap in bilayer graphene', *Nature*, vol. 459, no. 7248, pp. 820–823, 2009.

[76] K. Kostarelos and K. S. Novoselov, 'Graphene devices for life', *Nat. Nanotechnol.*, vol. 9, no. 10, pp. 744–745, Oct. 2014.

[77] R. Verma, B. D. Gupta, and R. Jha, 'Sensitivity enhancement of a surface plasmon resonance based biomolecules sensor using graphene and silicon layers', *Sens. Actuators B Chem.*, vol. 160, no. 1, pp. 623–631, 2011.

[78] V. C. Sanchez, A. Jachak, R. H. Hurt, and A. B. Kane, 'Biological interactions of graphene-family nanomaterials: an interdisciplinary review', *Chem. Res. Toxicol.*, vol. 25, no. 1, pp. 15–34, 2011.

[79] S.-R. Ryoo, Y.-K. Kim, M.-H. Kim, and D.-H. Min, 'Behaviors of NIH-3T3 fibroblasts on graphene/carbon nanotubes: proliferation, focal adhesion, and gene transfection studies', *ACS Nano*, vol. 4, no. 11, pp. 6587–6598, 2010.

[80] M. Kalbacova, A. Broz, J. Kong, and M. Kalbac, 'Graphene substrates promote adherence of human osteoblasts and mesenchymal stromal cells', *Carbon*, vol. 48, no. 15, pp. 4323–4329, 2010.

[81] N. Li *et al.*, 'The promotion of neurite sprouting and outgrowth of mouse hippocampal cells in culture by graphene substrates', *Biomaterials*, vol. 32, no. 35, pp. 9374–9382, 2011.

[82] W. C. Lee *et al.*, 'Origin of enhanced stem cell growth and differentiation on graphene and graphene oxide', *ACS Nano*, vol. 5, no. 9, pp. 7334–7341, 2011.

[83] S. Goenka, V. Sant, and S. Sant, 'Graphene-based nanomaterials for drug delivery and tissue engineering', *J. Controlled Release*, vol. 173, pp. 75–88, 2014.

[84] P. Huang *et al.*, 'On-chip and freestanding elastic carbon films for micro-supercapacitors', *Science*, vol. 351, no. 6274, pp. 691–695, Feb. 2016.

[85] H. Kim, K.-Y. Park, J. Hong, and K. Kang, 'All-graphene-battery: bridging the gap between supercapacitors and lithium ion batteries', *Sci. Rep.*, vol. 4, p. 5278, Jun. 2014.

[86] J. Liu *et al.*, 'Co3O4 Nanowire@ MnO2 Ultrathin Nanosheet Core/Shell Arrays: A New Class of High-Performance Pseudocapacitive Materials', *Adv. Mater.*, vol. 23, no. 18, pp. 2076–2081, 2011.

[87] Y. Ma, H. Chang, M. Zhang, and Y. Chen, 'Graphene-Based Materials for Lithium-Ion Hybrid Supercapacitors', *Adv. Mater.*, vol. 27, no. 36, pp. 5296–5308, 2015.

[88] J. K. Lee, K. B. Smith, C. M. Hayner, and H. H. Kung, 'Silicon nanoparticles–graphene paper composites for Li ion battery anodes', *Chem. Commun.*, vol. 46, no. 12, pp. 2025–2027, 2010.

[89] M. F. El-Kady, V. Strong, S. Dubin, and R. B. Kaner, 'Laser scribing of high-performance and flexible graphene-based electrochemical capacitors', *Science*, vol. 335, no. 6074, pp. 1326–1330, 2012.

[90] C. Liu, Z. Yu, D. Neff, A. Zhamu, and B. Z. Jang, 'Graphene-based supercapacitor with an ultrahigh energy density', *Nano Lett.*, vol. 10, no. 12, pp. 4863–4868, 2010.

[91] F. Wen *et al.*, 'Enhanced laser scribed flexible graphene-based micro-supercapacitor performance with reduction of carbon nanotubes diameter', *Carbon*, vol. 75, pp. 236–243, 2014.

[92] D. Teweldebrhan and A. A. Balandin, 'Modification of graphene properties due to electron-beam irradiation', *Appl. Phys. Lett.*, vol. 94, no. 1, p. 013101, 2009.

[93] A. C. Ferrari *et al.*, 'Raman spectrum of graphene and graphene layers', *Phys. Rev. Lett.*, vol. 97, no. 18, p. 187401, 2006.

[94] Z. H. Ni, T. Yu, Y. H. Lu, Y. Y. Wang, Y. P. Feng, and Z. X. Shen, 'Uniaxial strain on graphene: Raman spectroscopy study and band-gap opening', *ACS Nano*, vol. 2, no. 11, pp. 2301–2305, 2008.

[95] D. L. Andrews, *Molecular photophysics and spectroscopy*. Morgan & Claypool Publishers, 2014.

[96] J. W. Lichtman and J.-A. Conchello, 'Fluorescence microscopy', *Nat. Methods*, vol. 2, no. 12, pp. 910–919, 2005.

[97] B. Valeur and M. N. Berberan-Santos, *Molecular fluorescence: principles and applications*. John Wiley & Sons, 2012.

[98] I. Childres, L. A. Jauregui, W. Park, H. Cao, and Y. P. Chen, 'Raman spectroscopy of graphene and related materials', *New Dev. Photon Mater. Res.*, pp. 1–20, 2013.

[99] R. Beams, L. G. Cançado, and L. Novotny, 'Raman characterization of defects and dopants in graphene', *J. Phys. Condens. Matter*, vol. 27, no. 8, p. 083002, 2015.

[100] J.-A. Yan, W. Y. Ruan, and M. Y. Chou, 'Phonon dispersions and vibrational properties of monolayer, bilayer, and trilayer graphene: Density-functional perturbation theory', *Phys. Rev. B*, vol. 77, no. 12, p. 125401, 2008.

[101] D. L. Mafra *et al.*, 'Determination of LA and TO phonon dispersion relations of graphene near the Dirac point by double resonance Raman scattering', *Phys. Rev. B*, vol. 76, no. 23, p. 233407, 2007.

[102] J.-C. Charlier and S. Roche, 'Electronic and transport properties of nanotubes', *Rev. Mod. Phys.*, vol. 79, no. 2, pp. 677–732, May 2007.

[103] A. C. Ferrari and J. Robertson, 'Interpretation of Raman spectra of disordered and amorphous carbon', *Phys. Rev. B*, vol. 61, no. 20, p. 14095, 2000.

[104] Y. Kim, 'Magneto-Raman Spectroscopy of Graphene and Graphite', 2012.

[105] C. Thomsen and S. Reich, 'Double resonant Raman scattering in graphite', *Phys. Rev. Lett.*, vol. 85, no. 24, p. 5214, 2000.

[106] M. S. Dresselhaus, A. Jorio, A. G. Souza Filho, and R. Saito, 'Defect characterization in graphene and carbon nanotubes using Raman spectroscopy', *Philos. Trans. R. Soc. Lond. Math. Phys. Eng. Sci.*, vol. 368, no. 1932, pp. 5355–5377, 2010.

[107] K. N. Kudin, B. Ozbas, H. C. Schniepp, R. K. Prud'Homme, I. A. Aksay, and R. Car, 'Raman spectra of graphite oxide and functionalized graphene sheets', *Nano Lett.*, vol. 8, no. 1, pp. 36–41, 2008.

[108] O. Lehtinen, J. Kotakoski, A. V. Krasheninnikov, and J. Keinonen, 'Cutting and controlled modification of graphene with ion beams', *Nanotechnology*, vol. 22, no. 17, p. 175306, 2011.

[109] Y.-C. Lin, C.-Y. Lin, and P.-W. Chiu, 'Controllable graphene N-doping with ammonia plasma', *Appl. Phys. Lett.*, vol. 96, no. 13, p. 133110, 2010.

[110] D. Teweldebrhan and A. A. Balandin, 'Modification of graphene properties due to electron-beam irradiation', *Appl. Phys. Lett.*, vol. 94, no. 1, p. 013101, 2009.

[111] A. Hashimoto, K. Suenaga, A. Gloter, K. Urita, and S. Iijima, 'Direct evidence for atomic defects in graphene layers', *Nature*, vol. 430, no. 7002, pp. 870–873, 2004.

[112] I. Childres *et al.*, 'Effect of electron-beam irradiation on graphene field effect devices', *Appl. Phys. Lett.*, vol. 97, no. 17, p. 173109, 2010.

[113] A. Eckmann *et al.*, 'Probing the nature of defects in graphene by Raman spectroscopy', *Nano Lett.*, vol. 12, no. 8, pp. 3925–3930, 2012.

[114] A. C. Ferrari and D. M. Basko, 'Raman spectroscopy as a versatile tool for studying the properties of graphene', *Nat. Nanotechnol.*, vol. 8, no. 4, pp. 235–246, Apr. 2013.

[115] M. A. Pimenta, G. Dresselhaus, M. S. Dresselhaus, L. G. Cancado, A. Jorio, and R. Saito, 'Studying disorder in graphite-based systems by Raman spectroscopy', *Phys. Chem. Chem. Phys.*, vol. 9, no. 11, pp. 1276–1290, 2007.

[116] C. Casiraghi *et al.*, 'Raman spectroscopy of graphene edges', *Nano Lett.*, vol. 9, no. 4, pp. 1433–1441, 2009.

[117] L. M. Malard, M. A. A. Pimenta, G. Dresselhaus, and M. S. Dresselhaus, 'Raman spectroscopy in graphene', *Phys. Rep.*, vol. 473, no. 5, pp. 51–87, 2009.

[118] Z. Luo, C. Cong, J. Zhang, Q. Xiong, and T. Yu, 'The origin of sub-bands in the Raman D-band of graphene', *Carbon*, vol. 50, no. 11, pp. 4252–4258, 2012.

[119] V. Zolyomi, J. Kürti, A. Grüneis, and H. Kuzmany, 'Origin of the fine structure of the Raman D band in single-wall carbon nanotubes', *Phys. Rev. Lett.*, vol. 90, no. 15, p. 157401, 2003.

[120] J. C. Meyer, C. O. Girit, M. F. Crommie, and A. Zettl, 'Hydrocarbon lithography on graphene membranes', *Appl. Phys. Lett.*, vol. 92, no. 12, p. 123110, 2008.

[121] M. D. Fischbein and M. Drndić, 'Electron beam nanosculpting of suspended graphene sheets', *Appl. Phys. Lett.*, vol. 93, no. 11, p. 113107, Sep. 2008.

[122] B. Song, G. F. Schneider, Q. Xu, G. Pandraud, C. Dekker, and H. Zandbergen, 'Atomic-Scale Electron-Beam Sculpting of Near-Defect-Free Graphene Nanostructures', *Nano Lett.*, vol. 11, no. 6, pp. 2247–2250, Jun. 2011.

[123] J. Feng, W. Li, X. Qian, J. Qi, L. Qi, and J. Li, 'Patterning of graphene', *Nanoscale*, vol. 4, no. 16, pp. 4883–4899, 2012.

[124] F. Börrnert, L. Fu, S. Gorantla, M. Knupfer, B. Büchner, and M. H. Rümmeli, 'Programmable Sub-nanometer Sculpting of Graphene with Electron Beams', *ACS Nano*, vol. 6, no. 11, pp. 10327–10334, Nov. 2012.

[125] W. Xu and T.-W. Lee, 'Recent progress in fabrication techniques of graphene nanoribbons', *Mater. Horiz.*, vol. 3, no. 3, pp. 186–207, 2016.

[126] J. I. Paredes, S. Villar-Rodil, P. Solís-Fernández, A. Martínez-Alonso, and J. M. D. Tascon, 'Atomic force and scanning tunneling microscopy imaging of graphene nanosheets derived from graphite oxide', *Langmuir*, vol. 25, no. 10, pp. 5957–5968, 2009.

[127] L. Tapasztó, G. Dobrik, P. Lambin, and L. P. Biró, 'Tailoring the atomic structure of graphene nanoribbons by scanning tunnelling microscope lithography', *Nat. Nanotechnol.*, vol. 3, no. 7, pp. 397–401, Jul. 2008.

[128] M. C. Lemme *et al.*, 'Etching of graphene devices with a helium ion beam', *ACS Nano*, vol. 3, no. 9, pp. 2674–2676, 2009.

[129] A. N. Abbas *et al.*, 'Patterning, characterization, and chemical sensing applications of graphene nanoribbon arrays down to 5 nm using helium ion beam lithography', *ACS Nano*, vol. 8, no. 2, pp. 1538–1546, 2014.

[130] C. M. Weber, C. N. Berglund, and P. Gabella, 'Mask cost and profitability in photomask manufacturing: An empirical analysis', *Semicond. Manuf. IEEE Trans. On*, vol. 19, no. 4, pp. 465–474, 2006.

[131] C. Thiele *et al.*, 'Electron-beam-induced direct etching of graphene', *Carbon*, vol. 64, pp. 84–91, 2013.

[132] C. Stampfer, J. Güttinger, F. Molitor, D. Graf, T. Ihn, and K. Ensslin, 'Tunable Coulomb blockade in nanostructured graphene', *Appl. Phys. Lett.*, vol. 92, no. 1, p. 012102, Jan. 2008.

[133] L. Xie, L. Jiao, and H. Dai, 'Selective Etching of Graphene Edges by Hydrogen Plasma', *J. Am. Chem. Soc.*, vol. 132, no. 42, pp. 14751–14753, Oct. 2010.

[134] A. Dimiev, D. V. Kosynkin, A. Sinitskii, A. Slesarev, Z. Sun, and J. M. Tour, 'Layer-by-Layer Removal of Graphene for Device Patterning', *Science*, vol. 331, no. 6021, pp. 1168–1172, Mar. 2011.

[135] S. Dhar *et al.*, 'A new route to graphene layers by selective laser ablation', *AIP Adv.*, vol. 1, no. 2, p. 022109, 2011.

[136] J. Li, T.-F. Chung, Y. P. Chen, and G. J. Cheng, 'Nanoscale Strainability of Graphene by Laser Shock-Induced Three-Dimensional Shaping', *Nano Lett.*, vol. 12, no. 9, pp. 4577–4583, 2012.

[137] J. Li, G. J. Cheng, R. Zhang, and H. Jiang, 'Laser Shock Induced Nano-Patterning of Graphene', pp. 545–551, Jun. 2012.

[138] S. Lee *et al.*, 'Laser-Synthesized Epitaxial Graphene', *ACS Nano*, vol. 4, no. 12, pp. 7524–7530, Dec. 2010.

[139] M. Currie *et al.*, 'Quantifying pulsed laser induced damage to graphene', *Appl. Phys. Lett.*, vol. 99, no. 21, p. 211909, 2011.

[140] A. Roberts, D. Cormode, C. Reynolds, T. Newhouse-Illige, B. J. LeRoy, and A. S. Sandhu, 'Response of graphene to femtosecond high-intensity laser irradiation', *Appl. Phys. Lett.*, vol. 99, no. 5, p. 051912, Aug. 2011.

[141] Z. Lin *et al.*, 'Precise Control of the Number of Layers of Graphene by Picosecond Laser Thinning', *Sci. Rep.*, vol. 5, p. 11662, Jun. 2015.

[142] D. W. Li, Y. S. Zhou, X. Huang, L. Jiang, J.-F. Silvain, and Y. F. Lu, 'In situ imaging and control of layer-by-layer femtosecond laser thinning of graphene', *Nanoscale*, vol. 7, no. 8, pp. 3651–3659, Feb. 2015.

[143] W. Zhang *et al.*, 'Ti:sapphire femtosecond laser direct micro-cutting and profiling of graphene', *Appl. Phys. A*, vol. 109, no. 2, pp. 291–297, Nov. 2012.

[144] R. Sahin, E. Simsek, and S. Akturk, 'Nanoscale patterning of graphene through femtosecond laser ablation', *Appl. Phys. Lett.*, vol. 104, no. 5, p. 053118, Feb. 2014.

[145] B. E. Saleh, M. C. Teich, and B. E. Saleh, *Fundamentals of photonics*, vol. 22. Wiley New York, 1991.

[146] M. D. Shirk and P. A. Molian, 'A review of ultrashort pulsed laser ablation of materials', *J. Laser Appl.*, vol. 10, no. 1, pp. 18–28, Feb. 1998.

[147] M. v Allmen, 'Laser-beam interactions with materials', 1987.

[148] M. S. Brown and C. B. Arnold, 'Fundamentals of Laser-Material Interaction and Application to Multiscale Surface Modification', in *Laser Precision Microfabrication*, Springer, 2010, pp. 91–120.

[149] M. A. Ordal *et al.*, 'Optical properties of the metals al, co, cu, au, fe, pb, ni, pd, pt, ag, ti, and w in the infrared and far infrared', *Appl. Opt.*, vol. 22, no. 7, pp. 1099–1119, 1983.

[150] P. Gibbon, *Short pulse laser interactions with matter*. World Scientific Publishing Company, 2004.

[151] D. Fisher, M. Fraenkel, Z. Henis, E. Moshe, and S. Eliezer, 'Interband and intraband (Drude) contributions to femtosecond laser absorption in aluminum', *Phys. Rev. E*, vol. 65, no. 1, p. 016409, Dec. 2001.

[152] H. Ehrenreich, H. R. Philipp, and B. Segall, 'Optical properties of aluminum', *Phys. Rev.*, vol. 132, no. 5, p. 1918, 1963.

[153] F. Costache, M. Henyk, and J. Reif, 'Surface patterning on insulators upon femtosecond laser ablation', *Appl. Surf. Sci.*, vol. 208, pp. 486–491, 2003.

[154] J. D. Musgraves, K. Richardson, and H. Jain, 'Laser-induced structural modification, its mechanisms, and applications in glassy optical materials', *Opt. Mater. Express*, vol. 1, no. 5, pp. 921–935, 2011.

[155] V. S. Letokhov and V. P. Chebotayev, *Nonlinear laser spectroscopy*, vol. 4. Not Avail, 1977.

[156] Y.-R. Shen, 'The principles of nonlinear optics', *N. Y. Wiley-Intersci. 1984 575 P*, vol. 1, 1984.

[157] P. P. Pronko *et al.*, 'Avalanche ionization and dielectric breakdown in silicon with ultrafast laser pulses', *Phys. Rev. B*, vol. 58, no. 5, p. 2387, 1998.

[158] E. Yablonovitch and N. Bloembergen, 'Avalanche ionization and the limiting diameter of filaments induced by light pulses in transparent media', *Phys. Rev. Lett.*, vol. 29, no. 14, p. 907, 1972.

[159] J. K. Chen, D. Y. Tzou, and J. E. Beraun, 'A semiclassical two-temperature model for ultrafast laser heating', *Int. J. Heat Mass Transf.*, vol. 49, no. 1, pp. 307–316, Jan. 2006.

[160] L. Jiang and H.-L. Tsai, 'Improved Two-Temperature Model and Its Application in Ultrashort Laser Heating of Metal Films', *J. Heat Transf.*, vol. 127, no. 10, pp. 1167–1173, Jun. 2005.

[161] A. Vogel, J. Noack, G. Hüttman, and G. Paltauf, 'Mechanisms of femtosecond laser nanosurgery of cells and tissues', *Appl. Phys. B*, vol. 81, no. 8, pp. 1015–1047, Dec. 2005.

[162] D. W. Bäuerle, *Laser processing and chemistry*. Springer Science & Business Media, 2013.

[163] C. Earl, J. R. Castrejón-Pita, P. A. Hilton, and W. O'Neill, 'The dynamics of laser surface modification', *J. Manuf. Process.*, vol. 21, no. Supplement C, pp. 214–223, Jan. 2016.

[164] B. Rethfeld, D. S. Ivanov, M. E. Garcia, and S. I. Anisimov, 'Modelling ultrafast laser ablation', *J. Phys. Appl. Phys.*, vol. 50, no. 19, p. 193001, May 2017.

[165] R. D. Murphy, 'Femtosecond Laser Interactions at Interfaces and Their Applications.', 2013.

[166] D. Kawamura, A. Takita, Y. Hayasaki, and N. Nishida, 'Method for reducing debris and thermal destruction in femtosecond laser processing by applying transparent coating', *Appl. Phys. Mater. Sci. Process.*, vol. 82, no. 3, pp. 523–527, 2006.

[167] J. M. Vadillo, J. M. Fernandez Romero, C. Rodriguez, and J. J. Laserna, 'Effect of plasma shielding on laser ablation rate of pure metals at reduced pressure', *Surf. Interface Anal.*, vol. 27, no. 11, pp. 1009–1015, 1999.

[168] R. Le Harzic *et al.*, 'Comparison of heat-affected zones due to nanosecond and femtosecond laser pulses using transmission electronic microscopy', *Appl. Phys. Lett.*, vol. 80, no. 21, pp. 3886–3888, 2002.

[169] X. Liu, D. Du, and G. Mourou, 'Laser ablation and micromachining with ultrashort laser pulses', *IEEE J. Quantum Electron.*, vol. 33, no. 10, pp. 1706–1716, 1997.

[170] L. Lucas and J. Zhang, 'Femtosecond laser micromachining: a back-to-basics primer', *Appl. Energ.*, 2012.

[171] F. Korte *et al.*, 'Towards nanostructuring with femtosecond laser pulses', *Appl. Phys. A*, vol. 77, no. 2, pp. 229–235, 2003.

[172] D. Breitling, A. Ruf, and F. Dausinger, 'Fundamental aspects in machining of metals with short and ultrashort laser pulses', in *Lasers and Applications in Science and Engineering*, 2004, pp. 49–63.

[173] D. Giguère *et al.*, 'Laser ablation threshold dependence on pulse duration for fused silica and corneal tissues: experiments and modeling', *JOSA A*, vol. 24, no. 6, pp. 1562–1568, 2007.

[174] S. Nolte *et al.*, 'Ablation of metals by ultrashort laser pulses', *JOSA B*, vol. 14, no. 10, pp. 2716–2722, Oct. 1997.

[175] B. Zheng, G. Jiang, W. Wang, K. Wang, and X. Mei, 'Ablation experiment and threshold calculation of titanium alloy irradiated by ultra-fast pulse laser', *AIP Adv.*, vol. 4, no. 3, p. 031310, Mar. 2014.

[176] D. Ashkenasi, M. Lorenz, R. Stoian, and A. Rosenfeld, 'Surface damage threshold and structuring of dielectrics using femtosecond laser pulses: the role of incubation', *Appl. Surf. Sci.*, vol. 150, no. 1, pp. 101–106, 1999.

[177] A. C. Ferrari *et al.*, 'Science and technology roadmap for graphene, related two-dimensional crystals, and hybrid systems', *Nanoscale*, vol. 7, no. 11, pp. 4598–4810, Mar. 2015.

[178] A. Kumar and C. Huei, 'Synthesis and Biomedical Applications of Graphene: Present and Future Trends', in *Advances in Graphene Science*, M. Aliofkhazraei, Ed. InTech, 2013.

[179] J. H. Choi, J. Lee, S. M. Moon, Y.-T. Kim, H. Park, and C. Y. Lee, 'A Low-Energy Electron Beam Does Not Damage Single-Walled Carbon Nanotubes and Graphene', *J. Phys. Chem. Lett.*, vol. 7, no. 22, pp. 4739–4743, 2016.

[180] P. Blake *et al.*, 'Making graphene visible', *Appl. Phys. Lett.*, vol. 91, no. 6, p. 063124, 2007.

[181] V. K. Khanna, *Nanosensors: physical, chemical, and biological*. CRC Press, 2011.

[182] A. B. Kuzmenko, E. Van Heumen, F. Carbone, and D. Van Der Marel, 'Universal optical conductance of graphite', *Phys. Rev. Lett.*, vol. 100, no. 11, p. 117401, 2008.

[183] M. Green and M. Keevers, 'Optical properties of intrinsic silicon at 300 K', *Prog. Photovolt. Res. Appl.*, vol. 3, pp. 189–192, 1995.

[184] K. Stella, *Electronic dissipation processes during chemical reactions on surfaces*. disserta Verlag, 2011.

[185] Q.-W. Sheng *et al.*, 'Tunable graphene saturable absorber with cross absorption modulation for mode-locking in fiber laser', *Appl. Phys. Lett.*, vol. 105, no. 4, p. 041901, Jul. 2014.

[186] G. Kalita, L. Qi, Y. Namba, K. Wakita, and M. Umeno, 'Femtosecond laser induced micropatterning of graphene film', *Mater. Lett.*, vol. 65, no. 11, pp. 1569–1572, Jun. 2011.

[187] H. Abderrazak and E. S. B. H. Hmida, 'Silicon carbide: synthesis and properties', in *Properties and applications of Silicon Carbide*, InTech, 2011.

[188] V. L. Stolyarova, E. N. Plotnikov, and S. I. Lopatin, 'Bond Energies In Oxide Systems: Calculated and Experimental Data', *Inst. Silic. Chem. Russ. N Acad. Sci. Ul Odoevskogo KorpSankt Petersburg Russ.*, vol. 2, 1991.

[189] R. Walsh and J. M. Wells, 'Kinetics of the gas-phase reaction between iodine and trichlorosilane and the bond dissociation energy D (Cl 3 Si—H)', *J. Chem. Soc. Faraday Trans. 1 Phys. Chem. Condens. Phases*, vol. 72, pp. 1212–1220, 1976.

[190] S. Rajesh and Y. Bellouard, 'Towards fast femtosecond laser micromachining of fused silica: The effect of deposited energy', *Opt. Express*, vol. 18, no. 20, p. 21490, Sep. 2010.

[191] A. C. Ferrari, 'Raman spectroscopy of graphene and graphite: disorder, electron–phonon coupling, doping and nonadiabatic effects', *Solid State Commun.*, vol. 143, no. 1, pp. 47–57, 2007.

[192] L. G. Cançado *et al.*, 'Quantifying Defects in Graphene via Raman Spectroscopy at Different Excitation Energies', *Nano Lett.*, vol. 11, no. 8, pp. 3190–3196, Aug. 2011.

[193] D. Ziegler *et al.*, 'Variations in the work function of doped single- and few-layer graphene assessed by Kelvin probe force microscopy and density functional theory', *Phys. Rev. B*, vol. 83, no. 23, Jun. 2011.

[194] V. Panchal, R. Pearce, R. Yakimova, A. Tzalenchuk, and O. Kazakova, 'Standardization of surface potential measurements of graphene domains', *Sci. Rep.*, vol. 3, p. 2597, Sep. 2013.

[195] L. Colombo, R. M. Wallace, and R. S. Ruoff, 'Graphene growth and device integration', *Proc. IEEE*, vol. 101, no. 7, pp. 1536–1556, 2013.

[196] Y.-M. Lin *et al.*, '100-GHz transistors from wafer-scale epitaxial graphene', *Science*, vol. 327, no. 5966, pp. 662–662, 2010.

[197] X. Wang, Z. Cheng, K. Xu, H. K. Tsang, and J.-B. Xu, 'High-responsivity graphene/silicon-heterostructure waveguide photodetectors', *Nat. Photonics*, vol. 7, no. 11, pp. 888–891, 2013.

[198] Z. Jin, P. Owour, S. Lei, and L. Ge, 'Graphene, graphene quantum dots and their applications in optoelectronics', *Curr. Opin. Colloid Interface Sci.*, vol. 20, no. 5, pp. 439–453, 2015.

[199] E. Shi *et al.*, 'Colloidal antireflection coating improves graphene–silicon solar cells', *Nano Lett.*, vol. 13, no. 4, pp. 1776–1781, 2013.

[200] R. Won, 'Photovoltaics: graphene-silicon solar cells', *Nat. Photonics*, vol. 4, no. 7, p. 411, 2010.

[201] Y. Yao, X. Chen, H. Guo, Z. Wu, and X. Li, 'Humidity sensing behaviors of graphene oxide-silicon bi-layer flexible structure', *Sens. Actuators B Chem.*, vol. 161, no. 1, pp. 1053–1058, 2012.

[202] J.-H. Kim *et al.*, 'Work function engineering of single layer graphene by irradiation-induced defects', *Appl. Phys. Lett.*, vol. 103, no. 17, p. 171604, 2013.

[203] M. Z. Hossain, S. Rumyantsev, M. S. Shur, and A. A. Balandin, 'Reduction of 1/f noise in graphene after electron-beam irradiation', *Appl. Phys. Lett.*, vol. 102, no. 15, p. 153512, 2013.

[204] J. Son *et al.*, 'Hydrogenated monolayer graphene with reversible and tunable wide band gap and its field-effect transistor', *Nat. Commun.*, vol. 7, 2016.

[205] C. Zhang, L. Fu, N. Liu, M. Liu, Y. Wang, and Z. Liu, 'Synthesis of Nitrogen-Doped Graphene Using Embedded Carbon and Nitrogen Sources', *Adv. Mater.*, vol. 23, no. 8, pp. 1020–1024, Feb. 2011.

[206] A. L. M. Reddy, A. Srivastava, S. R. Gowda, H. Gullapalli, M. Dubey, and P. M. Ajayan, 'Synthesis Of Nitrogen-Doped Graphene Films For Lithium Battery Application', *ACS Nano*, vol. 4, no. 11, pp. 6337–6342, Nov. 2010.

[207] P. J. Larkin, W. G. Gustafson, and S. A. Asher, 'A new Raman cross section measurement technique monitors the tyrosine environmental dependence of the electromagnetic field strength', *J. Chem. Phys.*, vol. 94, no. 8, pp. 5324–5330, Apr. 1991.

[208] P. T. Araujo, M. Terrones, and M. S. Dresselhaus, 'Defects and impurities in graphene-like materials', *Mater. Today*, vol. 15, no. 3, pp. 98–109, Mar. 2012.

[209] I. Milošević *et al.*, 'Kohn anomaly in graphene', *Mater. Sci. Eng. B*, vol. 176, no. 6, pp. 510–511, 2011.

[210] M. Lazzeri and F. Mauri, 'Nonadiabatic Kohn anomaly in a doped graphene monolayer', *Phys. Rev. Lett.*, vol. 97, no. 26, p. 266407, 2006.

[211] S. Piscanec, M. Lazzeri, F. Mauri, A. C. Ferrari, and J. Robertson, 'Kohn Anomalies and Electron-Phonon Interactions in Graphite', *Phys. Rev. Lett.*, vol. 93, no. 18, Oct. 2004.

[212] F. Banhart, J. Kotakoski, and A. V. Krasheninnikov, 'Structural defects in graphene', *ACS Nano*, vol. 5, no. 1, pp. 26–41, 2010.

[213] V. V. Cheianov, V. Fal'ko, and B. L. Altshuler, 'The focusing of electron flow and a Veselago lens in graphene pn junctions', *Science*, vol. 315, no. 5816, pp. 1252–1255, 2007.

[214] T. Low, S. Hong, J. Appenzeller, S. Datta, and M. S. Lundstrom, 'Conductance asymmetry of graphene pn junction', *IEEE Trans. Electron Devices*, vol. 56, no. 6, pp. 1292–1299, 2009.

[215] E. C. Peters, E. J. Lee, M. Burghard, and K. Kern, 'Gate dependent photocurrents at a graphene pn junction', *Appl. Phys. Lett.*, vol. 97, no. 19, p. 193102, 2010.

[216] A. E. Gillam and E. S. Stern, 'Introduction to electronic absorption spectroscopy in organic chemistry', 1954.

[217] W. T. Elwell and J. A. F. Gidley, *Atomic-Absorption Spectrophotometry: International Series of Monographs in Analytical Chemistry*, vol. 6. Elsevier, 2013.

[218] W. L. Kruer, 'The physics of laser plasma interactions', 1988.

[219] G. Xing, H. Guo, X. Zhang, T. C. Sum, and C. H. A. Huan, 'The physics of ultrafast saturable absorption in graphene', *Opt. Express*, vol. 18, no. 5, pp. 4564–4573, 2010.

[220] S. Ekins, Y. Nikolsky, and T. Nikolskaya, 'Techniques: application of systems biology to absorption, distribution, metabolism, excretion and toxicity', *Trends Pharmacol. Sci.*, vol. 26, no. 4, pp. 202–209, 2005.

[221] S. Miret, R. J. Simpson, and A. T. McKie, 'Physiology and molecular biology of dietary iron absorption', *Annu. Rev. Nutr.*, vol. 23, no. 1, pp. 283–301, 2003.

[222] S. K. Sundaram and E. Mazur, 'Inducing and probing non-thermal transitions in semiconductors using femtosecond laser pulses', *Nat. Mater.*, vol. 1, no. 4, p. 217, 2002.

[223] A. V. Kolobov, P. Fons, A. I. Frenkel, A. L. Ankudinov, J. Tominaga, and T. Uruga, 'Understanding the phase-change mechanism of rewritable optical media', *Nat. Mater.*, vol. 3, no. 10, p. 703, 2004.

[224] J. Bonse, S. Baudach, J. Krüger, W. Kautek, and M. Lenzner, 'Femtosecond laser ablation of silicon–modification thresholds and morphology', *Appl. Phys. A*, vol. 74, no. 1, pp. 19–25, Jan. 2002.

[225] M. E. Siemens *et al.*, 'Quasi-ballistic thermal transport from nanoscale interfaces observed using ultrafast coherent soft X-ray beams', *Nat. Mater.*, vol. 9, no. 1, pp. 26–30, 2010.

[226] H. K. Park *et al.*, 'Temporal profile of optical transmission probe for pulsed-laser heating of amorphous silicon films', *Appl. Phys. Lett.*, vol. 61, pp. 749–751, Aug. 1992.

[227] R. Cerny, V. Chab, and P. Prikryl, 'Multiple-phase heat-conduction problems in pulsed laser processing of semiconductors', 1995.

[228] H. B. Callen, *Thermodynamics and an Introduction to Thermostatistics*. Wiley, 1985.

[229] J. Kaiser, T. Feng, J. Maassen, X. Wang, X. Ruan, and M. Lundstrom, 'Thermal transport at the nanoscale: A Fourier's law vs. phonon Boltzmann equation study', *J. Appl. Phys.*, vol. 121, no. 4, p. 044302, 2017.

[230] A. Menéndez-Manjón, P. Wagener, and S. Barcikowski, 'Transfer-matrix method for efficient ablation by pulsed laser ablation and nanoparticle generation in liquids', *J. Phys. Chem. C*, vol. 115, no. 12, pp. 5108–5114, 2011.

[231] C. P. Grigoropoulos, H. K. Park, and X. Xu, 'Modeling of pulsed laser irradiation of thin silicon layers', *Int. J. Heat Mass Transf.*, vol. 36, no. 4, pp. 919–924, 1993.

[232] J. R. Reitz, F. J. Milford, and R. W. Christy, *Foundations of electromagnetic theory*. Addison-Wesley Publishing Company, 2008.

[233] M. Born, E. Wolf, and E. Hecht, 'Principles of Optics: Electromagnetic Theory of Propagation, Interference and Diffraction of Light', *Nucl. Phys.*, vol. 53, no. 10, pp. 77–78, 2000.

[234] Z. Knittl and P. H. Berning, 'Optics of Thin Films', *Phys. Today*, vol. 30, no. 2, pp. 59–60, 1977.

[235] L. Jiang and H.-L. Tsai, 'Modeling of ultrashort laser pulse-train processing of metal thin films', *Int. J. Heat Mass Transf.*, vol. 50, no. 17–18, pp. 3461–3470, 2007.

[236] G. E. Jellison Jr. and H. H. Burke, 'The temperature dependence of the refractive index of silicon at elevated temperatures at several laser wavelengths', *J. Appl. Phys.*, vol. 60, pp. 841–843, Jul. 1986.

[237] W. Xiong *et al.*, 'Direct writing of graphene patterns on insulating substrates under ambient conditions', *Sci. Rep.*, vol. 4, p. srep04892, May 2014.

[238] S. K. Jang, J. Jeon, S. M. Jeon, Y. J. Song, and S. Lee, 'Effects of dielectric material properties on graphene transistor performance', *Solid-State Electron.*, vol. 109, pp. 8–11, 2015.

[239] Z. Peng *et al.*, 'Flexible boron-doped laser-induced graphene microsupercapacitors', *ACS Nano*, vol. 9, no. 6, pp. 5868–5875, 2015.

[240] Y. Song, Y. Luo, C. Zhu, H. Li, D. Du, and Y. Lin, 'Recent advances in electrochemical biosensors based on graphene two-dimensional nanomaterials', *Biosens. Bioelectron.*, vol. 76, pp. 195–212, 2016.